University of Strathclyde Glasgow

Patient-specific multi-dimensional CFD simulations based on 4D Flow-MRI for the haemodynamic assessment of aortic dissections and perfusion optimisation of vascular grafts

Scott MacDonald Black

Department of Biomedical Engineering

University of Strathclyde

This thesis is submitted for the degree of

EngD Medical Devices & Healthcare Technologies

2024

Declarations

This thesis is the result of the author's original research. It has been composed by the author and has not been previously submitted for examination which has led to the award of a degree. The copyright of this thesis belongs to the author under the terms of the United Kingdom Copyright Acts as qualified by University of Strathclyde Regulation 3.50. Due acknowledgement must always be made of the use of any material contained in, or derived from, this thesis.

Signed,

Scott Black
30th June 2024

Abstract

Aortic dissection is a vascular pathology which affects 5-30 per million people. Due to regions of high shear stress and weakness in the vessel wall, the intimal layer of the aorta tears, separating it from the media and creating a channel known as a false lumen. AD is a progressive condition due to the cyclical relationship between structural changes and haemodynamic instability. Often, it is fatal in the absence of surgical intervention, with mortality rates up to 90% depending on the dissection type and severity.

The preferred treatment for Type A and Type B aortic dissections is open and endovascular surgical intervention, respectively. With both treatment options, there are associated complications including graft migration, branch vessel hypoperfusion, endoleaks, stent strut fracture, thrombosis, and graft limb occlusion. Generally, these failure mechanisms are related to the internal flow regime and post-surgical haemodynamics.

At present, it is difficult to predict the internal haemodynamics within these grafts before they are deployed. Therefore, this thesis seeks to understand whether we can use 4D Flow-MRI in combination with CFD modelling to build pre-surgical models of aortic dissections to assist in surgical planning. Leveraging CFD in combination with 4D Flow-MRI mitigates the intrinsic limitations of each approach. With 4D Flow-MRI, it is possible to extract *in vivo* flow rates and wall motion, and elucidate qualitative and quantitative information on the evolution of blood flow throughout the cardiac cycle. However, the spatiotemporal resolution is limited and it is not possible to extract pressure or near-wall haemodynamics. CFD, in contrast, offers a significantly enhanced level of detail, permitting the calculation of clinically relevant parameters such as pressure, TAWSS, and OSI with high spatiotemporal resolution.

To generate high-fidelity CFD models would require a methodology to process the quantitative blood flow data to extract anatomical information and calibrate boundary conditions. Commonly, this requires multiple imaging scans and boundary conditions rely on invasive measurements or several assumptions from multiple sources. In this thesis, we seek to extract all relevant information from a single 4D Flow-MRI scan to generate patient-specific CFD models. To the best of our knowledge, this has not yet been performed before.

We therefore present a methodology to generate high-contrast anatomical images from retrospective 4D flow-MRI data. This permitted successful segmentation and reconstruction of a healthy aorta, along with the true lumen and branch vessels of the dissected aorta. However, it was not possible to generate sufficient contrast within the false lumen due to low flow rates.

To do so would require multi-VENC 4D Flow-MRI imaging which was not available during this study.

Though it is possible to directly prescribe pressure (from an invasive catheter) and flow (from 4D Flow-MRI) waveforms as BCs to the CFD model, this is inappropriate for several reasons. Primarily, this is because branch flow and pressure waveforms are part of the desired solution for surgical planning. Secondly, the direct prescription of flow waveforms fails to yield correct pressure measurements since the downstream resistance and compliance is not accounted for, unlike in 3EWM BCs. Thirdly, the prescription of pressure waveforms requires invasive catheter measurements and increased patient burden. Therefore, we describe a methodology for the rapid estimation and calibration of patient-specific Windkessel boundary conditions based on 4D Flow-MRI data. This yielded a perfusion distribution very similar to *in vivo* data without the need for requiring invasive pressure or flow measurements.

Finally, we evaluated the haemodynamic environment in the aortae of healthy volunteers and Type B aortic dissection cases via coupled 0D-3D numerical modelling. Such simulations may assist in determining regions of vessel wall instability to identify patients who are at the highest risk of false lumen rupture.

The present thesis shows that all the essential components required for a patient-specific CFD analysis could be derived from a single 4D Flow-MRI scan, with a view to replace CT imaging and non-specific boundary conditions. The methodologies presented could further be improved in the future, by utilising multi-VENC imaging and prescribing 4D Flow-MRI derived wall motion. This may reduce the burden on patients since it is a non-invasive, non-ionising approach which does not require intravenous contrast agents.

Funding

This work was supported in part by the UK Research and Innovation (UKRI) Engineering and Physical Sciences Research Council (EPSRC) Award Ref. EP/L015595/1 through the University of Strathclyde Centre of Doctoral Training. The author gratefully acknowledges the financial support provided by Terumo Aortic

Conflict of Interests /Competing Interests

This study received funding from Terumo Aortic. The funder was involved with interpretation of data and manuscript review of journal publications. Scott MacDonald Black has received a research grant from the UK Research and Innovation (UKRI) Engineering and Physical Sciences Research Council (EPSRC) Award Ref. EP/L015595/1 through the University of Strathclyde Centre of Doctoral Training.

Human Studies / Informed Consent

All procedures followed were in accordance with the ethical standards of the responsible committee on human experimentation (institutional and national) and with the Helsinki Declaration of 1975, as revised in 2000 (5). Informed consent was obtained from all patients for being included in the study.

Ethics Statement

The analysis of clinical CT and 4D Flow-MRI data involving human participants were reviewed and approved by South-East Scotland Research Ethics Committee (IRAS Project ID: 287048, REC Reference: 20/SS/0118).

List of Publications

Journal Articles

- **S. M. Black**, C. Maclean, P. Hall-Barrientos, K. Ritos and A. Kazakidi, "Reconstruction and Validation of Arterial Geometries from 4D Flow-MRI Images: A Novel Approach" *Cardiovascular Engineering and Technology* 14:655–676, 2023. https://doi.org/10.1007/s13239-023-00679-x.
- **S. M. Black**, C. Maclean, P. Hall-Barrientos, K. Ritos, A. McQueen and A. Kazakidi, "Calibration of Patient-Specific Boundary Conditions for Coupled CFD Models of the Aorta Derived from 4D Flow-MRI", *Frontiers in Bioengineering and Biotechnology*, 2023 11:1178483. https://doi.org/10.3389/fbioe.2023.1178483.
- M. Boumpouli, **S. M. Black**, A. Kazakidi, "Computational analysis of blood flow in healthy pulmonary arteries in comparison to repaired Tetralogy of Fallot results: a small cohort study" *Fluids* 9:85, 2024. https://doi.org/10.3390/ fluids9040085.
- **S. M. Black**, C. Maclean, P. Hall-Barrientos, K. Ritos and A. Kazakidi, "An Investigation of Type B Aortic Dissection Haemodynamics in Patient-Specific Models for Surgical Planning and Outcome Assessment" *in preparation.*

Oral Conference Presentations

- S. M. Black, K. Ritos, C. Maclean, R. Brodie, A. Kazakidi, "Perfusion optimisation for vascular grafts design used in the treatment of aortic disease", Terumo Academic Collaborations, Glasgow, 2019.
- S. M. Black, K. Ritos, C. Maclean, R. Brodie, A. Kazakidi, "Effect of Windkessel Boundary Conditions on 3D Blood Flow Simulations in the Aortic Arch" 33rd Scottish Fluid Mechanics Meeting, Dundee, 2020.
- S. M. Black, K. Ritos, C. Maclean, R. Brodie, A. Kazakidi, "Haemodynamic analysis of a patient-specific aortic arch geometry using 4D-MRI and computational fluid dynamics in a coupled 3D-0D framework", World Congress of Computational Mechanics, Virtual, 2020.
- S. M. Black, C. Maclean, P. Hall-Barrientos, K. Ritos, A. Boukis, and A. Kazakidi, "The Effect of Lumped Parameter Boundary Conditions in Image-Based Modelling of the Thoracic Aorta Through CFD", Virtual, 26th Congress of the European Society of Biomechanics, 2021.

- S. M. Black, K. Ritos, C. Maclean, R. Brodie, A. Kazakidi, "*Patient Specific CFD Models Investigated in a Novel 0D-3D Numerical Framework, Based on 4D-MRI and CT Imaging*", 16th United States National Congress on Computational Mechanics, Virtual, 2021.
- S. M. Black, C. Maclean, P. Hall-Barrientos, K. Ritos, and A. Kazakidi, "An In Silico Pipeline for Patient-Specific Haemodynamic Analysis of the Aorta", 27th Congress of the European Society of Biomechanics, Virtual, 2022.
- S. M. Black, C. Maclean, P. Hall-Barrientos, K. Ritos, and A. Kazakidi, "A Multi-Dimensional, Multi-Modality Approach to Optimise Perfusion in Vascular Stent-Graft",8th European Congress on Computational Methods in Applied Sciences and Engineering, Oslo, 2022.
- S. M. Black, C. Maclean, P. Hall-Barrientos, K. Ritos, and A. Kazakidi, "Numerical Investigation of Aortic Hemodynamics and Vascular Stent-Grafts Using 4D Flow-MRI and Patient-Specific CFD Models", Institute of Biological Engineering, Georgia (USA). 2022.
- S. M. Black, C. Maclean, P. Hall-Barrientos, K. Ritos, and A. Kazakidi., "Perfusion optimisation for vascular grafts design used in the treatment of aortic disease", Terumo Academic Collaborations, Glasgow, 2023.

Poster Conference Presentations

- S. M. Black, K. Ritos, C. Maclean, R. Brodie, Asimina Kazakidi, "Blood flow analysis of the aortic arch using computational fluid dynamics in a coupled 3D-0D framework", Scottish Cardiovascular Forum Annual Meeting, Glasgow, 2020
    - Winner of Best Poster Prize
- S. M. Black, K. Ritos, C. Maclean, R. Brodie, Asimina Kazakidi, "A Multi-Modality, Multi-Dimensional Approach to Investigate Blood Flow in the Thoracoabdominal Aorta Through CFD", BiomedEng21, Sheffield, 2021.

Contents

List of Figures

List of Tables

Abbreviations

0D:	Zero-dimensional
1D:	One-dimensional
3D:	Three-dimensional
3EWM:	Three-element Windkessel model
4D Flow MRI:	Four-dimensional flow magnetic resonance imaging
AD:	Aortic Dissection
BC:	Boundary condition
C:	Compliance
CFD:	Computational fluid dynamics
CPC-MRA:	Composite phase-contrast magnetic resonance angiogram
CSA:	Cross-sectional area
CT:	Computed Tomography
Dao:	Descending aorta
DBP:	Diastolic blood pressure
DICOM:	Digital Imaging and Communications in Medicine
DNS:	Direct numerical simulation
DSC:	Dice Similarity Coefficient
ECG:	Electrocardiogram
FEM:	Finite element method
FL:	False lumen
FSI:	Fluid-structure interaction
FVM:	Finite volume method
GCIO:	Grid convergence index
HD:	Hausdorff distance
LCCA:	Left common carotid artery
LES:	Large eddy simulation
LSA:	Left subclavian artery
MRA:	Magnetic resonance angiography
MRI:	Magnetic resonance imaging
OSI:	Oscillatory shear index
PCA:	Phase contrast angiogram
PC-MRI:	Phase contrast magnetic resonance imaging

PS:	Peak systole
PWV:	Pulse wave velocity
R:	Peripheral resistance
RANS:	Reynolds averaged Navier Stokes
RCCA:	Right common carotid artery
Re:	Reynolds number
RF:	Radiofrequency
ROI:	Region of Interest
RRT:	Relative resonance time
RSA:	Right subclavian artery
SA:	Systolic acceleration
SBP:	Systolic blood pressure
SD:	Systolic deceleration
SNR:	Signal to noise ratio
TAAD:	Type A aortic dissection
TAWSS:	Time averaged wall shear stress
TBAD:	Type B aortic dissection
TL:	True lumen
UDF:	User defined function
VENC:	Velocity encoding
VMTK:	Vascular Modelling Toolkit
WSS:	Wall shear stress
Z:	Characteristic impedance

Acknowledgements

I would like to thank my primary supervisor, Dr Asimina Kazakidi for her incredible support throughout this EngD research. Her dedication, patience, kindness, and understanding cannot be overstated. She was with me every step of the way, provided words of encouragement, and was instrumental in shaping this research. Thank you for proofreading articles, helping me prepare for conferences, for establishing collaborations, and for always checking in. Most of all, thank you for giving me the confidence to progress through the EngD and beyond. I honestly couldn't have asked for a better mentor.

I would also like to extend my thanks to my second supervisor, Dr. Konstantinos Ritos. His technical expertise was invaluable to this research, and his knowledge helped me navigate a lot of roadblocks along the way. Again, Konstantinos always provided words of support, guidance, and seemed to be able to answer any (of the many) questions that were thrown at him.

A huge thanks to Dr Craig Maclean, my industrial supervisor who went above and beyond to provide any support he could. Also, I'd like to express my gratitude to Dr Robbie Brodie, my second industrial supervisor who oversaw the project and ensured I had all the resources I needed. I'm truly grateful to both Craig and Robbie for their continued understanding while I figured out whether to pursue a corporate or startup career. I can't tell you how much I appreciate it - their patience and support during that period helped me get to where I am today.

Thank you to Dr Hall Barrientos, who provided 4D Flow-MRI data and clinical support throughout the entirety of this research. I don't know where I'd be without your support, expertise, and input.

To everyone in the Biofluids group, George, and Lauren, Maria, and Marianna – it was an absolute pleasure. The collaborative research was fantastic, but the friendships we made along the way were even better. Thank you also to Dr Alistair McQueen, a long-term friend and now research collaborator, for helping to develop the boundary condition calibration methodology.

Finally, I'd like to thank my family for their incredible support, in too many ways to list. To Jen and Ross, thank you for always asking how things were going. It was great to know that you guys seemed genuinely interested in my work. To Dad, thank you for the continual

motivation and giving me the drive to know I can do anything I set my mind to. To Mum, I don’t even know where to start. Thank you for everything, and your unlimited words of encouragement, even when times were tough. I couldn’t have done it without you guys.

1 Introduction

1.1 Aortic Pathology

Aortic pathology can manifest clinically in various forms, including aortic aneurysms, dissection, atherosclerosis, and trauma. Each condition carries distinct symptoms, treatment plans, and associated risks. Common to all pathologies is an altered geometry and morphology of the aortic wall which detrimentally impacts the blood flow regime.

1.1.1 Aortic Dissection

Aortic dissection (AD) is a relatively uncommon condition (5-30 per million people) which occurs when the intima of the aorta tears, resulting in separation from the media (Figure 1.1) [1] [2] [3]. Consequently, blood can then flow between the layers, creating a channel known as a false lumen (FL) or dissection [1]. The true lumen (TL) and FL are separated by a primary intimal flap, often with multiple distal tears which connect the lumina [4]. The FL is largely deficient in elastin and therefore cannot easily accommodate the tension applied to it during systolic expansion [5]. Therefore, rupture of the FL, resulting in significant internal bleeding, is a concern and can occur when the aortic wall stress exceeds the yield strength [1] [6]. Routinely, two or more intraluminal tears are found in AD patients [4].

AD is more common in the older population and those with risk factors such as hypertension and dyslipidaemia, smoking, and atherosclerosis [7] [8]. Further, roughly 65% of cases are male [7]. Some individuals are genetically predisposed, including those with connective tissue disorders including Marfan Syndrome, Ehlers-Danlos Syndrome, and Loeys-Dietz Syndrome [1] [7] [8].

Commonly, dissections are located in regions of high flow disturbance, generally within the thoracic aorta [1] [4] [9]. There are two types of dissection: Type A and Type B [7]. Type A aortic dissections (TAAD) develop in the ascending aorta and the aortic arch, and often begin immediately distal to the aortic valve [1] [7] [9]. Type B aortic dissections (TBAD) occur within the distal aortic arch or descending aorta, generally beginning immediately downstream of the left subclavian artery [1] [7] [9]. Further, Type B dissections can extend along the entire length of the aorta and propagate into the common iliac arteries [7]. Approximately 37.3% of dissection cases are Type A, which tend to be more of a surgical emergency due to their proclivity to rupture [5] [7]. The flow regime within the aorta of a dissection patient depends on many factors, including the number of intraluminal tears which connect the TL and FL, the size of these tears, the diameter of the FL, and the degree of thrombosis present within the FL

[4]. The flow regime within the FL, the flow and pressure differences between the TL and FL, and wall shear stress are key factors which influence the inevitable expansion of the FL and collapse of the TL [4].

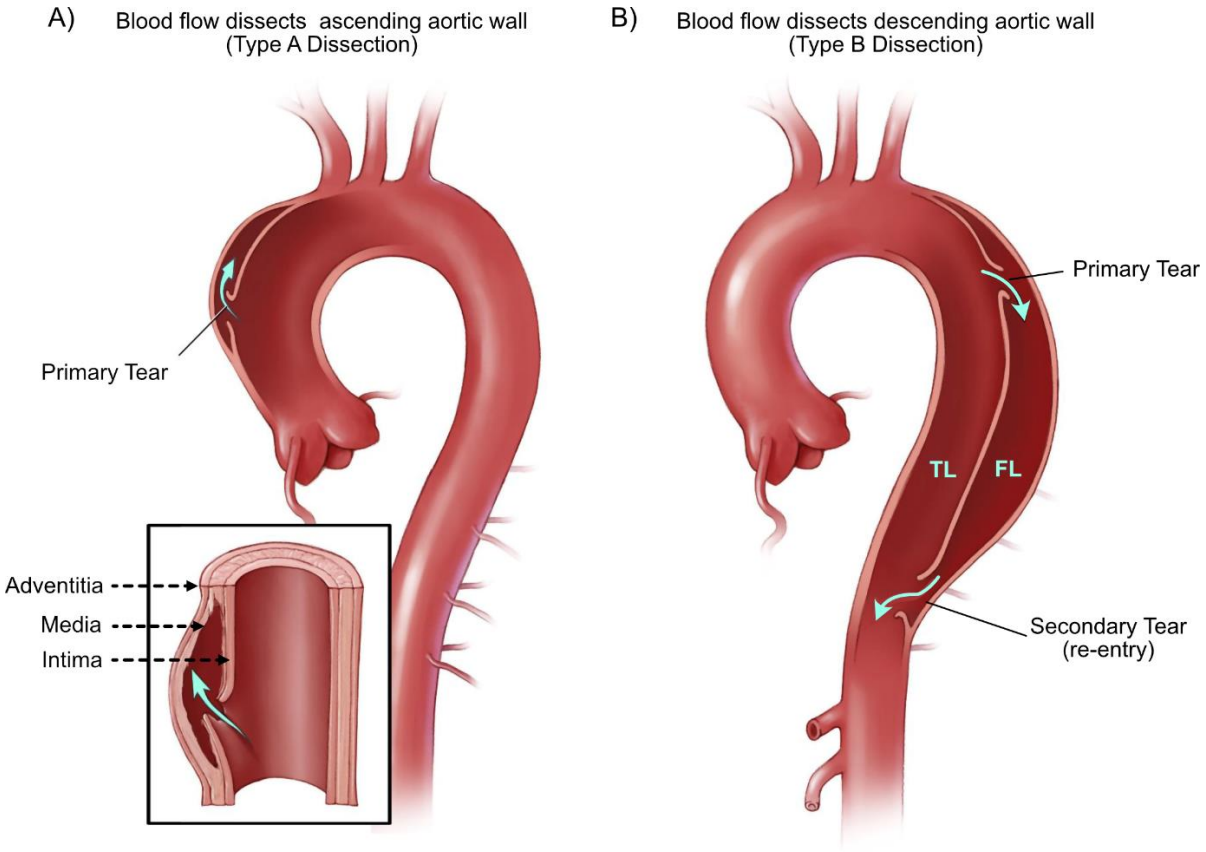

Figure 1.1: Modified figure from English and Klaas [10] showing a Type A and Type B aortic dissection, and the differentiation between the true lumen (TL) and false lumen (FL).

1.1.2 Complications Related to Aortic Dissection

In the absence of intervention, AD is a progressive condition due to the cyclical relationship between structural changes and abnormal flow. Haemodynamic instability induced by the dissection leads to morphological and structural changes of the true and false lumen. These morphological and structural changes then lead to further haemodynamic instability in a positive feedback loop which fuels disease progression. For example, increased pressure or volume of blood flow through the FL leads to rapid FL growth [4] [5]. This leads to increased occlusion of the TL and the resultant shear stress within the FL is augmented, further increasing the haemodynamic instability and risk of rupture [4] [5] [7].

Expansion of the FL often results in complete or partial obstruction of aortic branch vessels in 25-30% of patients, producing persistent or intermittent symptoms of peripheral organ

malperfusion, respectively [5]. This can occur in small or large branches, depending on the location of the dissection. For example, compression or obstruction of the coronary arterial ostium leads to myocardial ischaemia or infarction in 10-15% of cases [11]. Obstruction in larger branches such as the LSA, intercostal, and carotid arteries, often results in spinal and cerebral ischaemia [5].

Occlusion of the TL and aortic branches by the FL can be static or dynamic [5]. Static occlusion, which happens in 20% of cases, occurs when the FL propagates into a branch vessel, permanently obstructing blood flow [5]. Dynamic obstruction occurs in 80% of cases, and there are two discrete mechanisms for this [5]. Firstly, insufficient flow can result in hypoperfusion to a branch vessel which is supplied by the TL [5]. Secondly, the FL can intermittently prolapse into a branch ostium throughout the cardiac cycle, resulting in intermittent in flow obstruction [5].

1.1.3 Treatment for Aortic Dissection

TAAD presents as a surgical emergency. It is often fatal in the absence of rapid intervention, with mortality increasing in probability by 1-2% per hour [1] [3]. TAAD mortality rate is as high as 90%, while Type B is roughly 10% [12]. However, survival rates increase with appropriate medical and surgical intervention [1]. Even if the patient reaches hospital, the International Registry of Acute Aortic Dissection concluded that the overall in-hospital mortality for acute TAAD and TBAD of the thoracic aorta remains at 35% and 12% respectively [13].

The type of intervention depends on the dissection severity, location, comorbidities, and risk from surgery [8]. For TAAD, the standard treatment is open surgical intervention (Figure 1.2A). This is a procedure where the surgeon makes a large incision in the chest and opens the ribcage for full view of the thoracic cavity. Thereafter, the pathological aortic wall segment is resected and replaced with a synthetic graft [5] [13] [14]. This constitutes a major surgical procedure which requires general anaesthesia, prolonged periods of hypothermic circulatory arrest, and cardiopulmonary bypass [15] [12]. Further, the intervention must often be performed in multiple staged procedures, leading to an extensive recovery period [15] [16].

Conversely, in most patients with chronic TBAD, the conventional treatment is antihypertensive medications [12]. However, for acute TBAD cases which are associated with severe complications including aortic rupture, rapidly increasing disease severity, or peripheral limb ischaemia, surgical intervention is again the gold-standard care [12]. Recently,

endovascular repair (Figure 1.2B) has been introduced as the gold-standard treatment for chronic TBAD, with almost 40% of TBAD patients eventually requiring endovascular intervention [8] [13] [12]. This is a minimally invasive procedure in which a stent graft is deployed without resecting the native aorta. To do so, a surgeon makes an incision in the groin of a patient and a thin catheter is then threaded through the arterial network towards the location of the dissection, guided via x-ray fluoroscopy [7] [17]. The stent graft is then expanded *in vivo* to reinforce the artery wall from within [17]. Notably, since the graft must fit into the native vessel (instead of removing it and replacing it), computed tomography (CT) imaging is required before the procedure to assess the native vessel and understand the size and geometric requirements of the endovascular graft [7].

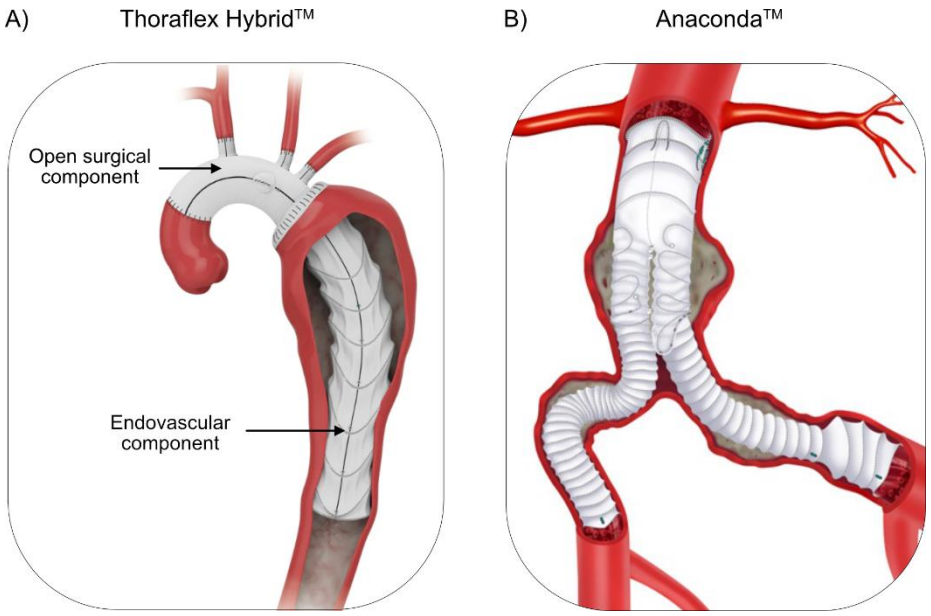

Figure 1.2: Images provided by Terumo Aortic which shows A) a Thoraflex Hybrid™ stent-graft which has an open component (aortic arch) and endovascular component (descending aorta) for treatment of the thoracic aorta, and B) an Anaconda™ stent-graft for the endovascular repair of the abdominal aorta and common iliac arteries.

1.1.4 Open vs Endovascular Surgery: Advantages and Disadvantages

1.1.4.1 Open Surgery

As previously described, open and endovascular surgery are two very different interventions, both of which are associated with their own advantages and disadvantages. Generally, open surgical intervention yields a more uniformly distributed post-surgical flow regime and better haemodynamics due to the geometry of these grafts [15]. This is important as disturbed flow at high wall shear rate regions (which exposes platelets to high shear) and recirculation zones provide a favourable haemodynamic environment for in-graft thrombus formation [16] [18].

Additionally, since there is a minimal requirement for surgical planning in comparison to endovascular procedures, open surgery is the gold standard treatment when rapid intervention is required in emergency cases.

However, due to the invasive nature of open surgery and high degree of trauma inflicted on the chest, it is associated with high mortality rates [15] [14]. Due to the anaesthesia, cardiopulmonary bypass and hypothermic circulatory arrest, there is an increased risk of hypoperfusion (reduced blood flow) in vital peripheral organs and spinal cord ischaemia [7] [12]. There is also a risk of renal failure, bleeding, infection, and post-surgical aneurysm formation [7] [14]. Thus, open surgery is associated with significant morbidity. Consequently, unless the patient presents with significant haemodynamic instability and acute symptoms (severe chest pain and neurologic deficits) an imminent risk of rupture, open surgery is avoided in favour of endovascular intervention [12].

1.1.4.2 Endovascular Surgery

In comparison with open surgery, endovascular intervention is associated with lower complication rates, reduced short-term mortality (10.6% vs 19%), shorter hospital stays, and is more economically viable [12] [19]. This is because it is a minimally invasive alternative which avoids excessive bleeding and blood transfusions, avoids injury to thoracic organs, and has reduced rates of infection since there is no open surgical cavity [12] [15] [19]. Therefore, endovascular repair is especially favourable in patients with co-morbidities who represent 'high-risk' cases who may not survive open surgery [14].

However, endovascular repair suffers from its own array of challenges. Since these stent-grafts are deployed within the native vessel, there is a risk that the graft obstructs a branch vessel ostium, resulting in increased difficulty maintaining patency of the branching visceral vessels [14]. For example, endovascular stents which encompass the descending aorta often obstruct the intercostal arteries, meaning it is imperative to preserve blood flow through the left subclavian artery to avoid spinal cord damage [5] [19]. Endovascular interventions also require regular follow up imaging to assess a variety of potential complications which are unique to this procedure. These include stent fracture and fatigue, graft migration, and endoleaks (post-surgical leakage of blood into the false lumen) [18] [20] [21]. Generally, these failure mechanisms of stent grafts are due to elevated regions of stress at bifurcations and fenestrations [21]. These are serious complications, as they often require a revision which must be done

through open surgery, thereby dramatically increasing the risk of morbidity and mortality [20] [22].

1.2 Post-surgical Malperfusion

Post-surgical malperfusion is a complication which is common to both open surgical and endovascular repair of aortic dissection [5]. This is because open and endovascular stent-grafts will inevitably alter local haemodynamics, especially if multiple different stent-grafts are deployed within the same patient [18]. If the malperfusion is severe enough, it can lead to peripheral organ ischemia which unfortunately is associated with a mortality rate of up to 45% [23]. There are several mechanisms which contribute to post-surgical malperfusion, related either to the positioning of the stent-graft itself, or the post-surgical flow regime.

1.2.1 Malperfusion due to Graft Positioning

To achieve optimal graft positioning which covers the entirety of the dissection, it is often the case that the graft itself will occlude the ostia of some branch vessels. For example, the deployment of an endovascular stent-graft in the thoracic aorta often requires coverage of the left subclavian artery and intercostal arteries [5]. Coverage of the LSA then induces cerebral malperfusion which, without reintervention to achieve a bypass, can result in stroke and death in 47% and 50% of patients, respectively [5] [23]. Additionally, coverage of the intercostal arteries is often necessary during the repair of a TBAD and can result in spinal cord ischaemia [5].

A second positional complication which results in reduced blood flow to certain regions is graft kinking. This is defined as an angulation of the stent-graft which occurs after surgical deployment, resulting in a region of stenosis and, at minimum, doubling of the peak systolic velocity [24]. Often, this occurs in branched sections of the stent-graft rather than the main body and occurs in 1.5% of all endovascular interventions [24]. Risk factors include tortuous native branch vessels, endograft twisting during deployment, or graft compression due to a pre-existing thrombus [24]. This is, however, a poorly understood phenomenon as the exact causation of kinking remains unknown [24].

1.2.2 Malperfusion due to Altered Haemodynamics

Malperfusion can remain after endovascular intervention due to a persistently patent FL [5] [23]. This means blood can still flow through the FL and can be observed to a degree in up to 50% of cases [5] [23]. If this FL remains patent, this predisposes the individual to a post-surgical aneurysm formation and risk of associated rupture [14].

A final, common cause of post-surgical malperfusion, particularly in endovascular stent-grafts, is intraluminal thrombosis [18]. This occurs in roughly 20% of cases and is characterised by the formation of a blood clot (thrombus) within the lumen, which subsequently reduces the vessel diameter and obstructs flow [18] [25] [26] [27]. Generally, there are three mechanisms by which the thrombus forms. Firstly, damage to the arterial wall caused by the stent-graft insertion can lead to an inflammatory cascade, resulting in the activation of platelets [18] [25] [26]. These activated platelets adhere to the vessel wall, form aggregates reinforced with the fibrin protein, and eventually grow to form a blood clot [25] [26]. Secondly, these platelets can become activated in regions of high shear stress, again leading to thrombosis [27]. Thirdly, thrombosis can occur due to blood stasis, as reduced or stagnant flow permits the accumulation of pro-coagulant molecules including thrombin [18] [25] [26] [27]. Stagnation and shear-related mechanisms of thrombosis are particularly apparent in regions where the main body bifurcates to smaller branch vessels [18].

In most cases, the aggregate of thrombotic material is low, meaning it does not present any clinical symptoms and does not require treatment [18]. However, in more severe cases, this can lead to graft limb occlusion (complete blockage of a branch segment) and micro-embolism which can lead to fatal multi-organ failure [18]. Generally, thrombotic deposits do not clear completely from the prosthesis lumen, even after postoperative anti-platelet or anticoagulation medication, so it is important to ensure this is avoided before it forms [18]. Therefore, it is clear that stent-graft deployment can have a significant adverse effect on arterial blood flow, and a substantial degree of complications stem from these abnormal flow regimes.

1.3 General Function of the Circulatory System

The cardiovascular system is an internal flow loop which pumps blood throughout the body via a sophisticated network of branching vessels known as arteries and veins [28]. It functions primarily as a nutrient and waste transport system, also facilitating hormone signalling, temperature regulation, and immune responses [28] [29]. Figure 1.3 illustrates the direction of blood flow through the heart during the cardiac cycle, comprising of two distinct phases known as systole and diastole.

During systole, oxygenated blood is ejected from the left ventricle of the heart when ventricular contraction causes the pressure within the ventricles to exceed the pressure within the blood vessels [28]. This means blood is ejected through the aortic valve from the left ventricle into

the aorta. This oxygenated blood is carried through the arterial tree towards the capillaries which permit nutrient exchange and waste removal with tissues and peripheral organs and tissue. The venous system then transports de-oxygenated blood back to the heart along the peripheral veins, through the vena cava, finally reaching the right atrium. During diastole, the ventricles relax and fill with blood from the atria in preparation for the next systolic contraction. In parallel, blood is ejected from the right ventricle through the pulmonary valve and into the pulmonary arteries where it is re-oxygenated. This is then returned to the left atrium and ventricle, where it is once again ejected into the aorta to continue the cycle.

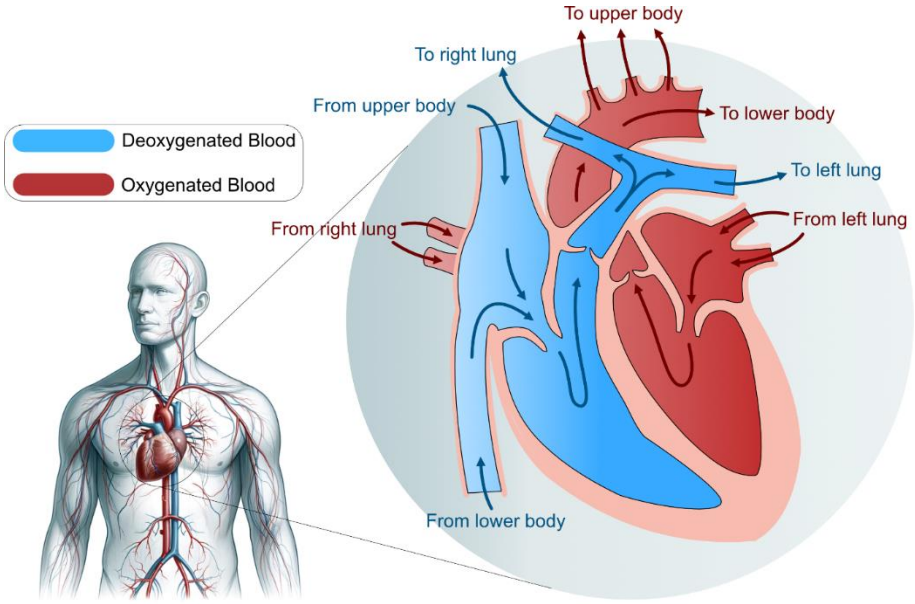

Figure 1.3: The internal circulation of oxygenated and deoxygenated blood within the heart, with arrows illustrating the direction of blood flow.

1.4 Blood Flow

1.4.1 Pulse Waveforms

Blood flow in arteries is highly pulsatile due to the differing cardiac phases and distensible arterial walls [29] [30]. When blood is ejected via ventricular contraction, the intraluminal vessel pressure increases, and the vessel wall distends locally to accommodate the rapid increase in blood volume during systole [29] [31]. Since blood is regarded as an incompressible fluid in larger arteries, the velocity of blood therefore has an inverse relationship with vessel cross-sectional area (Eq 1.1) [29] [31].

$$Q = AU \tag{1.1}$$

where Q is the volumetric flow rate, U is the velocity of blood flow, and A is the internal cross-sectional area of the vessel.

When the potential energy stored within the arterial walls is released during diastole, the restorative elasticity of the artery causes the arteries to contract, propelling blood towards the microcirculation [29] [31] [32]. This rhythmic expansion and contraction of the arteries therefore follows the cardiac rhythm and propagates in the form of waves, known as pulse waves [29]. In turn, this produces pressure and flow waves which propagate forward, away from the heart, where the peak of the flow wave precedes the peak of the pressure wave [29] [33]. The exact shape and magnitude of these pressure and flow waves varies between individuals, and patients with aortic disease will exhibit irregularities [17]. Systolic blood pressure (SBP) and diastolic blood pressure (DBP) are the highest and lowest pressures within an artery during the cardiac cycle, respectively.

A normal aorta exhibits a nonlinear stress-strain curve, is highly deformable, and, like all arteries, displays anisotropic mechanical properties [32] [34]. Due to the distensible arterial walls and their varying properties, viscoelastic damping occurs, where the highly pulsatile arterial pressure waveform is progressively smoothed as a function of increasing distance from the heart [29]. This protects the stiff peripheral vessels and microcirculation from large variations in blood pressure, and generates smoother flow through the capillaries [32] [35] [36].

A portion of these pulse waves are also reflected backwards, towards the heart, when a propagating wave encounters a structural discontinuity [29] [31]. This may be, for example, branching vessels, peripheral impedance, or variations in elastic wall properties or anatomical variations (including pathology) [29] [31]. Consequently. only a portion of the original pulse waveform is transmitted [31].

1.4.2 Flow Regime

The combination of high blood flow rate and the curvature of the aorta results in a unique and complex flow field, creating secondary flow dynamics, helical flow, and asymmetrical bulk flow [9] [17] [28] [37] [38]. Notably, the exact anatomical arrangement, and therefore flow regime, is also unique to the individual, though healthy aortae will exhibit very similar configurations [9] [17].

Flow within the aorta may be transiently turbulent [15]. The Reynolds number (Re), a dimensionless number used to categorise whether inertial or viscous forces prevail in the flow and thus indicate a laminar or turbulent flow, may be expressed as Eq 1.2:

$$Re = \frac{\rho U L}{\mu} \tag{1.2}$$

where ρ is the fluid density, μ is the dynamic viscosity, L is the characteristic length (hydraulic diameter for internal flows), and U is the fluid velocity [39]. Typically, the mean Re in healthy individuals is ~1000-1300, while the peak is ~3500-4800 [39]. Notably, these mean and peak values vary along the length of the aorta, with highest values in the ascending aorta, decreasing within the arch, and increasing again in the descending aorta [39].

In an internal flow through a pipe, one would expect the transition from laminar to turbulent flow to occur around Re of 2000-4000. However, pulsating flow introduces complexities since accelerating flow during systole tends to be more stable than steady flows, while decelerating flows during diastole tend to be less stable [6] [17] [30] [39]. The frequency of the cardiac pulse also affects flow stability [39].

This means that the Reynolds number for the transition to turbulent flow in the aorta tends to be in the region of 2600 to 11400, but is typically observed to be around 4000 [6] [17] [28] [30]. Therefore, a range of factors including anatomical arrangement, location along the aorta, pulse frequency, flow rate, and the stage of the cardiac cycle all influence turbulence. Understanding this flow regime is crucial as turbulence and velocity fluctuations likely play a role in the initiation and progression of aortic disease, contributing to haemolysis, platelet activation, thrombus formation, and atherosclerosis [39]. Figure 1.4 illustrates blood flow during the systolic and diastolic phases within the distal aortic arch of a healthy individual (see Chapter 5, Table 5.1 for demographic and imaging details).

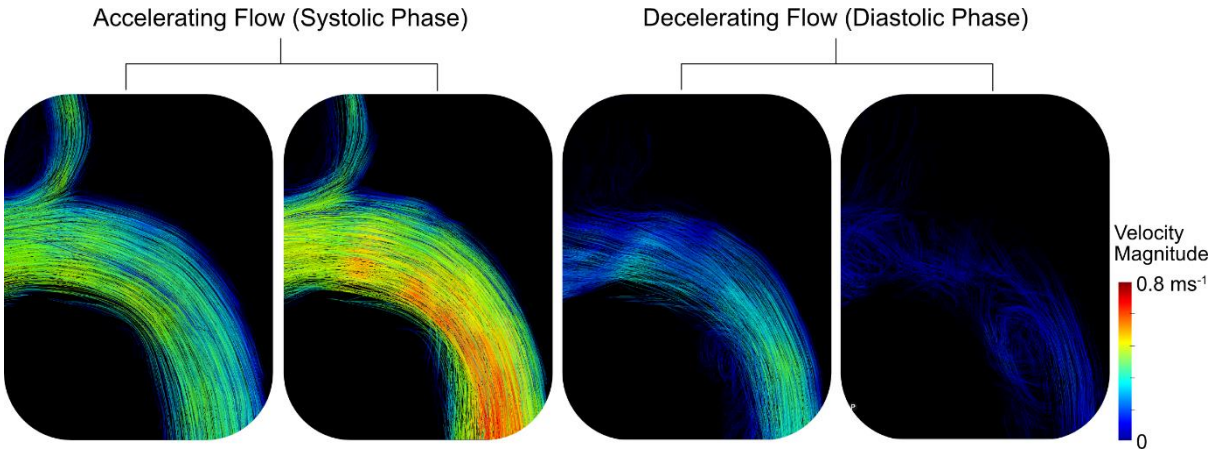

Figure 1.4: Velocity streamlines showing accelerating and decelerating flow. Decelerating flow has more turbulence and recirculation. Streamlines were extracted from 4D Flow-MRI images of an aortic arch of a healthy volunteer (see Chapter 5, Table 5.1 for details of the demographic and imaging data).

1.4.3 Perfusion Distribution

By responding to various stimuli which includes blood volume, hormones, nervous system activation, electrolytes, osmolarity, and medication, the blood vessel diameter is continually adjusted to regulate blood flow to peripheral organs [36]. For example, baroreceptors within the carotid sinus and aortic arch are key to the regulation of blood pressure. Decreased blood pressure leads to a reduction of arterial pressure, which reduces the stretch of baroreceptors and decreases the intensity of baroreceptor signalling [36]. This results in an increase in sympathetic nervous activity, yielding an increase in heart rate, vasoconstriction, and therefore blood pressure. Similarly, chemoreceptors located in the carotid body and aortic arch are stimulated when oxygen, carbon dioxide, and pH levels change. In this manner, the cardiovascular system can autoregulate blood flow, despite continual changes in blood pressure, to maintain a stable baseline state.

Due to this autoregulation, the perfusion distribution of blood in healthy individuals tends to follow a general trend. Roughly 5% of the cardiac output supplies the coronary circulation which perfuses the myocardium, 13% ± 1.4% enters the innominate artery, and 16% ± 2.9% is split between the left common carotid artery (LCCA) and left subclavian artery (LSA) [40] [41] [42]. The rest (71% ± 4.3%) flows through the descending aorta to supply the lower body [41] [42]. The optimal perfusion distribution is impacted by aortic disease, resulting in varying degrees of peripheral organ malperfusion, which is defined as a substantial decrease in blood supply to one or more organs [5] [23]. This can affect nearly all vascular beds and will inevitably lead to patient morbidity and, in more severe cases, mortality due to peripheral organ ischaemia [5] [23].

1.5 Blood Vessels

1.5.1 Arterial Tree

Arteries are thick walled, elastic blood vessels which accommodate the highest-pressure blood flow [29]. The aorta, for example, is the first and largest arterial segment of the human systemic circulation through which blood flows at roughly 5 litres per minute [34] [43]. This volume splits into four main fractions: the innominate artery, left common carotid artery, left subclavian artery and the descending aorta [41] [42]. With each bifurcation towards the periphery thereafter, the daughter branches of the arterial tree reduce in size from 2-4cm in diameter at the aorta, to 0.1mm diameter arterioles which perfuse the microcirculation [29] [44]. Within the microcirculation, capillaries are the smallest and most numerous blood vessels which can exhibit diameters of only 3-8 μm and account for the largest surface area of the vasculature to permit efficient nutrient exchange [29] [36] [44].

Fundamentally, the arterial network is comprised of dynamic structures which maintain homeostasis by continually adapting to acute and chronic changes in the mechanical

environment [34]. This is facilitated through continual remodelling of their internal structure, specifically for the maintenance of wall shear stress, pressure, and flow [34].

This internal structure can be described as follows. Artery walls are composed of three layers; the intima (inner layer), media (middle layer), and adventitia (outer layer) [32]. The intima consists of connective tissue, the basement membrane, and endothelial cells which interface with flowing blood [32]. The media contains elastin, smooth muscle cells, and collagen fibres, and is separated from the intima by a layer of elastic tissue known as the internal lamina [32]. Finally, the adventitia is composed primarily of stiff, fibrous collagen [32].

The composition and mechanical properties of these arterial walls change as a function of distance from the heart. For example, larger arteries like the aorta are thicker and more elastic, which is crucial to regulating left ventricular performance and arterial function of the entire cardiovascular system [29] [32] [36]. Smaller arteries contain more smooth muscle cells so are more rigid, leading to a stiffness gradient from the central arteries towards the periphery [29] [32] [36] [44].

1.5.2 Venous System

The venous system returns deoxygenated blood from the periphery towards the heart, converging from the capillaries to the venules and veins, culminating at the vena cava in an inverse tree structure [36]. These are thin-walled vessels which contain valves to aid in the preservation of unidirectional blood flow and are subjected to compression due to surrounding muscles which provide a secondary pumping mechanism to force blood towards the heart [36]. Like the arterial system, the central veins exhibit greater compliance due to increased elastin within the vessel walls to serve as a reservoir to accommodate increased blood volume [36].

1.6 Computational Fluid Dynamics

It is essential to understand the pre- and post-surgical haemodynamics to better inform surgical deployment and graft design to optimise flow and mechanical stresses. *In silico* (computer based) methods such as computational fluid dynamics (CFD) permit this testing in a simulated environment, thereby eliminating the need for time-consuming and expensive lab-based experiments.

As the field of cardiovascular modelling is so broad, there is a spectrum of methodologies which can be employed. This ranges from simplistic, yet efficient zero-dimensional (0D) models and extends to sophisticated, multi-dimensional models which can couple both one-dimensional (1D) and three-dimensional (3D) frameworks. Each approach is characterised by

a unique set of advantages, limitations, assumptions, and applicability to certain scenarios. Common to each methodology, however, is the requirement for patient-specific boundary conditions to achieve clinical validity. In the field of CFD, a fundamental rule exists in that the accuracy of the output is intrinsically linked to the quality of the input information.

1.6.1 Zero-Dimensional Models (Lumped Parameter)

0D models, also known as lumped parameter models, are used ubiquitously in the field of cardiovascular research due to their simplicity and computational efficiency [45]. These 0D models are a function of time only and assume a uniform distribution of pressure and flow variables, thus neglecting the spatial dimension [46]. Therefore, these 0D models simulate global haemodynamics and cannot capture local phenomena [36]. They range from a pure resistive (with a single resistor) to a simple Windkessel model modelled as a single resistor and capacitor, to a sophisticated Guyton model which considers some autonomic and hormone regulation phenomena [36].

Notably, these 0D models can be utilised in mono-compartmental or multi-compartmental configurations [36] [46]. Mono-compartmental models are used to capture the systemic response, represented as a single block, while multicompartmental discretise the systemic vasculature into several mono-compartmental sections [36]. This is a versatile approach as, depending on the requirements of the research, the vasculature can be partitioned into any number of segments. Thus, these 0D models are used for a range of purposes, from the analysis of systemic blood flow under healthy and unhealthy conditions, haemodynamic changes as a result of surgical intervention, the study of cardiovascular response as a result of neuro-regulation, and fundamentally, boundary conditions in multiscale computational modelling [36].

1.6.2 One Dimensional Models

1D models are more complex and computationally intensive than 0D models but provide a more physiologically accurate and extensive description of arterial haemodynamics. These models introduce a spatial dimension, meaning an arterial segment can be approximated along a characteristic length [47]. In this formulation, the arterial network is discretised into several individual sections of a certain length, with sections connected via nodes [48]. Consequently, this requires the prescription of geometric and tissue wall properties for each section, along with outflow BCs for each terminal branch [48].

Fundamentally, 1D models can reveal changes to instantaneous pressure and flow waveforms at any location along the vessel. This permits the study of pulse wave propagation and wave intensity analysis, which is not possible in the 0D domain [29] [36]. This is important as information relating to cardiac function, vessel wall elasticity, and peripheral organs are encoded within these pulse waves [36]. Traditionally, such models have been utilised to study arterial segments, but can be extended to elucidate pressure and flow information within the entire cardiovascular network, complete with ventricular to arterial coupling, regions of stenosis, pathological geometries, and deployed stent-grafts [36]. Therefore, 1D modelling is an extremely versatile tool. However, 1D models fail to offer the level of detail required to calculate haemodynamic quantities such as shear stress which are instrumental to the study of cardiovascular diseases [49].

1.6.3 Three Dimensional Models

3D CFD models can numerically compute the entire three-dimensional flow field within an artery where analytical solutions are not possible [31] [36] [46] [49]. Unlike reduced-order models, 3D approximations can account for the effects of vessel geometry on the flow regime, and vice versa [49]. By elucidating the complex spatial flow patterns, these models can be reliably used to calculate localised parameters which are invasive or complex to measure directly, such as wall shear stress, velocity streamlines, and vorticity among others [9] [36] [41] [49]. This is crucial, since abnormal blood flow dynamics and regions of high wall shear stress (WSS) contribute to the initiation, location, and progression of aortic diseases [9]. Fundamentally, CFD studies can calculate such clinical parameters with a high spatiotemporal resolution which surpasses any current imaging modality [50].

3D CFD models are also extremely flexible, permitting parametric investigations to evaluate how a range of independent factors affects blood flow [50]. For example, in the investigation of dissections where the anatomy is often unique to the patient, or in custom stent-grafts, CFD can provide an individualised analysis of flow in a simulated environment to support surgical planning [49] [50] [51] . This non-invasive analysis of patient haemodynamics has become an increasingly crucial role in the diagnosis of a range of cardiovascular diseases and optimisation of therapeutic medical devices [46] [51]. Consequently, it is likely that CFD will become a routine clinical tool in the future when used in conjunction with medical imaging [52]. This is especially true given the advancement of computer parallelised hardware and techniques for numerical analysis, meaning CFD remains a computationally intensive, but no longer prohibitive, task [36] [49].

1.6.4 Multi-dimensional Modelling & Boundary Conditions

Modelling the entire cardiovascular system in 3D or even 1D is not possible due to the millions of peripheral vessels which include arteries, arterioles, and capillaries, making it both impractical and computationally prohibitive [36] [53]. However, it is essential to capture the influence of these distal vessels on the localised flow within the 1D or 3D domain [46]. This is because emphasis solely on either global circulation or local flow yields only partial cardiovascular insights [46]. For example, vascular resistances in capillaries and arterioles significantly influence blood pressures in central arteries [51].

Multi-dimensional modelling provides a balance by coupling anatomically accurate 3D models to simpler 0D boundary conditions (BCs) which are representative of peripheral vasculature. The higher-order models, which capture the detailed flow field in local regions (solved numerically), are coupled with reduced-order boundary conditions (solved analytically), thereby creating a model where changes in one domain affect the other [46] [49] [54] [55] [56]. This combines the advantages of high- and low-order models, permitting practical and efficient use of computational resources [46] [56]. This approach also enhances physiological relevance by encompassing local and systemic factors.

1.6.5 Importance of Calibrated Boundary Conditions

BCs have a significant impact on the numerical results of CFD simulations, as local flow dynamics is heavily influenced by global conditions [36] [51] [52]. Additionally, these 0D BCs encapsulate and simplify the peripheral vascular network in a single model. Therefore, it is essential to accurately calibrate the model parameters [36]. Literature suggests that BC calibration is essential, and there are many approaches for BC calibration, with no universally accepted method [43] [46] [51] [54]. It is clear, however, that the calibration process depends on the simulation requirements and the clinical data available. Though it is possible to calibrate BCs based on invasive data, this increases patient burden. Thus, we suggest that BCs should be calibrated based on non-invasive, non-ionising, and readily obtainable *in vivo* clinical data. For clinical applications, to avoid delays in patient care, these BCs should be calibrated within an automated and computationally efficient framework.

1.6.6 CFD Modelling for Aortic Dissection

An array of studies has leveraged CFD modelling to elucidate key flow characteristics, assess near-wall haemodynamics, and predict outcomes in patient-specific models of TAADs and TABDs. These prior investigations have provided insights into the progression of aortic dissection, informed surgical planning, and highlighted the potential of CFD for both predictive and preventive applications.

1.6.6.1 Early Studies

Early studies by Rudenick *et al* [57], Chen *et al* [58] and Alimohammadi *et al* [59], among others, showed that CFD can be utilised to gain insights into complex AD haemodynamics which are difficult to quantify by other means. Alimohammadi *et al* [60] then expanded their work to evaluate the impact of compliant vessel walls through fluid structure interaction. Other studies have investigates the effect of heart rate on TABD, using CFD to simulate the effect of beta blockers and investigate hemodynamic metrics that influence disease progression [61].Stokes *et al* evaluated the effect of inlet flow, derived from 4D Flow-MRI, on oscillatory shear and glow helicity in the FL of TBAD, both of which have predictive potential in the long-term evolution of the pathology [62].

1.6.6.2 AD Initiation and Screening

Hohri *et al* utilised CFD as a tool to predict the occurrence of future TAAD in otherwise healthy aortae, via analysis of wall shear stress and vortical flow in the ascending aorta [63]. This shows that numerical methods may present attractive screening tools for pre-symptomatic individuals in high-risk groups [63]. Similarly, Zhu *et al* conducted a longitudinal study which showed that CFD can then be used after initiation of a TAAD as a non-invasive technique to predict the risk of further dilatation of the aortic wall which is typical of disease progression [64].

1.6.6.3 CFD for AD Disease Progression

CFD modelling has been used extensively to understand and predict disease progression for AD cases. For example, Dillon-Murphy *et al* [65] utilised CFD modelling to investigate the haemodynamic changes introduced by the dissection septum in the descending aorta, estimate of the additional stroke work imposed by the aortic dissection on the heart, and quantify of the impact of secondary intraluminal tears on aortic haemodynamics [65]. Zhu *et al* expanded on this analysis, evaluating morphological and hemodynamic features in TAADs in an effort to predict progressive aortic dissection based on patient-specific CFD simulations [66].

Specifically, they investigated the number of re-entry tears, as well as pressure difference between the true and false lumen.

Additionally, Moretti *et al* investigated flow patterns within the FL of aortic dissection cases, showing that a partially thrombosed dissection is the most prone to false lumen degeneration, and provided evidence on the likelihood of degeneration in different types of dissections [67]. Additionally, they validated the RANS approach for TABD as appropriately balancing the computational burden and modelling accuracy, yielding coherent results within an acceptable time [67].

Ikeno *et al* then showed that CFD could be used to predict postoperative increases in false lumen pressure and wall shear stress of chronic dissections after total arch replacement, showing CFD is beneficial for surgical planning and decision making for the avoidance of aneurysmal formation [68]. This built on earlier work by Tse *et al* who investigated post-aneurysmal development in a dissection patient [69]. Similarly, it has been shown that CFD can provide information on an array of haemodynamic parameters which can predict the progression of aortic lesions, estimate the effect of surgical intervention, and predict long-term patient prognosis for patients with aortic dissection [70].

Recent CFD studies have shown that high flow rates in the FL are associated with progressive dilatation, resulting in unstable aortic growth and dissection-related complications [71] [72]. Notably, a longitudinal studies by Fatma *et al* [71] and Xu *et al* [73] also showed that abnormal CFD derived WSS has been identified as a potential predictor for unstable aortic growth in TBAD patients. Xu *et al* also examined relative residence time, and the impact of this metric on thrombus formation, after which they validated a novel mathematical model for the prediction of thrombosis in TBAD, utilising fluid shear rate, residence time, and platelet distribution [73] [74]. Additionally, Wan *et al* [75] showed that FL thrombosis was also related to the number and location of intraluminal tears. They also showed that there is a tendency for thrombosis to form in the proximal end of the FL, based on low WSS and high relative residence time [75].

1.6.6.4 Fluid Structure Interaction in AD Studies

Zhu *et al* developed fluid structure interaction simulations on patient-specific TAAD models with a surgically replaced ascending aorta, evaluating flow patterns and wall shear stress [76]. Additionally, they show the importance of accounting for wall compliance in AD [76]. Similarly, Zimmerman *et al* generated high-fidelity CFD model of a TBAD using FSI

simulations to determine the quantitative and qualitative impact on hemodynamic metrics in amid variations in entry and exit tear area. They compared this against *in vitro* 4D Flow-MRI, using an MRI-compatible flow setup and showed good agreement between the 4D Flow-MRI and CFD models [77].

1.6.6.5 Experimental Validation of CFD Studies

Bonfanti *et al* developed a sophisticated framework for blood flow simulations of ADs, utilising minimal datasets commonly acquired during routine monitoring, including iterative boundary condition calibration [78]. They later expanded on this to demonstrate a simple and computationally efficient methodology to model arterial deformation and wave propagation phenomena in a 3D CFD models of dissected aortae [79]. Laterally, the same research group combined numerical and experimental methods to investigate patient-specific aortic dissection haemodynamic, validating their CFD models with experimental velocity data acquired through particle image velocimetry [80]. Following this, Franzetti *et al* improved upon the experimental benchmark via fluid dynamic visualisation and measurements as part of an ongoing effort to validate TABD CFD models in order to virtually simulate different surgical interventions such as open and endovascular stent-graft deployment [81].

1.6.6.6 Virtual Stent-Graft Deployment for AD Cases

Virtual stent-graft deployment is an emerging application of CFD modelling, as it allows for the evaluation of different endovascular repair scenarios in AD patients to optimize treatment strategies and predict potential complications.

Early studies modelled different endovascular stent-graft repair scenarios in TBAD patients by virtually occluding one or more tears to evaluate the haemodynamic effectiveness of aortic dissection treatments via computational modelling [58] [82]. They showed, for example, that occlusion of the entry and exit tear caused a decrease and increase in FL pressure, respectively [82]. Additionally, these studies indicated that a single stent-graft which occluded either the entry or re-entry tear (but not both) would not effectively reduce flow entering the FL [58]. This preliminary work provides an insight into CFD-derived surgical planning for stent-graft placement.

Recently, more sophisticated methods for virtual stent deployment have been developed and applied to the studies of TBAD [83] [84] [85]. For example, Kan *et al* virtually deployed a stent-graft within the thoracic aorta of a TABD patient and performed finite element analysis to understand stress distribution following deployment in an attempt to predict potential

complications [83]. However, these studies did not model blood flow in the post-deployment models, thus limiting the haemodynamic understanding available [83] [84]. Chen *et al*, however, demonstrated a deformable stenting algorithm for virtual deployment within TBAD aortae, after which they conducted CFD analysis to estimate several near-wall haemodynamic parameters, thus proving it is possible to do so to predict the post-surgical flow regime in this way [85]. Similarly, Fatma *et al* demonstrated that CFD-derived haemodynamics could be used to adverse outcomes like thrombus formation, widening of the entry tear section, and false lumen expansion in TBAD patients [71].

2 Methods

The process for creating CFD models for the analysis of aortic haemodynamics comprises of six general stages. This process begins with medical imaging to elucidate the anatomic and functional data required to perform the subsequent steps. Stage two involves the segmentation and reconstruction of those medical images to generate 3D models of the vasculature. Thereafter, the reconstructed geometries are discretised to create a computational mesh. Following this, parameter calibration is required to yield physiologically relevant boundary conditions. The penultimate stage is the numerical calculation step, where the full CFD simulation takes place. Finally, visualisation and analysis of the CFD solution is performed in the final stage, allowing for the interpretation of aortic haemodynamics. To generate clinically-relevant CFD models, it is essential to perform each stage accurately, as the quality of the numerical models is directly associated with the quality of the inputs [41] [50] [51] [54] [86] [87].

The first section of this Chapter describes CT imaging and magnetic resonance imaging (MRI). In this thesis, no medical imaging was performed. Our work focused exclusively on the post-processing of this imaging data for quantitative analysis and anatomical reconstruction. The second section of this Chapter discusses the general techniques of 1D and 3D CFD modelling which were used by the authors.

2.1 Medical Imaging

Medical imaging is a widely used tool by clinicians as an essential component in the diagnosis, disease progression, management, and post-intervention follow up to assess the response to surgery or medicine in cardiovascular disease [15] [19] [88] [89].

2.1.1 Computed Tomography

CT imaging is an x-ray based technique wherein a narrow x-ray tube is aimed at the patient and rapidly rotated around the body [90]. The x-rays pass through the body and are captured by digital detectors at the opposite side of the patient. While the x-ray tube is rotating, the table supporting the patient moves continuously to allow a volume of tissue to be imaged, comprised of several discrete slices [90]. Thus, coronal, sagittal, and transverse (axial) imaging planes can be captured, as illustrated in Figure 2.1.

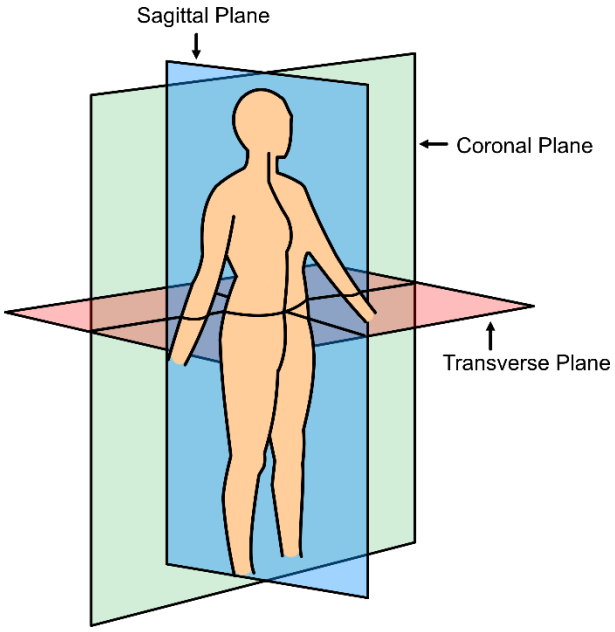

Figure 2.1: Medical imaging planes, showing the sagittal (blue), coronal (green), and transverse (red) planes intersecting a human body.

While CT imaging provides high spatial resolution and excellent visualisation of arterial structures, it relies on high-doses of ionising radiation and, often, intravenous contrast, making it less attractive for clinical use [4] [91] [92] [93]. In non-urgent situations, CT is increasingly replaced with MRI based techniques for angiography (imaging of blood vessels) [4] [90]. In emergency circumstances however, such as in the diagnosis of a suspected AD, CT imaging is the method of choice since it is fast, relatively cheap, ubiquitous, high-resolution, and has excellent sensitivity and specificity [92] [94] [93].

2.1.2 Magnetic Resonance Imaging

MRI is a non-invasive, non-ionising imaging modality which allows accurate visualisation of soft tissue structures including blood vessels [89]. This employs the manipulation of protons located within the body to build an image. Protons are randomly oriented, positively charged subatomic particles located in the nucleus of cells generally found in blood and soft tissues [95]

[93]. These protons possess a property known as ‘spin’ (precession around their axis) which determines the protons’ magnetic and electrical properties. In their natural state, these protons spin asynchronously and out of phase with each other [95].

When a strong magnetic field, generally in the range of 0.5-3 Tesla (T), is pulsed during an MRI sequence, this causes protons to alter their spin out of equilibrium, forcing them into the direction of the static magnetic field, B_0 [95]. A radiofrequency (RF) pulse is then applied perpendicular to B_0, flipping the proton spin axis normal to B_0. At this point, all protons are aligned parallel or antiparallel with each other, and spin at the same rate [95] [96].

When the RF pulse ends, the protons will gradually return to asynchronous spin precessions and lose phase coherence [96]. Further, these protons gradually realign with B_0 and release electromagnetic energy, inducing a voltage which can be measured in space and time by components within the MRI scanner [6]. The greyscale intensity of the pixel or voxel (3D pixel) is directly related to the quantity of electromagnetic energy released [95] [96]. Crucially, the time it takes for these protons to realign with B_0, along with the magnitude of energy released, is unique to the environment (e.g. tissue) in which these protons exist [95]. Therefore, it is possible to differentiate between tissues based on the magnitude and rate at which this energy is released by protons [95].

2.1.3 Phase Contrast MRI

Phase contrast MRI (PC-MRI) expands on these basic principles by introducing an additional magnetic gradient known as a bipolar gradient. In the context of cardiovascular research, PC-MRI is used to visualise and quantify the velocity of moving protons in blood within the arterial network [88] [96]. A bipolar gradient is applied to the region of interest (ROI) in the direction of blood flow for a set period of time and then a second gradient is pulsed in the opposite direction for an equal period (Figure 2.2) [88] [96].

Protons which are stationary within this region experience a positive phase shift, followed by a negative phase shift of the same magnitude [96]. This results in zero net phase change on stationary protons within organs and connective tissue. However, protons which are moving parallel to the bipolar gradient will experience different magnetic field magnitudes during the second bipolar gradient in comparison to the first. This is due to the change in the spatial position of the moving proton, resulting in a net phase shift which is proportional to proton velocity. For PC-MRI, the voxel intensity is based exclusively on the phase change, not the signal amplitude of electromagnetic radiation like standard MRI [96]. For cardiovascular

applications, images are acquired and averaged over several cardiac cycles using ECG gating to calculate the time-resolved blood flow [88] [96]. Generally, this is performed while the patient is holding their breath to minimise the motion artefacts caused by the expansion and contraction of the chest during breathing [88].

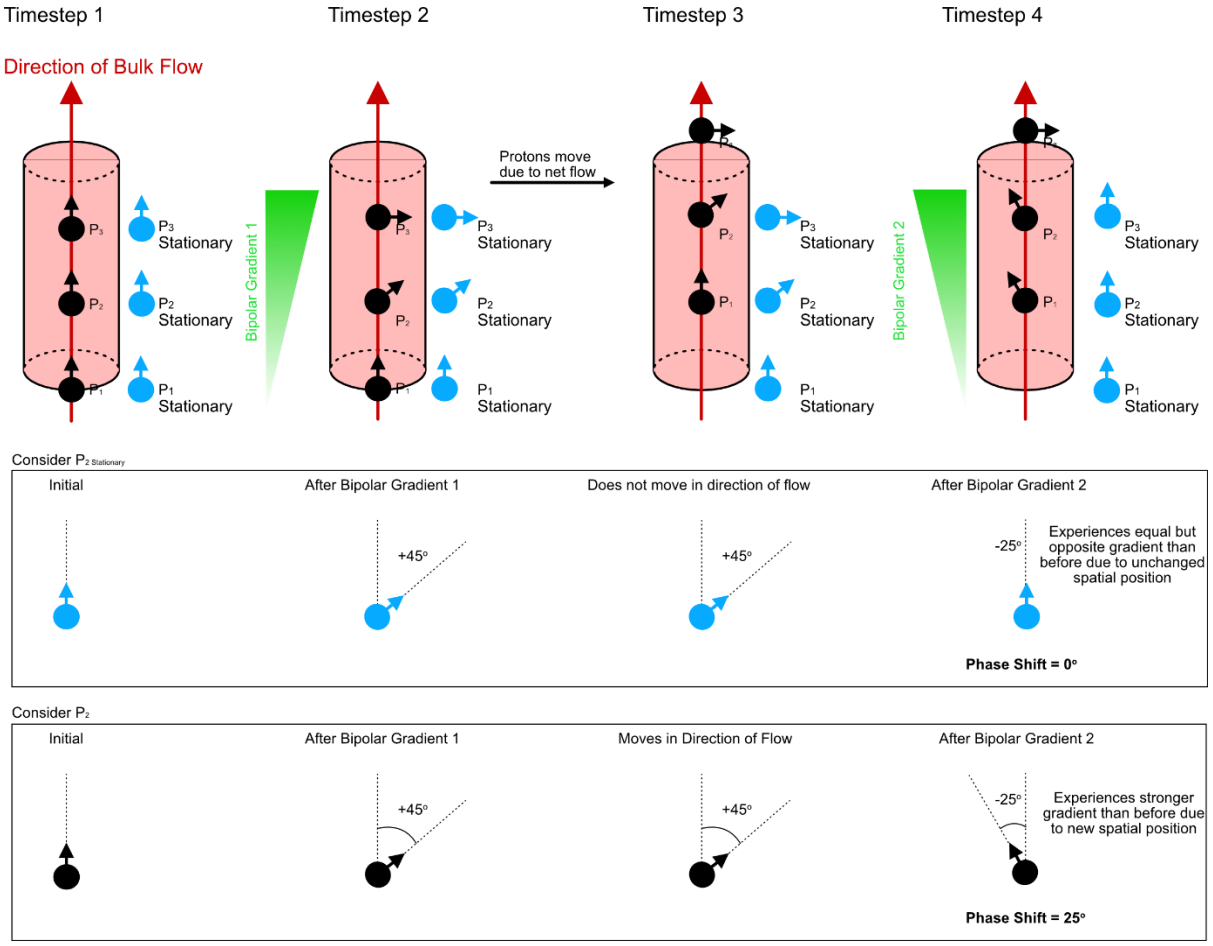

Figure 2.2: Schematic displaying how moving protons experience a phase change in the presence of multiple magnetic gradients during a phase contrast MRI (PC-MRI) sequence.

2.1.4 VENC

Velocity encoding (VENC) is a parameter which must be specified prior to performing a PC-MRI [88]. For a given strength of bipolar gradient, this VENC represents the maximum flow velocity that can be captured during an imaging sequence before aliasing occurs [88] [96]. If blood velocity exceeds the VENC, velocity aliasing means high flow rates are mirrored and incorrectly interpreted as low flow rates [88] [96].

Generally, aliasing can be minimised through an anti-aliasing post-processing step in commercial software [51] [88]. However, the optimal way to avoid aliasing is by prescribing

an appropriate VENC for a given study. Setting it too high makes it difficult to resolve and accurately quantify regions of low velocity, leading to significant noise in these regions [88]. Conversely, if VENC is too low, this results in velocity aliasing across a substantial portion of the ROI [88]. Consequently, VENC should be sufficiently high to minimise aliasing, but not so high as to degrade the signal to noise ratio in low velocity regions [88]. In clinical practice, VENC is set at 150-200cm s^{-1} in the thoracic aorta due to high flow rates in the aorta [88]. Notably, several studies have used multi-VENC, which allows one to capture a higher signal to noise ratio at low velocity regions, while avoiding aliasing of high velocities [9] [65]. This is, of course, a more complex scan sequence and not yet utilised routinely.

2.1.5 4D Flow-MRI

As discussed previously, velocity is encoded in one direction through a 2D plane during 2D time-resolved PC-MRI [4] [97]. Fundamentally, these planes of analysis must be decided prior to the imaging sequence and although anatomical landmarks can be used to assist with planning, accurate placement of the acquisition planes is difficult [35]. This can lead to underestimated blood velocities if the plane is not perpendicular to the direction of flow [35] [97]. This is particularly challenging in regions of complex flow, such as in aortic disease, where changes in the direction of flow occur throughout the cardiac cycle [97].

These drawbacks can be mitigated by utilising 4D Flow-MRI, where velocity is encoded in all three spatial dimensions and time [88] [97]. During the 4D sequence, one anatomical image (magnitude image) and three velocity-encoded images are acquired along three orthogonal directions (Vx, Vy, Vz) within the imaging volume of interest (Figure 2.3) [88]. This data is acquired overall several cardiac cycles and averaged, meaning it cannot account for beat-to-beat variations in flow and has a tendency to smooth features [88] [89].

Fundamentally, a number of studies which compare 4D flow to the widely accepted 2D time-resolved PC MRI and echocardiography have shown good agreement in blood flow quantification [88] [98].

Generally, the scan time is between 5-20 minutes depending on the spatiotemporal resolution of the imaging modality and the size of the ROI [51] [88] [99]. This is considerably longer than traditional 3D MRI scan times and is one of the reasons why 4D Flow-MRI has not yet been adopted globally as a routine clinical tool [89] [100].

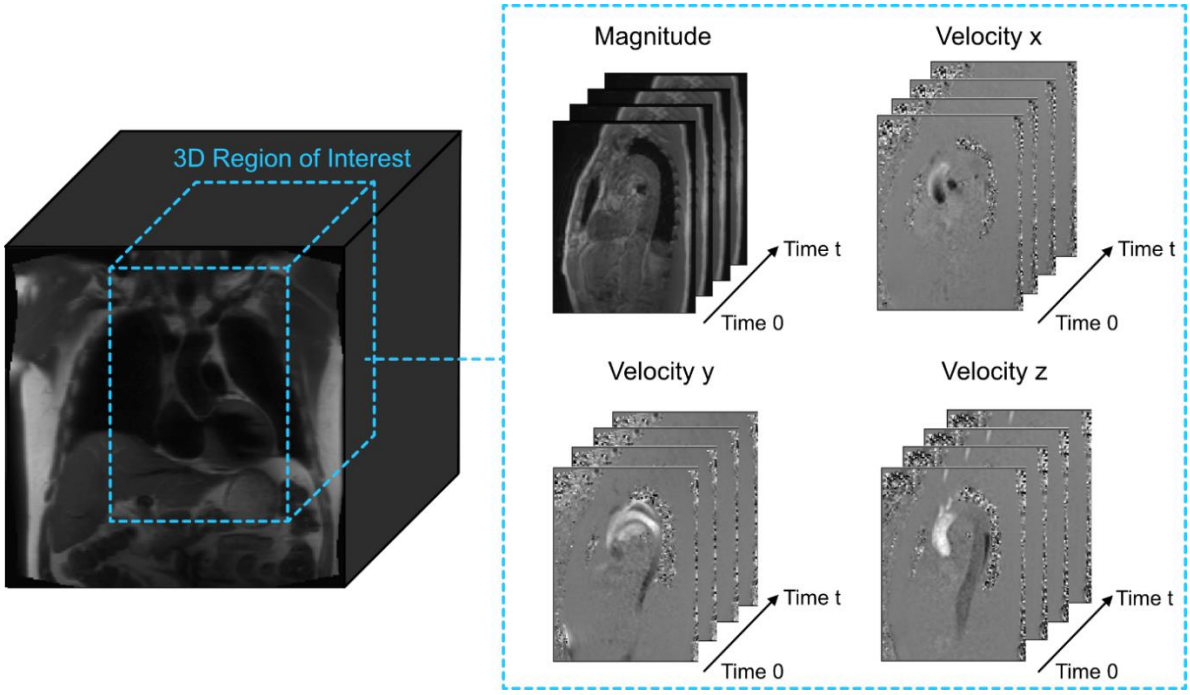

Figure 2.3: Three-dimensional ROI of a 4D Flow-MRI scan of the thoracic cavity, decomposed into the magnitude image stack, and image stacks which contain phase information, required to encode velocity in the x, y, and z directions of patient 1 (for further data details see Table 3.1 in Chapter 3).

However, 4D Flow-MRI exhibits several advantages over conventional techniques. Notably, it allows the user to retrospectively place an unlimited number of planes of analysis for blood flow, while *post-hoc* respiratory and ECG gating means images can be acquired in the absence of breath-holding by the patient [35] [37] [51] [88] [97]. Further, 4D Flow-MRI can effectively evaluate turbulent flow due to the volumetric 3D velocity encoding, and can be used to derive additional parameters which is not possible with other imaging modalities, including wall shear stress, pressure gradients, and fluid turbulence [37] [51] [98]. 4D Flow is the only method for measuring the 3D distribution of blood flow in vivo, *post hoc* [37].

If temporal resolution is too low, turbulent flow will not be adequately captured and peak velocities are likely to be underestimated [89] . If spatial resolution is too low, this will degrade image quality and induce uncertainties as to the location of the vessel walls, resulting in errors in near-wall parameters such as WSS [9] [37] [89].

2.1.6 4D Flow-MRI Visualisation

With 4D Flow-MRI, it was possible to visualise time-resolved 3D streamlines and path lines for both qualitative and quantitative analysis of flow [88]. Figure 2.4 illustrates an example of 3D velocity streamlines in the aorta and pulmonary arteries of a healthy patient during systole and diastole (see Chapter 5, Table 5.1 for data details). These streamlines are traces of the instantaneous 3D flow vector field for a discrete timeframe of the cardiac cycle [88]. Crucially, this was a useful way to analyse the temporal evolution of flow and identify flow features such as helical flow, jet flow, regurgitation, and recirculation to differentiate between healthy and pathological cases [88].

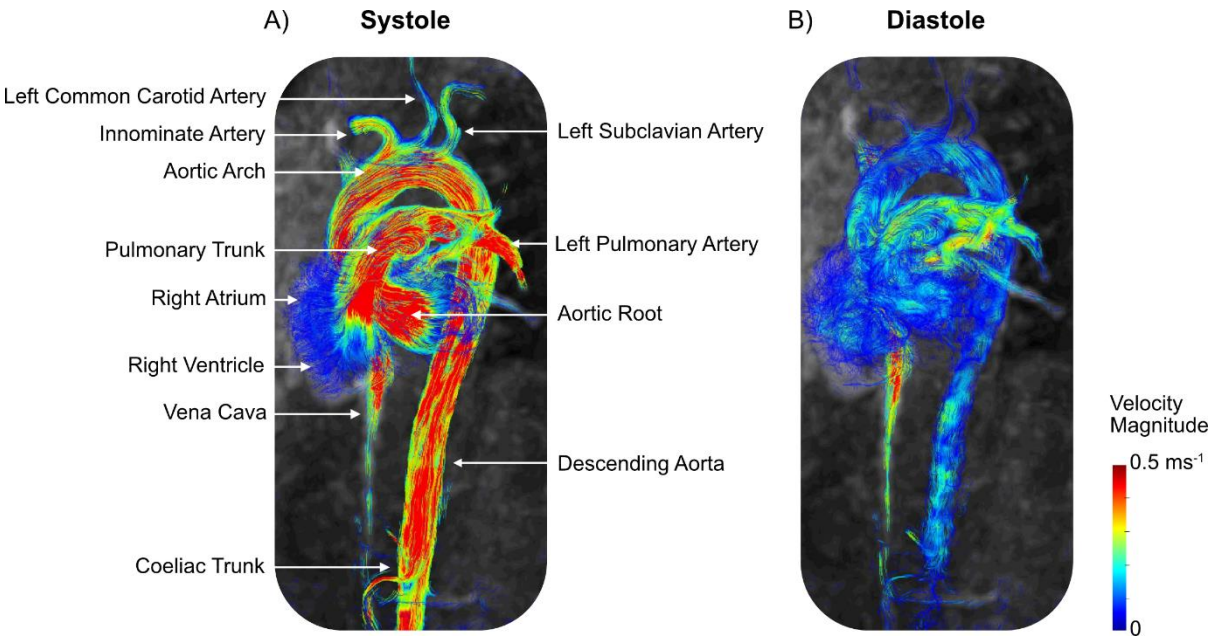

Figure 2.4: Instantaneous 4D Flow-MRI derived velocity streamlines of a healthy individual (volunteer 2) during A) systole and B) diastole, illustrating flow within the main vasculature of the thoracic cavity, including the aorta, supra-aortic branches, vena cava, and the pulmonary arteries (Data is from the patient cohort described in Chapter 5, Table 5.1).

2.1.7 Review on 4D Flow-MRI for Clinical Practice Relating to Aortic Dissection

Aortic dissections present a complex problem for medical imaging due to the presence of a TL and FL, each with different flow characteristics. While CT imaging remains the mainstay modality at present, 4D Flow-MRI is emerging as a valuable complementary diagnostic test for evaluating this pathology, among others [101]. It has also been widely used in research to assess haemodynamics within TBAD's from *in vivo* scans and for use in building *in silico* models [101] [102] [103] [62] [104] [4].

For example, recent studies have utilized 4D Flow-MRI to estimate FL pressurization and predict growth in dissection patients, based on the measurement of indirect parameters including the false lumen ejection fraction (FLEF) and the maximum systolic deceleration rate (MSDR) within the FL [102]. Additionally, recent technical advancements such as the virtual Work-Energy Relative Pressure (vWERP) technique, allows for non-invasive measurement of intravascular pressure drop from 4D Flow-MRI data [102]. Regarding the vWERP technique, this has recently been validated against invasive catheterization in-vivo, meaning it shows promise for future quantification of intravascular pressure changes in TBAD, leading to improved patient management [102]. For postoperative outcome prediction, 4D Flow-MRI also shows promise. For example, a study by Takahashi *et al* showed late complications following endovascular repair tended to occur in patients who exhibited a significantly higher volume of turbulent flow [105]. This tended to be due to helical and vortical flow structures which were induced by higher FL blood flow rate and velocity [105]. Overall, it is clear that the use of 4D Flow-MRI for the investigation of TBAD cases is growing.

With 4D Flow-MRI, recent studies have shown that the TL, with predominant systolic flow, can be distinguished from the FL, which can be thrombosed without significant flow inside [101]. Therefore, this modality allows for the quantitative confirmation of the presence or absence of flow within the FL, along with the precise volume of blood present, which has implications for disease prognosis and evolution [101].

In single-VENC scans, 4D Flow-MRI has a limited dynamic range [103]. Consequently, velocity aliasing is more likely to occur due to high flow rates in the TL, and noise is more likely to be induced due to slow or static flow rates in the FL [88] [101] [101] [104]. This is because the VENC value set in a single VENC 4D Flow-MRI acquisition is generally adjusted to the estimated peak velocity, thus limiting the evaluation of slow flows in the FL [101] [106]. Ideally, haemodynamic evaluation should maintain a high velocity-to-noise ratio (VNR) across the entire range of velocities encountered for the given pathology [106]. However, this range is broad in TBAD due to the large differences in flow within the TL and FL [101].

To address these limitations, recent studies have shown that it is possible to obtain low-VENC and high-VENC images within the same scan due to multiple velocity encoding (multi-VENC) [101]. With multi-VENC imaging, it was confirmed that a superior VNR was obtained throughout the aorta, with improved haemodynamic quantification within the FL [107] [108] [103] [109] [106].

Unfortunately, the acquisition of multi-VENC images leads to an increased scan duration which can be impractical in clinical settings [103] [101]. However, recent advancements have combined multi-VENC 4D Flow-MRI with acceleration techniques to reduce overall scan duration by up to 46.4% and make 4D Flow-MRI more clinically feasible, while retaining the ability to image a high dynamic range of velocities [103] [101] [106].

Compressed sensing is one technique that can significantly accelerate MRI acquisitions utilizing the inherent sparsity of MRI data [101] [108] [103]. Briefly, this technique avoids the collection of large amounts of raw data such as in conventional MRI, and takes advantage of the fact that images can be represented using fewer data points without compromising the information [101] [108]. This is because only a minor portion of the data holds clinically useful information, with most of the domain comprised of dark, background signals [108].

Other advanced acceleration techniques include parallel imaging such as SENSE (sensitivity encoding), GRAPPA (GeneRalized Autocalibrating Partially Parallel Acquisitions), and spatiotemporal acceleration techniques like k-t acceleration [110] [103]. It is also possible to decreases scan times buy utilising non-Cartesian k-space sampling, or by trading scan time against potential breathing motion artifacts [103].

Despite these advancements, challenges remain. For example, the need for high spatial and temporal resolution often conflicts with the need for shorter scan times [106]. Additionally, the requirement for post-processing resources, such as powerful graphics processing units, or cloud-based systems, adds complexity and cost for routine clinical application [106].

The previously outlined advances in accelerated multi-VENC imaging, along with diversification of acquisition methods have demonstrated the validity for 4D Flow-MRI for clinical practice. Consequently, 4D Flow is now available and supported by major MRI vendors. Additionally, commercially available post-processing tools have received FDA approval and European CE marking for clinical use in certain countries, with reimbursement options. These developments have expanded the user base and will permit more widespread clinical application of 4D Flow MRI. To date, it is integrated into routine clinical practice at multiple centers worldwide, although it is not as widespread as conventional MRI [106].

To drive further integration and proliferation of this imaging modality, clinical acquisitions need to be fast, with reliable quantification of flow and velocity [106]. For integrating 4D Flow-MRI into clinical practice for aortic dissections, optimizing scan parameters is therefore crucial. Of course, this is not possible on retrospective datasets, but prospective scans should

aim for spatial resolution <2.5mm³ and isotropic in nature, with VENC set approximately 10-25% above the maximum velocity, confirmed by prior 2D PC-MRI [102] [106] [111]. This confirmation is particularly important in regions of high jet flow including intraluminal tears, regions with substantial turbulence, and highly vortical blood flow [106]. The temporal resolution should be 30ms or shorter, and the scan time should be within 5 to 10 minutes [103] [106]. It is essential that 4D Flow-MRI measurement techniques are initially validated against established 2D PC-MRI techniques, ensuring less than 5% difference in calculated flow rates, especially at peak systole [106].

Further, retrospective ECG and respiratory gating are essential to improve image quality, with phase unwrapping employed to improve the accuracy of the flow and velocity measurements [106]. Regarding the clinical workflow for post-processing 4D Flow-MRI, this should include background phase offset correction, anti-aliasing, segmentation, visualization, and quantification in that order [106]. These acquisition and analysis protocols should be standardised to ensure consistency across different centres, and also facilitate multi-centre studies [106].

Future areas of development are likely to be in the automation of currently labour-intensive and non-standardised such as manual data processing and phase offset correction, and using neural networks to reduce noise and auto-calibrate for velocity aliasing [106]. This will improve reproducibility and efficiency to permit more widespread clinical translation [106]. Additionally, artificial intelligence may permit automatic mesh generation and quality assessment, prior to CFD modelling, as illustrated by Chen *et al* and Zhang *et al* [112] [113].

2.2 4D Flow-MRI Scan Sequence

4D Flow-MRI images were acquired using an MRI research 4D flow sequence (WIP 785A), from Siemens: 80 x 160 x 60 mm^3 imaging volume, 3.6mm x 2.4mm x 2.6mm acquired resolution, TR/TE (Repetition Time/Echo Time) =3.8/2.8ms, integrated parallel acquisition technique (iPat) 3. Notably, the scan sequence utilised in this study is anisotropic in spatial resolution. Velocity encoding (VENC) was 150 cm/s, with a scan time of ~ 8 min and 20-time frames between each R-R interval. Contrast media was not utilized. The acquisition used retrospective electrocardiogram (ECG) gating and respiratory gating navigator. CT images were obtained via a contrast-enhanced CT angiography (CE-CTA) helical scan, with no cardiac gating, using iodinated contrast material (100ml).

2.3 Segmentation and Reconstruction of Medical Images

The role of medical images exceeds simple observation of anatomical structures. Often, these 2D image sequences are used to locate, segment, and reconstruct regions of anatomical interest in 3D. Therefore, once medical images of a patient had been acquired, the first stage of building CFD models was the segmentation and reconstruction of the arterial geometry to create a computational model.

Fundamentally, each individual exhibits a unique aortic and arterial structure [94] [114]. For example, a normal branching pattern of the supra-aortic branches is observed in 70% of individuals of the global population, while 20-30% show a variation wherein the innominate and left common carotid arteries share combined ostia [94]. Consequently, these variations must be captured, as the reconstructed geometry significantly affects the results of CFD simulations [51] [94] [114].

Segmentation is the process of dividing a medical image into discrete regions (i.e. tissue boundaries) based on similar tissue properties, generally through analysis of signal intensity and image contrast [93] [115]. In the context of this thesis, segmentation was performed to distinguish and isolate blood vessels from surrounding connective tissue and organs in CT (Figure 2.5A) and 4D Flow-MRI (Figure 2.5B) images.

The aorta and surrounding tissue had similar greyscale ranges, meaning segmentation was a non-trivial task [93] [114]. Further, greyscale was not uniform within the aorta itself, meaning the signal intensity varied within tissues and between tissues [114] [115]. Segmentation can be automatic or semi-automatic, but no single segmentation technique is applicable to all scenarios [116]. Thresholding techniques are the most simple, and used ubiquitously throughout the literature, but generally require manual adjustments to correct for localised inaccuracies, noise, and signal artifacts [87] [93] [114] [115] [116] [117]. These manual corrections are particularly important in complex, pathological vessels such as patients with AD [114] [116].

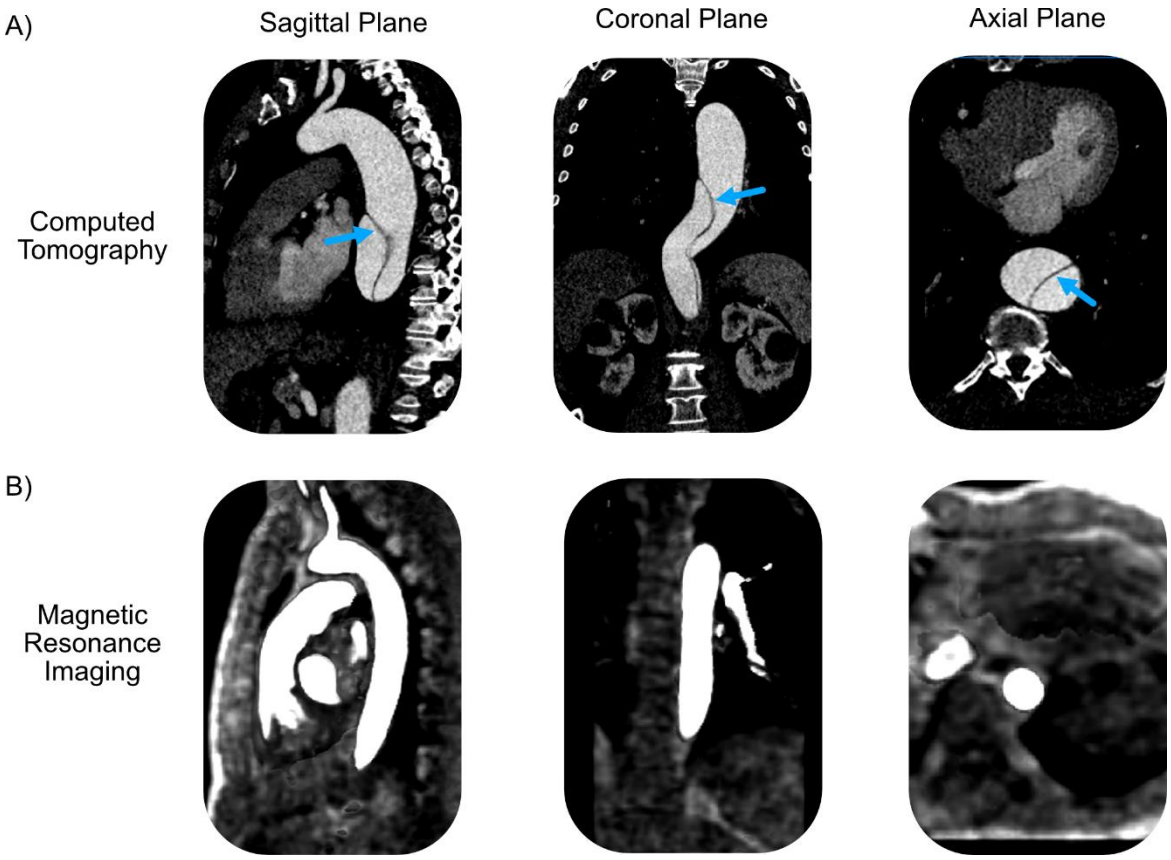

Figure 2.5: CT and MRI images which show that the vessel lumen has a different contrast to the surrounding tissues in both healthy (volunteer 1 - bottom) and AD (patient 3 - top) cases. Also, the images clearly show the difference between a A) aortic dissection and B) healthy aorta from medical images. Blue arrows show the partition between the true and false lumen in the AD patient. (Data is from the patient cohort described in Chapter 5, Table 5.1).

The segmentation process utilised throughout this thesis is described in more detail in Chapter 3, but Figure 2.6 provides an overview. Generally, contours around the aorta and each branch vessel were generated on SimVascular® based on intensity thresholding techniques, and then adjusted manually where applicable (Figure 2.6A). For individual vessel segments, several contours were created along the vessel centreline (Figure 2.6B) to create an approximation of the entire aorta and main branches (Figure 2.6C). Thereafter, these contours were lofted along the vessel centreline to create a 3D geometry, where each vessel segment is an isolated unit (Figure 2.6D). Finally, these isolated segments were stitched together to create a solid 3D model (Figure 2.6E). Notably, the true lumen (yellow) and false lumen (red) were segmented and reconstructed as separate bodies, as illustrated in Figure 2.6D.

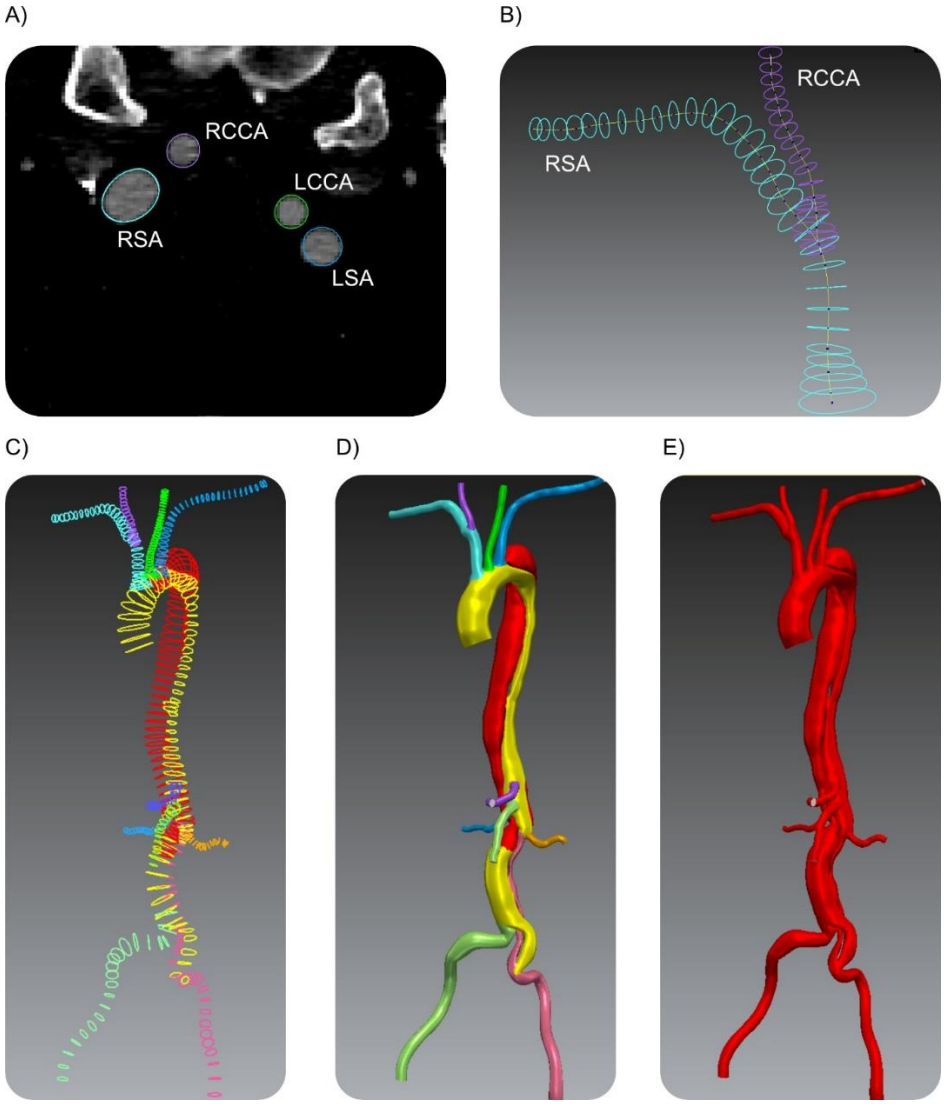

Figure 2.6: Segmentation and reconstruction process of an entire aortic geometry and main branches in an AD patient (patient 2) with an aortic dissection (see Table 5.1, Chapter 5 for further details), showing A) contour generation around the vessel lumen of a single image slice, B) multiple contours generates along the vessel centrelines, C) discrete contours of the entire thoracoabdominal aorta, with different colours for each aortic segment, D) 3D reconstruction of isolated aortic segments, and E) a solid aortic model with all segments stitched together.

2.4 Computational Fluid Dynamics

2.4.1 Mesh Generation

To converge on a numerical solution, the 3D domain of interest was spatially discretised into a finite number of smaller elements, commonly known as a mesh or grid [6] [16] [117]. Figure 2.7 illustrates this process. Generally, a mesh is composed of a combination of different elements, including hexahedral, tetrahedral, pyramidal, and/or polyhedral cells in a structured or unstructured arrangement [118] [119]. Structured meshes are comprised of regular, uniform

quadrilateral or hexahedral elements that are arranged in a controllable, user-defined pattern, with smooth transitions between elements. Conversely, unstructured meshes are comprised or irregular, non-uniform triangular, tetrahedral, or pyramidal elements which are non-uniformly distributed [118].

For complex geometries with chaotic flow patterns, such as the aorta and branches, an unstructured mesh is preferable [118]. This is because a structured mesh is not possible for many complex geometries, while unstructured meshes can be rapidly generated and allow automated clustering of cells in regions of expected fluid flow [118]. In such cases, unstructured meshes can generally be created with fewer elements, thus reducing computational expense. Crucially, all elements within the mesh must meet certain geometric criteria to achieve an adequate mesh quality, such as skewness (the difference between the shape of the cell and that of an equilateral cell of equal volume) and aspect ratio (the measure of the stretching of a cell) [117] [118]. Notably, poor-quality meshes decrease the simulation accuracy and destabilize the solution in regions of complex fluid flow [117] [118].

The first stage in discretising the aortic geometries was to generate a surface mesh using Ansys ICEM®. This Ansys software was chosen because it is a well-validated, commercial software for CFD applications. A triangular-dominant, patch-independent mesh was generated to create a hollow, 3D shell composed of several thousand individual 2D surface elements (Figure 2.7B & 2.7C). This surface mesh was generated using an Octree method which permits refinement of the mesh in complex regions where necessary but utilises larger elements where possible. In geometries such as the aorta, the Octree method was preferable since it is robust, meaning it can work for complex geometries [120].

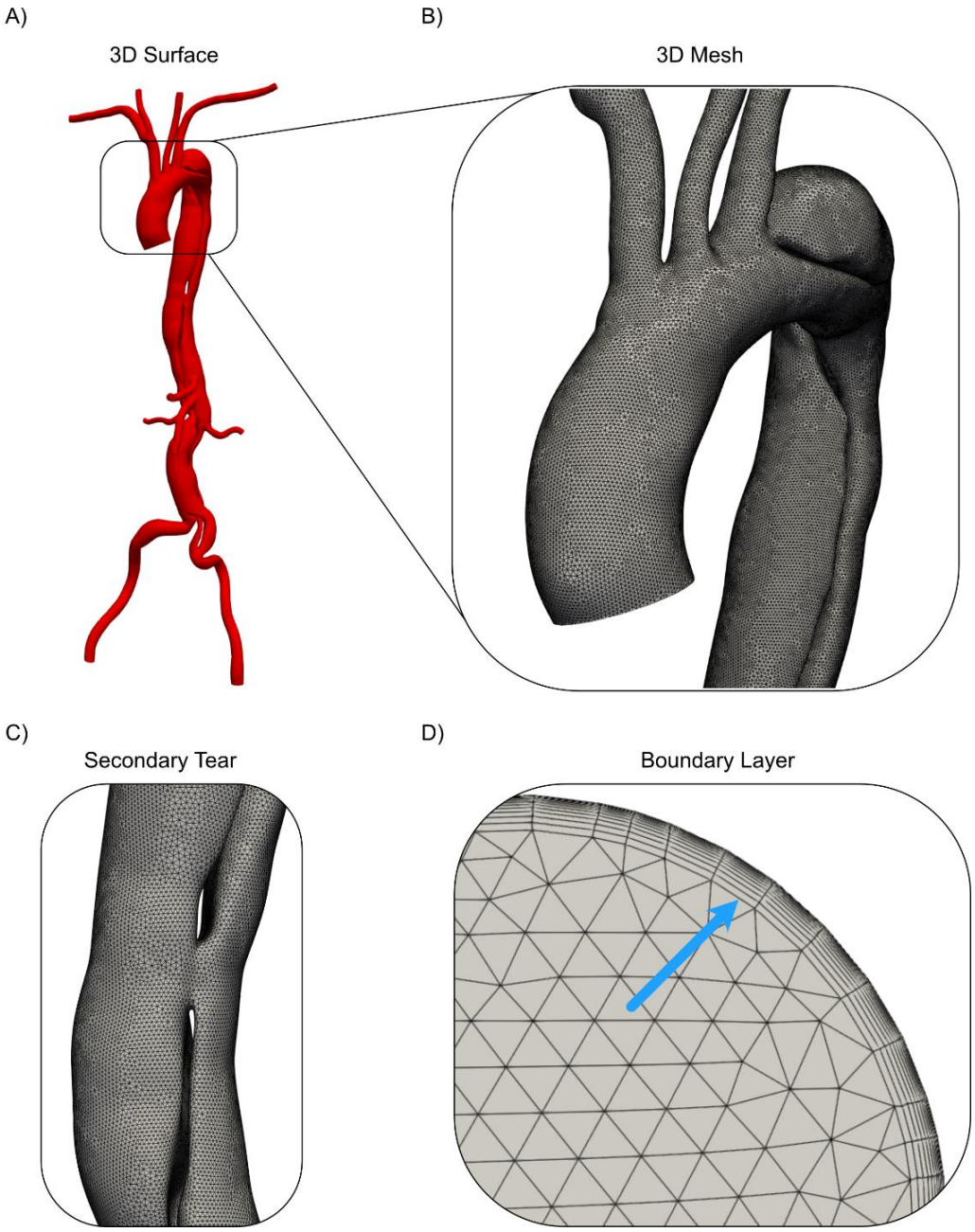

Figure 2.7: Meshing process illustrating A) the reconstructed 3D model of a thoracoabdominal aorta with a Type B aortic dissection, along with the triangular surface mesh of B) the aortic arch and C) descending aorta intraluminal tear. D) Blue arrow shows the boundary layer.

Each of these mesh elements had a set of boundary faces, edges, and nodes. The surface mesh was then smoothed to improve overall mesh quality by ensuring a good distribution of elements with optimal aspect ratios which obey the user-defined sizing constraints [120]. Smoothing is discussed in more detail in Chapter 3**.** The Octree surface mesh was then combined with a Delaunay volume mesh, dominated by 3D tetrahedral elements, as these two methods are known to work harmoniously to produce a high-quality mesh [120].

Crucially, a boundary layer (Figure 2.7D) was required to capture shear and boundary layer physics in the near-wall region [16] [118] [121]. This was essential for accurate numerical predictions of near-wall haemodynamics such as wall shear stress, and to enhance simulation stability [41] [117]. The boundary layer itself refers to fluid in the immediate vicinity of the blood vessel wall, where the effects of fluid viscosity dominate [122].

To be effective, the boundary layer y+ value was set to ≤1 due to the turbulence models used [121] [123] [124]. The initial boundary layer height, y, on all computational meshes was therefore calculated according to:

$$y = \frac{y^{+}v}{u_{\tau}} \tag{2.1}$$

where y^{+}=1, $\left(v = \frac{\mu}{\rho}\right)$ is the kinematic viscosity, μ is the dynamic viscosity, u_{τ} and is the friction velocity. The friction velocity was calculated as:

$$u_{\tau} = \sqrt{\frac{\tau_{\omega}}{\rho}} \tag{2.2}$$

where τ_{ω} is the wall shear stress. To estimate τ_{ω}, this was calculated from the skin friction coefficient, C_f, and free stream velocity, U_{∞}.

$$\tau_{\omega} = \frac{1}{2} C_f \rho U_{\infty}^{2} \tag{2.3}$$

For this study, U_{∞} was defined as the maximum velocity ($U_{Systole}$) of a single cardiac cycle [125]. Further, the Schlichting equation (Eq.2.4) was employed to calculate the skin friction coefficient as a function of Re at peak systole [122].

$$C_f = [2\, log_{10}(Re) - 0.65]^{-2.3} \tag{2.4}$$

An initial simulation was then performed with the estimated boundary layer height, and postprocessing revealed the true y+ for that specific simulation across all regions of the 3D geometry. The boundary layer was then refined as necessary to ensure the true y+ was <1 at all locations. The boundary layer was subsequently expanded exponentially by a factor of 1.2 to generate at least 10 layers of increasing element thickness (Figure 2.7D).

2.4.2 Mesh Independence

Generally, an increased number of elements in the computational mesh yields a more accurate numerical solution. This means that as the number of mesh elements is increased, the spatial

discretization error asymptotically approaches zero. However, it is not feasible to utilise an infinitely fine mesh as this becomes computationally prohibitive. Therefore, for a given CFD simulation, the spatial resolution of the mesh must be refined enough to ensure a valid result, but coarse enough to limit computational demand [117] [126]. An appropriate mesh density can be selected based on grid convergence analysis, also known as a mesh independence study [16] [126].

Consequently, a mesh independence study was conducted to determine the impact of successive mesh refinement on WSS, utilising the thoracic aorta of a patient with an aortic dissection (patient 2) as a representative case. For increasing mesh densities, WSS was analysed at several different regions of the thoracic aorta: 1) ascending aorta, 2) region of primary intraluminal tear, 3) innominate artery bifurcation, 4) left subclavian artery, 5) false lumen at the aortic arch, 6) secondary tear in the distal arch, 7) the descending aorta, and 8) secondary tear in the descending aorta. From these locations, an averaged WSS was calculated for each mesh density.

First, the order of convergence, p, was calculated as per:

$$p = \ln\left(\frac{f_3 - f_2}{f_2 - f_1}\right)\frac{1}{\ln(r)} \tag{2.5}$$

where f_1, f_2, and f_3 are the average WSS values for the different mesh densities, and r is the refinement ratio. Notably, f_1 represents the finest mesh, while f_3 represents the most coarse. A Richardson extrapolation (Eq. 2.6) was then performed to estimate the true value of the WSS parameter, based on the order of convergence previously calculated.

$$f_{h=0} = f_3 + \frac{f_1 - f_2}{r^P - 1} \tag{2.6}$$

Then, the grid convergence index (GCI) was calculated for each refinement level:

$$GCI = \frac{F_s|e|}{r^p - 1} \tag{2.7}$$

where F_s =1.25 is the safety factor, and $|e|$ is the error between the refinement levels. To ensure grid convergence was evaluated within the asymptotic range, and thus approaching a converged answer, the following relationship was confirmed [127].

$$\frac{GCI_{2,3}}{r^P \times GCI_{1,2}} \cong 1 \tag{2.8}$$

In this study, the tetrahedral surface mesh element size was decreased from 0.2mm to 0.06mm in length, corresponding to an increase in the total number of elements from roughly 1 million to 11 million, with a refinement ratio of 1.84. Figure 2.8 illustrates how the mean WSS integral changed with respect to mesh density, asymptotically approaching the Richardson extrapolation (dashed line) value of 0.449. As per Eq. 2.8, it was confirmed that the solution lies within the asymptotic region of convergence. At an element size of 0.1mm (3.8 million elements throughout the thoracic aorta), this resulted in an error (ε_h) of 2.29% with respect to the Richardson extrapolation. At this density, the error was deemed acceptable and successive mesh refinement was not worth the significant increases in computational expense of the simulations. Notably, the mesh density requirements for the calculation of WSS exceeded that of velocity and flow rate, meaning the mesh was also valid to compute bulk flow metrics.

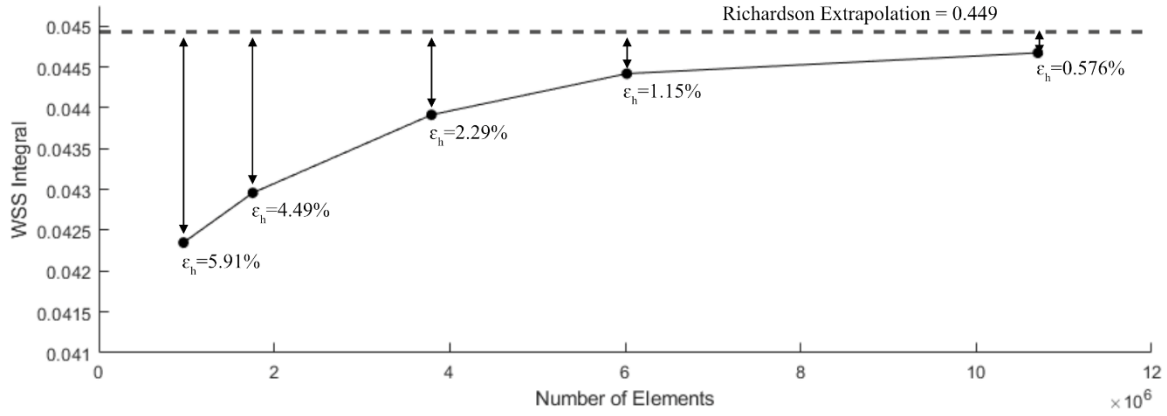

Figure 2.8: The results of a mesh independence study which evaluated the mean WSS integral, averaged over several locations of a thoracic aorta, when different mesh element sizes were utilised: 0.2, 0.15, 0.1, 0.08, and 0.06, corresponding to a mesh of 1 million, 1.8 million, 3.8 million, 6 million, and 10.1 million, respectively. The errors for each mesh density relative to the Richardson extrapolation were 5.91%, 4.49%, 2.29%, 1.15%, and 0.576%, respectively.

2.4.3 Numerical Methods

Computational simulation of blood flow requires the numerical solution of the governing equations of flow for continuity and momentum [36] [51] [118]. For compressible flows, or those involving heat transfer, an additional equation for energy conservation is required [36] [118]. It is known that blood flow may exhibit non-Newtonian features including shear-thinning and viscoelasticity. However, an incompressible, Newtonian fluid assumption is generally accepted when shear rates are high, such as in large arteries like the aorta where inertial forces dominate [6] [15] [16] [17] [41] [128] [129] [130] [131]. Consequently, the

dynamics of this flow can be fully described by solving the more simplified incompressible, Newtonian Navier Stokes equations.

The Navier Stokes equation for an incompressible Newtonian fluid, as described in Einstein summation convention, also known as tensor form, can be written as in Eq. 2.9 and Eq. 2.10 for continuity and momentum, respectively [31] [132]:

$$\frac{\partial u_i}{dx_i} = 0 \tag{2.9}$$

$$\frac{\partial u_i}{\partial t} + \frac{\partial}{\partial x_j}\left(u_i u_j\right) = -\frac{1}{\rho}\frac{\partial p}{\partial x_i} + v\frac{\partial^2 u_i}{\partial x_j \partial x_j} \tag{2.10}$$

where i,j = 1,2,3 are the vector components. Notably, this can be related to vector notation through the following operators:

$$\frac{\partial u_i}{\partial x_i} = \frac{\partial u_1}{\partial x_1} + \frac{\partial u_2}{\partial x_2} + \frac{\partial u_3}{\partial x_3} = \nabla.\vec{u},$$

$$\frac{\partial^2 u_i}{\partial x_i \partial x_i} = \frac{\partial^2 u_1}{\partial x_1^2} + \frac{\partial^2 u_2}{\partial x_2^2} + \frac{\partial^2 u_3}{\partial x_3^2} = \nabla^2\vec{u}$$

Three of the most common, validated, and accepted methods to solve these partial differential equations are the finite difference method (FDM), finite volume method (FVM), and finite element method (FEM), among many other formulations including the spectral method, immersed boundary method etc [117] [118]. Notably, this is not an exhaustive list of such methods. Both the FEM and FVM divide the geometry into an array of geometric elements, the shape and complexity of which depend on the numerical approximation [133]. Both the FVM and FEM are routinely used in CFD simulations of blood flow [133]. Furthermore, there are several advantages and disadvantages for each method, depending on the type of fluid or problem to be solved [133]. Regarding the FVM, the computational fluid domain is discretised into a series of small, discrete, and interconnected cells known as control volumes [118] [133]. The integral forms of the governing equations are then discretised into algebraic equations over each control volume, which are solved to calculate the dependent variables such as pressure and velocity at the centre of each cell [118] [133]. Fundamentally, the FVM is strictly conservative, meaning the total flux entering the cell is equal to that leaving it, thus guaranteeing that mass and momentum are conserved [133].

In this thesis, Ansys Fluent® was used to solve the Navier Stokes equations via the FVM, using pressure-based solvers [118]. Notably, Ansys Fluent® is well-documented, is widely used for

blood flow analysis, and has a validated implementation of the FVM [118] [117]. Furthermore, there are five algorithms within these pressure-based solvers which utilise pressure-velocity coupling to derive an equation for pressure, based on the results of the continuity and momentum equations [118]. One such algorithm is the Pressure-Implicit with Splitting of Operators (PISO) method, which is suggested for transient flow simulations in the presence of a complex unstructured mesh [118]. Therefore, the PISO algorithm was used for all transient simulations in this thesis. Since the PISO solver utilises an implicit time integration scheme, it is unconditionally stable with respect to the magnitude of the time step [118].

2.4.4 Turbulence Models

Turbulence modelling provides a closure term for the Navier Stokes equations [132]. In this thesis, modelling turbulence was essential to permit the accurate simulation of turbulent flows which are characterised by 3D, aperiodic swirling motions within the fluid, also known as eddies [118]. Notably, no single turbulence model is universally superior for all simulations, as all have their own advantages and limitations [118].

There is a range of turbulent length scales, beginning with large eddies which begin to dissipate and lose energy, creating successively smaller eddies (Figure 2.9) [118] [121]. For most cases, it is not essential to fully resolve these eddies, and a time-averaged depiction of flow is sufficient [121]. Consequently, simulations can be approached via a direct numerical simulation (DNS), large eddy simulation (LES), or the simpler Reynolds Averaged Navier Stokes (RANS) approach.

2.4.4.1 Direct Numerical & Large Eddy Simulations

In a DNS, every fluctuating motion in the turbulent flow is resolved in space and time for the whole spectrum of turbulence scales [118] [131]. This is the most accurate technique to simulate turbulence but requires significant and often prohibitive computational resources [131] [134]. For practical use, DNS is often too computationally intensive, and such a detailed description of flow is generally not required. Further, DNS is not possible in Ansys Fluent®, so turbulence modelling is required [118] [121]. Therefore, DNS was not considered in this thesis.

In a LES, only the larger eddies are resolved, while the smaller eddies are modelled, meaning LES falls between a DNS and RANS approach [118]. The rationale behind this approach is that by modelling less turbulence, and explicitly computing (resolving) more, then the error which is introduced by the modelling can be reduced.

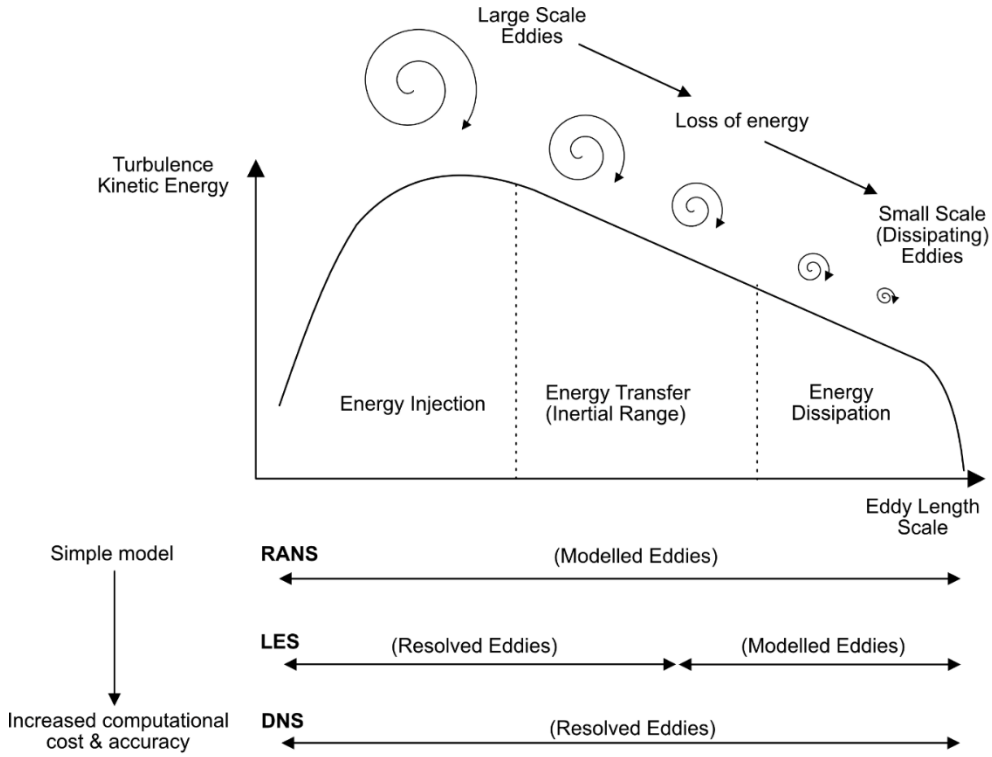

Figure 2.9: Illustration of turbulence (eddy) length scales with respect to turbulence kinetic energy, and how these eddies are resolved or modelled through different numerical approaches. A DNS approach fully resolves eddies at all scales, LES resolves larger eddies while smaller scales are modelled, while RANS simulations model the entire length scale.

While this is less computationally intensive than DNS, the computational cost remains orders of magnitude greater than a RANS model [118] [135]. Due to limited computational resources, LES was not considered in this thesis.

2.4.4.2 Reynolds Averaged Navier Stokes Simulations

All CFD simulations conducted within this thesis utilised RANS simulations. For these RANS simulations, the governing equations were solved for time-averaged flow behaviour and the magnitude of turbulent fluctuation. Consequently, the entire spatiotemporal range of turbulence was modelled rather than explicitly resolved [118] [121]. These simulations were therefore simpler than a DNS or LES approach, but required significantly less computational resources to achieve solution convergence [131].

In RANS models, variables within the Navier Stokes equations were decomposed into their mean and fluctuating components where, at any point in time [121] [132]:

$$u_i = \bar{u}_i + u_i', \qquad p_i = \bar{p}_i + p_i'$$

where $\bar{u}_i$ and $\bar{p}_i$ are the mean components, and and u' and p_i' are the fluctuating components. By substituting this into the Navier Stokes equations, this yields Eq. 2.11 and Eq. 2.12 for continuity and momentum, respectively:

$$\frac{\partial(\bar{u}_i+u_i')}{dx_i} = 0 \tag{2.11}$$

$$\frac{\partial(\bar{u}_i+u_i')}{\partial t} + \frac{\partial}{\partial x_j}\left((\bar{u}_i + u_i')(\bar{u}_j + u_j')\right) = -\frac{1}{\rho}\frac{\partial(\bar{p}_i+p_i')}{\partial x_i} + v\frac{\partial^2(\bar{u}_i+u_i')}{\partial x_j \partial x_j} \tag{2.12}$$

These equations can then be time-averaged, as follows:

$$\frac{\partial\overline{(\bar{u}_i+u_i')}}{dx_i} = 0 \tag{2.13}$$

$$\frac{\partial\overline{(\bar{u}_i+u_i')}}{\partial t} + \frac{\partial}{\partial x_j}\left(\overline{\bar{u}_i\bar{u}_j} + \overline{u_i'\bar{u}_j} + \overline{\bar{u}_i u_j'} + \overline{u_i'u_j'}\right) = -\frac{1}{\rho}\frac{\partial\overline{(\bar{p}_i+p_i')}}{\partial x_i} + v\frac{\partial^2\overline{(\bar{u}_i+u_i')}}{\partial x_j \partial x_j} \tag{2.14}$$

The time average of the fluctuating velocity is zero, because instantaneous fluctuations are random both in space and time, but the variance of these fluctuations is non-zero, i.e. [121]:

$$\overline{u'} = 0, \qquad \overline{u'^2} \neq 0$$

Therefore,

$$\frac{\partial\overline{(\bar{u}_i)}}{dx_i} = 0 \tag{2.15}$$

$$\frac{\partial\overline{(\bar{u}_i)}}{\partial t} + \frac{\partial}{\partial x_j}\left(\overline{\bar{u}_i\bar{u}_j} + \overline{u_i'u_j'}\right) = -\frac{1}{\rho}\frac{\partial\overline{(\bar{p}_i)}}{\partial x_i} + v\frac{\partial^2\overline{(\bar{u}_i)}}{\partial x_j \partial x_j} \tag{2.16}$$

Remembering that $\overline{\bar{u}_i} = \bar{u}_i$,

$$\frac{\partial\bar{u}_i}{dx_i} = 0 \tag{2.17}$$

$$\frac{\partial\bar{u}_i}{\partial t} + \frac{\partial}{\partial x_j}(\bar{u}_i\bar{u}_j + \overline{u_i'u_j'}) = -\frac{1}{\rho}\frac{\partial\bar{p}_i}{\partial x_i} + v\frac{\partial^2\bar{u}_i}{\partial x_j \partial x_j} \tag{2.18}$$

Which gives:

$$\frac{\partial\bar{u}_i}{dx_i} = 0 \tag{2.19}$$

$$\frac{\partial\bar{u}_i}{\partial t} + \frac{\partial}{\partial x_j}\left(\bar{u}_i\bar{u}_j\right) = -\frac{1}{\rho}\frac{\partial\bar{p}_i}{\partial x_i} + v\frac{\partial^2\bar{u}_i}{\partial x_j \partial x_j} - \frac{\partial}{\partial x_j}\left(\overline{u_i'u_j'}\right) \tag{2.20}$$

The Reynolds stress tensor is $\tau_{ij} = \overline{u_i' u_j'}$, which provides the averages effect of turbulent convection and then yields the final form of the RANS governing equations for continuity (Eq. 2.21) and momentum (Eq. 2.22) [121]:

$$\frac{\partial \bar{u}_i}{dx_i} = 0 \tag{2.21}$$

$$\frac{\partial \bar{u}_i}{\partial t} + \bar{u}_j \frac{\partial \bar{u}_i}{\partial x_j} = -\frac{1}{\rho}\frac{\partial \bar{p}_i}{\partial x_i} + v\frac{\partial^2 \bar{u}_i}{\partial x_j \partial x_j} - \frac{\partial \tau_{ij}}{\partial x_j} \tag{2.22}$$

Common RANS models include the k-epsilon (k-ε) and k-omega (k-ω) models, both of which are accurate for a wide range of applications, and require similar computational effort [118] [121]. Generally, the kω model performs better than the kε model when evaluating blood flow, especially around near-wall regions [136] [137]. Thus, the kω turbulence model was used for all CFD simulations within this thesis.

In this study, turbulence intensity, which is defined as the ratio of the root-mean-square of the velocity fluctuations, u', to the mean flow velocity, $\bar{u}$, was calculated as per equation 2.23.

$$I = \frac{u'}{\bar{u}} = (0.16 Re D_H)^{-\frac{1}{8}} \tag{2.23}$$

Where D_H is the hydraulic diameter of the inlet (aortic root) or outlet branch.

2.4.5 Boundary Conditions

BCs should be physiologically relevant, simple, robust, and computationally inexpensive [33]. Further, these BCs should be scalable and readily implementable on a parallel computing framework for numerous inlets and outlets [33]. Of course, there is a trade-off between accuracy and computational expense, but it should be noted that a good CFD model only requires relevant details which will improve the model for the intended objective [34]. A more complex model does not necessarily yield better clinical information [34]. As previously described, lumped parameter models, specifically the Windkessel model, can be prescribed as BCs for a coupled 0D-3D arterial CFD simulation. Chapter 4 of this thesis describes the use of this model in detail. In the present chapter, we describe how these BCs were coupled to the numerical model in Ansys Fluent®.

A User Defined Function (UDF) was used for the prescription of custom BCs in Ansys Fluent®. In this way, it was possible to couple the lumped parameter BC to the 3D numerical domain to solve for pressure and flow at the CFD model outlets [36] [56].

To understand this coupling, consider the outlet boundary of one terminal branch, for example the right subclavian artery (RSA). First, the Windkessel parameters were prescribed at the boundary, along with the time step size, fluid density, initial flow rate, and initial pressure. Upon initiation of the simulation, the outlet flow rate at the terminal boundary was calculated as a result of the first iteration of time step one. Thereafter, the 3-element Windkessel model (3EWM) equation was solved for pressure on the face of each element at the terminal boundary, using parallel computing nodes. The pressure contributions from each element face at the branch outlet were subsequently aggregated through a global summation process and averaged to determine the mean value across the entire boundary face. This process was repeated for each iteration within a single time step, and the resulting pressure was updated accordingly. At the end of the time step, the pressure was applied to the boundary face and the flow rate was calculated. This process was then repeated for the desired number of time steps.

2.5 Wall Treatment

There are two primary methods to treat the aortic wall during CFD simulations. For simplicity and to reduce computational expense, the wall is often assumed to be rigid, thus neglecting wall movement [15] [130]. As discussed in Chapter 1, however, the aortic wall is a compliant structure.

Consequently, it is possible to model this wall motion via a fluid-structure interaction (FSI) approach. FSI incorporates finite element modelling of the aortic wall to capture the effect of increasing and decreasing intraluminal pressure because of pulsatile blood flow [60]. It must be noted, however, that building an FSI model is very challenging as it relies upon clinical information which is not readily obtainable [119]. For example, one must prescribe vessel wall properties including elasticity and viscoelasticity, account for anisotropy in mechanical properties, prescribe wall thickness, and account for the influence of external tissue support [117] [60] [138]. This significantly increases the computational demand of the simulation, and each additional assumption introduces further potential sources of error. Therefore, both approaches have their own advantages and limitations. In this thesis, a rigid wall assumption was utilised.

Finally, it is known that the circulatory system does not work in isolation and is subject to both acute and chronic changes [36] [139]. Therefore, it is important to note that there are other sources of vessel wall motion, though these are generally not modelled in CFD simulations. For example, neuro-regulation, hormone control, cardiopulmonary coupling, and nutrient

transport all influence vasoconstriction and vasodilation [36] [139]. In this thesis, modelling these elements is out with the scope of work and they are therefore neglected.

2.6 1D Modelling

In a 1D formulation, the arterial network is decomposed into several arterial segments, each of which are connected at nodes [139]. In this thesis, the Nektar1D solver was utilised, where each segment was assumed to be an impermeable, compliant tube of a specific cross-sectional area, described by a single axial co-ordinate, x. Notably, wall compliance is generally included in 1D models due to the reduced computational expense in comparison to 3D modelling. Within this framework, fluid flow was unidirectional along the primary axial direction [139]. As a consequence of pulsatile blood flow through the 1D domain, the propagating pulse waves altered the intraluminal cross-sectional area of each vessel segment [139]. Conventionally, the arterial segment is assumed to be tethered in the longitudinal direction, meaning the pressure-induced wall deformity is only permitted to occur in the radial direction [139].

The dynamics of blood flow are governed by the 1D axisymmetric form of the incompressible Navier Stokes equations for continuity (Eq. 2.24) and momentum (Eq. 2.25) in a control volume, combined with an equation for a deformable vessel wall, whether elastic or viscoelastic [36] [49] [139] [140].

$$\frac{\partial A}{\partial t} + \frac{\partial (Au)}{\partial x} = 0 \tag{2.24}$$

$$\frac{\partial Q}{\partial t} + \frac{\partial}{\partial x}\left(\alpha \frac{Q^2}{A}\right) + \frac{A}{\rho}\frac{\partial p}{\partial x} = \frac{f}{\rho} \tag{2.25}$$

where A is the vessel cross sectional area, f is the frictional force per unit length, and $\alpha = \frac{1}{AU^2}\int u^2 d\sigma$ is a non-dimensional constant [139] [140]. Notably, the continuity and momentum equations grant two equations with three unknowns A, u, and p (or alternatively, A, Q, and p) [140]. Therefore, the next step is to define a relationship between p and A, known as the Tube law [36] [128] [139] [140] [141]:

$$p = p_e + \frac{\Gamma}{A_0\sqrt{A}}\left(\frac{\partial A}{\partial t}\right), \tag{2.26}$$

where,

$$p_e = p_{ext} + \beta\left(\sqrt{A} - \sqrt{A}_0\right),$$

$$\beta = \frac{\sqrt{\pi}h_0 E}{(1-v^2)A_0}, \qquad \Gamma = \frac{2}{3}\frac{\sqrt{\pi}\varphi h}{A_0}$$

where h_0 and A_0 are the vessel wall thickness and cross-sectional area in an equilibrium state, respectively. E is the wall Young's modulus, v is the Poisson ratio (~0.5), and p_{ext} is the constant external pressure [140]. p_e is the elastic component of pressure, φ is the wall viscosity, β is the wall stiffness, and Γ is the Euler gamma function. For purely elastic walls, $\Gamma = 0$, meaning pressure is only due to p_e, the elastic component [139]. For viscoelastic walls, $\Gamma \neq 0$. Eq. 2.24, Eq. 2.25, and Eq. 2.26 combine to yield one of the most general 1D model formulation of the governing equations [140].

2.7 Motivation and Objectives

CFD models are increasingly utilised in research and clinical practice for screening and diagnosis of vascular pathologies. They are also utilised in surgical planning, disease management and follow-up investigations after surgical intervention. However, these CFD models often rely on ionising imaging modalities to facilitate anatomic reconstruction. For example, in TBAD patients, CT imaging is the gold standard. Thereafter, to minimise assumptions and create patient specific models, the calibration or prescription of boundary conditions often requires invasive pressure measurements and additional scans which further increases the burden on the patient.

Thus, the primary hypothesis of this thesis is as follows: can we create fully patient-specific CFD models of TBADs based exclusively on a single, low-resolution 4D Flow-MRI scan? We hypothesize that it is possible to use quantitative blood flow information to retrospectively reconstruct the aorta, and calibrate physiologically relevant boundary conditions from temporally resolved branch flow rates and routine brachial cuff pressure measurements. If possible, these CFD models could be used as pre-surgical computational models into which stent-grafts could be virtually deployed. By doing so, one may predict the post-surgical flow regime and near wall haemodynamics within these grafts, which is currently poorly understood. This could be achieved through non-ionising, non-invasive methods without requiring intravenous contrast, thus minimising the burden to the patient.

In this thesis, we therefore aim to investigate blood flow within patient specific CFD models of the thoracoabdominal aorta of TBAD patients, and within the thoracic aorta of healthy volunteers. Specifically, we aim to:

1) Present a novel methodology to process retrospective 4D Flow-MRI images to enhance intraluminal contrast and signal intensity to permit threshold-based segmentation and reconstruction of the aorta and main branches.
2) Present a novel methodology to calibrate Windkessel boundary conditions for CFD modelling, based on non-invasive, quantitative branch flow information derived from 4D Flow-MRI.
3) Provide a comprehensive analysis on the blood flow regime of TBAD patients, with a focus on the impact of vessel geometry and boundary conditions on intraluminal haemodynamics.

3 Reconstruction and Validation of Arterial Geometries for CFD using Multiple Temporal Frames of 4D Flow-MRI Magnitude Images

In this chapter, we present a novel approach to create high contrast anatomical images from retrospective 4D flow-MRI data. For healthy and clinical cases, the 3D instantaneous velocity profiles at multiple cardiac time-steps were superimposed directly onto the 4D Flow-MRI magnitude images and combined into a single composite frame. This new Composite Phase-Contrast Magnetic Resonance Angiogram (CPC-MRA) resulted in enhanced and uniform contrast within the lumen. These images were subsequently segmented and reconstructed to generate 3D arterial models for CFD models. Further, the 3D geometries reconstructed from the 4D Flow-MRI derived CPC-MRA images were validated against the gold-standard of CT-based reconstructions. Using the time-dependent, 3D incompressible Reynolds-averaged Navier–Stokes equations, the transient aortic haemodynamics were then analysed in both the CT and 4D Flow-MRI derived geometries at the iliac bifurcation.

The work in this chapter was published, as per the following reference: S. M. Black, C. Maclean, P. Hall-Barrientos, K. Ritos and A. Kazakidi (2023), "Reconstruction and Validation of Arterial Geometries from 4D Flow-MRI Images: A Novel Approach" Cardiovascular Engineering and Technology 14:655–676. https://doi.org/10.1007/s13239-023-00679-x

3.1 Introduction

Accurate representation of the arterial geometry and blood flow regime plays a fundamental role in clinical practice for disease diagnosis, staging, treatment planning, and patient outcome monitoring [19] [142] [143]. The reconstruction of the aorta and main branches, in particular, is inherently challenging due to a high variability in diameter, shape, and overall geometry within the healthy and patient population [144]. In patients wherein a stent-graft has been deployed, metal-induced artifacts within medical images can further complicate this process [145].

Computational tomography (CT) is the preferred imaging modality for arterial visualization and reconstruction in clinical practice, especially where stent-grafts are present [94] [114] [146] [147]. However, CT scans utilize ionizing radiation, which is well-known to cause long-term health risks [148] [149] [150]. There is now a growing awareness in medical imaging to reduce radiation exposure where possible, especially in children and during asymptomatic screening [91] [92] [149] [151] [152] [153] [154] [155] [156] [157]. Additionally, ethical implications

prohibit the use of CT to generate anatomical or functional reference models within the healthy population.

Magnetic resonance angiography (MRA), a subset of MRI, is a non-ionizing alternative to CT imaging [94] [114] [158]. With the addition of intravenous contrast agents, the signal to noise ratio (SNR) and contrast to noise ratio (CNR) is increased significantly. However, in patients with high sensitivity to contrast agents, such as those with impaired renal function, the emergence of non-contrast MRA has been beneficial, including time of flight, phase contrast, and 4D Flow-MRI [5] [159] [160] [161] [162] [163] [164] [165].

4D Flow-MRI is a relatively recent development which captures the spatiotemporal evolution of 3D blood flow with full volumetric coverage throughout a continuous ROI at multiple cardiac time-steps [9] [166]. This time-resolved, respiratory and ECG gated acquisition permits post-hoc, dynamic visualization of the flow regime and quantification of several hemodynamic parameters [166]. Generally, arterial reconstruction from 4D Flow-MRI can be achieved through direct volume rendering within specific 4D flow software, or via contour-based segmentation of 4D Flow-MRI derived MRA, comprised of 2D image stacks [167]. With volume rendering, the user has limited control over the final geometry, which may falsely include parts of the surrounding tissue or exclude regions of low velocities, e.g. in curvature and branching points. Contour-based segmentation grants increased user control and has previously been performed via supervised (convolutional neural networks) and unsupervised (k-means clustering) machine learning, atlas-based approaches, deformable model algorithms, and blood vessel tracking algorithms [87] [116] [144] [168] [169] [170] [171] [172]. To utilize these segmentation techniques, the data must first be processed into discretized image stacks.

Due to the retrospective nature of this study and data availability, the 4D Flow-MRI images were not accompanied by standard and well-established images such as MRA or PC-MRA. PC-MRA, for example, is commonly used to generate images for blood vessel reconstruction and does not require intravenous contrast [173]. These angiographic images can, however, be created directly from the retrospective 4D Flow-MRI data [173]. Due to the complexity of the 4D Flow-MRI data, translating this information into images which clearly portrays the underlying anatomical structures is challenging [174]. However, the ability to generate contrast within the lumen in these retrospective datasets and prepare images for segmentation is essential for subsequent reconstruction.

Therefore, the aim of this Chapter is twofold. The primary aim was to outline a novel methodology to create a phase contrast angiogram by retrospectively superimposing the instantaneous 4D Flow-MRI-derived velocity profile at multiple, user-defined time-steps directly onto the magnitude image stack. As this methodology created a composite image, the resultant dataset was termed as a Composite Phase-Contrast Magnetic Resonance Angiogram (CPC-MRA). To validate this approach, a study was undertaken to compare the 4D Flow-MRI reconstructed geometries against CT-based reconstructions from a healthy volunteer and several clinical patients. The secondary aim was to evaluate haemodynamics from computational fluid dynamics (CFD) models, based on the reconstructed geometries from each imaging modality. This secondary study was to investigate whether minor changes in the reconstructed geometries had a large impact on CFD-derived haemodynamics. In each of the two studies, CT-imaging was utilized as the reference gold-standard approach. The CFD-derived velocities for each patient were then compared to that obtained directly from the 4D Flow-MRI data.

3.2 Methodology

3.2.1 Temporal Composite and Arterial Reconstruction

3.2.1.1 Imaging Datasets

4D Flow-MRI and CT data from three patients with arterial pathology in the thoracoabdominal region were acquired from the Queen Elizabeth University Hospital (QEUH). 4D Flow-MRI data was also obtained from a healthy volunteer (Table 3.1**).** Each clinical patient, hereafter termed patient 1, 2, and 3, was diagnosed with an abdominal Type B aortic dissection. Patient 1 had a previous Anaconda™ stent-graft deployed in the distal abdominal aorta, extending into the iliac bifurcation.

Table 3.1: Computed tomography (CT) and 4D Flow-magnetic resonance imaging (4D Flow-MRI) datasets obtained from a healthy volunteer and three clinical patients. AD = Aortic Dissection.

	Age	Sex	CT	4D Flow-MRI	Clinical Pathology	Anatomical Region
Volunteer 1	33	M	-	✓	-	Thoracic Aorta
Patient 1	68	M	✓	✓	Type B AD & Anaconda™ stent-graft	Iliac Bifurcation
Patient 2	55	M	✓	✓	Type B AD	Iliac Bifurcation
Patient 3	62	M	✓	✓	Type B AD	Iliac Bifurcation

3.2.1.2 4D Flow-MRI Scan Sequence

4D Flow-MRI images were acquired using the scan sequence (Siemens WIP 785A), previously outlined in Section 2.2.

3.2.1.3 Blood Velocity Visualization

The 4D Flow-MRI datasets were imported into Circle Cardiovascular Imaging Software (cvi42®, Calgary, Canada) and excess volume surrounding the aorta and its main branches was removed manually [175]. Thereafter, a mask (based on detected areas of flow) was applied to the 4D Flow-MRI magnitude images, and the threshold was set to ensure that the entirety of the aorta and branches were rendered. A mask correction was then employed to differentiate between static tissue, air filled regions, and regions of blood flow. From this mask, a rough, 3D volume render of the aorta was generated.

To visualize the velocity streamlines, the aorta and main branches were isolated from the heart and surrounding vasculature using a vessel centerline, created from multiple user-defined control points within the lumen. Figure 3.1A illustrates the velocity streamlines in the thoracic aorta of the healthy volunteer throughout a single cardiac cycle, while Figure 3.1B shows the abdominal aorta and iliac arteries of patient 1. It was evident that the instantaneous 3D velocity profile highlighted different regions of the lumen depending on the stage of the cardiac cycle. For example, the signal intensity in the ascending aorta, supra-aortic branches, and abdominal aorta was greatest during systolic acceleration (SA), peak systole (PS), and systolic deceleration (SD) respectively. Blood flow gradually became non-directional and low in magnitude as diastole was approached.

3.2.1.4 Geometry Reconstruction from 4D Flow-MRI

Figure 3.2 outlines the process of geometry reconstruction from 4D-Flow MRI images from multiple user defined time steps, at SA, PS, and SD. Centerlines were utilized only for streamline visualization (Figure 3.2B) and removed thereafter. Subsequent steps in the methodology therefore encompassed blood flow through all vasculature within the ROI to reduce inter- and intra-user variability. For the healthy volunteer and clinical patient, the 3D instantaneous velocity profile of blood at multiple (SA, PS, SD), discrete time points were utilized to generate contrast within the vessel lumen.

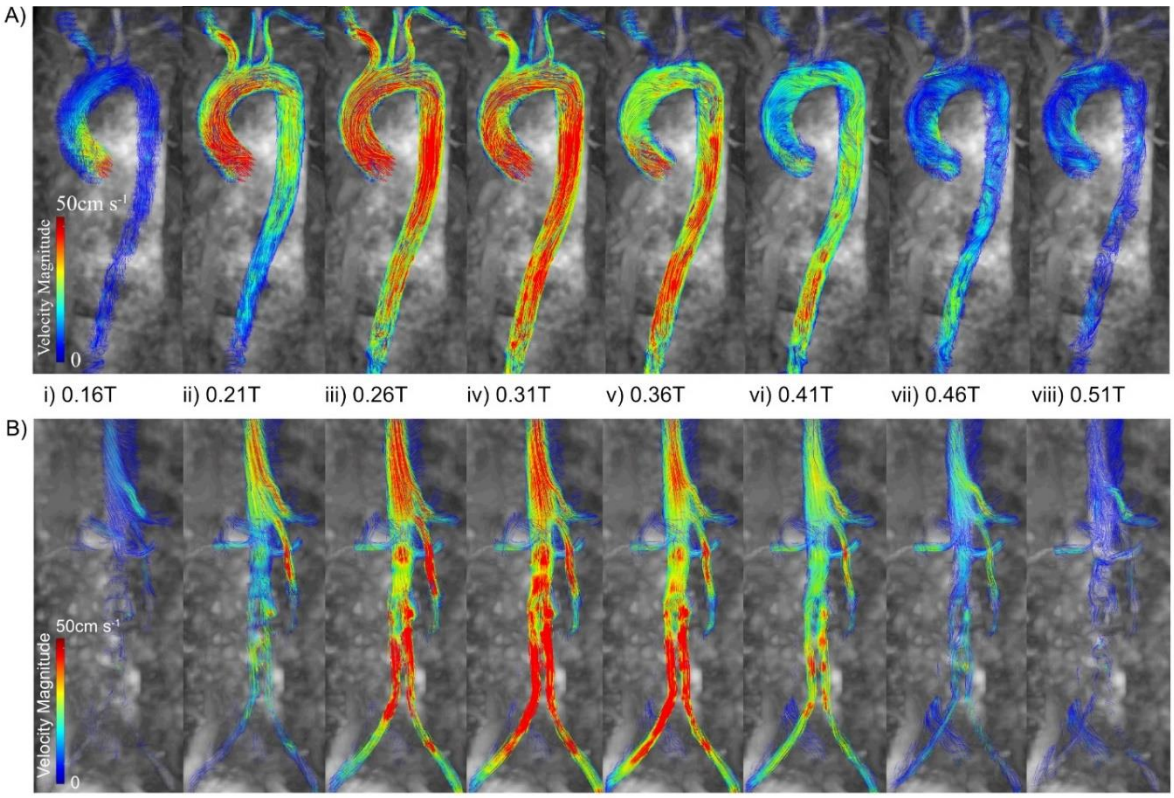

Figure 3.1 Velocity streamlines at consecutive time-steps throughout A) the thoracic aorta of a healthy volunteer, and B) the abdominal aorta and common iliac arteries of patient 1 with an Anaconda™ stent-graft. This was obtained from analysis of 4D Flow-MRI data on circle cardiovascular imaging software, cvi42®. All images are shown between a velocity scale of 0-50cm s^{-1} at time points throughout the cardiac cycle, where T is the cardiac period (0.21T: Systolic acceleration (SA); 0.26T: Peak systole (PS); 0.36T: Systolic deceleration (SD))

This data was extracted retrospectively from the 4D Flow-MRI data. To do this, the continuous ROI was first discretized to create a finite number of image slices in the transverse (axial) plane (n=1200 slices), coronal plane (n=500 slices), and sagittal plane (n=500 slices) at SA, PS, and SD. At each of these three-time steps, the discretized slices within the image stack were separated by a slice gap thickness of 0.35mm at (Figure 3.2C), which was the minimum possible gap thickness which could be created on cvi42®. The final resolution was, however, limited to 3.6 x 2.4 x 2.6 mm due to the acquisition sequence.

The 3D velocity profile at SA, PS, and SD, as calculated on cvi42®, overlaid directly onto each image within the DICOM stack via superimposition. In regions of non-zero blood velocity (i.e. within the lumen), the velocity signal was converted to a greyscale image, where pixel intensity within each slice of the image stacks was proportional to the instantaneous velocity magnitude of blood (Figure 3.2C). This generated additional contrast against the surrounding static tissue. The adopted velocity threshold for signal intensity for DICOM generation was 25 cm s^{-1}. A composite DICOM image, hereafter termed a Composite Phase-Contrast Magnetic Resonance

Angiogram (CPC-MRA) stack for each person was then created from images by combining the velocity enhanced DICOM stacks (Figure 3.2D) at SA, PS, and SD, (i.e. $SliceN_{PC-MRAS} = SliceN_{SA} + SliceN_{PS} + SliceN_{SD}$), where N is the slice number in the transverse, coronal, or sagittal plane. Crucially, superimposition and alpha blending were used to combine the images from each time step to ensure uniform intensity within the lumen. The contrast was then enhanced on the final DICOM stack by re-mapping the intensity values in the initial grayscale image to new values to fill the entire available intensity range using the Matlab® *imadjust* function [176]. This process of combining the image stacks was performed with an in-house Matlab® script (*https://doi.org/10.15129/2db504b8-3736-4ba0-9829-b7cc0c5db38a*) and is shown in Figure 3.2D for a single slice of the thoracic aorta.

The rationale behind the CPC-MRA images was as follows: if the user was to utilize only one time step, the resultant diameter in more distal regions of the aorta would be underestimated due to the temporal lag in arterial pulse waves which exhibit a reduced velocity and therefore reduced contrast. SA, PS, and SD were chosen as they generated the greatest degree of contrast throughout the entire aorta and branches when combined. Blood flow at previous and subsequent time steps was too low in magnitude to generate sufficient contrast for segmentation of the lumen. For each clinical patient and the healthy volunteer, the CPC-MRA DICOM stacks (generated from SA, PS, and SD) were then imported into the open-source software SimVascular® (https://simvascular.github.io/) [177].

To create a solid 3D model (Figure 3.3), the segmentation and reconstruction methodology outlined in Chapter 2, Section 2.2 was followed. Finally, the solid model was subsequently smoothed (10 iterations of constrained smoothing and decimation) as per the SimVascular® guidelines [177].

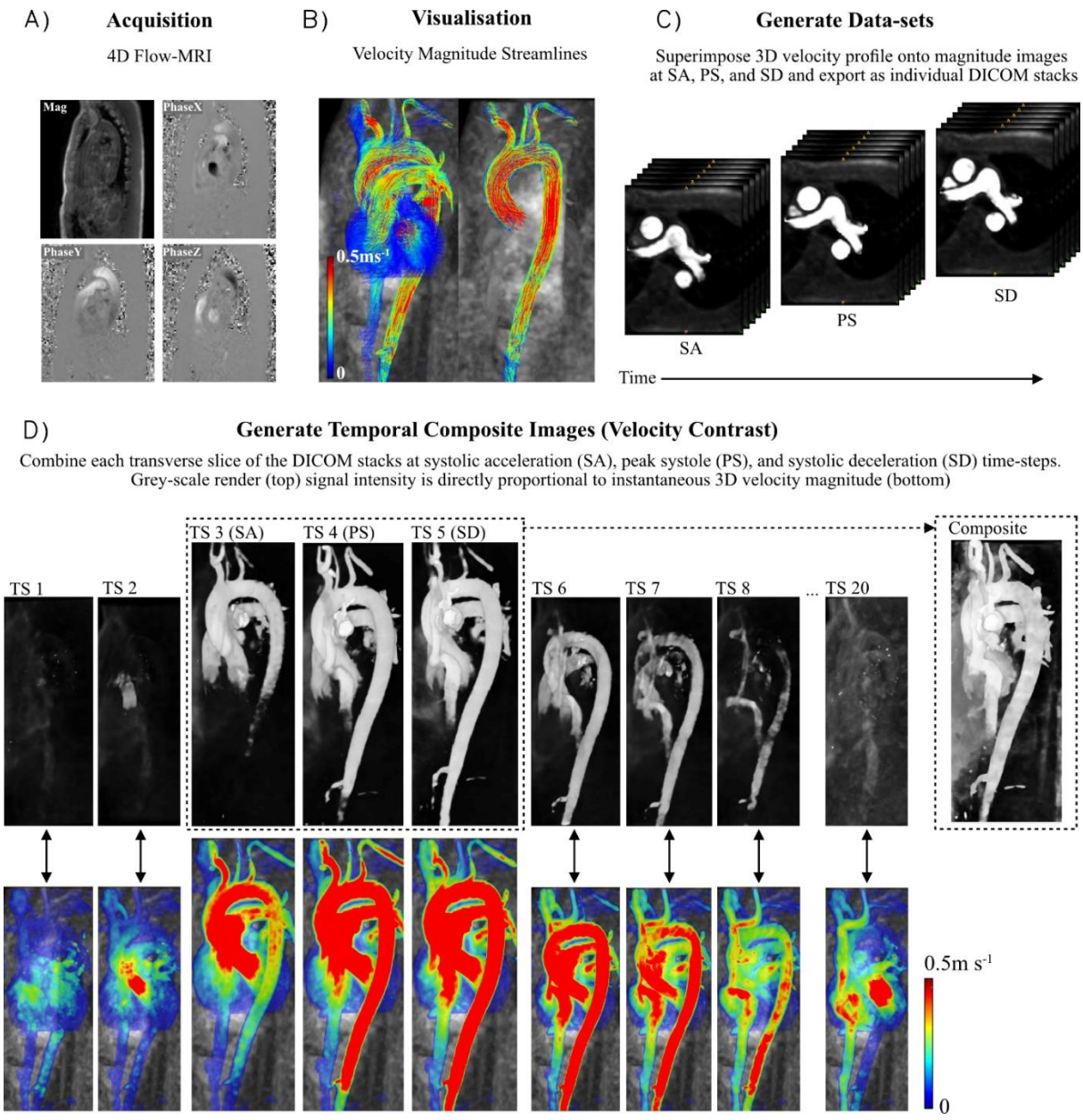

Figure 3.2: An illustration of the proposed CPC-MRA extraction from 4D Flow-MRI data of the thoracic aorta of the healthy volunteer. A) 4D Flow-MRI data acquisition at the thoracic aorta. B) 3D velocity encoding permitted analysis of velocity at any point in the region of interest (ROI), from which the aorta itself can be isolated for visualization. C) The 3D velocity profile was superimposed directly onto the magnitude images and the ROI was discretized along the axial plane to create a DICOM stack at SA, PS, and SD. D) The images at SA, PS, and SD were combined on a slice-by-slice basis to create CPC-MRA composite images in the axial, sagittal, and coronal plane. Velocity is directly proportional to signal intensity.

This smoothing was required as sharp corners can generate erroneously high regions of wall shear stress and adversely affect the accuracy of the computational simulations [17]. The reconstructed geometries were compared with the 4D-Flow MRI and CT images to ensure that the surface smoothing had no or minimal effect on the lumen dimensions.

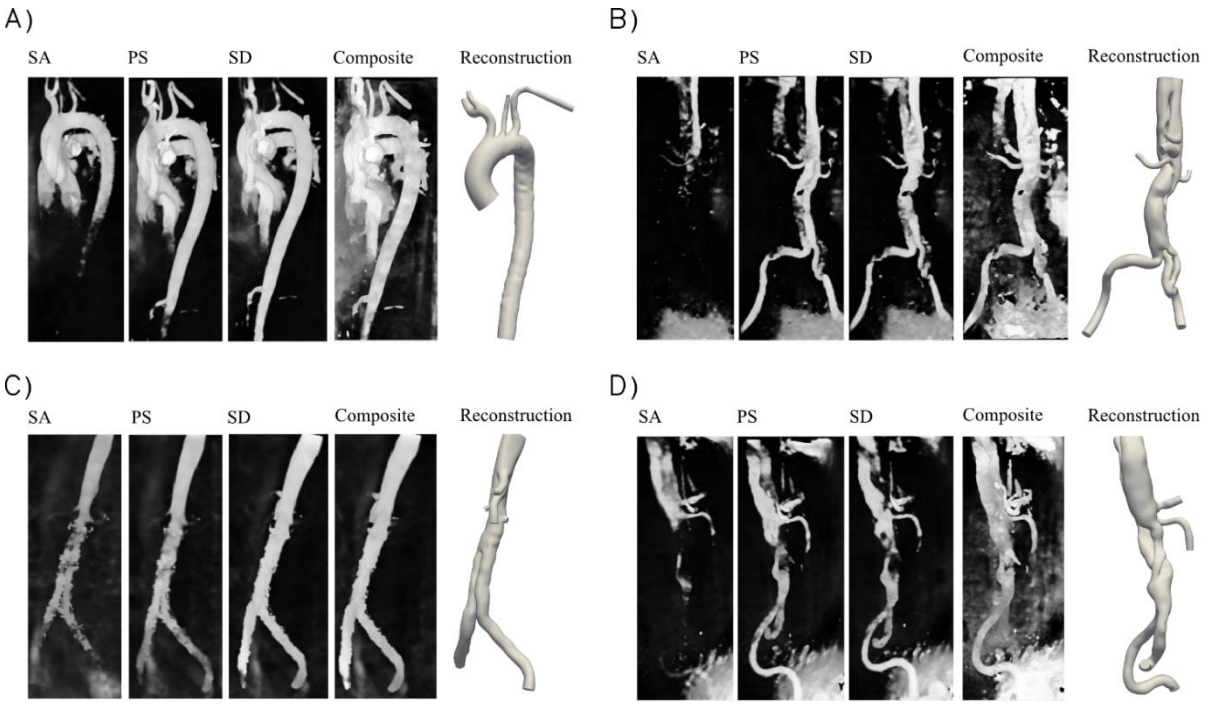

Figure 3.3: 3D greyscale render of the velocity-derived contrast at SA, PS, and SD, the 4D Flow-MRI CPC-MRA, and the final SimVascular reconstruction for the A) healthy volunteer, B) patient 1, C) patient 2, and D) patient 3.

3.2.2 Validation with Computed Tomography

3.2.2.1 Geometric Analysis

The 4D Flow-MRI based reconstruction methodology required validation against CT-derived models. As CT images were only available for clinical patients, this methodology was validated using the three clinical cases outlined in Table 3.1. CT and 4D Flow-MRI scans were performed on the same date for each patient. This validation comprised of five elements: (1) qualitative visual comparison of the 3D reconstructed arteries; (2) quantitative comparison of vessel centerline metrics including (i) *Radius:* Maximum inscribed sphere radius, (ii) *Curvature*: Inverse of the radius of the osculating circle [178], (iii) *Tortuosity*: The relative increment in length of a curve deviating from a straight line [178], and (iv) bifurcation angle; (3) *Hausdorff distance (HD):* The difference between two geometries by measuring their mutual proximity and the maximal distance between corresponding points of one relative to the other [179]; (4) *Dice Similarity Coefficient (DSC):* A spatial overlap index reflecting both size and localization agreement [180] ; and (5) quantitative comparison of near-wall hemodynamics from CFD simulations. Figure 3.4 illustrates this process as a flow chart.

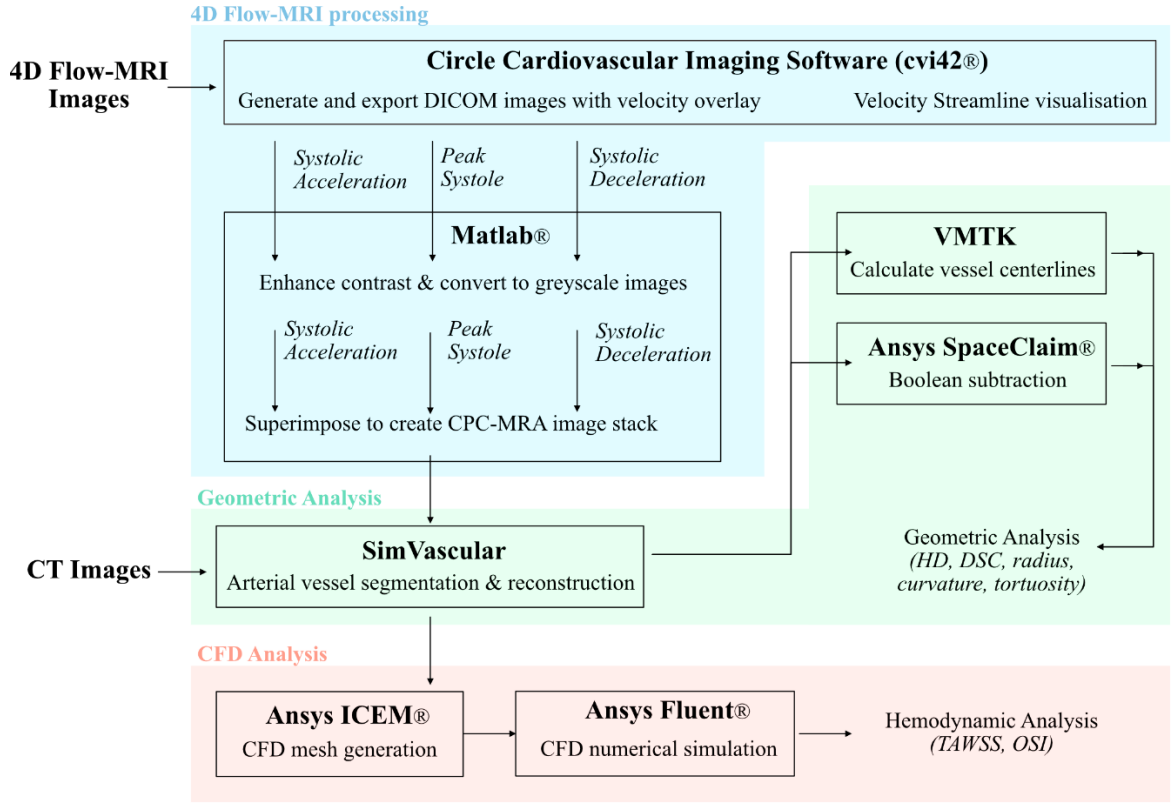

Figure 3.4: Flow chart to highlight the processing of the 4D Flow-MRI images to create the temporal composite (CPC-MRA) image stacks (Blue) and subsequent geometric analysis of the 4D Flow-MRI and CT-derived reconstructed models (green), and CFD analysis (orange).

Quantification of the inter-modality differences between the CT and 4D-Flow MRI-derived models was performed at the iliac bifurcation and common iliac arteries. This region provided a reference point common to both modalities and remained generally free from dissection. These aspects were important as the specific 4D Flow-MRI sequence utilized was not optimized for the analysis of a false lumen or small vessels. Bifurcations also generate complex hemodynamics and are inherently challenging to reconstruct, so geometric and hemodynamic comparisons at this region permit a robust analysis to be performed.

Curvature, κ(s), of the centerline, c(s), was defined as shown in Eq 3.1 [178].

$$\kappa(s) = \frac{|c'(s) \times c''(s)|}{|c'(s)|^3} \tag{3.1}$$

As the arc length, L, of the centerline and the Euclidean distance between the end points, D, was known, tortuosity, χ, was calculated as per Eq 3.2 [178].

$$\chi = \frac{L}{D} - 1 \tag{3.2}$$

If A represents the 4D Flow-MRI derived geometry and B represents the CT-derived geometry, the mathematical formulation for HD, H(A,B), is given in Eq 3.3 [181]. As HD is a measure of boundary similarity between two objects, a comparison between two identical objects would result in a HD of zero.

$$H(A,B) = \max\left(h(A,B), h(B,A)\right) \tag{3.3}$$

where,

$$h(A,B) = \max_{a\in A}\left(\min_{b\in B} d(a-b)\right) \tag{3.4}$$

$$h(B,A) = \max_{b\in B}\left(\min_{a\in A} d(b-a)\right) \tag{3.5}$$

where d represents the Euclidean distance between the points of the sets, h(A,B) is the forward HD, and h(B,A) is the backwards HD [181]. To ensure the 4D Flow-MRI and CT-derived models were oriented in the same plane, two points in the centerlines, the bifurcation reference point and the end point of the left iliac artery, were aligned**.** The HD between the boundaries of the 4D-Flow MRI and CT derived models was then analyzed at equally spaced, horizontal 2D planes (n=1000) throughout the reconstructed models. The gap between each discrete plane was extremely small, so this tended towards a continuous analysis over the full model. The 95th percentile of the HD was utilized to handle outliers [182].

The formulation for the DSC is given in Eq 3.6 [180]. DSC ranges from 0, indicating no spatial overlap between the 3D models, and 1, indicating a complete overlap [180].

$$DSC(A,B) = \frac{2|A\cap \mathrm{B}|}{|A|+|B|} \tag{3.6}$$

When applied to discrete data, $|A|$ and $|B|$ are the cardinalities (number of elements) of the two sets, and ∩ is the intersection. Therefore, to compute the DSC, the cardinalities of the 4D Flow-MRI and CT-derived models, and the respective Boolean intersection $|A \cap \mathrm{B}|$, for each patient were generated in Ansys SpaceClaim®.

The open-source Vascular Modelling Toolkit (VMTK) was used to compute vessel centerlines [183]. These centerlines were then resampled at 3mm intervals and smoothed with a factor of 0.5 and 100 iterations to remove noise which can generate localized parameter errors. A bifurcation reference system was generated within the software, following the methodology of Piccinelli *et al* [178]. Thereafter, bifurcation angles were obtained for each geometry, calculated from the difference between the in-plane angle of the common iliac vessels [184].

The abdominal aorta was truncated immediately upstream of the bifurcation reference point for both the 4D Flow-MRI and CT-derived models. This was to ensure that all 3D models began at a common anatomical landmark. Centerline measurements were performed distally to the bifurcation reference point. Patient 2 exhibited a small region of dissection in the left common iliac artery, resulting in a true lumen (TL) and false lumen (FL), so radius, R, was presented as $R=R_{TrueLumen}+R_{FalseLumen}$.

3.2.2.2 Computational Fluid Dynamics Model

The 4D Flow-MRI and CT-derived models for patients 1, 2 and 3 were discretized to create a tetrahedral computational mesh in Ansys ICEM®. To capture the viscous sublayer, the initial prism layer height (Δy_1) on the boundary was estimated at Δy_1=2.5e-3 m, such that y+ <1 [185]. To resolve the boundary layer, 10 prism layers were generated from this initial estimate, with an expansion ratio of 1.25.

Grid convergence, as described previously in Chapter 2 Section 2.3, was then established for wall shear stress by performing several steady state RANS simulations in Ansys Fluent®, employing a shear stress transport (SST) k-ω turbulence model [186]. The shear stress distribution was analysed at the iliac bifurcation upon convergence of the solution, and a surface integral over the entire geometry was performed to yield a single quantitative metric. Upon satisfying grid convergence, the RANS output simulation results were examined to ensure the mesh was compliant with the y+ criteria. Flow extensions were applied at the inlet (5D) and outlet (10D), where D was the inlet diameter of the respective patient vessel [187].

Transient aortic haemodynamics were computed within a rigid wall model with a no-slip boundary condition. Blood flow was modelled by solving the time-dependent, 3D, incompressible RANS equations for continuity and momentum, according to Eq 2.21 and 2.22, respectively [132]:

The governing equations were solved numerically via a FVM on Ansys Fluent®, employing a PISO algorithm with a second-order upwind scheme and k-ω SST turbulence model [188]. On average, each simulation required around 13 hours for 5 cardiac cycles on 35 Intel(R) Xeon(R) Gold 6138 CPU cores. Due to high shear rates within the aorta, blood was assumed to be a Newtonian fluid, with density 1060kgm^{-3} and dynamic viscosity, μ, 0.004 Pa s [189] [190]. Each simulation was run for 5 consecutive cardiac cycles. Turbulence intensity, prescribed at the inlet and outlets, is described in Table A.19.

For each patient, a 4D Flow-MRI derived flow waveform (Figure 3.5) was extracted immediately upstream of the bifurcation reference point, i.e., the same location at which the 3D geometries were truncated. This flow waveform was then converted to a parabolic velocity profile (dt=0.001s) [191]. To ensure the shape, phase and peak of the inlet profile was consistent for numerical analysis, these velocity profiles were prescribed at the inlet of the computational domain for both the 4D Flow-MRI and CT-derived CFD models. Raw inlet flow rate data is presented as mean±sd over 5 planes of analysis for each patient (Figure 3.5). The mean and peak (mean/peak) Reynolds number ($Re=\rho UD/\mu$ [192]) in the iliac arteries for patients 1, 2 and 3 was 453/1397, 389/1246, and 436/1260, respectively. At each outlet, a flow weighting was prescribed for the left and right (left/right) iliac arteries as 0.47/0.53, 0.65/0.35, and 0.53/0.47, respectively for patients 1, 2, and 3.

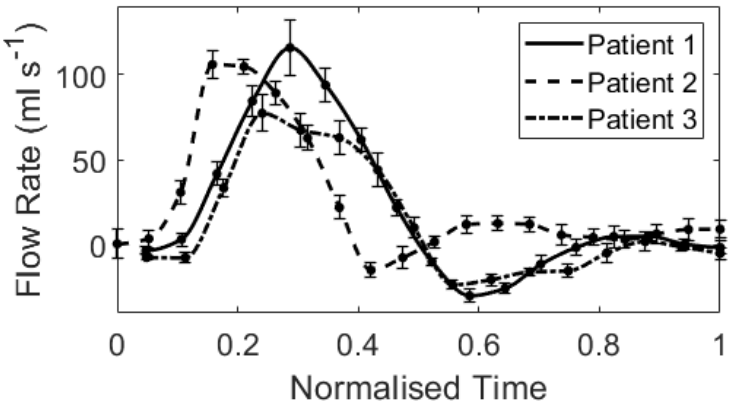

Figure 3.5 4D Flow-MRI derived flow waveforms extracted from the abdominal aorta, immediately proximal to the iliac bifurcation. At each time point (n=20) throughout the cardiac cycle, the cross-sectional flow rate was calculated from 5 planes of analysis for each patient. These planes were equally spaced in the axial direction to discretely sample a volume of blood flow, from which a mean flow rate could be calculated. For each patient, this flow rate is presented as mean±sd. Flow rate was then interpolated between each time point with a cubic function to generate a waveform with a time step of 0.001s for CFD analysis.

Haemodynamic analysis was performed only on the 5th cycle upon achieving a time-periodic solution, where the TAWSS and OSI were investigated, via a user defined function (UDF), using the following definitions [193] [194]:

$$TAWSS = \frac{1}{T}\int_0^T |\vec{\tau}_\omega|\, dt \tag{3.7}$$

$$OSI = \frac{1}{2}\left(1 - \frac{\left|\int_0^T \vec{\tau}_\omega dt\right|}{\int_0^T |\vec{\tau}_\omega| dt}\right) = \frac{1}{2}\left(1 - \frac{|\vec{\tau}_{mean}|}{TAWSS}\right), \tag{3.8}$$

where $\vec{\tau}_{mean} = \frac{1}{T}\int_0^T \vec{\tau}_\omega \, dt$, $\vec{\tau}_\omega$ is the instantaneous wall shear stress vector, dt is the time step, and T is the time for one full cardiac cycle. OSI characterizes the degree of shear reversal in pulsatile flow, ranging from 0 for unidirectional flow, to 0.5 which is indicative of a reversing flow with no mean direction of shear [195]**.** The upper 5% and lower 5% of TAWSS and OSI ($N_{Elements}$ ~ 1100) were compared between modalities for each patient. These extremes were chosen for analysis since elevated TAWSS can be indicative of platelet activation and thrombus formation, while low and oscillatory regions can create stagnant flow and graft limb occlusion [28].

Finally, based on the normalized vessel centerlines and CFD simulations, a correlation and Bland-Altman plot for CT and 4D Flow-MRI derived vessel radius, curvature, TAWSS, and OSI was generated for each patient.

3.2.2.3 Sensitivity Analysis

An intra-user dependence study was performed to investigate the variability in arterial reconstruction resulting from manual segmentation of a single user. Here, patient 3 was chosen since there was no presence of a stent-graft of aortic dissection at this location. Thus, the CT and 4D Flow-MRI data for patient 3 were repeatedly segmented and reconstructed 5 times on SimVascular® by a single user. For each model, the previously described methods in Section 3.2.2.1 and 3.2.2.3 were employed to investigate vessel radius, curvature, and near-wall hemodynamics. To facilitate these simulations, only the forward flow was considered at the inlet to reduce computational demand.

3.2.2.4 TAWSS Normalisation

The TAWSS distribution for each patient was normalized with respect to TAWSS at the left iliac outlet, calculated analytically as follows.

$$\tau_\omega = -\mu \frac{du}{dy} \tag{3.9}$$

where,

$$\frac{u}{u_{max}} = 1 - \left(\frac{2y}{h}\right)^2 \tag{3.10}$$

where h is the radius, $y = h/2$, the velocity at the apex of the fully developed flow, $U_{max} = \frac{3}{2}U_{inlet}$, and μ=0.004 Pa s.

$$\frac{du}{dy} = \frac{-8u_{max}y}{h^2} \tag{3.11}$$

$$\tau_{\omega} = \frac{8\mu u_{max} y}{h^2} \quad (3.12)$$

At each point within a single cardiac cycle, the instantaneous τ_{ω} was calculated at the inlet of the CT CFD model on Matlab® to determine a time-averaged value at the inlet, $\tau_{\bar{\omega}} = \int_0^T \tau_{\omega} dt$. For patient 1, 2, and 3, $\tau_{\bar{\omega}}$ was equal to 0.439Pa, 0.600Pa, and 0.248Pa respectively.

3.3 Statistical Analysis

Statistical analysis was performed on Minitab® to investigate the geometric and hemodynamic data during validation of the 4D Flow-MRI-derived models against CT-derived models, and for the intra-user sensitivity analysis. To determine normality of the data distribution, an Anderson Darling normality test was employed, which concluded both the geometric and hemodynamic data distributions were non-normal ($p<0.05$). Consequently, non-parametric statistical tests were employed as these perform well with skewed distributions and those which are better represented by the median instead of the mean. Further, as the 4D Flow-MRI and CT images were acquired from the same patients, the data was considered dependent. Therefore, a combination of Signed Rank tests and 1-Sample Wilcoxon tests were utilized. Hereafter, the difference between the dependent samples was calculated and the distribution of these differences were analysed to ensure symmetry. If symmetry was not observed, a Johnson Transform was applied to transform the data and generate a more symmetrical distribution. If a transform was not possible, a Signed Rank Test was employed instead of a 1-Sample Wilcoxon. Outliers were removed on all data sets which were detected using the Grubbs Test. One exception to this method was the sensitivity analysis data for vessel curvature, which could be transformed to generate a normal distribution prior to hypothesis testing. In this case, a paired t-test was utilized. In all cases, the significance level, $\alpha=0.05$.

3.4 Results

3.4.1 Reconstruction of healthy aortae and great vessels from 4D Flow-MRI

Figure 3.6 illustrates the 4D Flow-MRI-derived model of volunteer 1 (thoracic aorta, Figure 3.6A) and clinical patients (abdominal aorta, Figure 3.6B-D). These are proof of concept examples which demonstrate that, with the proposed 4D Flow-MRI derived CPC-MRA images, it is possible to reconstruct the thoracic and abdominal aortae of a both healthy volunteers and clinical patients. With 4D Flow-MRI, the stent struts of patient 1 were not visible and therefore could not be reconstructed. Further, as this study focuses on the flow lumen, the struts of the Anaconda™ stent were not segmented from the CT images.

Figure 3.6 compares the standard magnitude images, which come as part of the 4D sequence, against the CPC-MRA images derived from the proposed methodology. For the clinical patients, CT images are also included. Images were acquired from the same locations in the transverse, sagittal, and coronal planes for each modality to permit a direct comparison. As evidenced, the image quality of the magnitude images was very poor due to low SNR and contrast, hence they can generate only a very rough and ambiguous outline of the vessel lumen. Often, the lumen was indistinguishable from surrounding tissue. The CPC-MRA images, however, yield a much clearer lumen with high and uniform signal intensity, which distinctly contrasts against surrounding static tissue and air-filled regions. CT images portrayed a more accurate representation of true and false lumen of the abdominal aorta in patients 2 and 3. This is because a single-VENC MRI sequence was utilized for 4D Flow-MRI and therefore it was not possible to capture flow (and therefore signal intensity) in both the true and false lumen simultaneously. By altering the velocity threshold of the CPC-MRA images, it was possible to retrospectively increase the signal within the false lumen, but the limited spatial resolution of the sequence prohibited delineation between the true and false lumen.

As the temporal CPC-MRA images combine SA, PS, and SD, this ensures all areas of the lumen demonstrate maximum signal intensity, overcoming the temporal lag of blood velocity through cardiac cycle, as distal regions are not underestimated due to low blood velocity. Consequently, segmentation was simple to perform via threshold-based segmentation. It was also possible to increase the signal intensity by decreasing the velocity threshold on cvi42®. A range between 25-40cm s^{-1} produced the best results, with low noise. At <25cm s^{-1}, it became difficult to distinguish the lumen due to noise, and at >40cm s^{-1}, there was a risk of underestimating lumen diameter. This range is expected to change according to the initial signal-to-noise ratio of the acquisition sequence, presence and stage of pathology, and the anatomical site of interest.

To highlight the CPC-MRA images in more detail, Figure 3.7 was produced with false color on Matlab®. Regions in white indicate areas of the lumen common to each time step, while regions in magenta and green indicate where signal intensity varies during PS and SD respectively. Taking Figure 3.7C as an example, this shows the lumen of the ascending and descending aorta. As the phase of the cardiac cycle transitions from SA to SD, a noticeable notch of decreased signal intensity develops in the descending aorta (white arrows). Thus, if images from PS or SD were viewed independently, one may assume this dark region was a

kink in the geometry, or simply a narrowed area of the lumen. However, this dark region was not observed during SA.

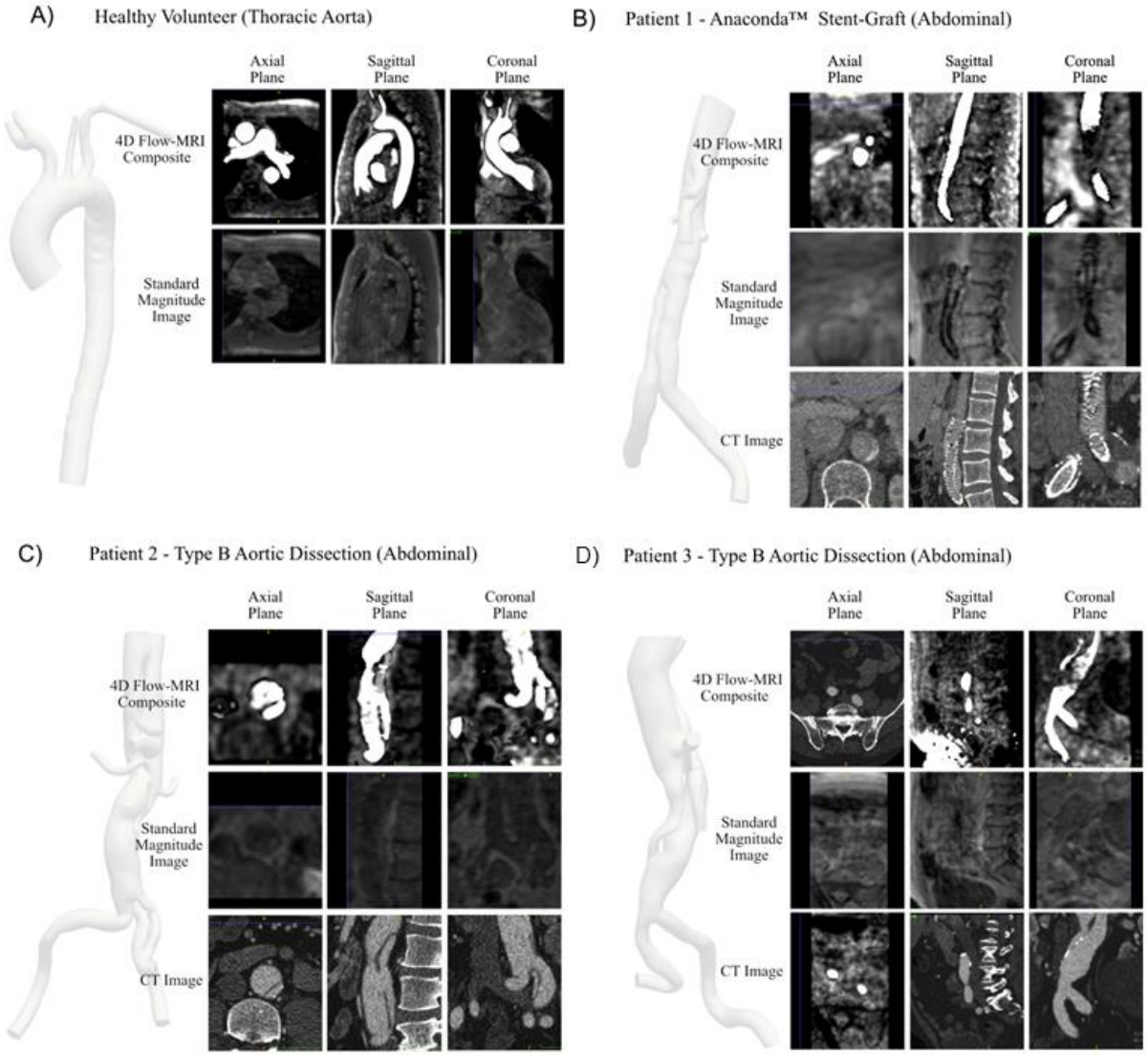

Figure 3.6: A computational model of A) the thoracic aorta, reconstructed from the healthy volunteer, and the abdominal aorta and common iliac arteries, reconstructed from the 4D Flow-MRI CPC-MRA images for B) patient 1, C) patient 2, and D) patient 3. The 3D models were created from the 4D Flow-MRI CPC-MRA images. Slices from the transverse, sagittal, and coronal planes from each case illustrate the arterial lumen from each DICOM dataset (CT, standard MRI magnitude image, 4D Flow-MRI CPC-MRA). CT images were not available for the healthy volunteer due to ethical considerations. The stent struts of patient 1 are not visible in the reconstructed model as 4D Flow-MRI yields data only on the flow lumen.

Analysis of the velocity streamlines on cvi42® confirmed this was a region of recirculating flow which began at PS, leading to slow moving flow and reduced velocity magnitude [196]. Hence, the final temporal CPC-MRA image, which combined all three time-steps, filled in this region to create a more representative lumen. Figures 3.7D-F highlight the CPC-MRA images

created from patient 1 at the region of the Anaconda™ stent-graft. Though they are MRI-compatible, the Anconda™ nitinol rings induced noise from metal beam-hardening artifacts during data acquisition which degraded the image quality of the corresponding 4D Flow-MRI CPC-MRA somewhat [197].

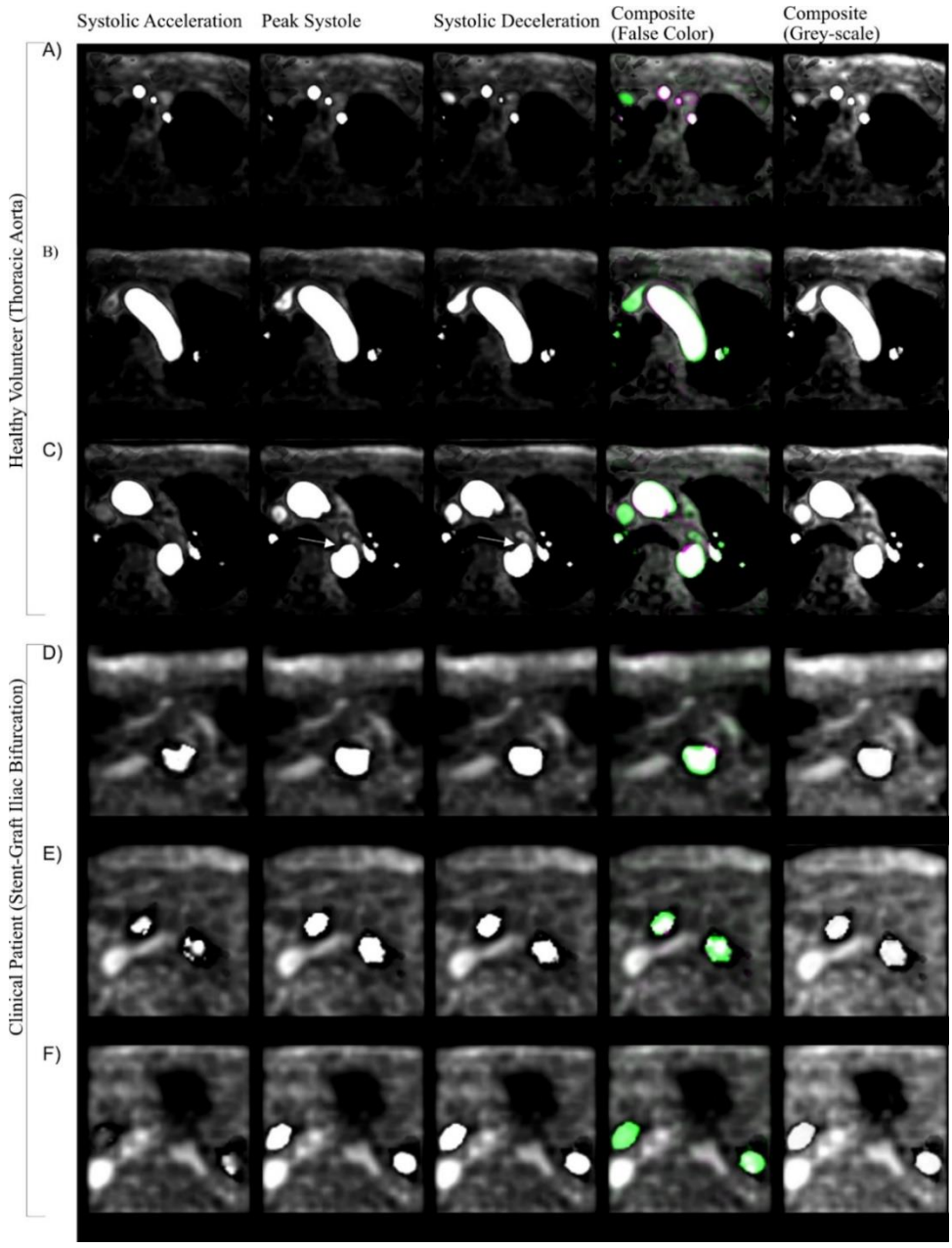

Figure 3.7: Individual time steps at systolic acceleration, peak systole, and systolic deceleration used to create the CPC-MRA image. False color images are used for visualization while greyscale for segmentation. (A-C) Healthy volunteer: A) Supra-aortic branches, B) Aortic arch, C) Ascending and descending aorta. (D-F) Clinical patient 1 with Anaconda™ stent-graft: D) Abdominal aorta, E) Common iliac arteries (more proximal), and F) Common iliac arteries (more distal). White regions in the false color CPC-MRA image show where the three time steps exhibit the same lumen intensity. Magenta and green regions demonstrate where the intensities differ. All images were obtained at a velocity threshold of 25cm s^{-1} on cvi42®

3.4.2 Validation on patient-specific iliac arteries

The mean tortuosity, radius and curvature were calculated from both the left and right iliac arteries of each of patients 1, 2, and 3, and were grouped (Table 3.2) according to imaging modality for statistical analysis. Statistical analysis discussed in this work is made in relation to the comparison of CT vs 4D MRI-derived reconstructions and not regarding patient statistics. A Wilcoxon Signed Rank test was performed to evaluate inter-modality differences in radius and curvature along the length of the centerline. No statistically significant inter-modality variation existed for either variable ($p>0.05$). There was an insufficient number of data points to determine the statistical significance for differences in vessel tortuosity and bifurcation angle as these were not sampled along the vessel centerlines. The bifurcation angles calculated in VMTK for CT and 4D-Flow MRI were, respectively: 10.1^o, 27.6^o for patient 1, 78.3^o, 65.4^o for patient 2, and 62.4^o, 57.5^o for patient 3. Individual values of tortuosity for CT and 4D-Flow MRI were, respectively: 0.465±0.0657, 0.517±0.0792 for patient 1, 0.325±0.0584, 0.353±0.0359 for patient 2, 0.0792±0.0111, 0.0907±0.00520 for patient 3.

Table 3.2: Mean parameters obtained from the left and right iliac arteries of clinical patients (n=3) for the CT and 4D-MRI derived models.

	Left Iliac			**Right Iliac**		
	CT	MRI		CT	MRI	
Tortuosity	0.291±0.174	0.307±0.185	-	0.289±0.232	0.333±0.256	-
Curvature (m^{-1})	0.207±0.0704	0.232±0.0757	($p>0.05$)	0.290±0.163	0.279±0.125	($p>0.05$)
Radius (mm)	6.62±0.0691	6.77±0.0256	($p>0.05$)	6.72±0.0725	6.91±0.0426	($p>0.05$)

While there was no statistically significant difference in overall radius and curvature, there was a degree of variability between the CT and 4D-Flow MRI derived models. Figure 3.8 illustrates the quantitative differences in vessel anatomy. The radial interquartile range (IQR) was consistently smaller for the 4D Flow-MRI models, illustrating less variability in the data compared to CT. Moreover, the median values for 4D Flow-MRI were typically larger than that of CT, indicating that the 4D Flow-MRI derived model may tend to overestimate the vessel radius. The helical CT scan was acquired as a breath-hold scan, in the absence of cardiac (ECG) gating, whilst 4D Flow-MRI was acquired with retrospective ECG and respiratory gating. As such, the CT images represent a snapshot at an arbitrary point within the cardiac cycle, while the 4D Flow-MRI images were created from three well-defined, systolic cardiac phases. It is

therefore possible that the 4D Flow-MRI and CT images were captured at slightly different points in the cardiac cycle

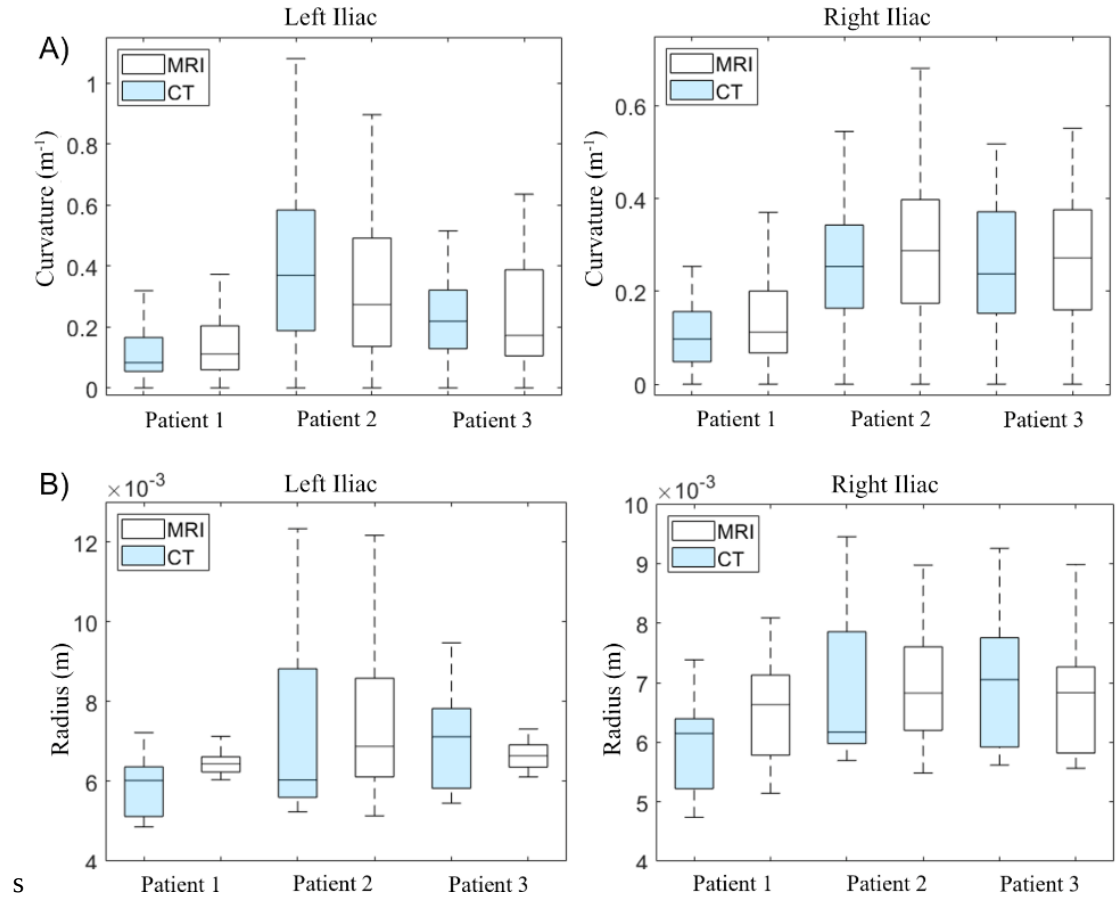

s

Figure 3.8 A) Curvature and B) radius of the left and right iliac arteries for CT (light blue) and MRI (white) derived models. These parameters were calculated from the vessel centerlines of patients 1, 2, and 3.

Qualitatively, the geometry of the CT and 4D Flow-MRI-derived models were similar, as shown in Figure 3.8 and Figure 3.9. DSC and HD were also included in the analysis as both are widely used to evaluate medical image segmentations to reflect both the lumen size and localization agreement [198] [199]. The DSC was 0.681, 0.736, and 0.736, for patient 1, 2, and 3, respectively. The mean inter-modality HD for patients 1, 2, and 3 was calculated as 5.62±1.44mm, 7.38±2.56mm, and 5.18±1.11mm, respectively. Notably, patient 2 reported the highest pattern of curvature and the largest inter-modality HD.

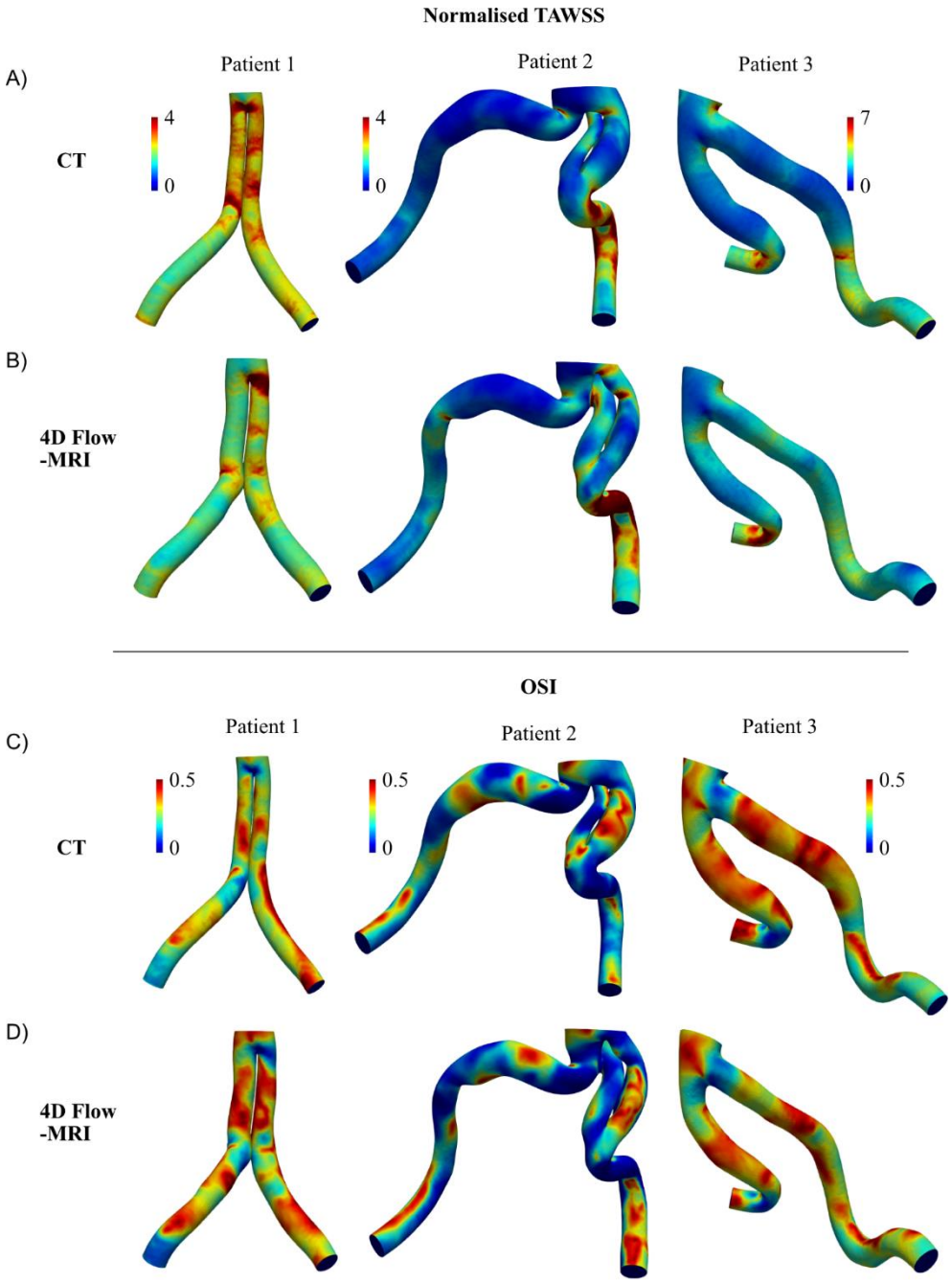

Figure 3.9 A, B) TAWSS and C, D) OSI distribution across the CT and 4D-MRI derived models of the iliac bifurcation of patients 1 (left), 2 (middle) and 3 (right) calculated from the final cardiac cycle of a patient-specific CFD simulation. TAWSS was normalized as per Section 3.2.2.3. Visible for patient 2 is a small region of dissection which extended into the proximal section of the left common iliac artery.

The heterogeneous TAWSS and OSI distribution across the CT and 4D Flow-MRI-derived models are shown in Figure 3.9. A Signed Rank test and a Wilcoxon Signed Rank test compared the inter-modality differences in maxima (top 5% of values) and minima (bottom 5% of values) TAWSS across each entire geometry. A significant difference between CT-derived and 4D Flow-MRI derived TAWSS and OSI was present at both extremes within the CFD models ($p<0.05$).

Localized differences in TAWSS were most apparent in regions of high curvature and at the bifurcation point. The absolute TAWSS values in the CT models ranged from 0.199-1.56Pa, 0.0289 – 2.16Pa, and 0.0856-0.899Pa in patients 1, 2, and 3, respectively. Similarly, for the 4D-Flow MRI cases, these values ranged from 0.177-1.43Pa, 0.0635 – 2.55Pa, and 0.0862-0.948Pa.

Figure 3.10 illustrates a correlation plot and Bland-Altman plot for the vessel radius, curvature, TAWSS, and OSI data obtained from each patient for both CT and 4D Flow-MRI derived models. The Pearson correlation coefficient for each metric was, respectively, 0.46, 0.69, 0.77, and 0.98 ($p<0.05$). Due to non-normally distributed data, the Bland-Altman limits of agreement were presented as $\pm 1.45 \times$ IQR of the inter-modality difference.

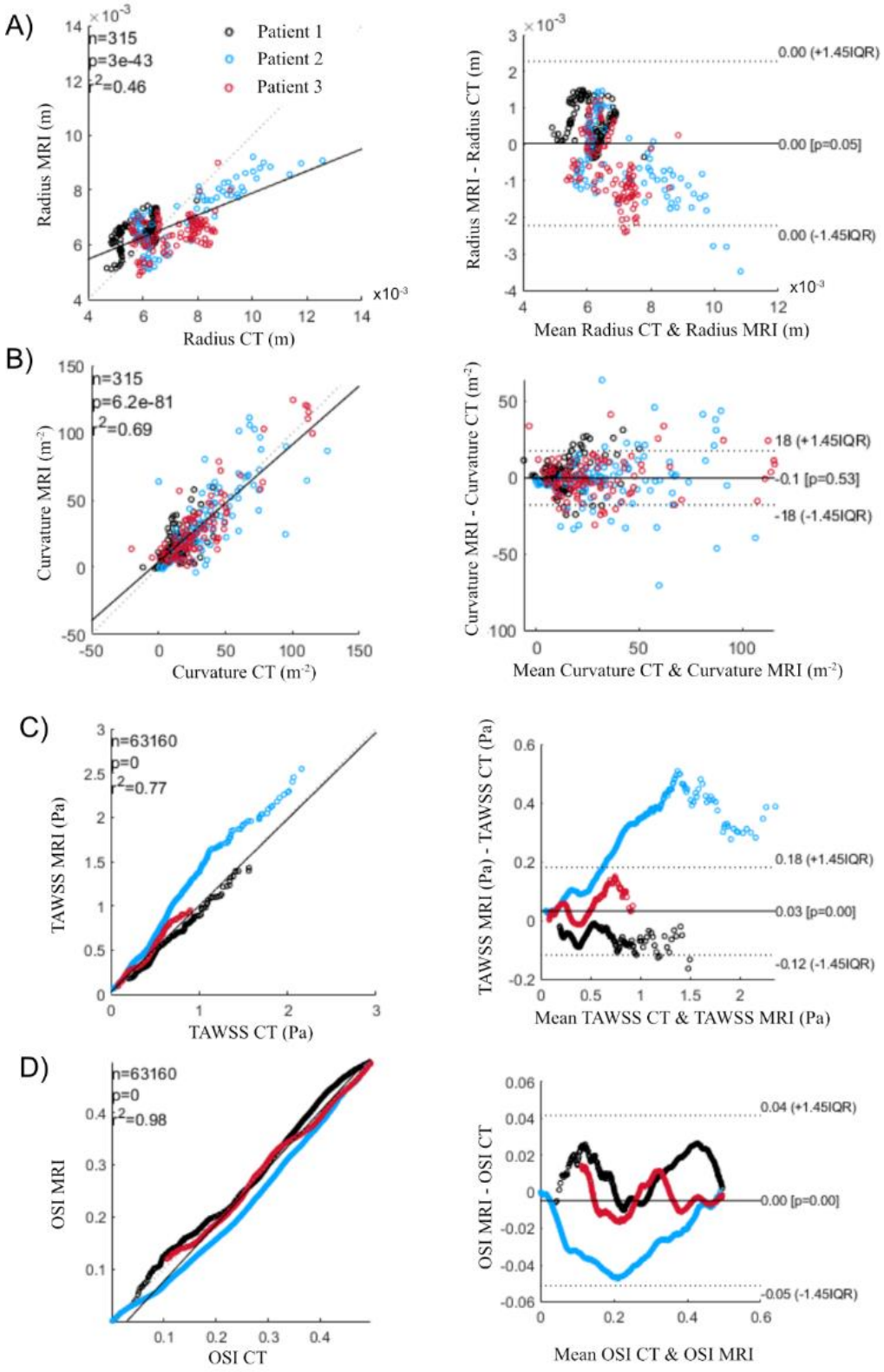

Figure 3.10: (Left) Correlation and (Right) Bland-Altman plots for patients 1, 2, and 3 at the iliac bifurcation and common iliac arteries, displaying A) vessel radius, B) vessel curvature, C) TAWSS, and D) OSI.

3.4.3 4D Flow MRI vs CFD

The specific 4D Flow-MRI sequence (WIP 785A) used in this study was not calibrated to extract wall shear stress. Therefore, blood velocity streamlines calculated from the CT and 4D Flow-MRI derived CFD models were compared against the *in vivo* streamlines of velocity magnitude obtained directly from 4D Flow-MRI imaging (Figure 3.11). Qualitatively, the overall velocity profiles are similar between the CFD models and *in vivo* data. However, there were quantitative differences regarding, for example, the maximum through-plane velocities observed at multiple locations throughout the iliac branches. Between patients 2 and 3, the CT-derived CFD models underestimated velocity by 12% and 29% on average during peak systole and systolic deceleration, respectively. Conversely, the MRI-derived models overestimated blood velocity by 9.1% and 0.1%, respectively. Thus, the MRI-derived CFD models demonstrated a smaller discrepancy with the *in vivo* data. Regarding patient 3, these discrepancies were amplified, where differences in velocity of 48% to 90% were observed between the CFD models and *in vivo* data, likely due to significant noise and signal artefacts introduced within the 4D Flow-MRI images by the metal-alloy rings of the Anaconda™ stent-graft.

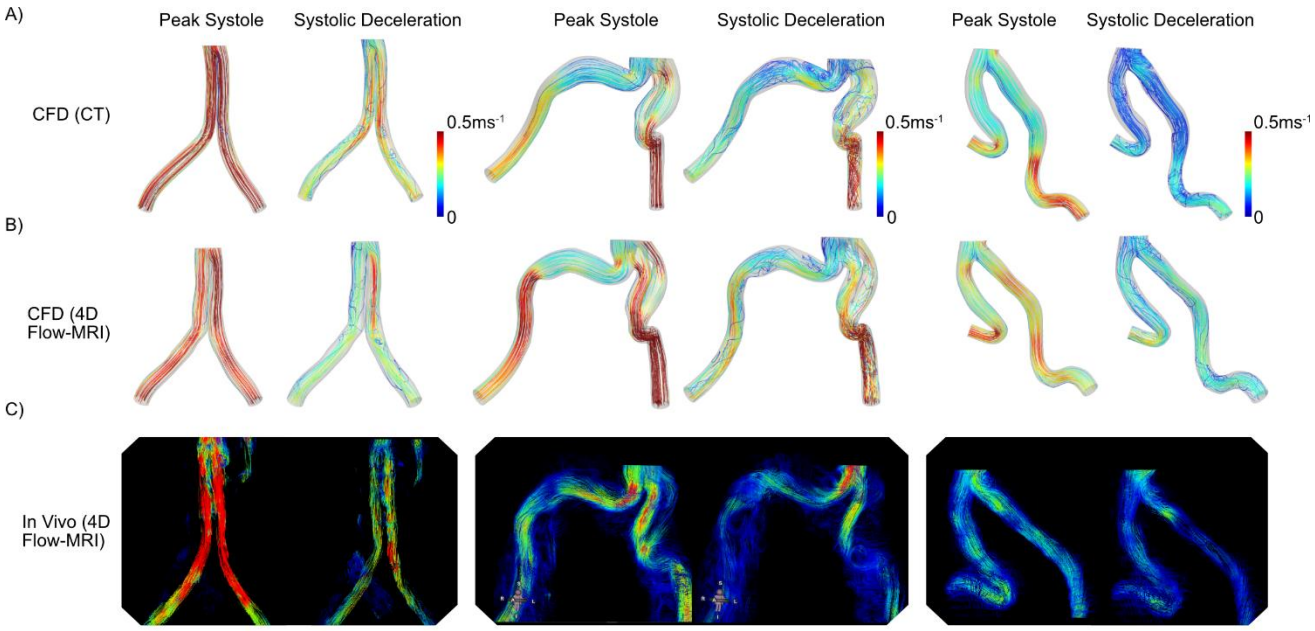

Figure 3.11: Blood velocity streamlines through the iliac bifurcation and proximal iliac arteries of patients 1, 2, and 3, extracted from A) CFD models reconstructed from CT images, B) CFD models reconstructed from 4D Flow-MRI images, and C) in vivo 4D Flow-MRI (measured in cvi42®). The same value range of 0-0.5 ms^{-1} was used for all cases.

3.4.4 Sensitivity Analysis

Intra-user errors, introduced during manual segmentation, were statistically significant for vessel radius and near-wall hemodynamics for both CT and 4D Flow-MRI ($p<0.05$). However, there were no significant user-dependent variations concerning the curvature of the vessels ($p>0.05$). The localized differences in radius are evident from Figures 3.12A and 3.12B where, for example, the 4D Flow-MRI derived models underestimated the lumen of the proximal left iliac, and subsequently overestimated the distal portion. Additionally, the variance in radial data in the 4D Flow-MRI models was consistently lower than that of CT.

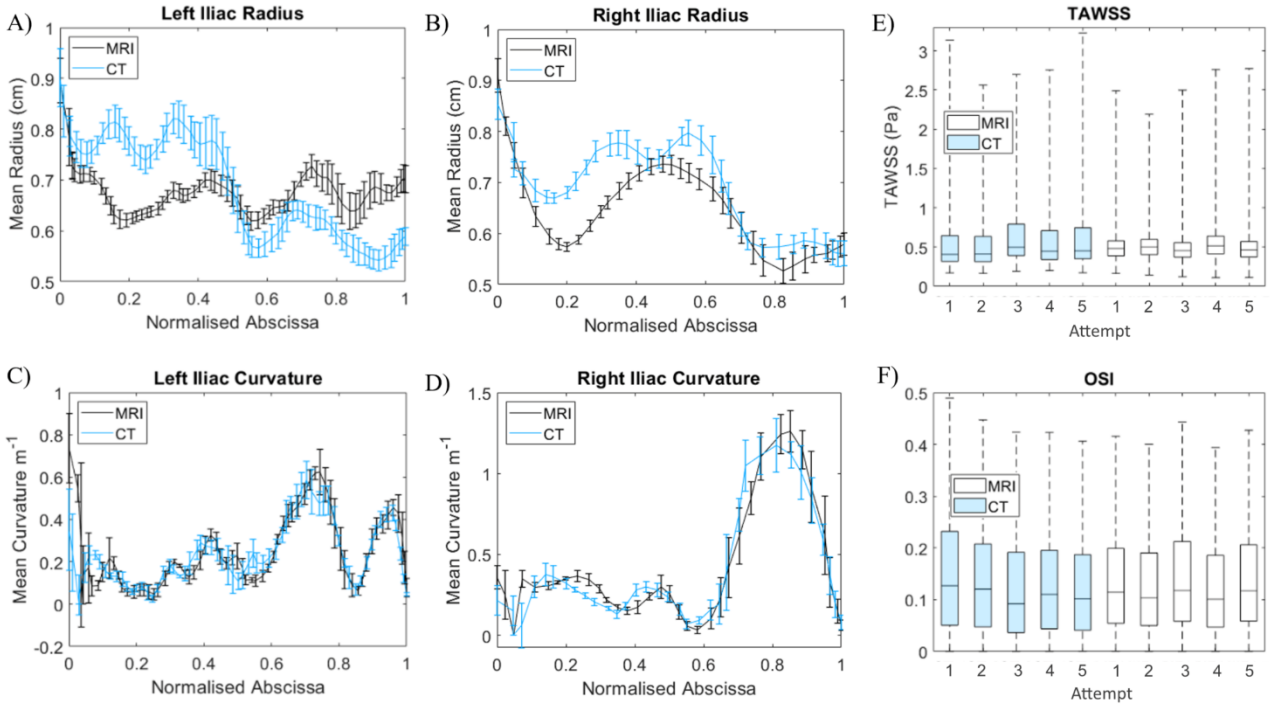

Figure 3.12: Intra-User Dependence (n=5) results for vessel geometry and near-wall hemodynamics for both CT (light blue) and 4D Flow-MRI (black) derived models of patient 3. A) Left and B) right iliac radius, and C) left and D) right iliac vessel curvature, where results are presented as mean±sd. E) Box plot of TAWSS and F) OSI evaluated over the entire iliac geometry for CT (light blue) and 4D Flow-MRI (white).

Intra-user variations at regions of maximum TAWSS was ±0.29Pa for CT and ±0.24Pa for 4D Flow-MRI (Figures 3.12E and 3.12F). Consequently, the user may induce an error of up to 0.53Pa in CFD simulations due to differing perceptions of the lumen during segmentation. Contour plots of TAWSS and OSI distributions for each of the reconstructions can be found in the Supplementary Material. Intra-user CT-derived tortuosity for the left and right iliac was 0.40±0.002 and 0.54±0.014, respectively. Similarly, tortuosity as calculated from the 4D Flow-MRI models was 0.44±0.002 and 0.60±0.013 for the left and right iliac arteries.

TAWSS distributions **(**Figure 3.13**)** were obtained from CFD analysis of patient 3 during the sensitivity analysis to determine the effect of intra-user segmentation errors. Segmentation and reconstruction of the geometry was performed 5 times for both CT and 4D Flow-MRI. Qualitatively, the TAWSS distribution remains relatively constant within each modality, though larger inter-modality discrepancies are apparent. Elevated regions of TAWSS are visible at the point of bifurcation and regions of increased curvature.

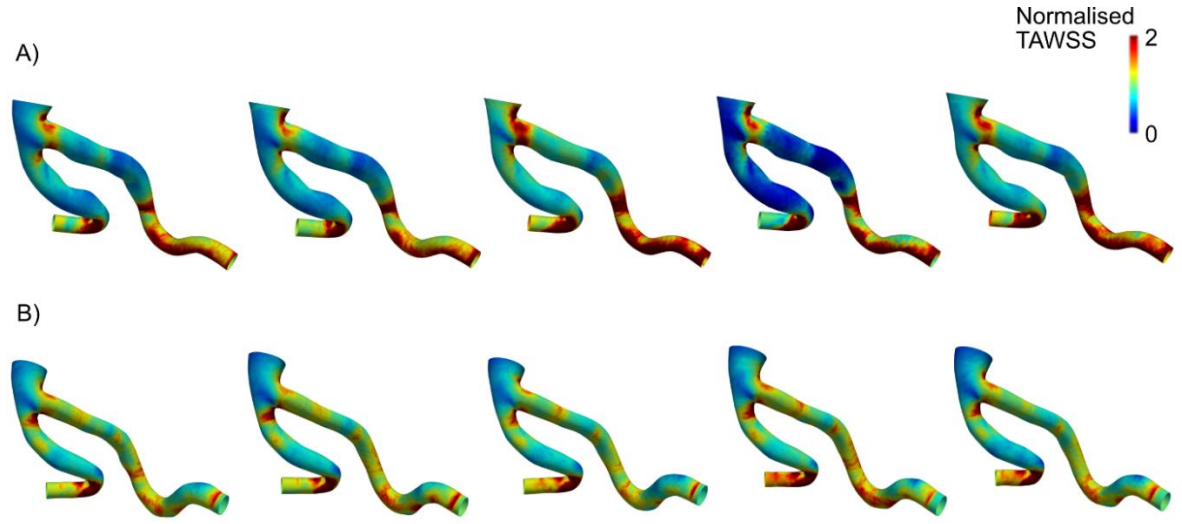

Figure 3.13: TAWSS distribution for patient 3, obtained via CFD simulations of the A) CT and B) 4D Flow-MRI derived geometries. Each modality was segmented and reconstructed 5 times.

Similarly, OSI distributions obtained from the sensitivity analysis are visible in Figure 3.14. Again, minimal qualitative differences exist within each modality. However, differences between the CT and 4D Flow-MRI cases are more apparent. Elevated regions of OSI occur at areas of low TAWSS.

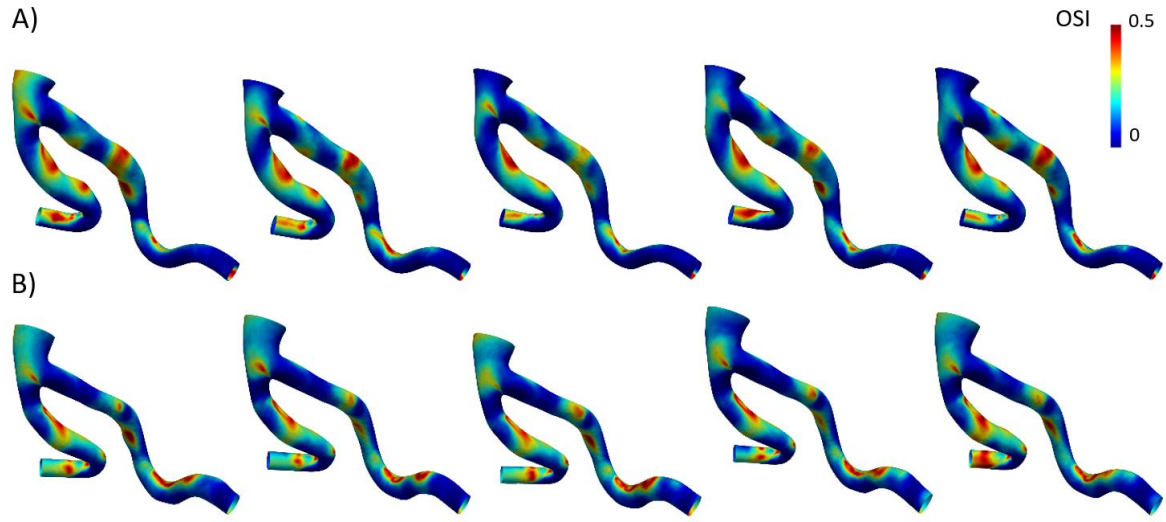

Figure 3.14: OSI distribution for patient 3, obtained via CFD simulations of the A) CT and B) 4D Flow-MRI derived geometries. Each modality was segmented and reconstructed 5 times.

3.5 Discussion

The purpose of this study was to develop a novel dataset for the segmentation and reconstruction of patient-specific aortic geometries from retrospective 4D Flow-MRI images. The geometric and CFD-derived hemodynamic parameters obtained from this approach were then compared against CT-derived models, as CT is the gold-standard imaging modality.

3.5.1 CPC-MRA Composite Images

With the CPC-MRA DICOM stack demonstrated in this study, a clear lumen with uniform signal intensity was observed, distinctly contrasting with surrounding static tissue. Signal intensity within the lumen was proportional to blood velocity magnitude, meaning no ionizing radiation or intravenous contrast agents were required to generate contrast. The boundaries of the vessel lumen were generally well defined, but due to low near-wall velocities which are typical of internal flows, a small region of reduced signal intensity, and hence contrast, was observed around the vessel wall. The creation of these composite image stacks was required to segment the arterial lumen directly from retrospective 4D Flow-MRI data due to the absence of accompanying images such as conventional MRA or phase contrast angiogram (PCA).

In some cases, it may be possible to segment the vessel lumen directly from the magnitude images which form part of the 4D Flow-MRI data. In this study however, these images demonstrated poor contrast and low SNR to the extent that in many regions, the lumen was indistinguishable from surrounding tissue. Therefore, it was not possible to segment and reconstruct the vessel geometry directly from these magnitude images. The CPC-MRA images present a significant improvement regarding contrast and signal intensity when compared to the magnitude images (Figure 3.5), making the lumen relatively simple to segment. This methodology is therefore beneficial for extracting the lumen for CFD models as an alternative to standard techniques in retrospective datasets. As the final CPC-MRA images were generated by superimposing information on the same slice over multiple time steps, contrast was generated without sacrificing any spatial information along the transverse axis [94] [200] [201].

The temporal CPC-MRA methodology utilizes the same underlying principles as a PCA, where a phase shift due to the movement of blood is proportional to fluid velocity. These PCA images require prospective planning as vessel contrast and signal intensity is generated during the scan. The 4D Flow-MRI CPC-MRA, however, generated this PCA-type image in a different way. The CPC-PCA was generated from the interpolated 3D velocity profile of retrospective datasets, where these instantaneous velocity profiles were superimposed directly onto the 4D

Flow-MRI magnitude images at multiple, user-defined timesteps. This meant the signal to noise ratio of the final angiogram could be controlled *post-hoc* by the user by simply altering the velocity threshold. Additionally, this postprocessing approach suppresses background noise and reduces the signal from nearby veins because of the slow venous flow. For example, it was possible to increase the velocity threshold to suppress the vena cava and enhance arterial visibility. The opposite is also true, as this approach allows the user to increase signal intensity in branches or regions which experience reduced flow, including aneurysm sacs and the false lumen of an aortic dissection, potentially overcoming a limitation of single-VENC MRI. To validate this however, future work is required to assess this methodology with increased spatial resolution against a multi-VENC sequence [65]. Finally, it is known that in pathological situations involving jet flow, such as aortic dissection, a signal void can appear in the conventional PCA. With the CPC-MRA methodology, regions of jet flow had the opposite effect, as the final signal was enhanced.

The ability to create this temporal CPC-MRA with user-defined time steps is a significant advantage when operating with velocity-based contrast, as regions of recirculating, oscillatory, or regurgitated flow can result in localized drops in signal intensity. As these flow phenomena are often transient, the previous or subsequent time steps, which exhibit a different instantaneous profile, can capture these regions when overlaid as a CPC-MRA. These areas of atypical flow are, however, important clinically, so they can also be analyzed on a time-step by time-step basis within the cvi42® software. Though there are several advantages to this technique, it must be noted that only three user-defined timesteps were utilized to create the final CPC-MRA images, out of a total of 20 time points throughout the cardiac cycle. Prior to systolic acceleration, and following systolic deceleration, blood flow, and therefore signal intensity, was too low in magnitude to generate sufficient contrast throughout the lumen. Therefore, reconstruction is constrained only to the mid-systolic phases, meaning information regarding vessel geometry at the end-systolic and diastolic phases was not elucidated. It is possible that this was the result of an overestimated VENC parameter during the MRI imaging sequence, meaning flow was only captured optimally over a limited phase shift range (systolic phases).

Other studies in literature utilise deep learning techniques such as. convolutional neural networks trained on large datasets which are capably of automatically segmenting the arterial geometry from 4D Flow-MRI magnitude information [202] [203] [168]. These are state-of-the-art, automated and objective methodologies which are repeatable and could be integrated

into a clinical pipeline for rapid anatomical reconstruction. However, these techniques lack generalisability, meaning it is unclear whether they can cope with highly individualised pathologies like aortic dissection. Additionally, some of these studies utilise pre-processing techniques to generate 3D phase contrast MRA images, which leads to a loss of temporal information [204] [203] [168]. To improve generalisability, other studies utilise iterative algorithms which include both phase and magnitude information to automatically segmenting the lumen and reduce noise [205]. Notably, these iterative algorithms have only been tested on *in vitro* phantoms however, so the clinical validity remains unknown. Other studies create similar image stacks from 4D Flow-MRI imaging based on more complex algorithms and transformations, and then generating a conventional maximum intensity projection which is known to result in loss of spatial information [173]. In comparison, the CPC-MRA images presented in our study present a simple, yet robust alternative which can be readily performed in commercial software and could be combined with simple, yet automated segmentation techniques.

3.5.2 Clinical Relevance

Due to the inherent safety of 4D Flow-MRI, the methodology outlined in this study may be particularly beneficial for the reconstruction of arterial geometry in such patients who have received a stent-graft, as they require serial examinations and cumulative radiation dosages which cannot be avoided with CT, especially in the radiosensitive abdominopelvic region [92] [158]. However, it is essential to perform additional studies to address the effect of metal artifacts first and determine if the effect of these could be minimised. Additionally, the preliminary functional information may aid in classifying endoleaks and locating any intraluminal tears in cases of aortic dissection, which can be visualized as regions of high velocity jet flow [117] [206] [207].

Consequently, 4D Flow-MRI based models and alternative ways to generate luminal contrast may become increasingly sought after. Current data cannot yet demonstrate that this approach yields a more effective assessment when compared to CT imaging. This methodology may also be useful for pregnant patients, where there is a lack of clinical data on the usage of Gadolinium based contrast agents [208] [209] [210]. It must be noted however that the metal stent struts were not visible from the 4D Flow-MRI data, meaning this methodology could not yield information on stent integrity, such as fractures, and therefore could not entirely replace CT angiography for post-operative monitoring.

Finally, by utilizing this methodology, it is possible to generate reference models which include both anatomical and functional flow information within the healthy population without ethical concerns. This includes screening of asymptomatic patients, where the 3D anatomical models of otherwise healthy individuals can be created for geometric and CFD-based analysis, as it is accepted that near-wall hemodynamics can be utilized to predict regions of aneurysm formation and future primary entry sites of aortic dissections [211] [63]. When combined with the raw functional information yielded from the same 4D Flow-MRI scan, these models may contribute towards the era of preventative medicine.

3.5.3 Validation

Validation of the 4D Flow-MRI velocity-derived dataset against the current gold standard, CT angiography, was crucial. A small discrepancy between the geometry of the CT and 4D Flow-MRI-derived models was expected due to the inherent differences in the acquisition of these imaging sequences. The potential differences in cardiac phase during which the CT and CPC-MRA images were obtained may be reflected in the HD and DSC metrics, which were utilized in this study to compare models from two independent imaging modalities scans for each patient. Consequently, a reduced DSC and increased HD was expected, with respect to those same metrics applied to segmentations within a single modality. Nevertheless, literature suggests a good overlap occurs when DSC >0.7, which was found in the inter-modality comparison of patients 2 and 3, with patient 1 ~0.7 [180].

Vessel segmentation was performed manually, so the observer's interpretation of the lumen generated a degree of geometric variability in the CFD models. Nevertheless, no statistically significant differences in vessel radius or curvature were observed between CT and 4D Flow-MRI-derived models ($p<0.05$). Regarding the latter, the lower standard deviation for vessel radius, and lower inter-quartile range for TAWSS, indicate the 4D Flow-MRI-based reconstruction methodology may not elucidate the variability in vessel radius to the same degree as CT. Though no significant difference was found, it must be noted that localized inter-modality differences in the geometric parameters were present, most notably concerning the vessel radius, likely due to the low near-wall velocities mentioned previously.

CFD analysis indicated these small differences in vessel geometry amplified any differences in the blood flow regime. This resulted in statistically significant inter-modality differences in near-wall hemodynamics at the upper and lower extremes of TAWSS and OSI ($p<0.05$). For example, a further analysis reveals the regions of increased inter-modality TAWSS differences

are spatially correlated to regions of increased radial disparities which subsequently alter blood velocity, and therefore TAWSS, for a given flow rate. These discrepancies in vessel radius have a marked impact on the resultant hemodynamics because blood velocity is non-linearly related to radius. However, Figure 3.10 demonstrates that there still exists a strong correlation between the CT and 4D Flow-MRI derived TAWSS and OSI, where R^2 is 0.77 and 0.98 respectively. Additionally, Figure 3.11 indicates that the proposed methodology to create images based on retrospective 4D Flow-MRI data does not systematically underestimate or overestimate the lumen when compared to CT. This can be inferred since blood velocity is not consistently higher or lower in the 4D Flow-MRI-derived CFD models when compared to the CT-derived CFD models. It is important to note, however, that a larger study is required to validate this claim.

As the upper and lower extremes of TAWSS and OSI are important in clinical applications, the inter-modality discrepancies must be highlighted [28] [189]. Within this study, these regions differed by only 0.39Pa and 0.035Pa, respectively, between CT and 4D Flow-MRI. Further, the sensitivity analysis determined that the user may be responsible for up to ~0.53Pa of this discrepancy, due to variations in lumen interpretation. As such, the true inter-modality difference in TAWSS may be negligible. These differences are also low in comparison to the high shear stresses (>5-10Pa) which can induce platelet activation, and therefore may not be clinically significant. However, these discrepancies should be noted when assessing the risk of thrombosis [28].

3.5.4 CFD vs In Vivo 4D Flow-MRI

Regarding blood velocity, the MRI-derived CFD models demonstrated a superior degree of qualitative similarity to the *in viv*o data when compared to the CT-derived models. However, it is important to acknowledge that disparities persisted, which can be attributed to various factors. Primarily, manual errors introduced by the operator during vessel segmentation likely contributed largely to this, as these were regions of challenging anatomy, encompassing features such as aortic dissection and a stent-graft. In the case of the latter, the presence of metal components in the stent-graft likely resulted in local field disruptions, thus causing significant artifacts during the acquisition of 4D Flow-MRI [212]. Aside from geometric differences and signal artifacts, it is important to consider the inherent differences between 4D Flow-MRI imaging and CFD modeling. In recognition of these differences, quantitative discrepancies between the two approaches are commonly observed in literature [89] [99] [213] [62]. Firstly, the spatiotemporal resolution is very high for the CFD models, but very low for

the *in vivo* scan sequence. This mismatch of resolution is known to introduce differences in resultant blood velocity, especially in regions of increased flow [99] [213]. Secondly, the scan sequence utilized in this study exhibited a coarse resolution of 3.6 x 2.4 x 2.6 mm^3, though literature suggest a minimum resolution of 1.5mm x 1.5mm x 1.5mm is desirable [89]. Accordingly, it is reasonable to assume that the lower-resolution 4D Flow-MRI scans can induce errors in the flow field since the results relies increasingly on data interpolation. Due to the retrospective nature of the dataset, this could not be refined [89]. Thirdly, it should be recognized that the 4D Flow-MRI scan did not incorporate isotropic spatial resolution, thereby causing the resulting velocity measurements to be directionally dependent, unlike the CFD models [89]. Finally, the assumption of rigid walls and the absence of the proximal aorta in the numerical domain likely contributed to the differences in CFD vs *in vivo* velocity profiles. To validate these statements however, a larger study is required.

3.5.5 Limitations and Future Work

There were several limitations to this study, mainly due to the retrospective nature of the 4D Flow-MRI data set. Firstly, a low number of geometries (n=3) were used for validation purposes due to limited patient data. More data are required to ascertain the reliability of the novel methodology proposed for dataset generation. This study, however, was intended as a proof-of-concept analysis to demonstrate how the novel methodology may contribute towards the reconstruction of 4D Flow-MRI images for use in CFD, particularly for retrospective datasets in the absence of standard images such as MRA and PCA.

However, with numerous data points for each modality for both radius and curvature, it was possible to determine statistical significance in relation to the comparison of CT vs 4D Flow-MRI-derived reconstructions, and not regarding patient statistics. Additionally, validation was restricted to healthy and stented regions of the clinical patients as the 4D Flow-MRI sequence utilized in this study was not optimized for visualization of the false lumen. To include larger, more complicated regions of pathology, future studies would require multi-VENC 4D Flow-MRI imaging, which can capture significantly different velocities within the same scan. Further, the limited spatial resolution of the research-based 4D Flow-MRI sequence used to acquire the images in this study may have affected the validation study. Due to the intrinsic resolution of the dataset, this could not be improved.

An unsteady parabolic profile was prescribed at the inlet of the CFD domains. It was not possible to extract the decomposed spatial velocity profile from cvi42®, and therefore this could not be prescribed directly as a Dirichlet boundary condition at the inlet.

The rigid wall assumption affects the accuracy of clinically relevant CFD-derived hemodynamic metrics including TAWSS and OSI [62] [214]. By omitting the compliance of the native arteries for example, TAWSS is generally overestimated, particularly due to elevated wall shear stress at peak systole [62].

Future work will integrate 4D Flow-MRI time-resolved data regarding vessel wall motion into the numerical model to improve the accuracy of the CFD simulations by creating a moving boundary method (MBM) model [62] [214]. To do so, the geometry of the vessel must be captured at all stages of the cardiac cycle. Therefore, future prospective studies will iteratively reduce and optimize the VENC parameter to capture blood velocity, and therefore signal intensity during the late-systolic and diastolic phases. These MBM simulations can then be performed at a substantially reduced computational cost in comparison to fluid-structure interaction (FSI) models, can account for external loads applied by surrounding tissue, and utilized data which is measurable in vivo, thus limiting the required assumptions [62] [214].

3.6 Conclusion

In this Chapter, a novel dataset was created from multiple 4D Flow-MRI-derived images at reproducible time steps throughout the cardiac cycle, yielding a temporal CPC-MRA image dataset. This study presents proof-of-concept examples of how functional 4D Flow-MRI data can be retrospectively translated to generate 3D anatomical models for geometric analysis and CFD in healthy and stent-graft cases. The blood velocity-based approach yielded uniform signal intensity throughout the lumen, clearly contrasting with surrounding static tissue while preserving the 3D relationships of overlapping vascular anatomy. Fundamentally, the outlined methodology required no ionizing radiation or intravenous contrast and could be performed on retrospective data sets. This processing of the 4D Flow-MRI data prepares it for most image segmentation methodologies, from thresholding to machine learning and convolutional neural networks. Finally, the proposed pipeline for 4D Flow-MRI derived image creation may be used for 3D model generation of healthy and stented aortae in cases where 4D Flow-MRI is available, for example when screening for aortic disease, pregnant women, or children.

3.7 Research Contribution

In Chapter 3, we extracted the 3D instantaneous velocity profile from 4D Flow-MRI data at discrete, repeatable cardiac timesteps which encompassed systolic acceleration, peak systole, and systolic deceleration. This methodology was utilised to generate retrospective image stacks of the vessel lumen for subsequent segmentation and reconstruction in healthy volunteers and TABD patients. Reconstructed geometries of the iliac bifurcation, based on this methodology, were compared against CT-derived reconstructions from the same patient population as a proof-of-concept study. The research contributions from this Chapter were:

1) A novel methodology was proposed to generate Digital Imaging and Communications in Medicine (DICOM) image stacks of the vessel lumen, based on blood velocity from multiple cardiac timesteps. This was performed on retrospective 4D Flow-MRI datasets.
2) This methodology produced uniform signal intensity within the lumen and could retrospectively enhance vessel contrast and signal to noise ratio by superimposing the velocity profile directly onto the base 4D Flow-MRI magnitude images.
3) As a proof-of-concept study, the iliac bifurcation was reconstructed directly from 4D Flow-MRI data in the absence of accompanying images such as conventional maximum intensity projections from magnetic resonance angiography. With this methodology, signal intensity and contrast were generated from single axial slices across multiple time steps with this method, rather than combining multiple axial slices within a single time step. Therefore, the 3D relationships of the vascular anatomy were preserved.
4) The geometry of the 4D Flow-MRI derived reconstructions were validated against CT-derived reconstructions through several metrics including vessel radius, curvature, Hausdorff distance, and dice similarity coefficient.

4 Calibration of Patient-Specific Boundary Conditions for Coupled CFD Models of the Aorta Derived from 4D Flow-MRI

In this chapter, we build on the previous work of anatomical reconstruction to convert these geometries into CFD models, complete with inlet and outlet boundary conditions. Therefore, this chapter presents a novel reduced-order computational framework for the iterative flow-based calibration of 3-Element Windkessel Model (3EWM) parameters to generate patient-specific BCs. These parameters were calibrated using time-resolved flow information derived from retrospective 4D Flow-MRI. For a healthy and dissected case, blood flow was then investigated numerically in a fully coupled zero dimensional-three dimensional (0D-3D) numerical framework, where the vessel geometries were reconstructed from medical images.

The work in this chapter was published as per the following reference: S. M. Black, C. Maclean, P. Hall-Barrientos, K. Ritos, A. McQueen and A. Kazakidi (2023), "Calibration of Patient-Specific Boundary Conditions for Coupled CFD Models of the Aorta Derived from 4D Flow-MRI", Frontiers in Bioengineering and Biotechnology 11:1178483. https://doi.org/10.3389/fbioe.2023.1178483

4.1 Introduction

The aorta is the largest arterial segment of the human systemic circulation and exhibits a complex flow regime [17] [41] [43]. This region can be affected by AD, characterized by a primary intimal tear which results in the creation of a FL, and additional secondary intraluminal tears [4] [69] [73]. This FL forms when blood flows through the intimal tear and into the medial layer of the aortic wall, creating a secondary channel which extends longitudinally beside the native lumen [69]. As the FL demonstrates a proclivity to expand and potentially rupture, there is a risk of serious morbidity and mortality in the absence of intervention [4] [69] [59].

Capturing this complex blood flow regime *in vivo* is challenging, but 4D Flow-MRI presents a reliable, non-invasive tool for such analysis. Crucially, velocity is encoded in three principal spatial directions and time, permitting 3D evaluation of the dynamic evolution of blood flow throughout an entire cardiac cycle [9] [98]. Fundamentally, this quantitative analysis can be performed post hoc at any point in a ROI due to complete volumetric coverage [88] [215]. To date, 4D Flow-MRI has been used to observe and quantify a range of hemodynamic parameters including wall shear stress, peak velocity, flow rate and regurgitant fraction, in healthy and dissected aortae [4]. Previous studies indicate however that the calculation of near-wall

hemodynamic parameters like WSS via 4D Flow-MRI may be inaccurate due to poor spatial and temporal resolution [9].

CFD models can overcome this limitation, portraying the distribution of near wall hemodynamics with unparalleled spatiotemporal resolution [50] [185]. Through CFD, it is also possible to investigate numerically the effect of isolated factors in a controlled environment, e.g. by setting different boundary conditions BCs to which the aortic flow regime is very sensitive [45] [52]. Utilizing CFD models to expand upon clinical data may aid clinicians with diagnostic decision making due to the ability to accurately replicate complex intra-aortic hemodynamics [45] [216]. For example, these models may indicate sites of future dissection or aneurysm development [69].

Presently, it is not possible to model the entire systemic circulation in 3D due to lack of imaging resolution and the prohibitively expensive computational cost [56] [217]. Further, while distal vasculature accounts for most of the vascular resistance, the clinically relevant flow phenomena such as jet flow and recirculation in the case of AD, because of intraluminal tears, develop within larger vessels [217]. Therefore, a multi-dimensional approach is required to incorporate all relevant domains in a unified model. As such, complex spatiotemporal flow behavior is solved in the high-fidelity 3D domain, while the effect of distal vasculature is estimated through computationally efficient, reduced order BCs [45] [167] [190]. To generate patient-specific CFD models, these BCs must be physiologically accurate, robust, and simple to implement on a parallel computing framework [33].

A zero-dimensional (0D) 3-Element Windkessel Model (3EWM) is therefore commonly employed at the outlet boundaries to describe the pressure-flow relationship due to distal vasculature [193] [218] [78]. Clinical application of such BCs requires patient-specific tuning of the Windkessel parameters, which is not a trivial task, and for which there is no single, agreed upon methodology [59] [218]. Previous studies describe root finding algorithms, Kalman filtering, and iterative calibration loops [49] [56]. Often, these studies impose parameters which are calibrated based on invasive pressure measurements, empirical laws, and many require arterial pulse wave velocity (PWV) to be estimated [45] [218]. These calibration approaches become extremely difficult in the presence of arterial pathology as highly individualized changes in vessel morphology create a chaotic flow regime which cannot be readily estimated [59] [219] Moreover, current calibration methodologies often rely on non-patient-specific data from previous literature, leading to further inaccuracies [73] [78].

4D Flow-MRI derived parameter calibration eradicates the need for assumptions since functional flow and anatomical information can be obtained in parallel from a single, non-invasive, non-ionising scan of the patient. Therefore, the aim of this study is to outline a methodology to generate patient-specific 3EWM BCs derived from retrospective 4D Flow-MRI images of a healthy and a dissected aorta. This study will then demonstrate the application of these BCs in the generation of a patient-specific, coupled 0D-3D CFD model for a healthy and dissected aorta as proof-of-concept examples. To the best of our knowledge, this has not previously been performed, and our results are the first to demonstrate the efficacy and value of such a framework.

4.2 Materials and Methods

4.2.1 Data Acquisition

4D Flow-MRI images of the aortae of two patients, one healthy (33-year-old male) and one with a dissected aorta (55-year-old male), were acquired via a Siemens research 4D Flow-MRI sequence (WIP 785A), previously described in Section 2.2. CT images were obtained for the dissected aorta. For both modalities, the imaging sequences have previously been described in Chapter 3. Figure 4.1 summarizes this methodology, showing the dissected aorta as an example.

4.2.2 3D Arterial Reconstruction

The thoracic aorta of the healthy volunteer was reconstructed from 4D Flow-MRI data using the methodology described in Black et al [220]. In brief, a 3D MRA was created by deriving contrast from the instantaneous velocity magnitude of blood during systolic acceleration, peak systole, and systolic deceleration (Figure 4.1B). These images were then superimposed to create a temporal composite DICOM stack of images which exhibited high contrast in the vessel lumen.

For the AD case, multi-VENC MRI imaging is required to allow for the precise segmentation of the false lumen [220]. As this was not available, the geometry of the dissected aorta was reconstructed from CT images (Figure 4.1C). The image stack for each individual was then processed in SimVascular® (https://simvascular.github.io/), where segmentation and reconstruction was performed as per Chapter 2 and 3. Flow extensions were added at the inlet (5×D) and outlets (10×D), where D was the diameter of the terminal branch These are extensions of the meshed domain at the inlets and outlets in the direction which is normal to the boundary face. Flow extensions improve numerical convergence, accuracy and stability of

the CFD model by ensuring the location of the boundary faces do not influence results within the domain of interest [187] [216]. Flow extensions were added to ensure the results of the branch outlets were not affected by flow at the entrance to these branches [130]. This avoids uncertainties caused by imposing boundary conditions by ensuring flow is fully developed by the time it reaches the outlet face [30] [37].

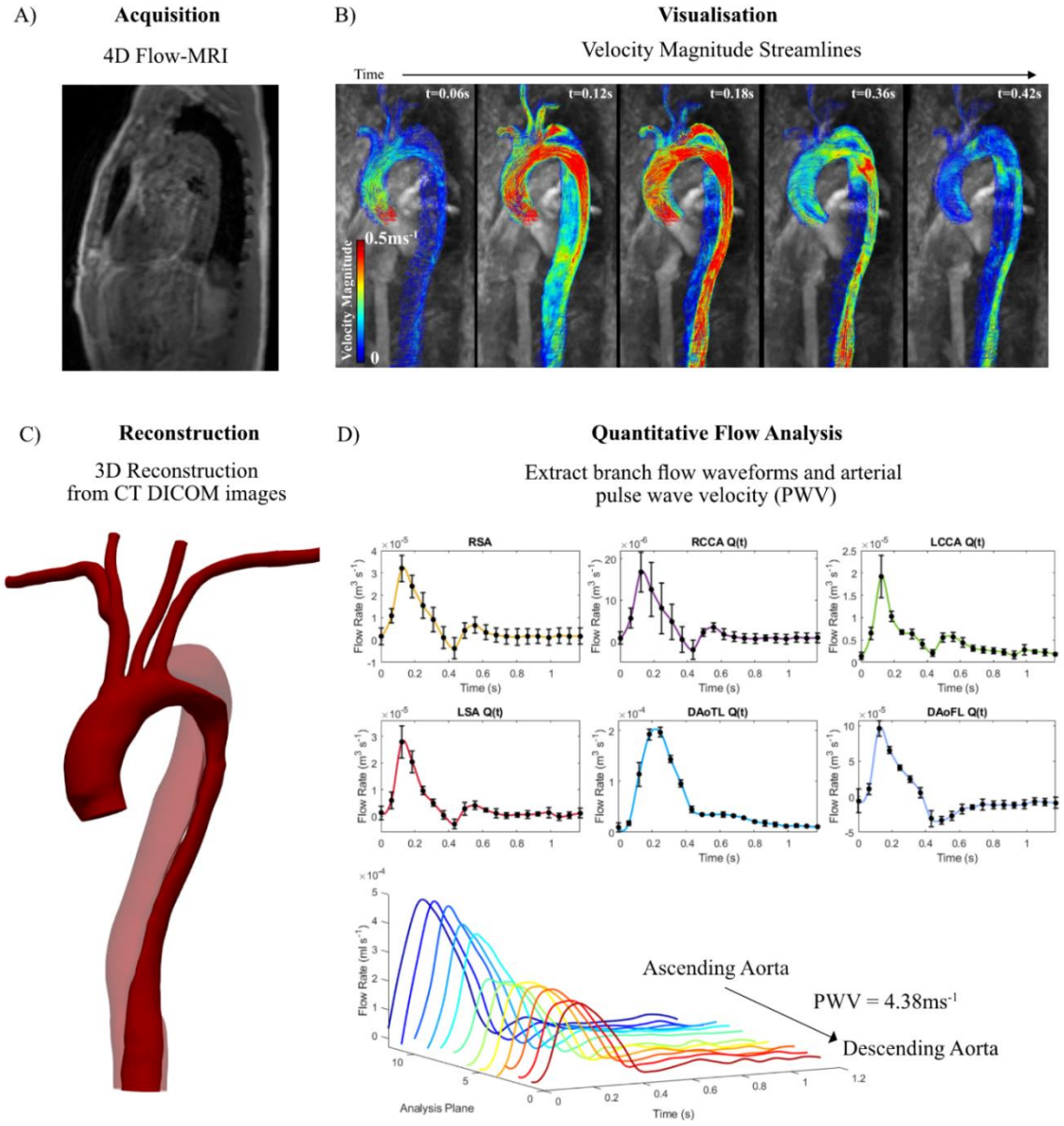

Figure 4.1: Information derived from 4D Flow-MRI and CT data for the aortic dissection patient, illustrating (A) 4D Flow-MRI acquisition, (B) visualisation of velocity streamlines on Circle Cardiovascular Imaging Software® at multiple time points throughout the cardiac cycle (t = 0.06, 0.12, 0.18, 0.36, and 0.42 s), (C) reconstructed geometry of the dissected thoracic aorta, illustrating the true lumen (solid color) and the false lumen (transparent), and (D) branch flow waveforms and pulse wave velocity (PWV) extraction which were used to generate patient-specific 3-Element Windkessel boundary conditions. PWV was extracted directly from Circle Cardiovascular Imaging Software®.

4.2.3 CFD Methodology

To discretize the 3D models for numerical investigation, a tetrahedral mesh was generated in Ansys ICEM CFD® as per Chapter 2 and 3. To resolve the viscous sublayer, an initial boundary layer height of 0.0015m was prescribed to ensure y+<1 throughout the geometry. Thereafter, 11 additional prism layers were generated utilizing an exponential expansion ratio of 1.2 (i.e. $h_n = h_1 e^{(n-1)p}$, where h_1 is the initial height, n is the number of prism layers, h_n is the height of each subsequent layer, and p is the exponent).

To ensure mesh independence, a grid convergence study was performed, as per Chapter 2, which evaluated TAWSS at multiple regions throughout the geometry where the most complex flow was expected. This included the area around each intraluminal tear, the supra-aortic branch ostia, and the innominate bifurcation. A total of 3.8 million elements (excluding flow extensions) were required to ensure mesh independence, such that the computed TAWSS was less than 2.5% different than the Richardson Extrapolation.

Blood flow was simulated by solving the 3D, time-dependent, incompressible, Reynolds-averaged RANS equations for continuity and momentum corresponding to Eq 2.21 and 2.22, respectively [132]. These governing Navier Stokes equations were solved numerically in Ansys Fluent® utilizing a finite volume method, a standard k-ω turbulence model, and PISO algorithm at 10 iterations per time step (dt=0.001s) [188]. Notably, the standard k-ω turbulence model was utilized, as opposed to the k-ω SST utilised in Chapter 3, since it has been shown to be more accurate when compared to experimental data and maintain stability in regions of stagnation and high fluid acceleration which are common in AD cases [136] [137].

CFD Simulations were performed on a single node of the ARCHIE-WeSt cluster at the University of Strathclyde. These required ~16 hours on average to solve 5 cardiac cycles on 35 Intel Xeon Gold 6138 (Skylake) processors at 2.0 GHz and 4.8 GB RAM per core. Blood was assumed to be Newtonian due to high shear rates within the true lumen, with a density of 1060 kgm^{-3} and a dynamic viscosity, μ, of 0.004 Pa s [186]. Though a shear-thinning Newtonian model is more accurate to model the effect of low-velocity blood flow within the FL, the simpler Newtonian model was utilised throughout as the purpose of this proof-of-concept study was primarily to investigate the effect of parameter calibration while all other parameters remained constant. Further, a Newtonian assumption is commonly used throughout literature in CFD modelling of aortic dissection [60] [221] [66] [67]. The purpose was not to generate high-fidelity models complete with Newtonian flow and compliant walls.

Hemodynamic analysis was performed on the 5th cardiac cycle when time-periodicity was obtained, where pressure and flow rate altered by less than 1.5% in consecutive cardiac cycles. This was to ensure convergence for unsteady flows. TAWSS and OSI were calculated as per Eq 3.7 and 3.8.

4.2.4 Boundary Conditions

Outlet Windkessel BCs were estimated from geometric parameters and arterial PWV, while inlet waveforms were extracted directly from *in vivo* data. The outlet BCs were subsequently calibrated against 4D Flow-MRI-derived *in vivo* blood flow data at each branch of the thoracic aorta. Figure 4.2 details a flowchart of the calibration methodology and CFD analysis.

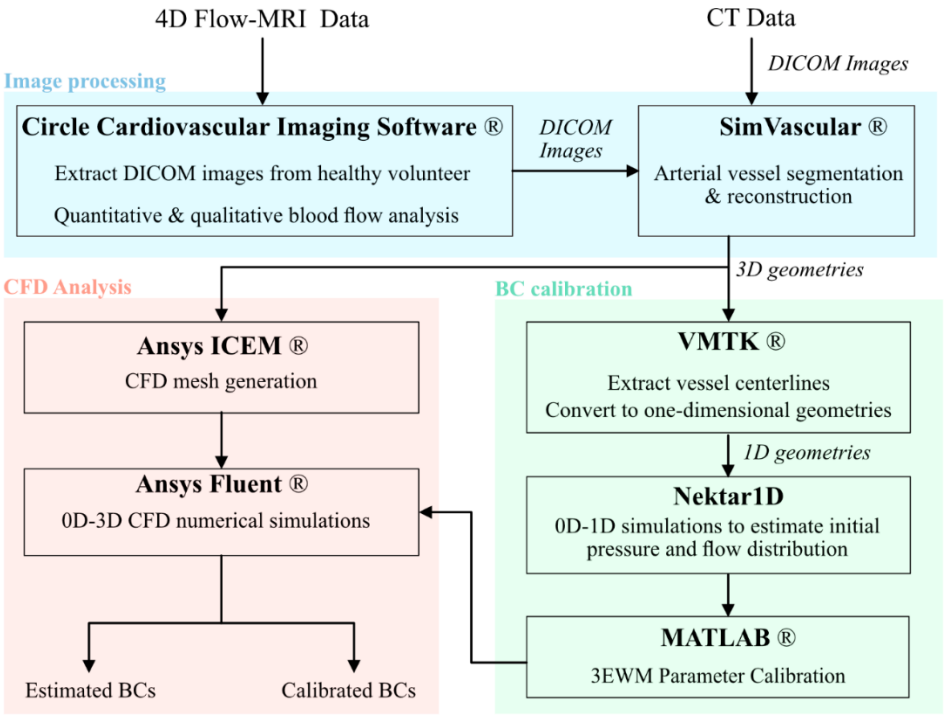

Figure 4.2: Flowchart of the methodology and software used to generate patient specific CFD models of the thoracic aortae including image processing, boundary condition calibration, and numerical analysis.

4.2.4.1 Inlet Profiles

The inlet profiles for the CFD models were extracted from the 4D Flow-MRI images. On Circle Cardiovascular Imaging software (cvi42®), analysis planes (n=5) were placed at the ascending aorta of the healthy volunteer and dissected patient. In both cases, these planes were equally spaced 0.25D apart proximally and distally, with the initial plane corresponding to a location parallel to the apex of the pulmonary arch [222]. These MRI-derived flow waveforms (Figure 4.3) were converted to a velocity profile, interpolated to generate a constant time step size (dt=0.001s), and repeated for 5 cardiac cycles. Spatially, a uniform profile was assigned. Only

one cardiac cycle was available from 4D Flow-MRI, so the cardiac pulse at the inlet was assumed to be periodic for the multi-cycle simulations.

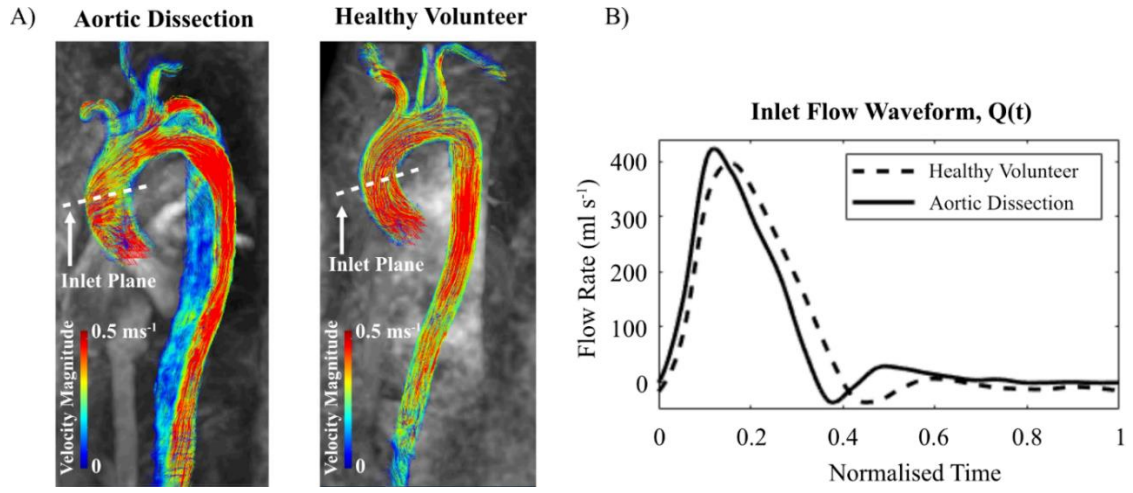

Figure 4.3: (A) Velocity magnitude streamlines extracted from cvi42® at peak systole within the thoracic aorta of the aortic dissection patient and healthy volunteer. (B) 4D Flow-MRI derived flow waveform within the ascending aorta for each case.

4.2.4.2 Outlet Branch Flow Waveforms

Average branch flow waveforms (Figure 4.1D) at the outlets were extracted from the 4D Flow-MRI data using cvi42®. For the RSA, right common carotid artery (RCCA), LCCA, LSA, descending aorta true lumen (DAoTL), and the descending aorta false lumen (DAoFL), 5 planes of analysis were placed normal to the longitudinal axis of the vessel, spaced 0.5D apart.

4.2.4.3 Pulse Wave Velocity

Arterial PWV (Figure 4.4) is defined as the propagation speed of the systolic flow velocity wave front, or propagation speed of the pressure wave as it traverses the vasculature [35]. This is a measure of aortic compliance and is a predictor of future cardiovascular morbidity and mortality [100] [35]. It is possible to estimate PWV based on geometric and material properties, but this would require several assumptions and data which is difficult to extract, leading to potential sources of error [29] [49] [223] [224] [225]. Recently, it has been shown that 4D Flow-MRI is an accurate method to non-invasively measure PWV, and has been shown to have good intra- and inter-operator reproducibility [100] [226].

Therefore, 4D Flow-MRI derived PWV was calculated on cvi42® for the healthy and dissected aortae. 12 planes of analysis, equally spaced throughout the aorta from the proximal ascending region to distal descending region, were retrospectively placed to calculate PWV, following the previously described methodologies in literature [100] [227] [228]. Notably, this calculated

the mean PWV of the thoracic aorta, not localised differences in each branch and aortic segment [100]. The PWV of the healthy case was calculated as 7.85ms^{-1}, while the dissected case was equal to 4.38ms^{-1}. PWV is later utilized for boundary condition estimation.

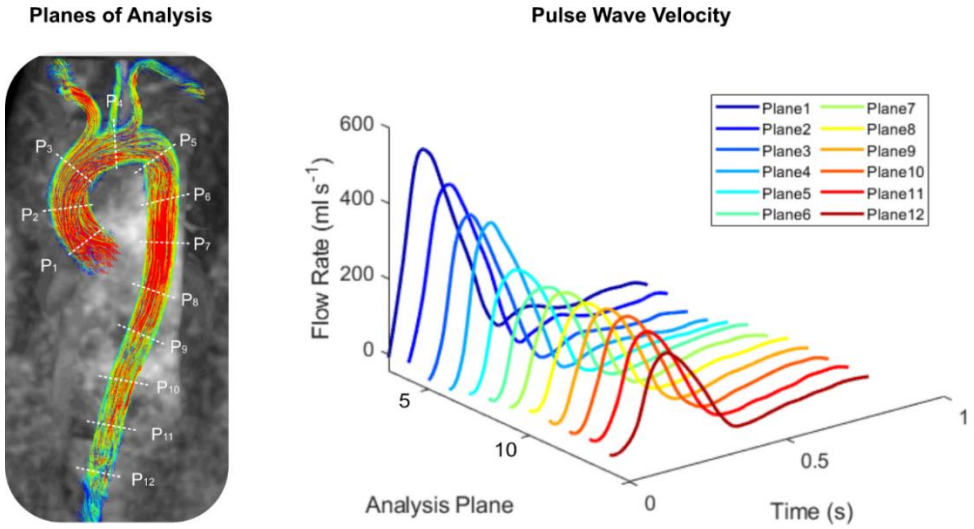

Figure 4.4: Location of each of the 12 planes of analysis used to calculate the mean pulse wave velocity within the thoracic aorta of the healthy volunteer.

4.2.4.4 Windkessel Model

The mono-compartmental 3EWM (Figure 4.5) is a hydraulic electric analogue, which models the total resistance and compliance of the peripheral vasculature to provide a dynamic description of the downstream physics [36] [54] [229]. This represents the systemic arterial network but neglects the venous system which is represented as a zero-pressure sink [36]. In an electrical circuit, the voltage gradient drives current against electrical resistance, while in the Windkessel model, the pressure gradient drives blood flow against hydraulic resistance [36]. The 3EWM is solved as an ordinary differential equation (Eq 4.1) which acts as a simplified description of the branching arterial network with only a few parameters, meaning it can model the properties of the global arterial tree, but neglects the spatial variation of the parameters [36] [46] [54] [230] [229]. Notably, these BCs are a significant improvement on flow-split or constant pressure alternatives [231].

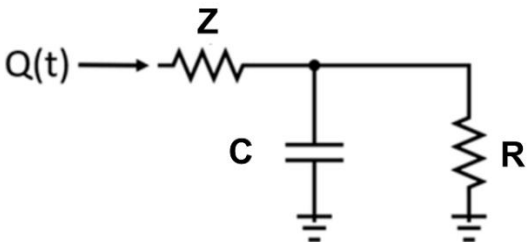

Figure 4.5: Schematic of a 3-element Windkessel model represented as a hydraulic-electric analogous, where the blood flow, Q(t), is the input. The characteristic impedance, Z, is in series with the rest of the circuit, while the compliance, C, and peripheral resistance, R, are in parallel with each other.

The characteristic impedance (Z) is equal to the oscillatory pressure (P) divided by the oscillatory flow (Q), while capacitance (C) represents distal vessel wall compliance, and resistance (R) denotes the total peripheral vascular resistance, primarily due to the capillary beds [54] [216] [230].

$$\left(1+\frac{Z}{R}\right)Q(t)+CR\left(\frac{dQ(t)}{dt}\right)=\frac{P(t)}{R}+C\left(\frac{dP(t)}{dt}\right) \qquad (4.1)$$

Notably, Z represents the combined effect of frictional loss, fluid inertia, vessel wall elasticity, and improves the high frequency performance of the model [33] [36] [128]. Therefore, the 3EWM yields a more accurate prediction of aortic pressure when compared to a two-element Windkessel model [232] [233]. It is possible to use a 4EWM but this requires a further assumption of inertance which is difficult to estimate, and therefore has the potential to introduce further errors [229]. Thus, 3EWM BCs are relatively simple, yet are widely accepted to be highly reliable and provide a good estimate of the aortic pressure profile [229] [234]. Consequently, they have been used extensively in CFD studies and their effectiveness is widely accepted in literature, for studies involving healthy volunteers and aortic dissections [45] [59] [218] [78] [235] [79].

To facilitate numerical analysis, the 3EWM was discretized (Eq 4.2) via the Backwards Euler finite difference method. At each terminal branch, the discretized 3EWM was coupled implicitly to the 3D numerical domain via a UDF in Ansys Fluent®. Here, the 0D 3EWM provides a pressure boundary condition for the 3D CFD domain, while the 3D domain specifies flow rate changes for the 0D BC. Consequently, the entirety of the vasculature distal to the 3D domain was described by a single ZRC combination for each branch. With these assigned parameter values, it was possible to calculate pressure and flow as part of the numerical solution [56].

$$P^{n+1}=\frac{\beta P^{n}+Q^{n+1}(R+Z+Z\beta)-Z\beta Q^{n}}{(1+\beta)},\ \text{where}\ \beta=\frac{RC}{\Delta t} \qquad (4.2)$$

Where n is the discrete timestep. To reduce the number of cycles required to achieve a time-periodic solution, pressure was initialized to 101 mmHg (diastolic clinical pressure) for the dissection case, and 80mmHg (healthy diastolic reference pressure) for the healthy case [15].

4.2.4.5 3EWM Parameter Estimation

This study utilizes the arterial geometry, pulse wave velocity, and geometric scaling factors which describe the successive branching of peripheral vasculature to generate initial estimates for the 3EWM parameters [49] [47] [236] [237]:

$$Z = \frac{\rho c_{pwv}}{A_0} \tag{4.3}$$

$$R = Z\left(\frac{\lambda}{2\varphi^4 - \lambda}\right), \qquad \frac{1}{2\varphi} < \lambda < \frac{1}{2\varphi^2} \tag{4.4}$$

$$C = C_o\left(\frac{2\lambda\varphi^3}{1-2\lambda\varphi^3}\right), \qquad C_o = \frac{A_0 l}{\rho(c_{pwv})^2}, \tag{4.5}$$

where λ=0.68 and $\varphi = \sqrt{0.6}$ are the chosen geometric scaling factors extracted from literature [49] [47], c_{pwv} is the 4D Flow-MRI derived arterial PWV in the thoracic aorta (healthy = 7.85ms^{-1}, dissected = 4.38ms^{-1}), ρ is the blood density (1060 kgm^{-3}), A_0 is the average branch vessel cross sectional area, and l is the branch vessel length. For each vessel segment, the 3D model was converted to a one-dimensional (1D) geometry in VMTK, and the computed centerlines were utilized to obtain A_0 and l (Table 4.1).

Table 4.1: Branch vessel length and cross-sectional area for the dissected and healthy aortae when converted to a one-dimensional geometry.

Branch	**Branch Length (m x10^{-1})**		**Mean Cross Sectional Area (m^2 x10^{-5})**	
	Dissection	Healthy	Dissection	Healthy
RSA	1.10	0.25	4.04	7.03
RCCA	0.46	0.34	1.34	3.91
LCCA	0.80	0.66	3.35	3.46
LSA	1.48	1.35	3.05	6.75
DAoTL	1.87	2.61	12.50	43.50
DAoFL	1.85	-	25.70	-

To determine the net peripheral resistance (R_T) required to generate a clinically accurate mean blood pressure, Eq 4.6 was employed [49] [238].

$$R_T = \frac{P_{Mean}}{\bar{Q}_{in}}, \; P_{Mean} = P_{Dia} + \frac{1}{3}\left(P_{Sys} - P_{Dia}\right), \tag{4.6}$$

where $\bar{Q}_{in}$ is the mean inlet flow rate, P_{Sys} is the target systolic pressure, and P_{Dia} is the target diastolic pressure. For the dissected case, P_{Sys} and P_{Dia} were taken to equal 189mmHg and 101 mmHg, respectively, which was obtained via a brachial pressure cuff measurement to

complement the 4D Flow-MRI data. For the healthy case, P_{Sys} and P_{Dia} were assumed to be 120mmHg and 80mmHg, respectively, as pressure data was not available for the healthy volunteer [15].

For the estimated parameters, it was then checked to ensure that:

$$\frac{1}{R_T} = \sum_{j=2}^{M} \frac{1}{Z^j + R^j} \tag{4.7}$$

Where M is the number of terminal branches (excluding j=1 as that is the aortic root inlet). Table 4.2 outlines the estimated 3EWM parameter values for each terminal branch.

Table 4.2: Initial estimates for the parameters of the 3EWM at each branch of the healthy and dissected models.

Branch	**Windkessel Parameters (Estimated)**					
	Z (x10^7) [Pa s m^{-3}]		**R(x10^9) [Pa s m^{-3}]**		**C(x10^{-10}) [m^3 Pa^{-1}]**	
	Dissection	**Healthy**	**Dissection**	**Healthy**	**Dissection**	**Healthy**
RSA	11.5	6.53	2.65	1.50	3.91	0.477
RCCA	34.6	11.7	7.97	2.70	0.546	0.364
LCCA	13.9	13.3	3.19	3.05	2.36	0.621
LSA	15.2	6.80	3.5	1.57	3.98	2.5
DAoTL	3.71	1.05	0.854	0.243	20.6	31.1
DAoFL	1.81	-	0.415	-	41.9	-

4.2.5 0D-1D Modelling

1D modelling was required to generate an initial estimate of pressure and flow waveforms at each branch of the thoracic aorta. For each geometry, the 1D domain was constructed from vessel centerlines of the reconstructed aortic geometries. These centerlines were partitioned into a finite number of discrete segments ($N_{Dissection}$=22, $N_{Healthy}$=9). For each arterial segment, the cross-sectional area and axial length were prescribed, based on the average values as computed from the centerline of that segment. The elastic wall properties were modelled via the Nektar1D empirical law, where the stiffness parameter for each vessel segment was calculated as a function of arterial PWV, blood density, and the average cross-sectional area of that segment. At each terminal branch, the estimated 3EWM BCs were coupled, thereby creating a 0D-1D model [36]. The 4D Flow-MRI derived, patient-specific velocity waveform was applied at the inlet of this model and a fully elastic simulation was performed using the Nektar1D solver over 20 cardiac cycles [239]. This 0D-1D simulation required ~1 second per cardiac cycle on 2 cores (Intel® Core™ i9-10900X CPU). A detailed description of the equations and numerical scheme used to solve them has been described previously in literature

[29]. The pressure and flow waveforms were extracted when the solution became time-periodic.

4.2.6 Parameter Calibration

4.2.6.1 The Nelder-Mead Algorithm

The *fminsearch* function in Matlab utilises the Nelder Mead algorithm, also known as the Simplex Search algorithm, which is designed to solve multidimensional unconstrained optimisation problems for nonlinear functions where there are no constraints imposed on the set of possible solutions [240] [241]. This is a direct search method where the goal is to minimise the objective function $f(x), for\ x \in \mathbb{R}^n$, of n real variables [241] [240]. The term 'direct search' can be described as a sequential examination of iterative solutions, where each solution is compared with the 'best' up to that point [242]. Essentially, if the objective function of iteration $(i + 1)$ is less than iteration i, then the Nelder Mead algorithm is moving in the right direction. Such direct methods are advantageous as they are relatively simple to implement and can be readily applied to many nonlinear optimisation problems, but still perform well in practice [242].

A simplex (Figure 4.6) is a set of (n+1) points and vertices in $\mathbb{R}^n$, where $\mathbb{R}^n$ is the collection of ordered lists of n real numbers, and n is the dimension of the function we seek to optimise [241]:

$$\mathbb{R}^n = \{(x_1 \dots x_n : x_j \in \mathbb{R}\ for\ j = 1, \dots, n\}$$

If, for example, n=3, then $\mathbb{R}^3$ is the set of all possible ordered triples. Geometrically, this would represent all points in 3D. For a 1D function, the simplex is a line segment [242]. For a 2D function, the simplex is a triangle [242]. For a 3D function, the simplex is a tetrahedron [242].

$$\mathbb{R}^3 = \{(x_1, x_2, x_3 : x_j \in \mathbb{R}\ for\ j = 1,2,3\}$$

Notably, x_1 is always the best point, and x_n is always the worst. The simplex then goes through a series of transformations: reflect, expand, contract, shrink (Figure 4.6) [241] [242]. During reflection, the worst point is reflected over the centroid to be in a better position. This is then expanded to determine if moving further in this direction is better. If the expansion point is better than the reflected point, the iteration is complete [241] [242]. If the expansion point is not better than the reflected point, the simplex may do an inside or outside contraction to evaluate a point closer to the centroid [241] [242]. Finally, the simplex can shrink towards the best point to make all points better [241] [242]. This process is then repeated one point at a

time until a convergence criterion is met [241] [242]. Essentially, the simplex walks around the function space, moving one point at a time, trying different parameters until converging on a global or local minimum of the objective function.

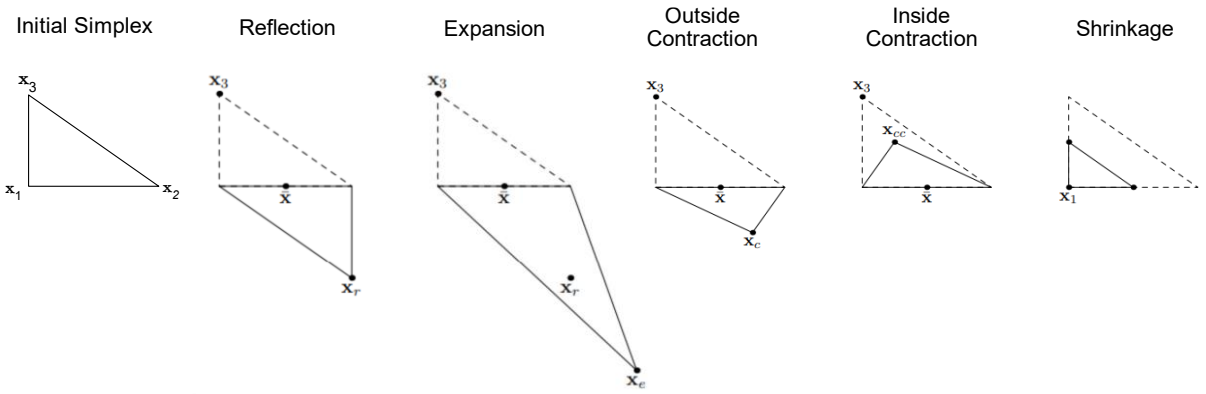

Figure 4.6: Nelder Mead steps. x_r is the reflection point, $\bar{x}$ is the centroid of all points (except the worst point, x_3), x_e is the expansion point, x_c is the outside contraction point, x_{cc} is the inside contraction point, and x_1 is the best point [241]. *In our case, x_1, x_2, and x_3 are the windkessel parameters, and the simplex is walking over the objective function which is the error between the in vivo and computed flow rate.*

4.2.6.2 Calibration

To calibrate the 3EWM parameters in order to generate patient-specific BCs, Eq 4.2 was first rearranged to yield Eq 4.8, thereby making the Windkessel flow rate (Q_{WK}) the subject of the equation. For each terminal branch of the CFD domain, Q_{WK} was calculated as per Eq 4.8, using the estimated parameters (Table 4.2) and the 0D-1D derived pressure waveforms. When Q_{WK} reached a time-periodic solution, the waveform over a single cardiac cycle was then compared against the *in vivo*, 4D Flow-MRI derived flow waveforms (Q_{inVivo}) for each branch. All flow rates are presented in the units of m^3s^{-1}.

$$Q_{WK}{}^{n+1} = \frac{(1+\beta)P^{n+1} + Z\beta Q_{WK}{}^{n} - \beta P^{n}}{R + Z(1+\beta)} \tag{4.8}$$

For each terminal branch, the errors (ε_j) present between the clinical (Q_{inVivo}) and simulated (Q_{WK}) data points was calculated as per Eq 4.9:

$$\varepsilon_j = \sum_{i=1}^{T} (Q_{WK}(t_i) - Q_{\text{inVivo}}(t_i))^2 \tag{4.9}$$

Where T is the duration of a single cardiac cycle, $j = 1, 2, \ldots, M$ where j is the related terminal branch and M is the total number of branches, and $t_i, i = 1, 2, \ldots,$ T are the measurement time points, where dt=0.001s.

The Windkessel parameters were then iteratively changed to minimise ε by employing the *fminsearch* routine, where n=3 is the dimension of the problem, via an in-house Matlab® script at each branch of the thoracic aorta (Figure 4.7A). Therefore, the aim of the calibration process was to find a parameter combination at each branch which resulted in a flow waveform which was most representative of the clinical 4D Flow-MRI data. This utilised a direct search method (Nelder-Mead simplex algorithm) where n=3 is the dimension of the problem. The initial Windkessel parameter estimates formed the initial simplex. Thereafter, the routine implemented the series of reflection, expansion, contraction, and shrinkage transformations. The final simplex hosts the best-fitting parameter values that correspond to the smallest error (ε_j), within a user-defined tolerance limit of 10^{-6} for the 3EWM parameters and 10^{-8} for ε_j. Finally, the calibrated, patient specific 3EWM BCs were coupled to the 3D model (Figure 4.7B).

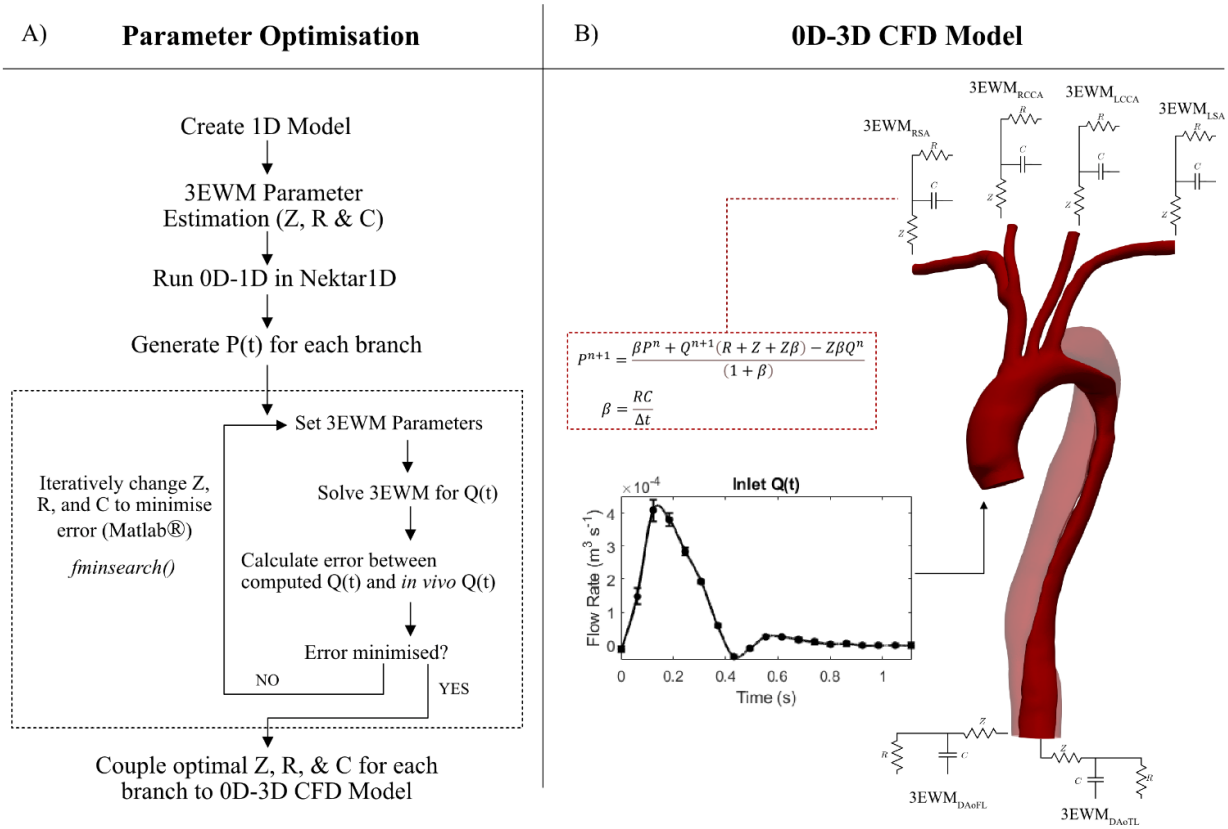

Figure 4.7: (A) Detailed flow diagram of the methodology used to calibrate impedance (Z), resistance (R), and compliance (C) of the 3EWMS BCs. (B) 0D–3D CFD model set-up, where each branch was coupled with a 3EWM. At the inlet, a 4D Flow-MRI derived flow waveform was converted to a parabolic velocity profile. The discretised 3EWM equation describes the pressure (P) and flow (Q) relationship at each branch, where n denotes the current iteration.

To elucidate how the calibration process impacted the parameter combinations, Figure 4.8 illustrates the iterative process for Z, R, C, and the objective function for a single branch (i.e. right subclavian artery). Each Windkessel parameter converged on a final value after roughly 100 iterations. Similarly, the objective function, which is the error between the computed and *in vivo* flow rates is converged on a minimum value.

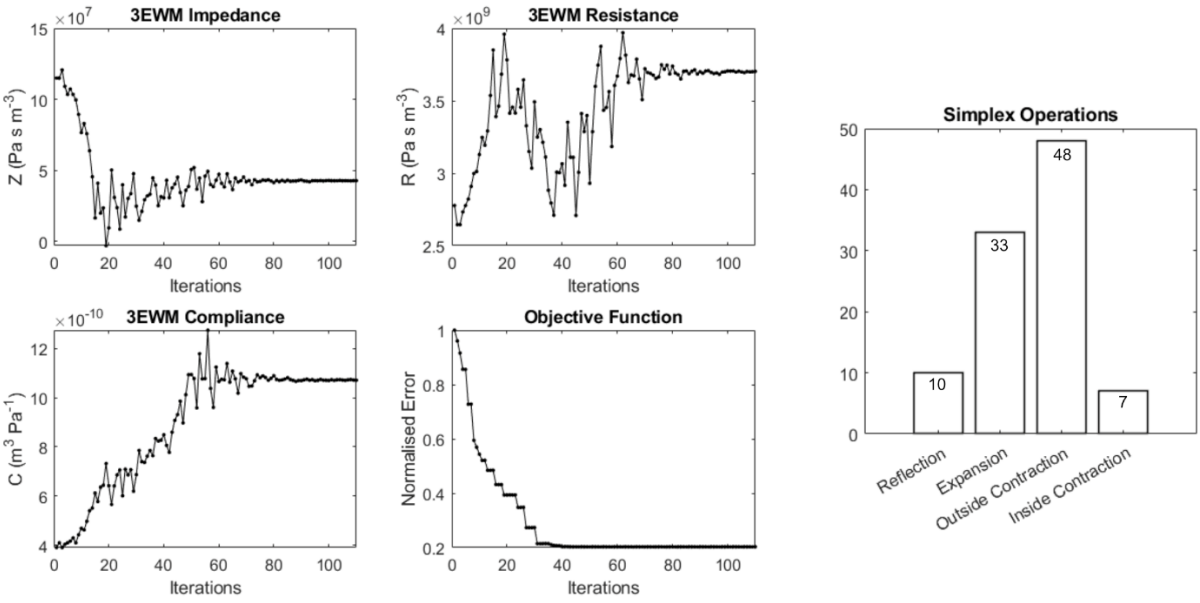

Figure 4.8: Nelder Mead optimisation of 3EWM parameters for the right subclavian artery, showing the normalised objective function and the number of steps for reflection, expansion, outside contraction and inside contraction after prescription of the initial simplex. No shrinkage of the simplex was present in this optimisation process. Convergence required ~100 iterations.

4.3 Results

Results are presented below in a series of tables and figures, describing the calibrated 3EWM parameters and the CFD-derived perfusion distribution, pressure, TAWSS, and OSI. These results demonstrate the application of these calibrated BCs on a healthy volunteer and clinical patient with aortic dissection as proof-of-concept examples. We show that our methodology yields a perfusion distribution which very closely matches *in-vivo* 4D Flow-MRI-derived data, and physiologically accurate near-wall hemodynamics.

4.3.1 3EWM BC Calibration (0D – Matlab®)

To create patient-specific BCs, a total of 18 parameters were calibrated for the dissected case, and 15 for the healthy case. This was an iterative process, requiring 20 cardiac cycles per iteration, and 100-120 iterations per parameter combination. To complete this process with the combination of reduced order, computationally efficient 0D and 1D models described in this study, it required only 3.5 minutes per branch, on average. The final 3EWM parameters which were calculated after completion of the simplex-based calibration are presented in Table 4.3.

Table 4.3: Final 3EWM parameter combination for each branch of the dissected and healthy models upon completion of the calibration process.

Branch	**Windkessel Parameters (Calibrated)**					
	Z ($x10^{7}$) [Pa s m^{-3}]		R ($x10^{9}$) [Pa s m^{-3}]		C ($x10^{-10}$) [m^{3} Pa^{-1}]	
	Dissection	Healthy	Dissection	Healthy	Dissection	Healthy
RSA	4.27	0.137	3.70	1.82	1.07	3.65
RCCA	3.85	0.296	3.53	3.22	1.08	1.38
LCCA	3.98	0.303	3.44	3.82	0.632	1.50
LSA	3.71	0.842	3.94	1.94	1.22	4.20
DAoTL	0.204	0.391	0.290	0.177	11.2	46.6
DAoFL	1.64	-	7.92	-	5.80	-

When evaluated within the 0D Matlab® framework, the calibrated parameters yield a more accurate and physiologically relevant flow waveform for each branch of the thoracic aorta for the AD patient (Figure 4.9) and healthy volunteer (Figure 4.10). In both cases, the calibrated parameters dramatically reduced the cumulative least squares difference (LSD) error between the computed and *in vivo* data. Regarding the dissected case, the error for the RSA, RCCA, LCCA, LSA, DAoTL, and DAoFL, was reduced with respect to the estimated parameters by 75.1%, 88.6%, 74.4%, 74.5%, 98.9%, and 92.2%, respectively. In the healthy case, these cumulative LSD errors were reduced by 81.8%, 75.3%, 56.2%, 58.4% and 88.8%, respectively.

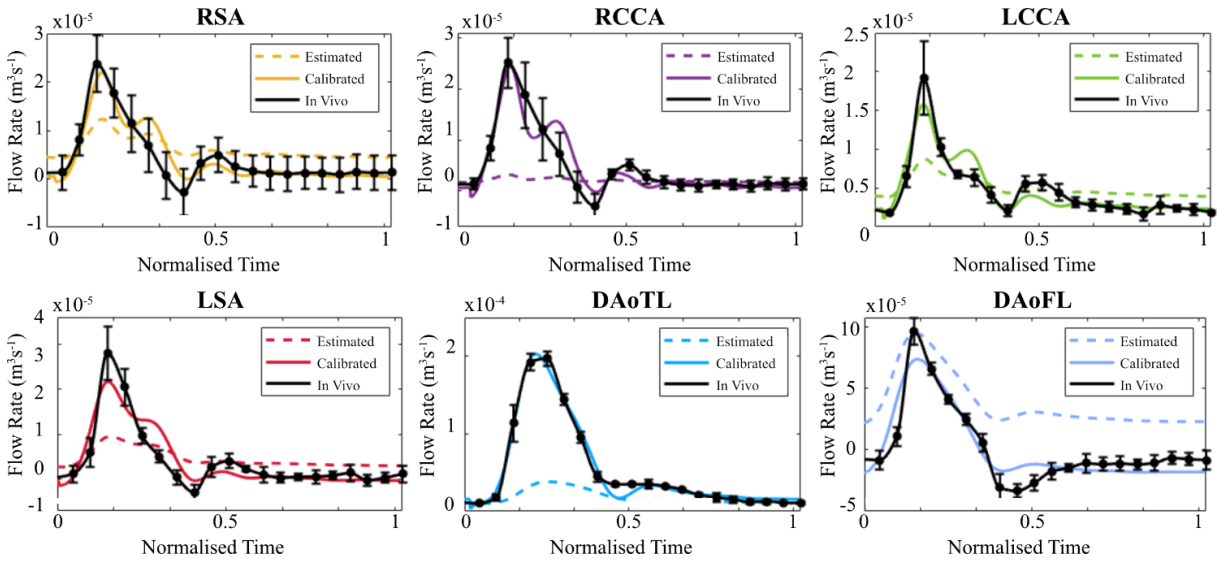

Figure 4.9: Flow waveforms for each branch of the thoracic aorta for the patient with an AD as calculated via the 0D 3EWM before (dashed colored lines) and after (solid colored lines) calibration of Z, R, and C. The in vivo 4D Flow-MRI derived waveforms are shown in black (mean ± standard deviation).

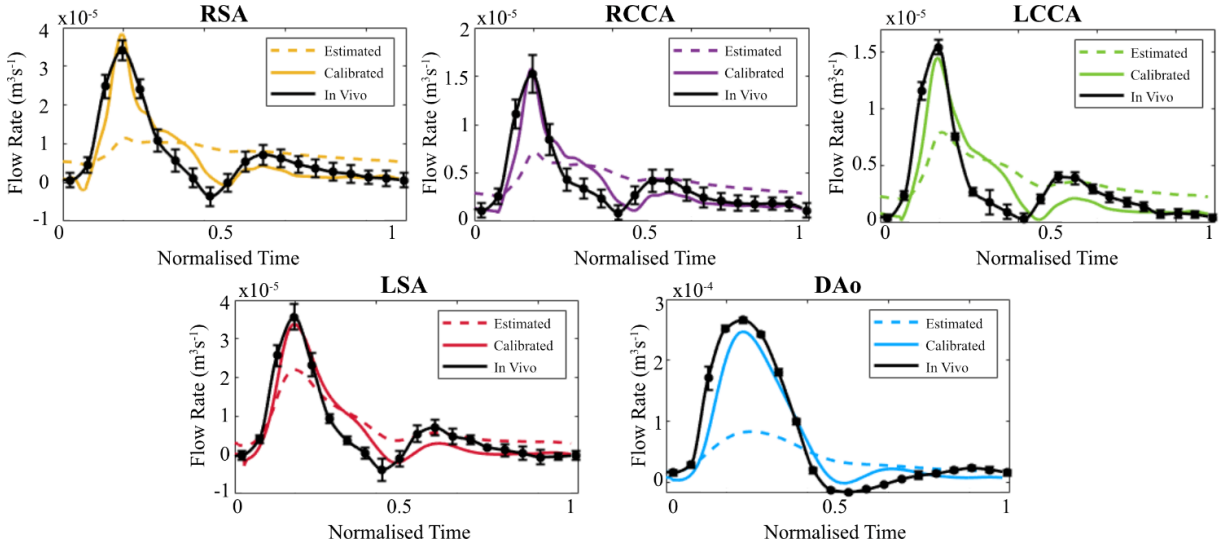

Figure 4.10: Flow waveforms for each branch of the thoracic aorta for the healthy volunteer as calculated via the 0D 3EWM before (dashed colored lines) and after (solid colored lines) calibration of Z, R, and C. The in vivo 4D Flow-MRI derived waveforms are shown in black (mean ± standard deviation).

4.3.2 0D-3D CFD Model

4.3.2.1 Perfusion Distribution

BC calibration substantially improved the net perfusion distribution (Figure 4.11) throughout the aorta in both the healthy and dissected cases. This was particularly evident in the dissection model, where calibration of the 3EWM parameters reduced the error in the TL from 47.0% to 2.5%, and in the FL from 50.8% to 2.87% with respect to the *in vivo* data. At the other branches,

and in the healthy model, the error reductions were less dramatic, though still presented an improvement. The exception to this was the LCCA branch of the healthy model, where calibration increased the error with respect to *in vivo* data.

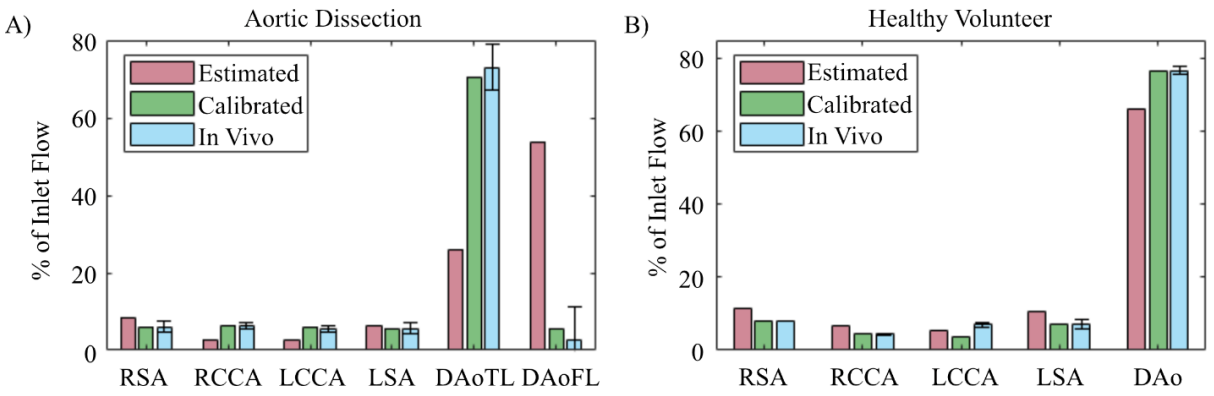

Figure 4.11: Blood flow perfusion distribution throughout the 0D–3D CFD model of the (A) aortic dissection and (B) healthy volunteer, before (red) and after (green) BC calibration, in comparison with (blue) in vivo 4D Flow-MRI obtained data. Error bars represent mean ± standard deviation.

4.3.2.2 Arterial Pressure

The choice of BCs impacted the pressure at each branch of the 0D-3D CFD models (Table 4.4). Generally, calibration of the 3EWM parameters tended to dampen the pulse pressure as a result of an increased diastolic pressure and decreased systolic pressure when compared to the estimated parameters.

Table 4.4: Systolic pressure, diastolic pressure, pulse pressure, and mean arterial pressure obtained from 0D-3D CFD models of the aortic dissection and healthy volunteer. For each variable, mean ± standard deviation was calculated by averaging across the supra-aortic branches and descending aorta. Reference values for the healthy volunteer were obtained from literature [15].

	Estimated BCs	**Calibrated BCs**	**In Vivo Clinical Data**
Dissection			
Systolic Pressure (mmHg)	189 ± 2.66	167 ± 10.5	189
Diastolic Pressure (mmHg)	103 ± 0.05	117 ± 0.59	101
Pulse Pressure (mmHg)	86.0 ± 2.66	50.0 ± 10.5	88
Mean Arterial Pressure (mmHg)	130 ± 0.93	130 ± 4.26	130

Healthy Volunteer	**Estimated BCs**	**Calibrated BCs**	**Literature**
Systolic Pressure (mmHg)	151 ± 4.85	125 ± 5.30	120
Diastolic Pressure (mmHg)	47.6 ± 0.81	51.5 ± 0.78	80
Pulse Pressure (mmHg)	103 ± 4.91	80 ± 5.36	40
Mean Arterial Pressure (mmHg)	82.1 ± 1.88	76.0 ± 1.75	93.3

4.3.2.3 TAWSS, OSI, and Pressure Distribution

Near-wall hemodynamics are affected both by the arterial geometry and applied boundary conditions [29] [243]. Notably, the effect of smoothing the reconstructed geometries as outlined in the methodology will not significantly influence these results [244]. Figure 4.12 illustrates the distribution of TAWSS, OSI, and pressure distribution in the AD case before and after BC calibration. In both the estimated and calibrated models, regions of elevated TAWSS were identified immediately distal to each supra-aortic branch ostia. With the estimated 3EWM BCs, other elevated regions of TAWSS were localized to the primary tear and the distal region of the aortic arch within the proximity of the secondary tear.

Further, TAWSS was minimal in both the TL and FL with the estimated BCs (Figure 4.12 A&B), and there was negligible difference in the magnitude of TAWSS between these lumens. After BC calibration, TAWSS was reduced in the bulbous FL of the aortic arch by up to 2.04Pa and was increased at the TL region immediately distal to the descending secondary tear by up to 14.4 Pa (Figure 4.12C). Additionally, calibration increased the TAWSS throughout the supra-aortic branch vessels. Finally, calculation of a surface integral at each tear region revealed that BC calibration can alter TAWSS by 14.5% at the primary tear to 46.6% at the distal secondary descending tear.

Regarding OSI, the spatial distribution throughout the ascending aorta and supra-aortic branches remained generally unchanged after BC calibration, though there was a general increase in magnitude. There was, however, a marked qualitative and quantitative difference in the OSI in the descending TL and FL between the estimated and calibrated models, most notably in the distal region. After calibration, OSI within the TL was reduced by up to 0.49, and OSI within the FL was increased by up to 0.43 (Figure 4.12C). Considering OSI is a non-dimensional quantity bounded between 0-0.5, these are substantial changes. Finally, BC calibration had a marked effect on the average pressure distribution, reducing pressure by as much as 16mmHg. This BC calibration also resulted in a more uniform distribution of pressure throughout the supra-aortic branch vessels.

Regarding the healthy volunteer, TAWSS was substantially reduced in the LSA following BC calibration, by up to 5.05 Pa (Figure 4.13C). To a lesser degree, a subsequent increase was apparent around the base of the brachiocephalic and RSA arteries. Throughout the main body of the aorta however, there were minimal differences in TAWSS between the estimated and calibrated models.

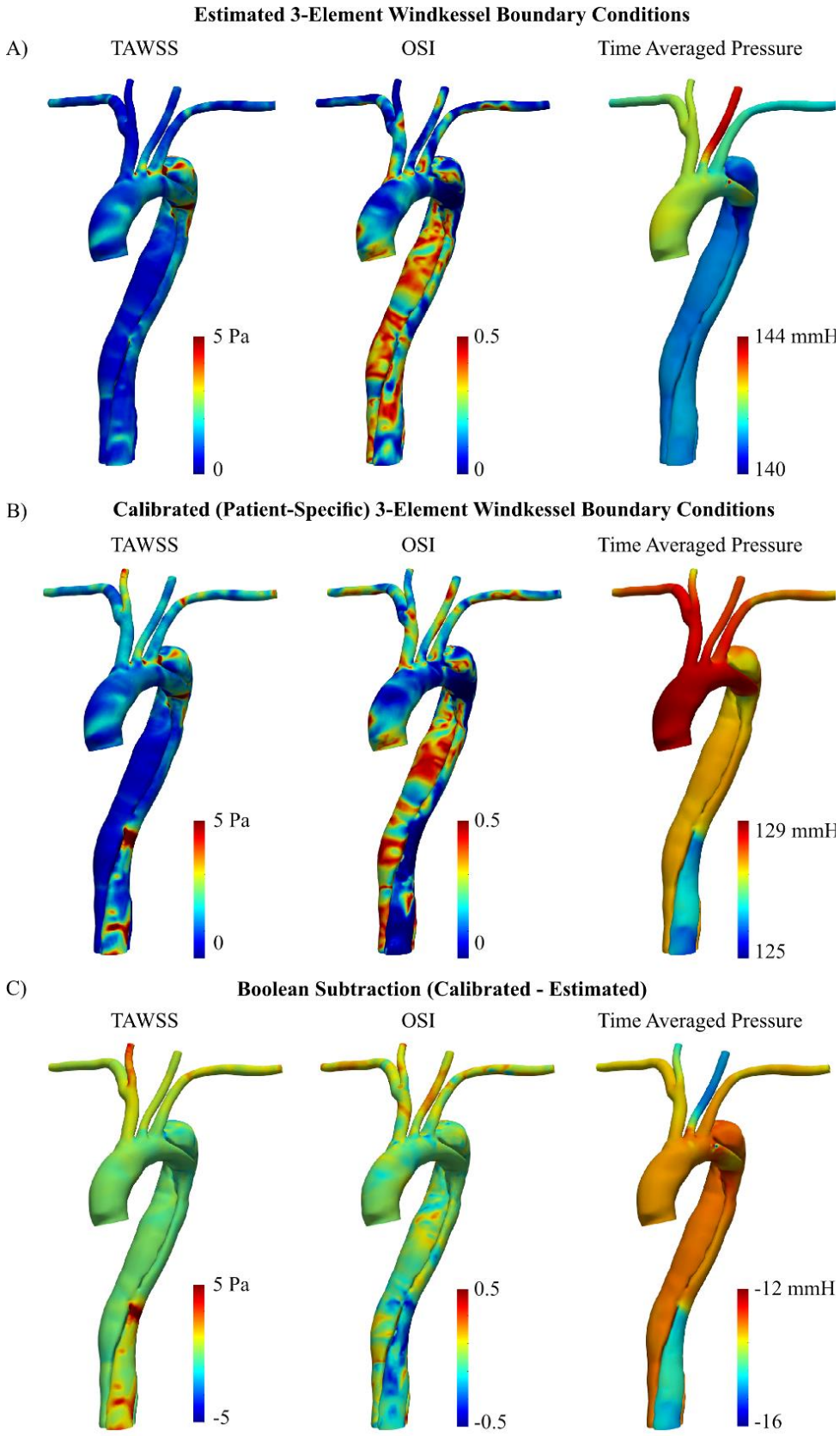

Figure 4.12: TAWSS, OSI, and time averaged pressure of dissected aorta, obtained via 0D–3D CFD simulation using (A) estimated, and (B) calibrated 3EWM BCs. (C) Boolean difference ($Distribution_{Calibrated} - Distribution_{Estimated}$*) throughout the models.*

BC calibration maintained the spatial pattern of OSI throughout the entire aorta, primarily altering the magnitude (Figure 4.13 A&B). Notably, the calibrated model showed regions of elevated OSI throughout the supra-aortic branches and in the region immediately proximal to the brachiocephalic artery when compared to the estimated case (Figure 4.13C). Conversely, throughout the descending aorta, BC calibration had a reduced effect, altering OSI by ~0.2 (Figure 4.13C). Time-averaged pressure was reduced by 15.3mmHg to 16.4mmHg following BC calibration. This was expected due to the well-known phenomena of pulse pressure amplification, where arterial stiffness and therefore systolic blood pressure increases from the central aorta towards the peripheral brachial artery [245] [246]. Since pressure was calculated from brachial cuff measurements at the periphery, one would therefore expect the central aortic pressure to be lower, which BC calibration has yielded.

4.3.2.4 CFD vs 4D Flow-MRI Blood Velocity

The calibrated 0D-3D CFD model of the type B aortic dissection qualitatively captured the complex flow regime within the TL and FL of the thoracic aorta when compared against *in vivo* data (Figure 4.14**).** For example, the CFD model successfully depicted the region of flow recirculation within the false lumen of the aortic arch between the primary and secondary tear. Additionally, the model captured regions of high flow at the primary tear, the superior boundary of the FL, and through the TL at the distal section of the aortic arch. Quantitatively, CFD analysis resulted in overestimation of blood velocity during the systolic cardiac phases, and a subsequent underestimation (increased flow reversal) during the diastolic phases. Therefore, while the net flow through each branch was successfully calculated, there are discrepancies in the instantaneous velocity magnitude between the CFD models and *in vivo* data. This was most apparent during peak systole and systolic deceleration.

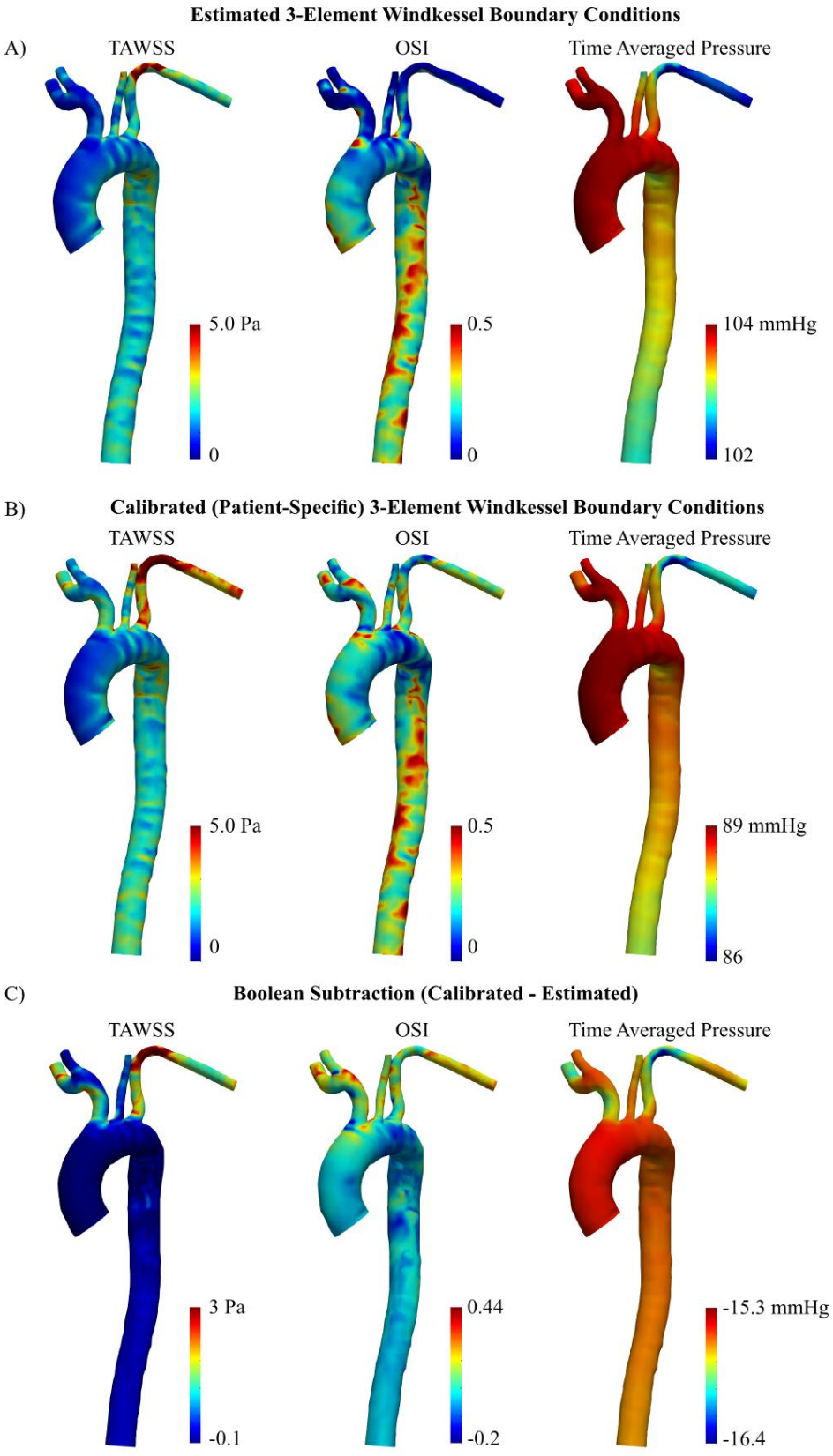

Figure 4.13: TAWSS, OSI, and time averaged pressure of healthy aorta, obtained via 0D-3D CFD simulation using (A) estimated, and (B) calibrated 3EWM BCs. (C) Boolean difference ($Distribution_{Calibrated} - Distribution_{Estimated}$) *throughout the models.*

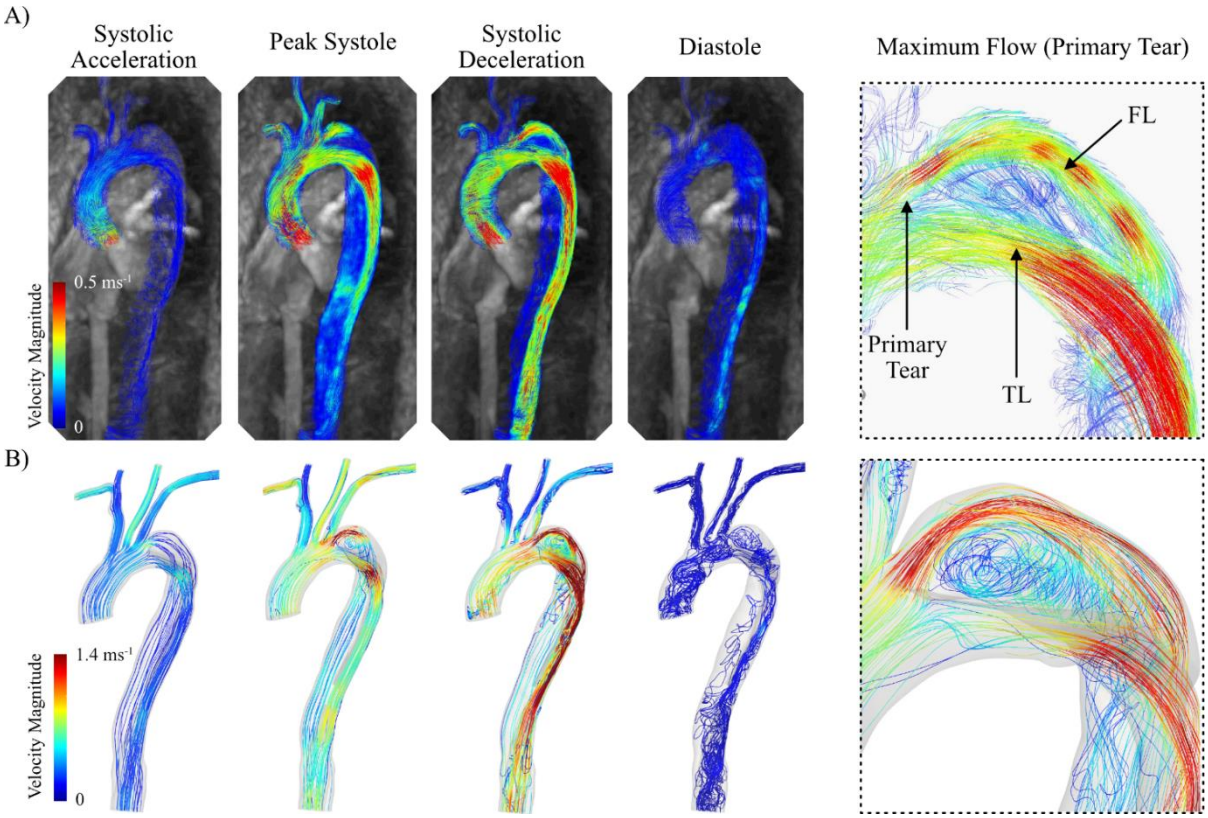

Figure 4.14: Instantaneous blood velocity magnitude streamlines of the type B thoracic aortic dissection obtained from (A) 4D Flow-MRI and (B) CFD modelling at systolic acceleration, peak systole, systolic deceleration, and diastole. Also visible is the maximum velocity within the FL immediately distal to the primary tear, as extracted from both CFD and 4D Flow-MRI.

4.4 Discussion

Patient-specific branch flow rates are not often prescribed as BCs in CFD models. This is because the prescription of such profiles can lead to inaccurate pressure calculations and tend to overprescribe the model for any future parametric analysis [230]. Thus, the 3EWM model is ubiquitously used instead for the prescription of physiologically relevant BCs [46] [56]. This study outlines a methodology to calibrate these 3EWM models to generate patient-specific BCs and proof-of-concept examples illustrate that the resultant CFD models have the capability to elucidate patient-specific hemodynamics which are consistent with previous literature and clinical measurements. It is possible that, in the future, CFD models calibrated from 4D Flow-MRI blood flow data may be utilized to derive hemodynamic parameters which cannot otherwise be extracted from *in vivo* data and hence may contribute to clinical decision making. For example, such models may highlight a potentially high-risk rupture site of the false lumen.

4.4.1 4D Flow-MRI Processing

Literature shows that 4D Flow-MRI quantification of non-laminar blood flow shows good correlation against the reference gold standard (2D phase contrast MRI) [97] [247]. Thus, calibration of the 3EWM BCs against the 4D Flow-MRI derived flow rates was deemed appropriate. PWV is a well-established measurement which is positively associated with aortic stiffness and is readily obtained from 4D Flow-MRI [226] [248]. Conventionally, MRI-derived PWV is limited to 2-4 pre-defined planes of analysis [249] [250]. Since 4D Flow-MRI was utilized in this study, it was simple to retrospectively place 12 analysis planes throughout the entire length of the thoracic aorta, thereby improving the reliability of the measurement [100] [227]. The healthy volunteer exhibited a PWV of 7.85ms^{-1}, further demonstrating the validity of this approach as literature suggests the median PWV of a large cohort of healthy individuals (n=3071) is 7.2 ms^{-1} [228].

4.4.2 BC Calibration

Literature suggests that 1D models are sufficiently accurate to be used during the calibration of outlet BC parameters [238]. The combination of 0D and 1D models utilized in this study facilitated rapid, computationally efficient parameter calibration. To determine the most effective calibration algorithm on Matlab®, multiple different multivariate solvers (*fminsearch*, *fmincon*, *fminunc*) were tested. It was confirmed that *fminsearch* consistently minimised the error between the computed and *in vivo* flow rate to the greatest degree. To further demonstrate the reliability of this method, the initial parameter input estimates were manually and individually perturbed by a factor of 0.125, 0.25, 0.5, 2, 4, and 8 to determine the sensitivity of the model to local variations. Even with these perturbations, the solution converged on the same parameter combination each time. The effectiveness of this approach is evident from the reduction in cumulative LSD error between the computed and *in vivo* flow rates by 74.4-98.2% and 56.2-88.8% in the dissected and healthy case, respectively. Notably, the calibration process also satisfied the requirement of R>>Z in all branches, where the characteristic impedance in mammals is generally 5-7% of the peripheral resistance [33] [229].

Small discrepancies remained between the computed and *in vivo* waveforms after calibration. It is possible that this was partly a result of a non-patient-specific pressure waveform generated by the 0D-1D models since the calibration process was sensitive to changes in the initial pressure waveform. It was not possible to validate these waveforms in the absence of time-resolved clinical pressure data. Discrepancies between the *in vivo* and calibrated computed flow waveforms may also be explained as follows. Firstly, it may not be possible to exactly fit

a relatively simple function like Eq 4.8 to the complex *in vivo* flow waveforms. Secondly, it is possible that the algorithm to minimize the error function during calibration may fall within a local minimum as opposed to the global minimum, meaning the solution may not be unique [36]. However, the 3EWM parameter combination which produces a global minimum may include values so different from the initial estimates that they are not physiologically relevant (i.e. negative values, impedance greater than resistance, extremely high or low value for one or more parameter). To summarize, it is possible to settle on a set of parameters which produce a mathematical match of flow rate to reduce ε_j without the parameters being physiologically relevant [36]. We combat this by providing good estimates (Eq 4.3-5) and then performing checks (Eq 4.6-7), and ensure R>>Z, all of which confirm the parameters fall within a physiologically relevant range.

Finally, it is understood that 4D Flow-MRI is subject to intrinsic errors, meaning the *in vivo* flow rate which acts as the ground truth in this study, contains a degree of uncertainty. It would be possible to reduce these uncertainties if invasive flow and pressure probes were used, but this would increase the burden on the patient. Therefore, the 4D Flow-MRI related errors were deemed an acceptable limitation due to its non-invasive nature of measuring flow rate.

4.4.3 0D-3D CFD Model

The combination of 4D Flow-MRI and coupled 0D-3D CFD models produced a comprehensive picture of the complex flow regime and near-wall hemodynamics in both the healthy and dissected aortae.

4.4.3.1 Perfusion Distribution

The impact of BC calibration was more significant in the dissected model when compared to the healthy case, indicating that the initial geometry-based estimates failed to predict the complex and highly individualized flow regime as a result of aortic pathology such as AD [49] [47]. This is because the severity, location, number of intraluminal tears, and overall geometry of the pathology varies significantly on a case-by-case basis. For example, the estimated BCs demonstrated a tendency to overestimate flow at the outlet of the FL due to the increased vessel diameter and the expectation of decreased hydraulic resistance. As a result of continuity, this caused a subsequent underestimation of flow within the TL. The BC calibration process, however, rectified this issue to generate a more physiologically accurate perfusion distribution which is comparable to the *in vivo* data and previous studies [4]. This improvement is important since blood flow rate and flow regime are key factors which influence the expansion of the FL,

the successive collapse of the TL, and degree of peripheral organ malperfusion in AD [4] [5] [59]. Further, the calibrated models yield increased flow through the supra-aortic branch vessels, which was also observed in the 4D Flow-MRI data. This observation is both clinically relevant and expected, as patients with AD often experience this increase in flow due to an elevated hydraulic resistance in the descending aorta [231]. The effect of BC optimization was less pronounced in the healthy case, though an improvement in the perfusion distribution was still notable, especially through the descending aorta.

4.4.3.2 TAWSS and OSI

Accurate portrayal of near-wall hemodynamics is fundamental as the 3EWM parameters play a crucial role in the regulation of the arterial structure, and the initiation and progression of disease [28] [251]. For example, initiation of the primary tear of an AD often occurs immediately distal to the LSA due to flow disturbance within this region [9]. Notably, this is where the primary tear is located for the AD patient in this study.

In both aortae, the TAWSS exhibited a heterogeneous spatial distribution, as expected [9]. In the healthy case, there were localized, elevated regions of TAWSS (~5 Pa) immediately distal to the supra-aortic branch ostia, which is spatially consistent with previous studies [9] [130]. As there was no pathology in the geometry of the healthy individual, the estimated BC models were well equipped to predict the spatial distribution of TAWSS and OSI. Thus, calibration in the healthy case served mainly to alter the magnitude of near-wall hemodynamics.

In the case of the AD, calibration exhibited a more marked effect on both the magnitude and spatial pattern of these parameters. In the calibrated model, TAWSS in the TL was increased due to increased flow in the relatively narrow lumen, which is consistent with literature [4] [69]. Further, the TL also experienced a reduction in OSI which is indicative of an increased degree of unidirectional flow, as expected [192]. Conversely, OSI was increased in the FL, indicative of a more chaotic flow regime. Analysis of the 4D Flow-MRI images confirmed that both of these findings are consistent with the *in vivo* data as the regurgitation fraction was low in the TL and high in the FL. These findings are also consistent with previous studies [73] [59]. Further, regions of considerably elevated TAWSS following BC calibration were observed at each intraluminal tear, and were a result of jet flow through the narrow opening [69] [59]. Notably, the estimated model failed to capture this in the region of the secondary tear in the descending aorta but was rectified following BC calibration. These findings indicate the importance of BC calibration to generate patient-specific CFD models and clinically relevant

results. This is particularly important in cases of AD, where the flow regime is highly dependent on the dissection location and severity [4] [78] [252].

It was not possible to derive WSS directly from 4D Flow-MRI due to software limitations, meaning the CFD-derived WSS distributions could not be validated clinically. However, it is important to note that literature suggests WSS derived from 4D Flow-MRI studies is underestimated compared to other method, due to the low temporal and spatial resolution compared to CFD [9]. Therefore, a comparison may not have been possible regardless.

4.4.3.3 Pressure

In the presence of an AD with small secondary tears, one would expect a large pressure difference between the TL and FL, with higher pressures in the former [78] [57]. However, the AD presented in this study has two large tears, one being the primary tear at the LSA (17mm) and the other being the secondary tear in the distal descending aorta (19mm) [57] [253]. In the presence of such large tears, there is a tendency for pressure within the TL and FL to equalize, which was demonstrated throughout the proximal aorta in this study [57]. A further reduction of velocity within the FL and increase in regurgitation then occurs distal to the descending secondary tear. This results in a higher pressure in the FL compared to the TL in the distal aorta which is consistent with previous literature [4] [73] [59]. Capturing this pressure gradient is essential as it can influence expansion of the FL and compression of the TL, resulting in a potential hypertensive crisis or at worst, fatal rupture of the aortic wall [59] [252]. This was only captured after BC calibration.

In the AD case, the estimated BCs more accurately capture the magnitude of systolic and diastolic blood pressure as obtained from a brachial cuff measurement. However, they induce an almost identical systolic and diastolic pressure at all branch outlets, which contradicts previous literature [69] [78] [252]. Conversely, prescription of the calibrated BCs dampens the pulse pressure (~41mmHg) and reduces systolic blood pressure, thereby creating a discrepancy between the computed and clinical data. This can be explained due to the well-known phenomena of pulse pressure amplification, where arterial stiffness and therefore systolic blood pressure increases from the central aorta towards the peripheral brachial artery [245] [246]. Literature suggests that in the age range of 50-60 years old, the central aortic pressure should be 9±6mmHg lower than the observed brachial pressure. In this study, the decrease in central systolic blood pressure and pulse pressure after BC calibration, when compared to the brachial cuff measurement, accounts for this phenomenon and therefore yields a more physiologically

relevant magnitude. After BC calibration, diastolic pressure also increased, though literature suggests it should remain relatively constant with regards to the brachial measurement [254]. Future studies will include the 1D model within the calibration process and compliant walls within the CFD model to investigate the effect of these added components in the calculation of the final diastolic pressure.

In the healthy case, prescription of these estimated BCs significantly overestimates systolic blood pressure by ~31mmHg, and underestimates diastolic pressure by ~32mmHg. After calibration, these errors are reduced to ~5mmHg and ~29mmHg, respectively. Notably, these are still significant discrepancies. Without modelling aortic wall compliance in the 3D domain however, it is not possible to determine the exact consequence of BC calibration [4] [78].

4.4.3.4 CFD vs 4D Flow-MRI Blood Velocity

While the CFD models accurately captured the net flow throughout the aorta in the healthy and dissected cases, the BC calibration methodology resulted in discrepancies in instantaneous velocity magnitude. This was due in part to the calibration methodology, and in part due to the fundamental differences between the *in vivo* data and CFD models. The calibration process was performed using a combination of 1D and, primarily, 0D modelling and optimization. The reason for this was to avoid the prohibitive computational cost associated with 3D modelling, as an extensive number of iterations were required. Consequently, the 3EWM parameters which were calibrated within these lower order models produced slightly different results when coupled to the 3D CFD model. Future work will aim to improve the calibration process to capture the instantaneous velocity magnitude of blood more accurately by integrating the Nektar1D solver into the calibration process to include the effects of the 1D spatial domain, wave reflections, and vessel wall compliance.

Due to the inherent differences between CFD modelling and 4D Flow-MRI, discrepancies in blood velocity are unavoidable [89] [99] [213]. There are several reasons for this. Firstly, the rigid wall CFD models did not account for arterial compliance, meaning the cross-sectional area of the lumen could not expand to accommodate the increased flow during systole (to reduce blood velocity) or contract during diastole (to increase blood velocity). In contrast, the 4D Flow-MRI derived velocities account for this compliance. Further, the CFD spatiotemporal resolution is very high compared to the relatively coarse spatial and temporal resolution of 4D Flow-MRI, which is known to result in blood velocity differences, primarily in regions of elevated flow [99] [213]. Further, the 4D scan sequence utilized to obtain the retrospective data

employed a spatial resolution of 3.6 x 2.4 x 2.6 mm which is coarser than the minimum resolution suggested in literature (1.5mm x 1.5mm x 1.5mm), resulting in increased data interpolation to calculate *in vivo* blood velocity [213]. Additionally, the scan sequence employed an anisotropic spatial resolution, indicating that the final *in vivo* results are directionally dependent unlike the CFD models [213].

4.5 Limitations and Future Work

It is acknowledged here that there are some limitations in this study. Only one healthy and one AD case is considered, which were intended as proof-of-concept examples and not as a clinical study. Through these cases it is demonstrated how the novel methodology contributes towards the development of patient-specific BCs for arterial CFD models. In the future, this methodology will be implemented on a larger cohort to evaluate the distribution of hemodynamics on healthy and diseased patients.

The 0D-1D model used to generate the initial pressure waveform could not capture the complex secondary flows, regurgitation, and regions of recirculation which are present around the intraluminal tears [29] [238]. In the dissected case, these uncertainties were likely magnified around the intraluminal tears.

After the initial pressure and flow waveforms were estimated with 0D-1D modelling, the iterative BC calibration was performed using only a 0D solver. Future work will integrate the 0D-1D model with the Nelder Mead (*fminsearch*) algorithm to ensure wave reflections and spatial variation in the arterial geometry are accounted for during calibration. Additionally, viscoelastic wall properties will be utilized in place of the elastic wall assumption to generate more physiologically accurate pressure waveforms. Further, the spatial and temporal resolution of the retrospective 4D Flow-MRI data was limited, likely introducing an intrinsic error in the BC calibration process. Future work will require a prospective 4D Flow-MRI scan with improved spatiotemporal resolution and a multi-VENC sequence to capture blood flow more readily within the supra-aortic branches and FL. Also, a drawback to in vivo blood flow measurements is that these flow measurements are approximations based on the results of phantom studies, meaning the overall error is difficult to estimate from phase contrast techniques [255].

To reduce computational demand, a rigid wall assumption was utilized for the 0D-3D CFD models. However, it is known the aorta distends to accommodate increases in blood volume throughout the cardiac cycle [29]. In cases of AD, this wall motion becomes more important

[78]. Future work will therefore include fluid structure interaction (FSI) to replicate vessel wall compliance. Additionally, the simulations performed in this study were restricted to one node on the high-performance computing cluster, resulting in relatively long simulation times. Future work will expand upon these proof-of-concept results to generate high-fidelity CFD models which shall be simulated across multiple parallel nodes.

Spatially, a uniform inlet profile was prescribed in the absence of decomposed x, y, and z velocity magnitudes from the *in vivo* data. Though literature suggests an idealized paraboloid is sufficient in the absence of such data, it still fails to capture the effect of the aortic valve on blood flow through the aortic root. Where applicable, future studies will extract the 3D spatial inlet profile from PC-MRI to overcome this issue.

In all models, blood was assumed to be a Newtonian fluid. Literature suggests Newtonian fluids yield increased peak fluid velocity magnitude, along with a decreased wall shear stress and pressure drop in comparison to non-Newtonian numerical models [256]. In AD cases, in particular, blood viscosity is of particular importance in the low-flow regions of the proximal and distal FL [60]. Here, blood viscosity plays a greater role than in other aortic diseases [60]. In future work, a shear-thinning Newtonian model for blood viscosity should be utilised.

4.6 Conclusion

To create high-fidelity arterial CFD models, it is essential to prescribe accurate BCs. This Chapter outlines a novel approach for the calibration of patient-specific, physiologically relevant 3EWM BCs based on *in vivo* flow waveforms obtained from retrospective 4D Flow-MRI. Based exclusively on non-invasive measurements, the arterial impedance, resistance, and compliance parameters were rapidly calibrated in a computationally efficient, reduced order framework. This calibration was particularly important in cases of AD to elucidate the intricate crossflow between the TL and FL and capture flow phenomena in the highly individualized morphological features of the pathology. Following parameter calibration, blood flow was modelled in a coupled 0D-3D numerical framework, yielding physiologically relevant haemodynamics in proof-of-concept examples. These CFD models exhibited a perfusion distribution which closely matches the clinical data, and offer promising preliminary results regarding OSI, TAWSS, and pressure distribution. By enhancing the information obtained from 4D Flow-MRI, this combination of CFD and medical imaging yields useful insights towards a comprehensive understanding of patient-specific aortic haemodynamics.

4.7 Research Contribution

In Chapter 4, we utilised quantitative *in vivo* flow data from 4D Flow-MRI imaging to calibrate patient-specific Windkessel models for use as 0D BCs. This involved a combination of 0D and 1D modelling to calibrate these parameters within a reduced order framework for enhanced computational efficiency. These Windkessel boundary conditions were then applied to CFD models in a coupled 0D-3D numerical framework to investigate the resultant perfusion distribution, flow regime, and near wall haemodynamics before and after calibration. The primary contributions from this Chapter were:

1) A novel methodology was presented to calibrate patient-specific Windkessel parameters including impedance, compliance, and net peripheral resistance from *in-vivo* branch flow rates obtained from 4D Flow-MRI data.
2) The calibrated Windkessel BCs resulted in a net perfusion distribution through the outlets of the CFD models which matched the *in-vivo* flow data. This investigation was conducted within the thoracic aorta of one healthy and one TBAD case as a proof-of-concept study.
3) Flow-based BC calibration was particularly necessary in the TBAD case to capture the pathological division of flow between the TL and FL, with BC calibration yielding more accurate results in relation to the *in vivo* data. Consequently, this suggests that BCs of TBAD cases cannot be estimated exclusively based on vessel geometry and geometric laws. Instead, they must be calibrated based on branch flow waveforms as presented in this study. In the healthy thoracic aorta, BC calibration resulted in a more accurate perfusion distribution with respect to the *in vivo* data, though the differences were less substantial.
4) Finally, BC calibration substantially affected the magnitude and spatial distribution of TAWSS and OSI within the true and false lumen of the AD. The calibrated BCs, based on our proposed methodology, also yield a more physiologically accurate representation of near wall haemodynamics.

5 Chapter 5: An Investigation of Type B Aortic Dissection Haemodynamics in Patient-Specific Models for Surgical Planning and Outcome Assessment

Throughout Chapter 3 and Chapter 4, a novel methodology was described to reconstruct anatomically accurate arterial geometries and calibrate 3EWM BC's from 4D Flow-MRI data to create patient-specific CFD models. In Chapter 5, we utilise these methodologies to investigate in-depth the haemodynamics throughout the full thoracoabdominal aorta of four TBAD patients and three healthy volunteers as case studies.

5.1 Introduction

Macroscopic visualisation and quantification of flow within the aorta is one of the most well-studied areas within 4D Flow-MRI [88]. Applications include the identification of patients at risk of forming aneurysms and dissections, and investigation of the flow regime in patients who exhibit aortic pathology [88]. Understanding and predicting the morphological evolution of the TL in a patient with AD is a complex task, and simple metrics such as the degree of aortic dilation cannot capture the entire picture [73]. For example, the number and size of intraluminal tears contribute significantly to the disease prognosis [253]. It is also essential to understand shear-stress-related factors, the interaction of flow between the TL and FL, the flow regime within the FL, intraluminal pressure, and the overall branch perfusion distribution [60] [69] [73] [59] [252]. Thus, the clinical consensus is that imaging alone is not sufficient, since 4D Flow-MRI cannot capture many of these elements as described previously.

Analysis of pre- and post-surgical haemodynamics in patient-specific cases is critical for the perfusion optimisation of vascular grafts used to treat aortic disease conditions. Computational models could be used for treatment planning for surgical intervention. Since abnormal near-wall haemodynamics are involved in the initiation and progression of a TBAD, we can use CFD models to assist in triaging cases for the intervention of chronic TBADs, thus assisting clinical decision-making [28] [252] [257] [258]. When a suitable patient is identified, it would then be possible to virtually insert a stent-graft into the computational model to predict post-surgical haemodynamics and identify regions of concern. This is essential as stent failures generally occur in regions of elevated WSS, while graft migration has been shown to occur due to high perfusion pressure gradients which induce a displacement force on the graft [21] [259] [260]. Further, the geometry of the graft may induce platelet activation through high WSS, or the accumulation of pro-coagulant molecules in regions of stagnation, both of which can result

in thrombosis and graft limb occlusion [18] [27]. After surgery, these CFD models in combination with 4D Flow-MRI could be utilised to analyse the resultant perfusion distribution, turbulence, recirculation, stagnation, endoleaks pressure distributions and localised regions of pathological TAWSS and OSI.

If one could construct patient-specific, pre-surgical CFD models of TBAD's from a single 4D Flow-MRI scan, this could represent an advancement in treatment planning for arterial stent-grafts. This is because these models would be based on non-invasive methods, non-ionizing imaging, and would permit the virtual insertion of stent-grafts. It must be noted, however, that 4D Flow-MRI is not yet a routine modality in global clinical practice. This Chapter seeks to explore several aspects of this statement, with the following aims.

First, we examined whether the segmentation and reconstruction methodology proposed in Chapter 3 could capture the full thoracoabdominal aorta in multiple TBAD patients. Thereafter, we assessed the effectiveness of the 3EWM BC calibration methodology, proposed in Chapter 4 to ascertain whether an accurate perfusion distribution was maintained in significantly more complex cases. This investigation was performed via CFD modelling on the thoracic aorta of three healthy volunteers, and the full thoracoabdominal aorta of three TBAD patients. The investigation also evaluated the inter-patient variability in the branch perfusion distribution, intraluminal pressure distribution, TAWSS, OSI, and the interaction of flow between the TL and FL to supplement the 4D Flow-MRI data. Additionally, the differences in near-wall haemodynamics between healthy volunteers and TBAD patients was studied.

Next, we investigated the difference in pre- and post-operative (stent-graft) haemodynamics within the abdominal aorta of a single patient through CFD modelling. This was to determine the impact of changes in the vessel geometry while BCs remain constant as part of a sensitivity analysis.

Finally, we assessed the impact of different sets of 3EWM BCs on the haemodynamics of a single TBAD patient. This was to highlight the impact of changing 3EWM BCs on a constant, complex vessel geometry.

5.2 Methods

5.2.1 Data Acquisition & Data Demographics

Crucially, all imaging datasets were obtained with the same scan sequences as previously described in Chapter 3. This chapter expands on the foundational work of Chapters 3 and 4

which validated an approach to reconstruct the aorta from 4D Flow-MRI (patients 1-3: iliac bifurcation), and calibrated 3EWM BCs (volunteer 1 & patient 2: thoracic aorta).

In Chapter 5, we incorporated additional healthy volunteers (volunteer 2 & 3). For all healthy volunteers, imaging was restricted to the thoracic aorta. Further, we introduced a new clinical patient (patient 4). For each TBAD patient, the ROI was expended to incorporate the entire thoracoabdominal aorta to permit a more comprehensive analysis. It is important to note that only patient 1 had available imaging data from pre- and post-operative scans. Table 5.1 summarises the data available, and the investigations conducted.

Table 5.1: Computed tomography (CT) and 4D Flow-magnetic resonance imaging (4D Flow-MRI) datasets obtained from a healthy volunteer and three clinical patients. AD = Aortic Dissection.

	Age	**Sex**	**Clinical Pathology**	**MRI/CT**	**Pre-/Post-surgery**	**Region of Interest**	**Investigation**
Volunteer 1	33	M	-	Yes/No	-	Thoracic	Patient-specific CFD model
Volunteer 2	57	M	-	Yes/No	-	Thoracic	Patient-specific CFD model
Volunteer 3	27	M	-	Yes/No	-	Thoracic	Patient-specific CFD model
Patient 1	68	M	Type B AD & Anaconda™ stent-graft	Yes/Yes	Post-abdominal (pre-thoracic)	Thoraco-abdominal	Patient-specific CFD model
Patient 1	68	M	Type B AD & Anaconda™ stent-graft	Yes/Yes	Pre- & Post-	Abdominal	Pre vs postoperative haemodynamics (Same BCs, different geometry)
Patient 2	55	M	Type B AD	Yes/Yes	Pre-	Thoraco-abdominal	Patient-specific CFD model
Patient 3	62	M	Type B AD	Yes/Yes	Pre-	Thoraco-abdominal	Patient-specific CFD model
Patient 4	52	F	Type B AD	No/Yes	Pre-	Thoraco-abdominal	Sensitivity Analysis (Same geometry, different BCs)

5.2.2 Pulse Wave Velocity

Arterial PWV was calculated for the thoracic and abdominal sections of each patient, where applicable. This followed the methodology outlined in Chapter 4 (Figure 4.4), using 12 planes of analysis, equally spaced along the length of the aorta. Table 5.2 lists the calculated values, while Appendix A.1 illustrates the blood flow as a function of time for each plane used to calculate PWV. 4D Flow-MRI imaging was not available for patient 4, meaning PWV was not calculated. Notably, the abdominal aorta demonstrated lower PWV values overall when

compared to the thoracic aorta. This may be attributed to the greater coverage of the dissection throughout the abdominal regions in comparison to the thoracic regions.

Table 5.2: Pulse wave velocities as calculated on cvi42® from 4D Flow-MRI data of healthy volunteers and clinical patients in the thoracic and abdominal regions.

	Thoracic PWV (ms^{-1})	**Abdominal PWV (ms^{-1})**
Volunteer 1	6.42	-
Volunteer 2	9.93	-
Volunteer 3	4.37	-
Patient 1	9.73	3.31
Patient 2	4.38	4.90
Patient 3	8.50	4.20
Patient 4	-	-

5.2.3 Arterial Reconstruction

The aorta of each healthy volunteer (Figure 5.1) was reconstructed from CPC-MRA images following the methodology described in Chapter 3. Again, imaging data was only available for the thoracic aorta of these volunteers.

CPC-MRA images of the thoracic aortae of the healthy volunteers were generated, along with CPC-MRA images of the thoracoabdominal aortae of the TBAD patients. This yielded sufficient contrast to reconstruct the vessel geometries of the healthy volunteers which was essential since healthy individuals should not undergo CT imaging. For the TBAD cases, sufficient intraluminal contrast was generated to reconstruct the TL, but did not permit enough contrast within the FL to permit accurate and reliable reconstruction throughout the entirety of the geometry. For example, Figure 5.2 illustrates the lack of contrast within the FL of patient 1 in the thoracic region in the transverse, axial, and coronal planes. From these images, one would assume there was no FL at this location. However, CT imaging confirmed the presence of a FL. This lack of contrast with the CPC-MRA images for TBAD patients can be explained due to the imaging VENC being too high to capture the low blood velocity within the FL [60] [59]. As these datasets were retrospective, and alteration of the VENC would require prospective planning, it was not possible to change this parameter.

Therefore, the TABD arterial geometries (Figure 5.3) were segmented and reconstructed from CT images. Segmentation and reconstruction of the TL, FL, and intraluminal tears were

performed as per Chapter 4. Notably, Figure 5.3 also highlights the differences between individual TBADs, showing that this is a highly individualised aortic pathology, influenced by the size, number and location of the primary, secondary, and re-entry tears, along with the size and configuration of the TL and FL.

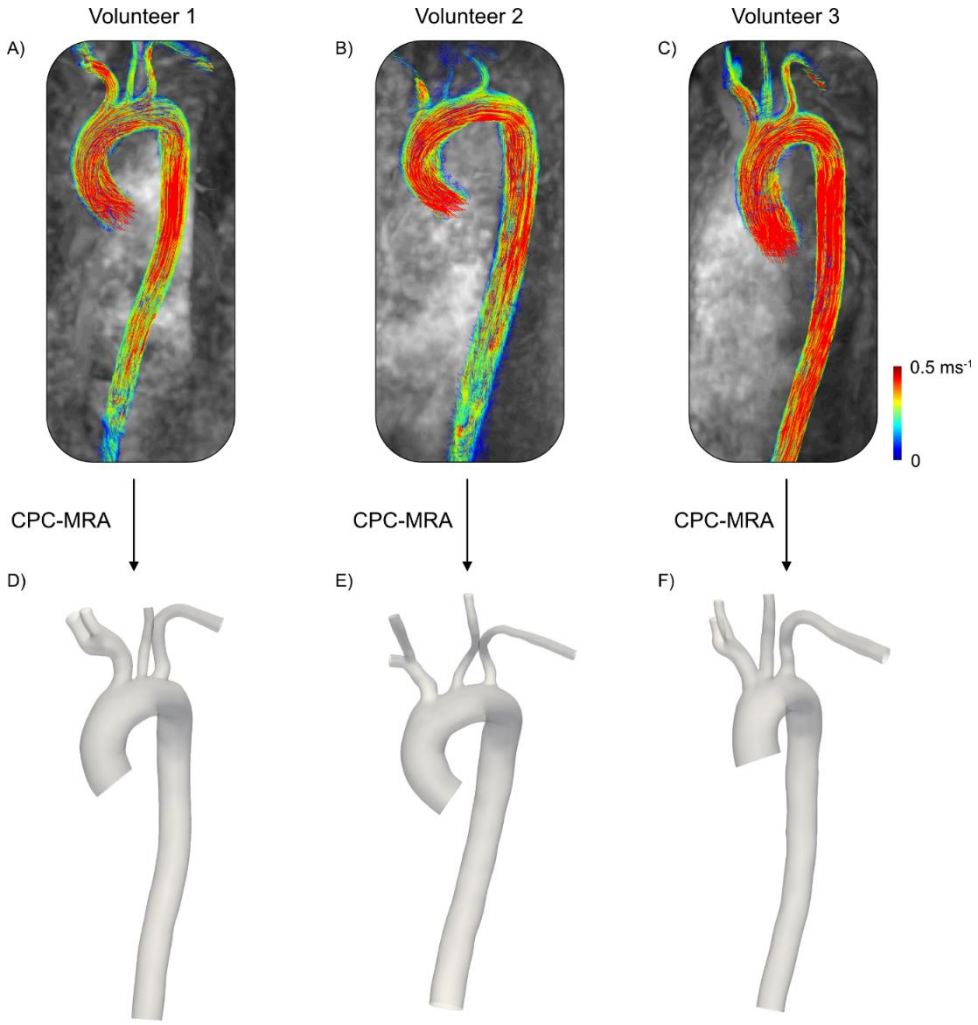

Figure 5.1: A-C) 4D Flow-MRI generated velocity streamlines at peak systole of the healthy volunteers. D-F) Reconstructions of the thoracic aorta of each volunteer based on the CPC-MRA method (Chapter 3).

Patients 1 and 4 exhibit a primary entry tear immediately distal to the LSA and a single, re-entry between the left and right renal arteries. Similarly, Patient 2 presents with a primary tear at the LSA region but displays several secondary tears in the thoracic descending aorta and abdominal aorta, before culminating in a final re-entry tear in the left iliac artery. Patient 3 also has several intraluminal tears, with a primary tear located in the mid-thoracic descending aorta. However, this is relatively uncommon since the typical initiation site for a TBAD is in the arch region, distal to the LSA [9]. For each patient, it is likely that several small intraluminal tears

were present but were not captured due to their size in comparison to the resolution of the 4D Flow-MRI and CT images.

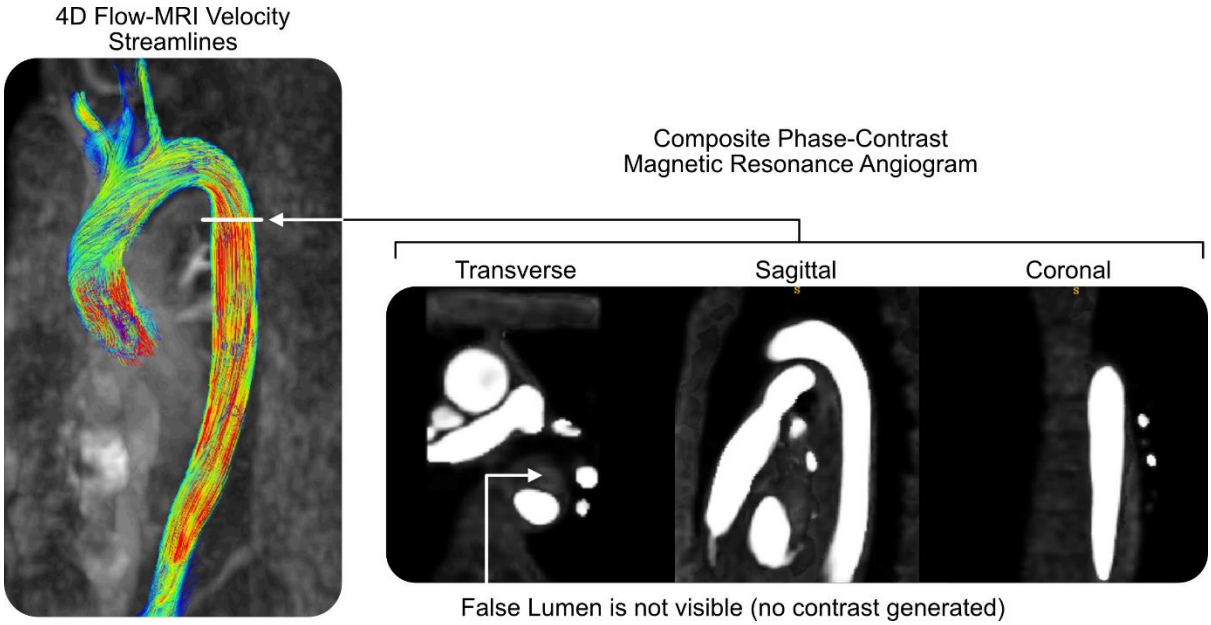

Figure 5.2: A) 4D Flow-MRI streamlines of the thoracic aorta of TBAD patient 1, with flow only visible in the true lumen in the descending aortic region. B) CPC-MRA images which show clear contrast within the TL, but no contrast within the FL.

In AD patients, it is known that the FL can compress the TL due to increasing pressure within the FL [252] [253]. This was apparent, particularly in Figures 5.3B & 5.3C, where the FL was generally more bulbous and exhibited a greater cross-sectional area than the TL. This difference in cross-sectional area was quantified along the length of the aortic segment (Appendix A.2), determining that the TL was on average 2-4 times smaller in area when compared to the FL for patients 2, 3, and 4. For patient 1 however, the TL was 2.4 times larger on average than the FL. This suggests that patient 1 developed the dissection more recently since the FL had not had time to grow due to aneurysmal degeneration of the FL vessel wall [59] [257].

Patient 1's clinical history indicated that the patient initially presented with bilateral common iliac artery aneurysms, which were treated with the deployment of a Gore® Viabahn endovascular stent-graft. However, an extensive TBAD later developed, requiring a revision surgery to replace the Gore® Viabhan stent with an Anaconda™ stent-graft to manage the distal abdominal aorta and iliac arteries. At the time of this study, the patient was still awaiting treatment for the thoracic component of the dissection (geometry as shown in Figure 5.4B).

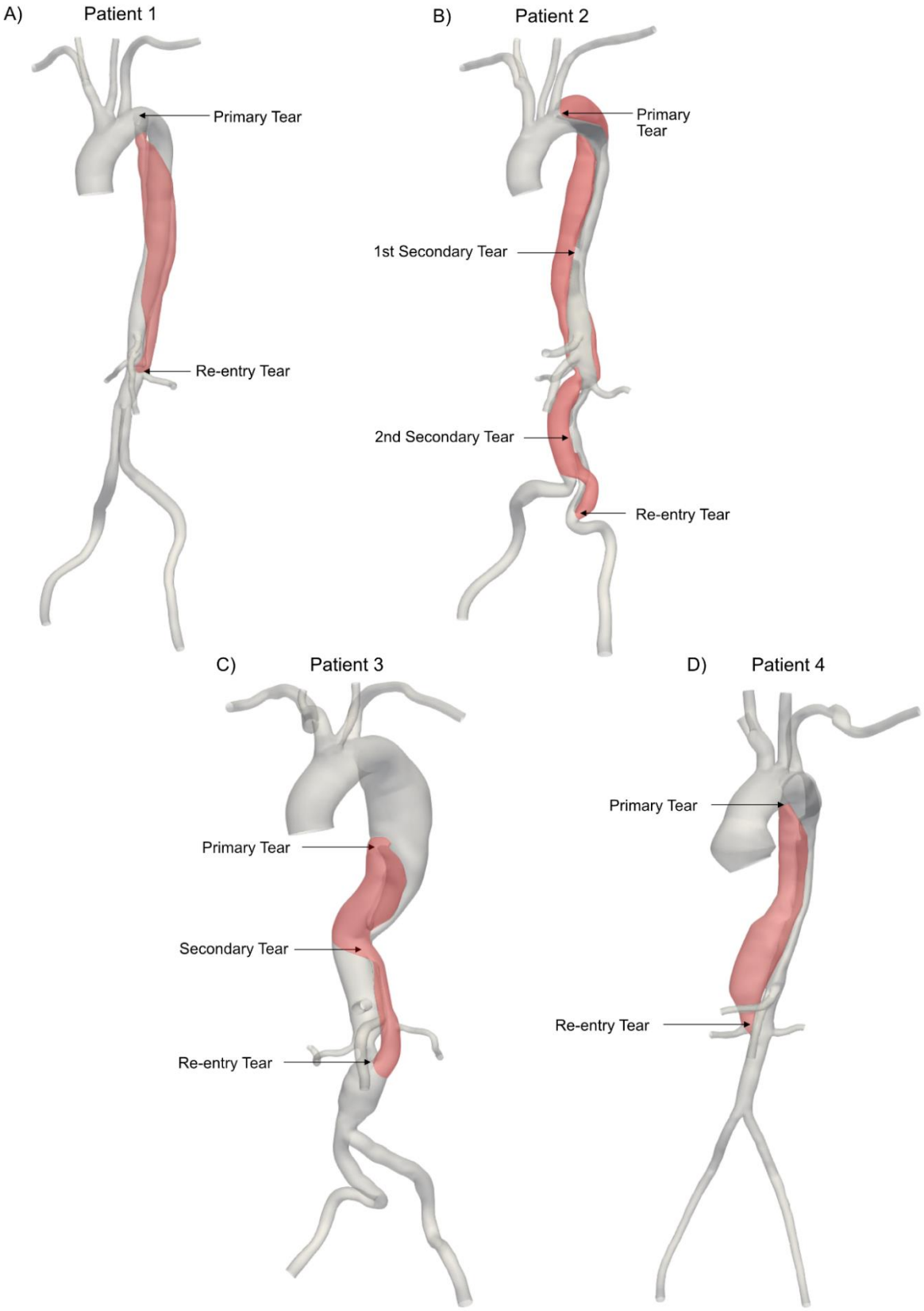

Figure 5.3: CT-based reconstructions of the thoracoabdominal aorta of A) patient 1, B) patient 2, C) patient 3, and D) patient 4, showing the true lumen, false lumen (red), and primary & secondary tears.

Patient 1 had imaging data pre- and post-surgery. This meant that in addition to analysing the haemodynamics of the full thoracoabdominal aorta impacted by the TBAD (Figure 5.3A), it was also possible to conduct a focused investigation on the haemodynamic changes at the iliac bifurcation before and after initial intervention. Figure 5.4A shows the presence of common iliac artery aneurysms (pre-surgery), and Figure 5.4B shows the abdominal aorta following intervention with the Anaconda™ graft. This gave a small insight into the use of 0D-3D modelling to evaluate pre- and post-surgical haemodynamics for stent-graft deployment.

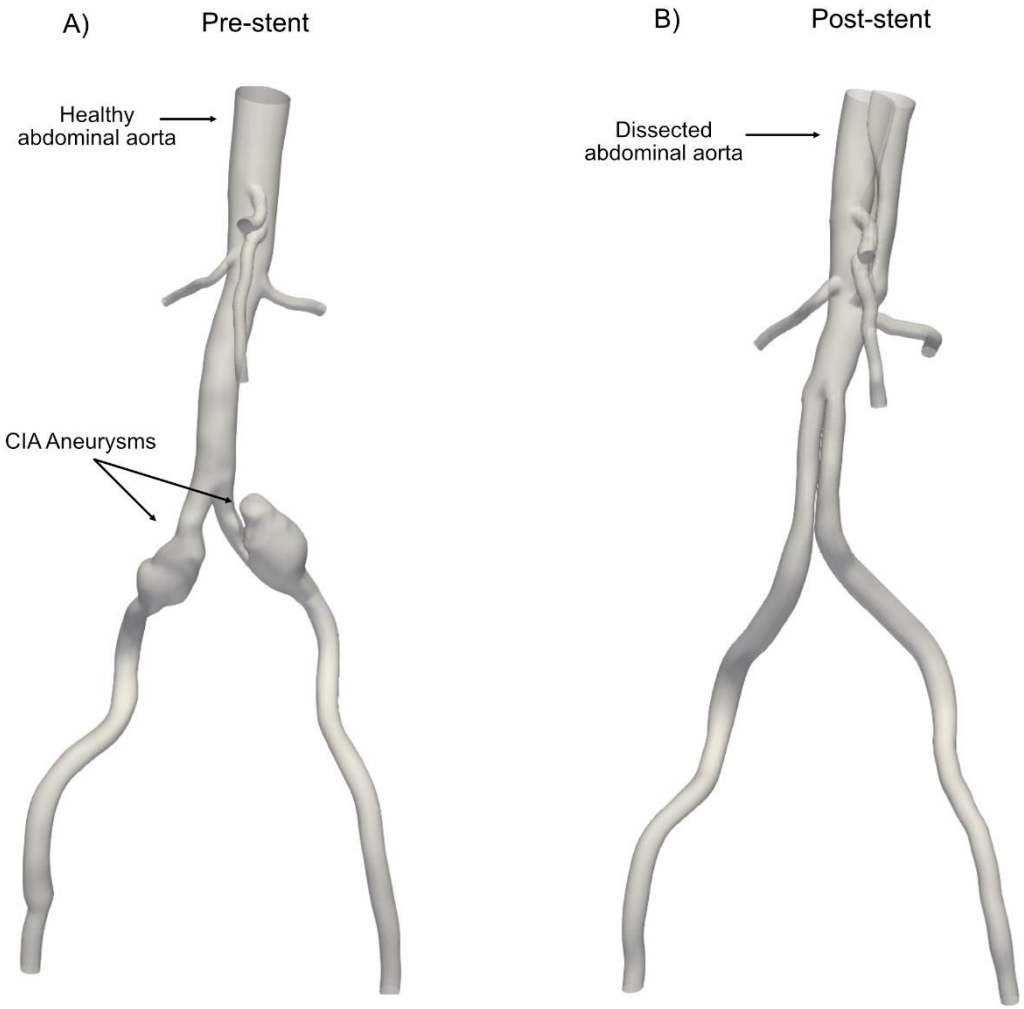

Figure 5.4: CT-based reconstructions of A) pre- and post-operative abdominal aorta before (left) and after (right) endovascular surgical intervention to treat bilateral common iliac aneurysms.

5.2.4 4D Flow-MRI Inlet Profiles

As per Chapter 4, a 4D Flow-MRI derived flow-waveform in the mid-ascending aorta was extracted for each healthy individual (Figure 5.5A) and dissection patient (Figure 5.5B). This was then converted to a periodic velocity profile for the prescription of the inlet BC of all numerical simulations. Spatially, a uniform profile was prescribed, which can be justified by

previous in vivo measurements and mathematical models from literature [17] [47] [31] [130] [38].

For the pre-and post-surgical abdominal model, a 4D Flow-MRI derived flow waveform (Figure 5.5C) was extracted from the abdominal aorta, perpendicular to the direction of bulk flow. The analysis planes were spaced 0.5D apart, beginning immediately upstream of the coeliac trunk, where D was the diameter of the aorta. Similarly, this was converted to a periodic velocity profile.

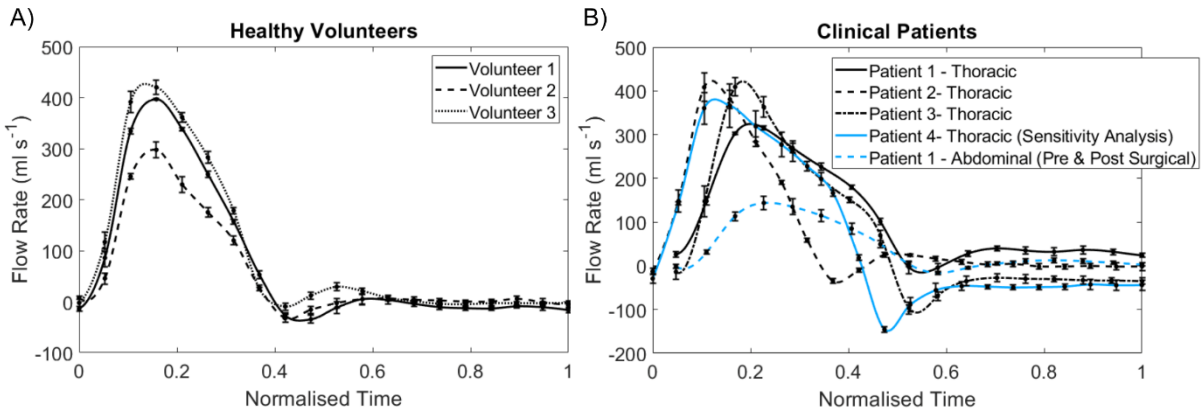

Figure 5.5: 4D Flow-MRI derived flow waveforms for the A) healthy volunteers and B) clinical patients, extracted from the ascending aorta, at a location parallel to the apex of the pulmonary artery. At each time point throughout the cardiac cycle, the cross-sectional flow rate was calculated from 5 planes of analysis for each patient, placed normal to the direction of blood flow. These planes were equally spaced in the axial direction to discretely sample a volume of blood flow, from which a mean flow rate could be calculated. For each patient, this flow rate is presented as mean±sd.

5.2.5 1D Reconstructions & Modelling

Following the methodology described in Chapter 4, 1D models of each healthy volunteer and clinical patient were created from the reconstructed 3D arterial geometries. Figure 5.6 shows the 1D model of the full thoracoabdominal aorta and branches of patient 2 as an example. This patient was selected at random to reduce redundancy in results presentation. The complete results for the other patients are available in the supplementary material. This model was partitioned into 33 discrete segments and included both the TL (solid lines) and FL (dashed lines) which bifurcated and converged with the TL at multiple sections. Appendix A.3 illustrates the remainder of the dissected 1D models, along with each healthy case. Additionally, Appendix A.4 lists the length, radius, area, and elasticity of each segment for each individual.

For each case, the corresponding 4D Flow-MRI derived inlet profile (Figure 5.5) was prescribed at the ascending aorta. At each terminal branch, the 1D model was coupled to the estimated 3EWM BCs (Appendix A.5), which were estimated utilising equations 4.3 - 4.7 as described in Chapter 4. Wall elasticity was prescribed for each vessel segment based on equation 2.25, with $\Gamma = 0$. Thereafter, a coupled 0D-1D simulation was performed on Nektar1D over 20 cardiac cycles, generating a pressure waveform at each terminal branch. Figure 5.6 also shows the resultant pressure waveforms obtained during the 20^{th} cardiac cycle when the solution reached convergence.

5.2.6 CFD Methodology

As per Chapter 4, the estimated 3EWM parameters were subsequently calibrated on Matlab, utilising the Nelder-Mead Algorithm and equations 4.8 and 4.9 for each terminal branch of each individual. Appendix A.6 lists the calibrated parameters for each CFD simulation, showing that each patient and volunteer has a unique set of BCs.

For each aortic geometry presented in Figures 5.1 and 5.3, a patient-specific 0D-3D CFD model was created to allow for the numerical investigation of the flow field and near-wall haemodynamic parameters. In line with the methodology described in Chapter 4, the 3D geometries were discretised to create a mesh on Ansys ICEM CFD® and solved numerically in Ansys Fluent®. The 0D-3D CFD simulations were performed on a single node of the ARCHIE-WeSt cluster at the University of Strathclyde, utilising 35 computational cores. For the pre- and post-operative abdominal aortic geometries of patient 1, as illustrated in Figure 5.4, the 3EWM BCs remained constant in each configuration. Consequently, we sought to understand how surgical intervention alters arterial haemodynamics, exclusively due to changes in geometry.

Finally, the aortic geometry of patient 4 (Figure 5.3D) was utilised to conduct a sensitivity analysis. To do so, the 3D geometry was kept constant while three distinct sets of 3EWM BCs were prescribed to the branch outlets and a coupled 0D-3D CFD simulation was performed. These are termed BC1 (Appendix A.6: Table 1), BC2 (Appendix A.6: Table 2), and BC3 (Appendix A.6: Table 3). This allowed for the investigation of how arterial haemodynamics are affected by changes to the BCs.

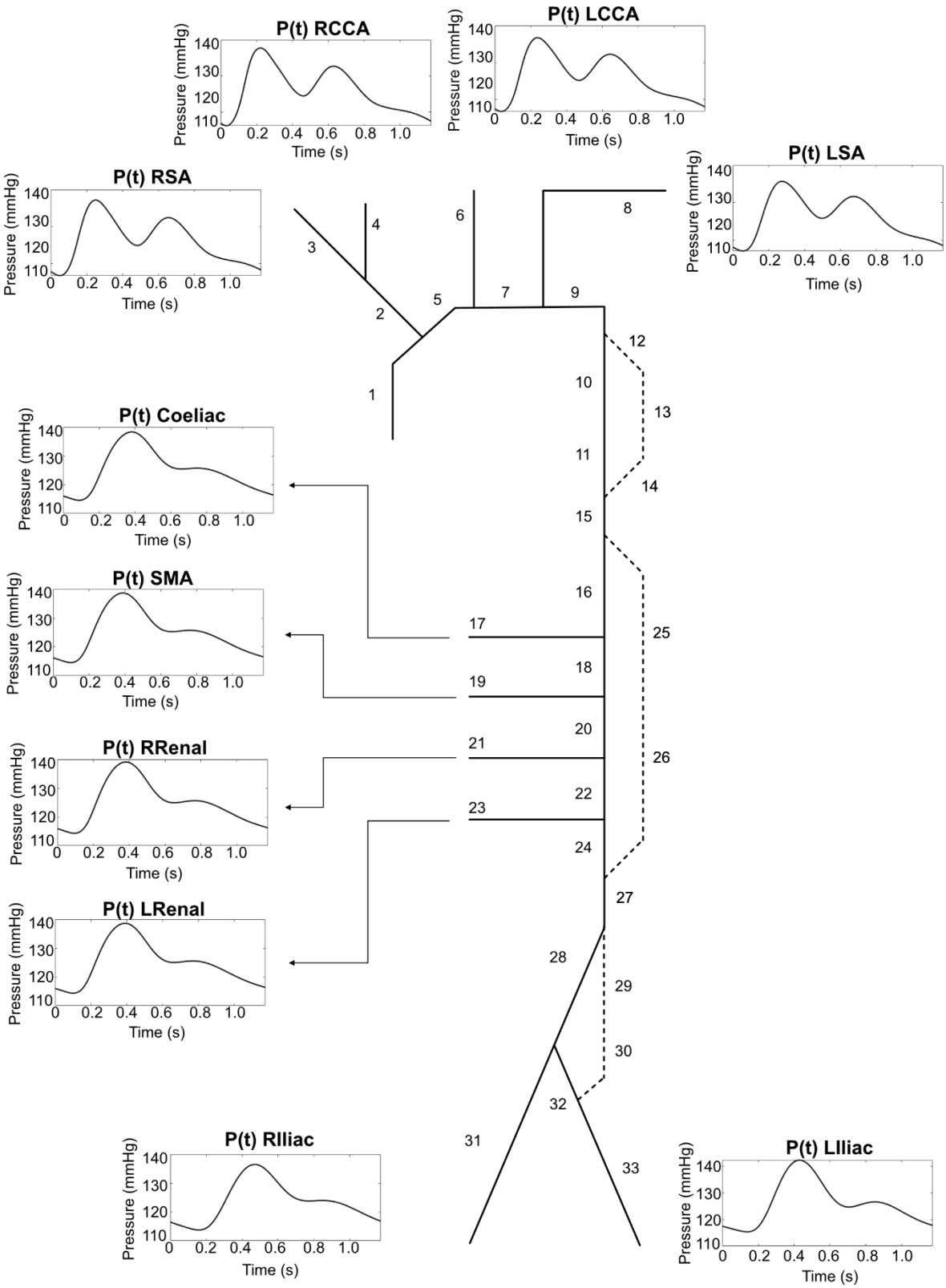

Figure 5.6: Schematic of the 0D-1D model of patient 2, showing 33 discrete arterial segments and including the true lumen (solid line) and false lumen (dashed line). At each terminal branch, the resultant pressure waveform after 20 cardiac cycles is presented.

5.3 Results

5.3.1 Perfusion Distributions

From Chapter 4, it is known that the calibrated 3EWM BCs yield an accurate perfusion distribution when compared to in vivo data in the thoracic aorta. This section seeks to expand that investigation to incorporate the entire thoracoabdominal aorta where applicable and expand the number of datasets used to validate this claim. However, it is appreciated that this remains a very limited number of datasets. For each case, the perfusion distribution is presented as the net flow through each branch, calculated as a percentage of the inflow at the ascending aorta.

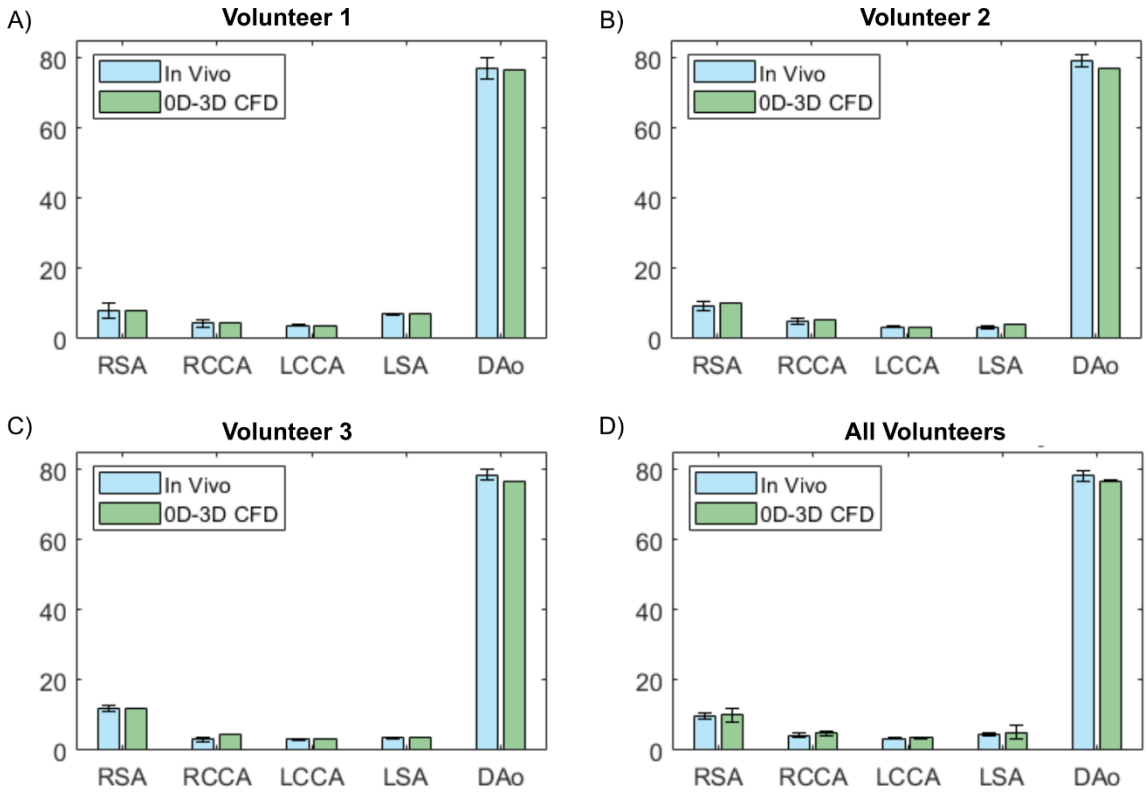

Figure 5.7: Blood flow perfusion distribution throughout the 0D–3D CFD model (green) of (A) healthy volunteer 1, B) healthy volunteer 2, C) healthy volunteer 3, and D) averaged across all healthy volunteers in comparison with (blue) in vivo 4D Flow-MRI obtained data. Error bars represent mean ± standard deviation.

For volunteer 1 (Figure 5.7A), volunteer 2 (Figure 5.7B), and volunteer 3 (Figure 5.7C) the mean difference between the *in vivo* and CFD-derived perfusion distribution was 0.174% ± 0.161%, 0.913% ± 0.808%, and 0.699% ± 0.739%, respectively. For all cases, the largest difference occurred at the descending aorta, at 0.433%, 2.22%, and 1.47%, respectively. When averaged across all healthy volunteers (Figure 4.7D), the mean difference between the *in vivo* and CFD-derived flow rates was 0.587% ± 0.535%.

Similarly, the CFD-derived perfusion distribution was compared to the 4D Flow-MRI derived *in vivo* flow data for the clinical patients. While the healthy volunteers demonstrated a consistent pattern of the largest difference occurring at the descending aorta, the clinical patients exhibited increased variability and larger discrepancies overall. Patient 1 (Figure 5.8A), patient 2 (Figure 5.8B), and patient 3 (Figure 5.8C) exhibited a mean difference of 2.32% ± 2.25%, 0.134% ± 0.0971%, and 3.28% ± 5.34%. However, differences between the CFD and *in vivo* flow rates in individual branches were as large as 7.67% in the coeliac artery of patient 1, 16.4% in the right iliac artery of patient 2, and 16.4% in the superior mesenteric artery of patient 3. Patient 4 was not included in this comparison due to lack of 4D Flow MRI data (Table 5.1).

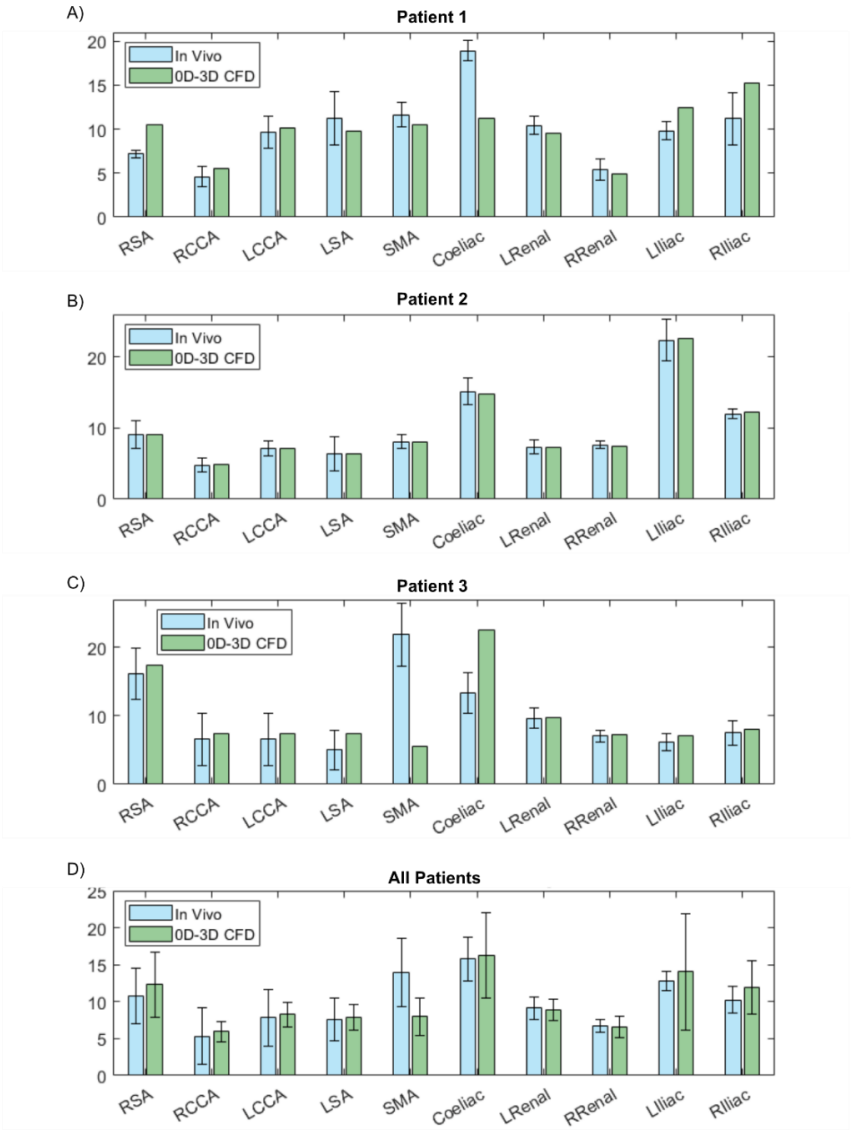

Figure 5.8: Blood flow perfusion distribution throughout the 0D–3D CFD model (green) of (A) clinical patient 1, B) clinical patient 2, C) clinical patient 3, and D) averaged across all healthy volunteers in comparison with (blue) in vivo 4D Flow-MRI obtained data. Error bars represent mean ± standard deviation.

5.3.2 **Instantaneous Flow Waveforms**

The comparison of the perfusion distribution between the CFD-derived and *in vivo* data in Chapter 4 centred around the net flow through each branch. Therefore, this analysis omitted the temporal details of the flow waveform. Consequently, it is crucial to include a comparison of the instantaneous waveforms while containing flow information as a function of time throughout the cardiac cycle. This analysis was performed for each clinical patient and healthy volunteer. Figure 5.9 shows an example of these waveforms for a dissected case (Patient 2). The flow waveforms for the remaining patients can be found in Appendix B.1.

In general, there was a tendency for the CFD models to overestimate flow at systole, followed by a subsequent underestimation of flow at the beginning of the diastolic phase, immediately following systolic deceleration. During diastole, the *in vivo* and CFD-derived flow rates converged to a minimal error by end-diastole. Patient 2, for example, exhibited a percentage error between 56.7% - 69.9% during systole in the thoracic aorta, and between 43.9% - 100% in the abdominal aorta. Interestingly, Patient 1, who had an endovascular stent graft (unlike Patient 2), exhibited a reduced percentage difference ranging from 6.92%-60.1% in the thoracic aorta during systole, and from 52.1%-94.4% in the abdominal aorta. The presence of the stent graft increases wall stiffness, which therefore may make the rigid-wall assumption of the CFD models more valid, as hypothesized previously by Zhu et al. [76]. Regarding healthy volunteer 1, these errors at systole were between 29.8% - 67.7%.

Though there were discrepancies in the magnitude of flow, the shape of the instantaneous flow waveforms was relatively consistent with the *in vivo* data in the thoracic region and at the iliac arteries for all dissection patients. However, in the coeliac to renal artery region, the CFD-derived flow waveforms were more significantly out of phase and tended to oscillate, suggesting there are sustained periods of flow reversal between t=0.2-0.6s during the cardiac cycle. Similar results were found for the remaining patients and the healthy volunteers, as illustrated in Appendix B.1.

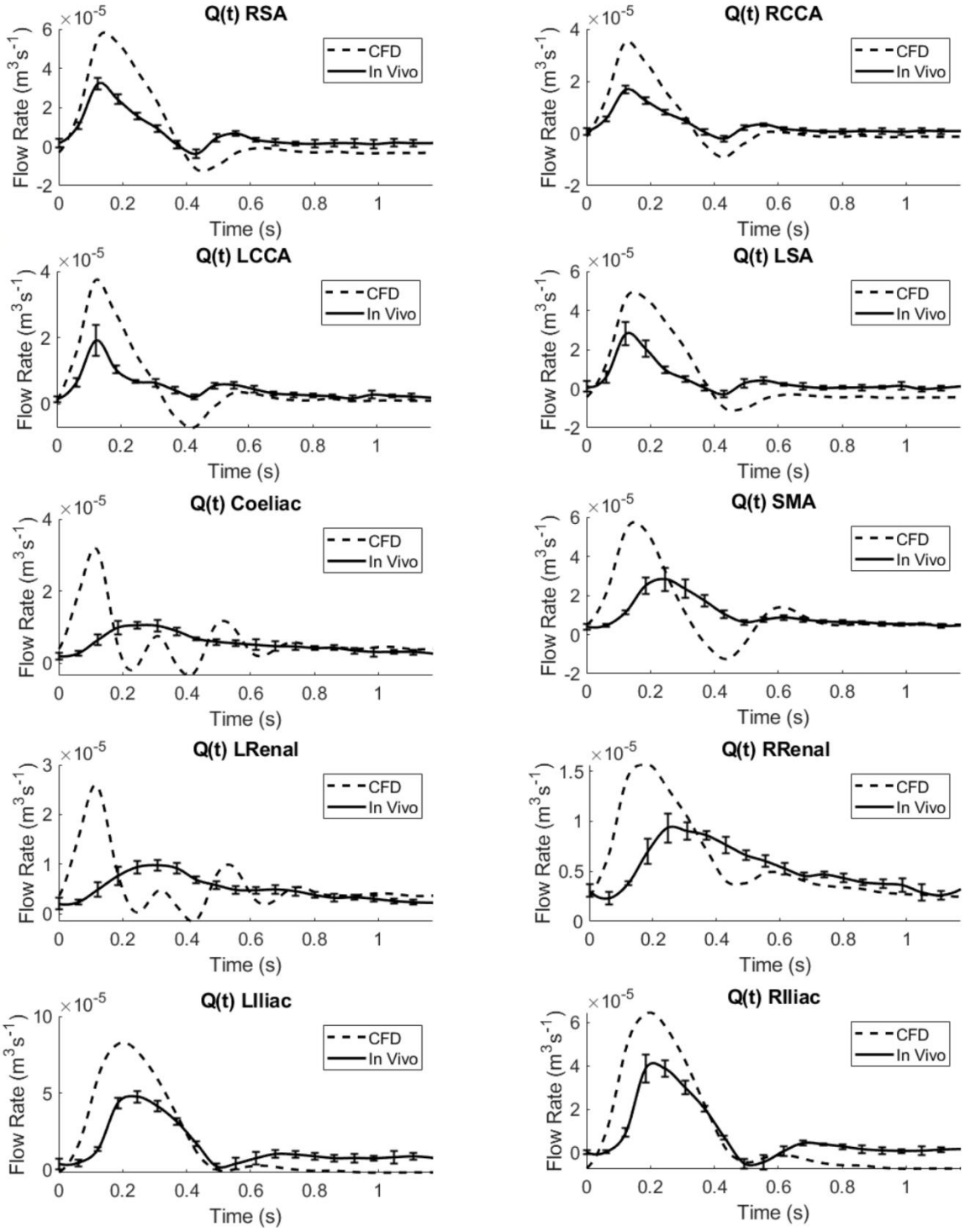

Figure 5.9: Instantaneous flow waveforms as derived from CFD models (dashed line) with calibrated 3EWM BCs and in vivo 4D Flow-MRI data (dashed line) at each terminal branch of the thoracoabdominal aorta of patient 2. Error bars represent mean ± standard deviation.

5.3.3 Flow in the True and False Lumen

It was also possible to investigate the relationship of flow between the TL and FL for the dissected aortae (Figure 5.10). For patient 2, the majority of blood flowed through the true lumen in the thoracic and abdominal aorta, at 96.3% and 86.4%, respectively, when compared to the FL. Conversely, for patient 3, the false lumen received the majority of blood flow, where 62.4% and 69.3% of blood flow are observed in the FL of the thoracic and abdominal aorta, respectively. Additionally, this analysis shows that for these patients, the ratio of flow between the TL and FL remains relatively consistent as a function of increasing distance along the vessel (Figure 5.10E & F), despite the presence of several secondary intraluminal tears.

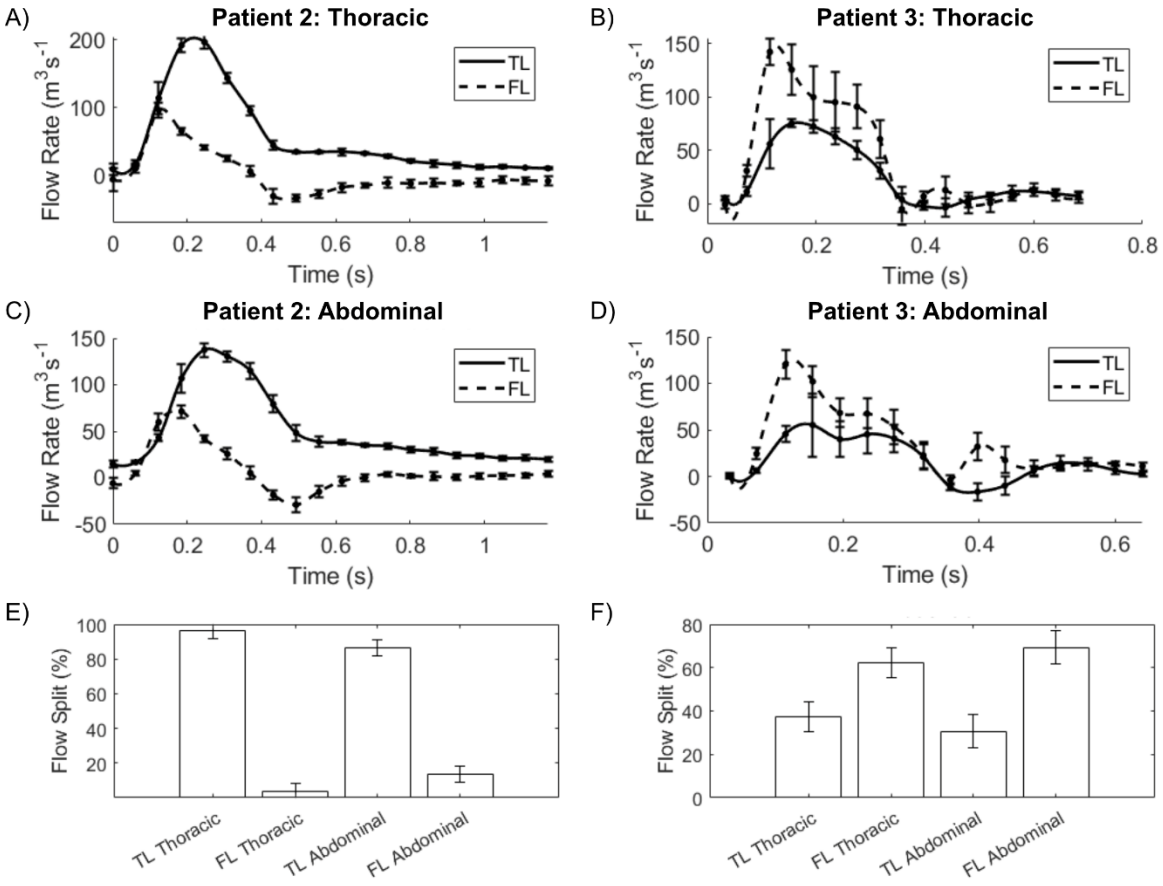

Figure 5.10: Analysis of in vivo 4D Flow-MRI blood flow in the TL and FL of patient 2 and patient 3. Flow splits were calculated with respect to the total flow going through the TL and FL combined.

5.3.4 0D-3D CFD Near-Wall Haemodynamics

5.3.4.1 Healthy Volunteers

For the healthy individuals, the maximum values of TAWSS (Figure 5.11 A-C) were 6.91 Pa at the innominate bifurcation, 4.78 Pa at the primary curve in the LSA, and 9.85 Pa at the innominate bifurcation for volunteer 1, 2, and 3, respectively. The spatial distribution of TAWSS was relatively consistent. In each case, regions of high, localised TAWSS was observed immediately distal to the supra-aortic branch ostia, the distal posterior aortic arch, and the primary curvature of the LSA, all of which are consistent with the literature [6]. Similarly, all cases exhibited regions of low TAWSS on the lateral ascending aorta and the proximal anterior section of the arch. Further, in all cases, a higher magnitude of TAWSS was observed on the inferior section of the arch compared to the superior portion.

Regarding OSI (Figure 5.11 D-F), the spatial distribution again remained relatively constant. Elevated values, indicative of oscillatory flow, were located along the anterior section of the descending aorta, the lateral ascending aorta, around the curvature of the LSA, and in the region of the innominate bifurcation.

Finally, the time-averaged pressure (Figure 5.11 G-I) of the healthy volunteers retained a fairly constant spatial distribution between individuals, with maximum magnitudes of 75-87mmHg observed in the ascending aorta. Generally, the time-averaged pressure decayed as a function of distance from the inlet, with a notable region of decreased pressure at the inferior section of the LSA at the location of peak curvature. For all volunteers, the CFD-derived global systolic pressure matched well with the generally accepted healthy reference pressure of 120mmHg (Table 5.3). However, the CFD-derived diastolic pressure was underestimated with respect to a healthy diastolic reference pressure of 80mmHg.

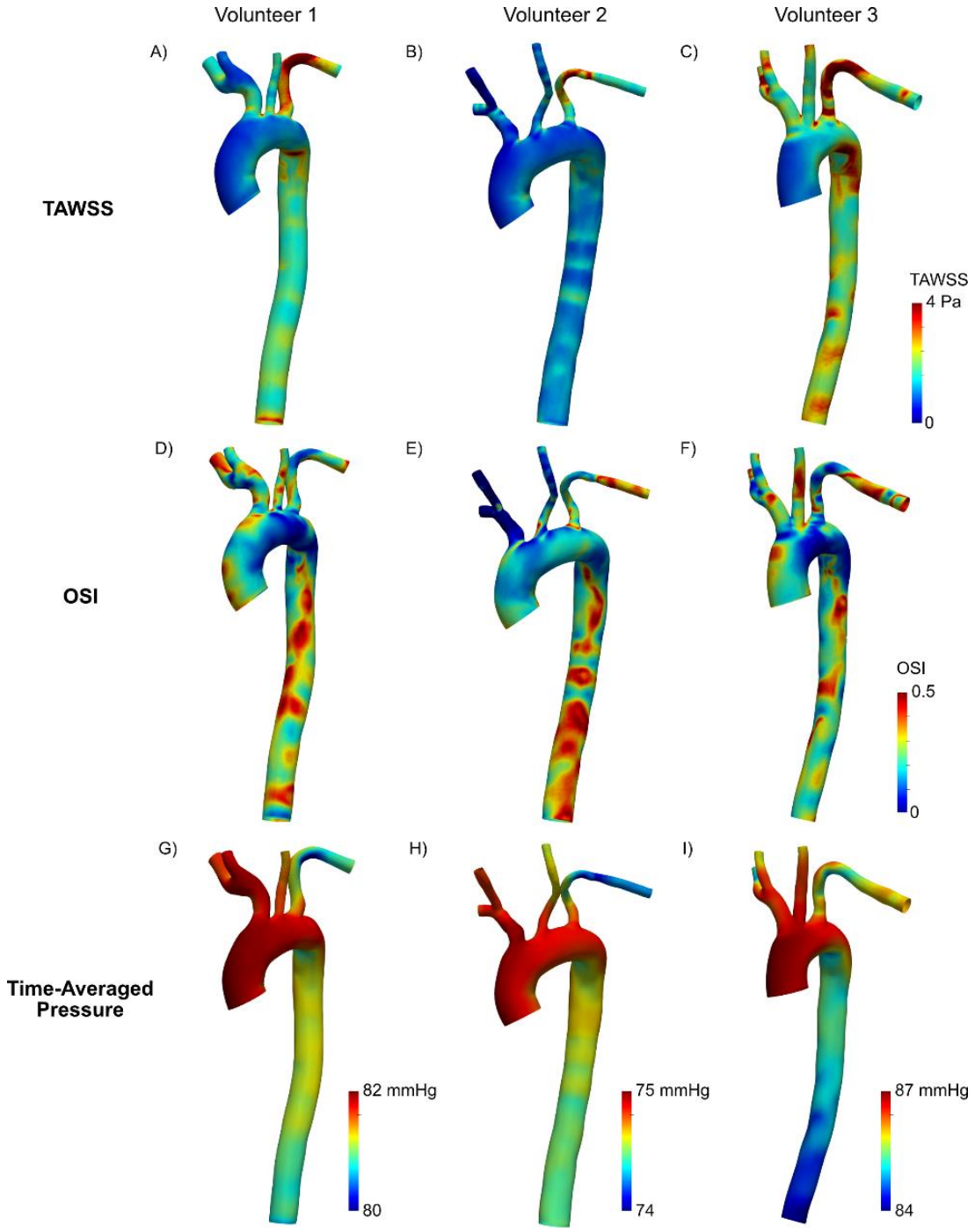

Figure 5.11: TAWSS (top), OSI (middle) and time-averaged pressure (bottom) of the healthy (A, D, G) volunteer 1, (B, E, H) volunteer 2, and (C, F, I) volunteer 3 in the thoracic aorta as a result of a 0D-3D CFD simulation. Note that each patient has a different colour scale.

Table 5.3: Systolic, diastolic, and mean arterial pressures calculated for each healthy volunteer in comparison to healthy reference values obtained from literature.

	Global Systolic Pressure (mmHg)		**Global Diastolic Pressure (mmHg)**		**Global Mean Pressure (mmHg)**	
	CFD	Reference	CFD	Reference	CFD	Reference
Volunteer 1	126 ± 6.31	120	49.9 ± 1.1	80	82.2 ± 0.261	93.3
Volunteer 2	122 ± 6.36	120	34.2 ± 0.84	80	74.9 ± 0.214	93.3
Volunteer 3	119 ± 7.37	120	65.9 ± 2.52	80	86.3 ± 0.386	93.3

5.3.4.2 Clinical Patients

Regarding the clinical patients, there were some commonalities regarding the TAWSS distribution (Figure 5.12). As a reminder, patient 4 was not accompanied with 4D Flow-MRI data, so a patient-specific CFD model was not created. The geometry of patient 4 was used exclusively for a sensitivity analysis.

In each case, the FL exhibited a noticeable reduction in TAWSS magnitude compared to the TL. Additionally, regions of elevated TAWSS were observed around the primary, secondary, and re-entry tears, particularly in the distal end of the tears. Finally, and similar to the healthy individuals, each patient showed typical regions of elevated TAWSS distal to the branch ostia and at the innominate artery bifurcation. In fact, all bifurcations were characterised by increased TAWSS around the branch ostia.

Beyond these general trends, the overall distribution of TAWSS was highly individualised and unique to each patient, leading to large inter-patient discrepancies in both magnitude and spatial location. Quantitatively, the maximum TAWSS values were located around the SMA (34 Pa) and coeliac artery (21 Pa) of patient 1, the primary tear (17.8 Pa) of patient 2, and the coeliac artery (13.8 Pa) and left renal artery (9.76 Pa) of patient 3. Thus, patient 1 displayed maximum TAWSS values roughly 3.5 times greater than patient 3 (35 Pa vs 13.8 Pa). Finally, when considering the differences in TAWSS between the primary tear region, patient 2 exhibited TAWSS quantities almost 4.5 greater than patient 3 (17.8 Pa vs 3.99 Pa).

To highlight the differences in spatial distribution, patient 2 exhibited a region of elevated TAWSS in the superior and anterior section of the distal aortic arch, and around the LSA branch ostia. This was not observed in patients 1 or 3. Conversely, the proximal descending aorta of patient 3 is was bulbous than that of patients 1 and 2, yielding comparatively low velocities and TAWSS. Patient 1 did not present with secondary tears, unlike patients 2 and 3. This meant

that the distribution of TAWSS was more homogeneous throughout the TL and FL. Therefore, the area of the TL and FL, the number and size of intraluminal tears, and the location of these tears all contributed to a unique TAWSS distribution for each patient.

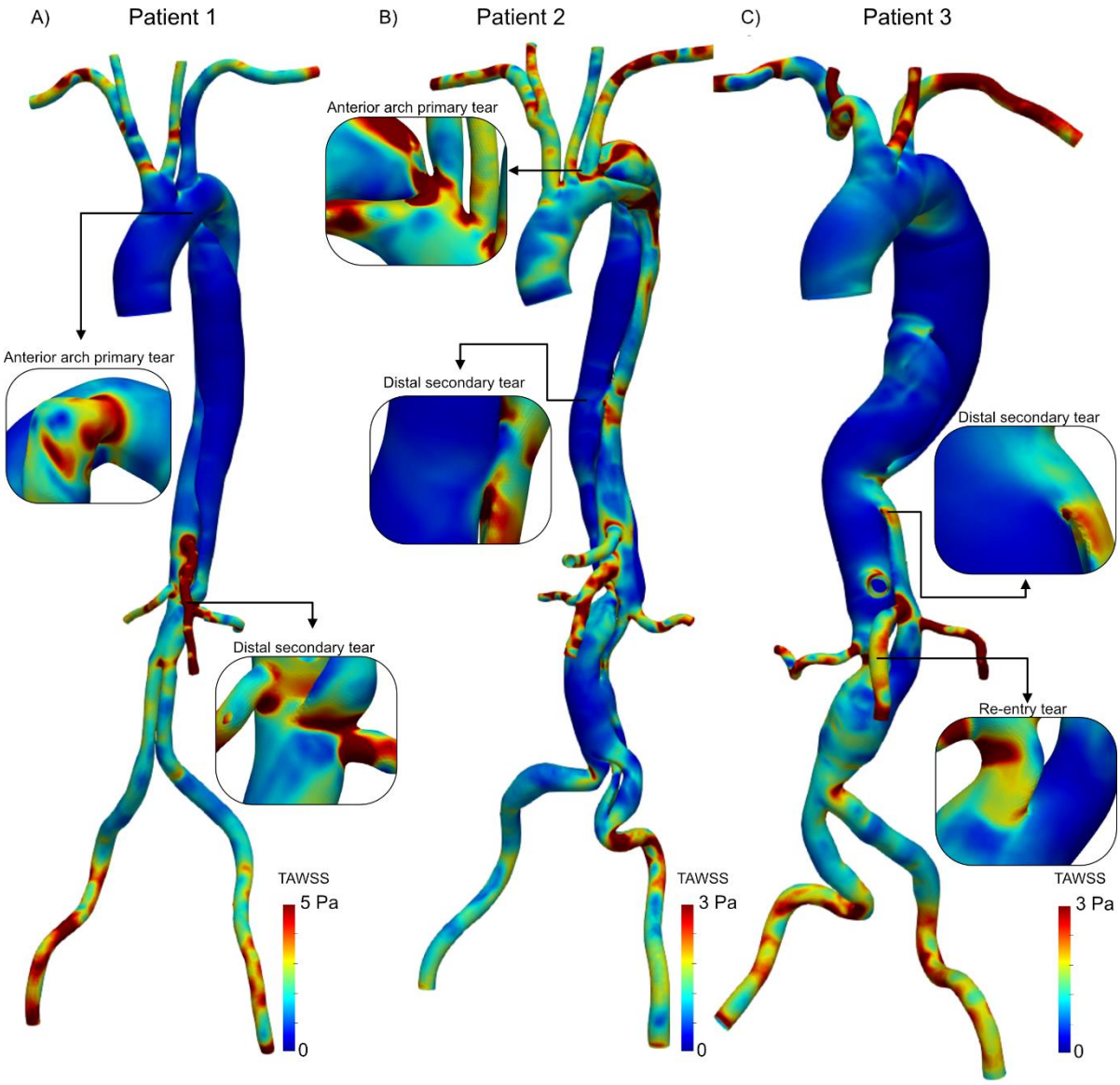

Figure 5.12: TAWSS distribution throughout the thoracic aorta of A) patient 1, B) patient 2, and C) patient 3 as a result of 0D-3D CFD simulations. Note, patient 1 is shown with a slightly different colour bar range than the other two patients.

To understand why TAWSS was elevated around the intraluminal tears, particularly in the distal sections, an analysis of the velocity streamlines was conducted. This was performed for both the *in vivo* and CFD-derived results. Figure 5.13 illustrates the CFD-derived velocity streamlines at peak systole, demonstrating a clear correlation between tear-induced jet flows and locations of elevated TAWSS due to increased blood velocity. Taking Figure 5.13B as an example, blood flow impinged on the superior vessel wall of the FL, inducing vortical flow.

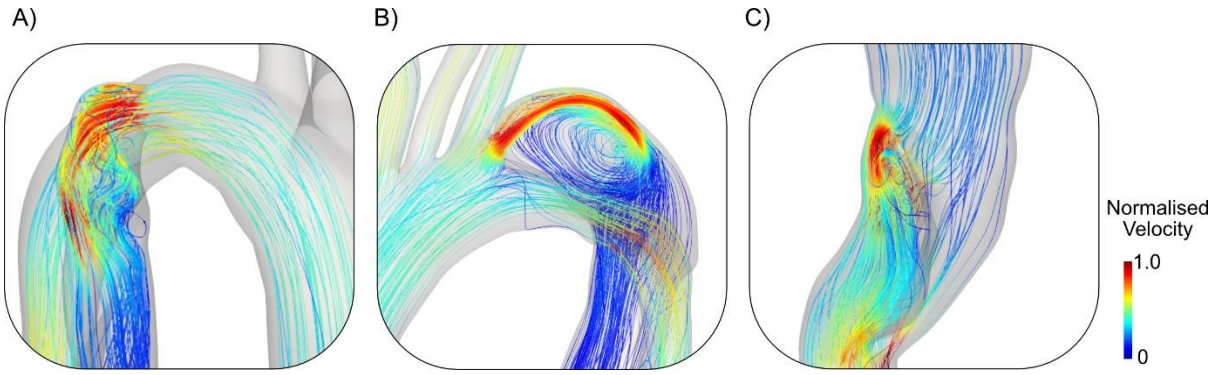

Figure 5.13: Primary tear velocity streamlines at peak systole for A) patient 1 (posterior arch), B) patient 2 (anterior arch), and C) patient 3 (descending aorta). Normalised velocity according to the maximum velocity for each patient.

Regarding OSI, again there were some commonalities and some significant inter-patient variability in the spatial distribution which was observed (Figure 5.14). Common to all patients was the observation that the OSI within the FL greatly exceeded that of the TL. This suggests that the flow regime within the TL remained generally unidirectional. However, flow within the FL was more multi-directional with flow reversal, secondary flows, and recirculation. Further, each patient exhibited localised, elevated regions of OSI at the proximal, superior section of the ascending aorta. Finally, the branch vessels, excluding the iliac arteries, generally displayed a reduction in OSI when compared to the main body of the aorta, though each shows elevated regions around the branch ostia.

Regarding the differences in OSI, the number, size, and location of the intraluminal tears between patients had a notable effect. For example, patient 1 had a homogeneous (consistently higher) OSI pattern in the FL compared to both other patients. However, the two patients with multiple secondary tears had a more heterogeneous pattern. This suggests that the absence of secondary tears may induce an increased disturbance and multi-directionality in the flow regime within the FL. Additionally, the proximal descending aorta of patient 3 was characterised by a bulbous dilation of the vessel wall, leading to a large, elevated region of OSI even though it was proximal to the primary tear. As this bulbous section was unique to patient 3, so too was the OSI distribution.

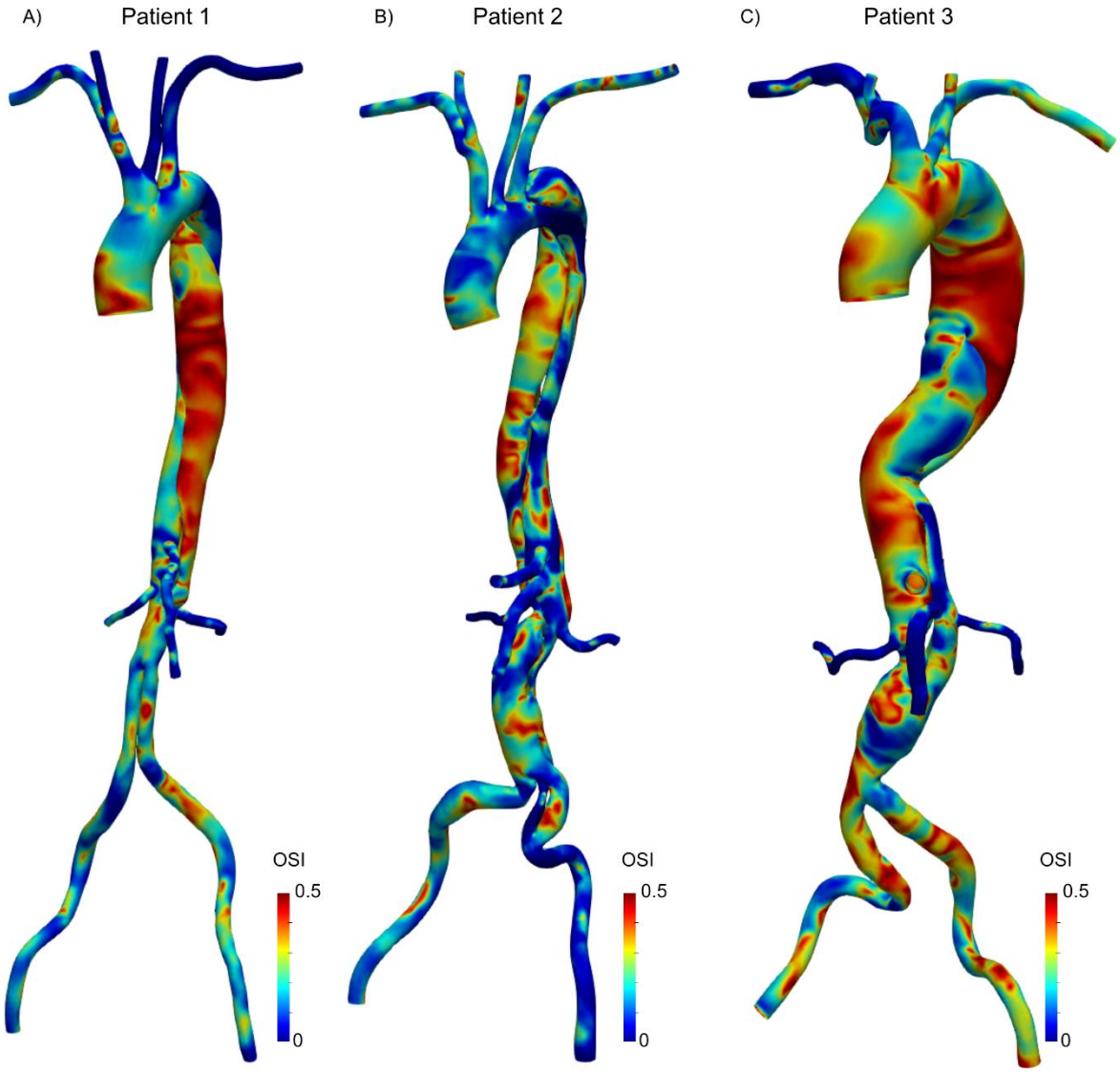

Figure 5.14: OSI distribution throughout the thoracic aorta of A) patient 1, B) patient 2, and C) patient 3 as a result of 0D-3D CFD simulations.

To further investigate what leads to these individualised distributions, an analysis of the velocity streamlines was conducted at different phases of the cardiac cycle. Figure 5.15 illustrates these streamlines for patient 2 at regions of elevated OSI. This focused primarily on the locations surrounding the primary, the 1st and 2nd secondary tears, and the re-entry tear. It was apparent that blood flow was stable and unidirectional during SA and PS, then becoming less stable during SD and into diastole. Figure 5.15 shows how the velocity profile distal to the intraluminal tears became more disturbed during systolic deceleration. This was also confirmed via analysis of the *in vivo* 4D Flow-MRI data.

Figure 5.15 also highlights a clear interaction and multi-directional exchange of blood flow between the secondary intraluminal tears. Observation of the proximal (1st) secondary tear

shows velocity streamlines entering the TL from the FL during systolic acceleration, followed by streamlines entering the FL from the TL during peak systole. Additionally, at the distal (2nd) secondary tear, a portion of the blood flow perfusing the left renal artery was supplied via the FL. This tracked towards the renal artery through retrograde perfusion out of the FL and along the TL.

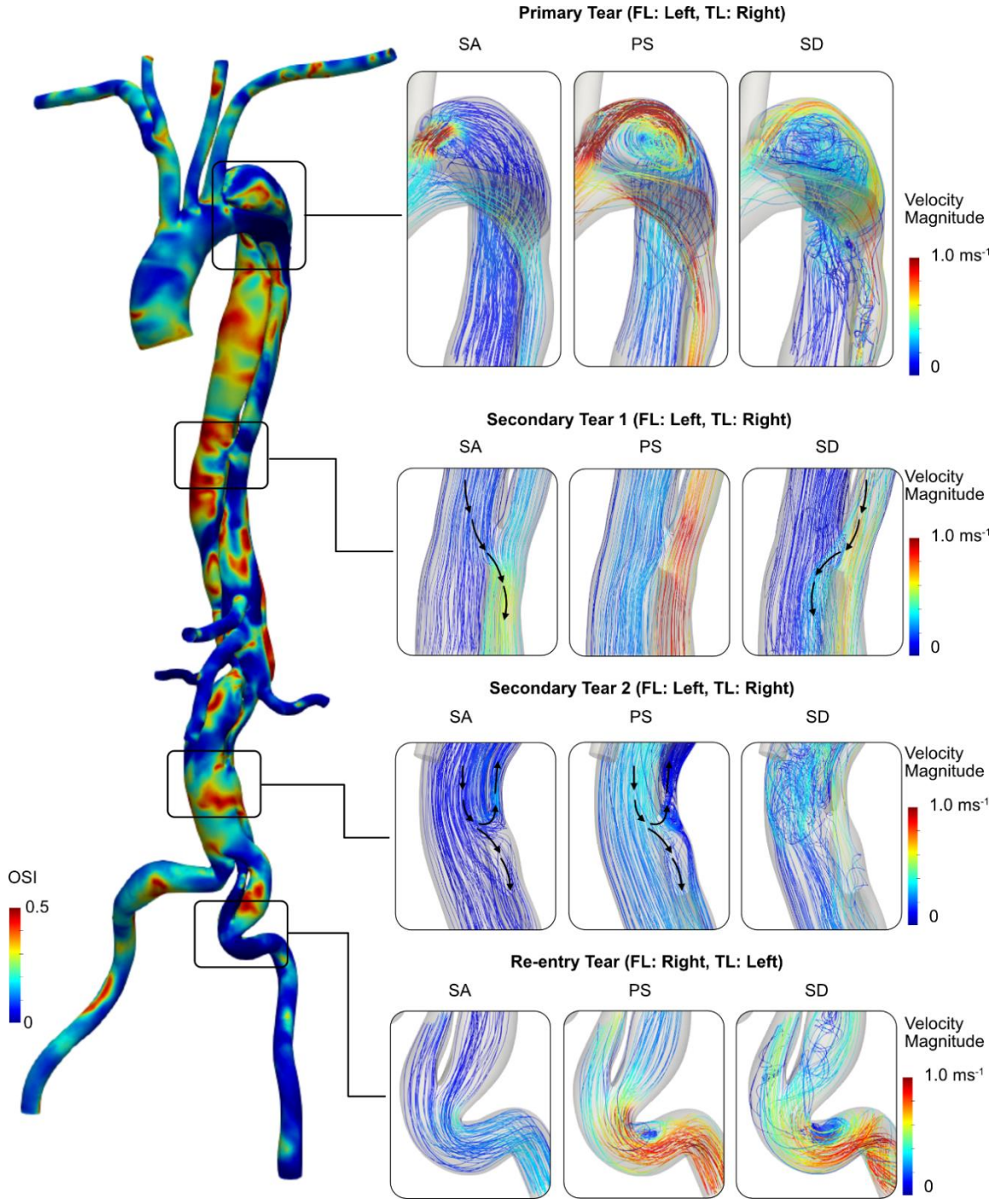

Figure 5.15: CFD-derived velocity streamlines, illustrating blood flow within the thoracoabdominal aorta of patient 2 during systolic acceleration (SA), peak systole (PS), and systolic deceleration (SD) at regions of elevated OSI around intraluminal tears.

Finally, Figure 5.16 illustrates a relatively constant time-averaged pressure between TL and FL for each patient. Notably, patient 2 did not exhibit a pressure drop in the TL distal to the proximal secondary tear. This contrasts Figure 4.12 in Chapter 4, when only the thoracic aorta was modelled. This suggests that truncating the aorta and prescribing 3EWM BCs can have upstream pressure effects on the simulation. Time-averaged pressure ranged from 101mmHg to 143mmHg, again decaying as a function of distance from the heart. Generally, the abdominal branch vessels exhibited a reduced pressure compared to the proximal and distal sections of the main body of the aorta. This indicates that pressure not only decays as a function of distance to the heart, but also independently along the branch vessels, regardless of location. Overall, the lowest pressures were observed in patient 3, possibly due to the more bulbous nature of the aorta. Notably, the time-averaged pressures in the clinical patients were up to 14mmHg – 68mmHg higher than the healthy counterparts. This makes sense since hypertension is a common symptom of TBADs [17] [252].

In comparison to the clinically obtained systolic and diastolic pressures, derived via a brachial cuff measurement, the patient-specific CFD models tend to yield relatively accurate systolic measurements. However, they tend to overestimate during diastole (Table 5.4).

Table 5.4: Systolic, diastolic, and mean arterial pressures calculated for each patient in comparison to reference values obtained clinically via brachial cuff measurements.

	Global Systolic Pressure (mmHg)		**Global Diastolic Pressure (mmHg)**		**Global Mean Pressure (mmHg)**	
	CFD	**Clinical Measurement**	**CFD**	**Clinical Measurement**	**CFD**	**Clinical Measurement**
Patient 1	166 ± 13	165	117 ± 5.23	77	138 ± 1.48	106
Patient 2	173 ± 5.34	189	117 ± 0.341	101	141 ± 0.845	130
Patient 3	121 ± 4.79	122	79 ± 1.06	69	99.3 ± 0.798	86

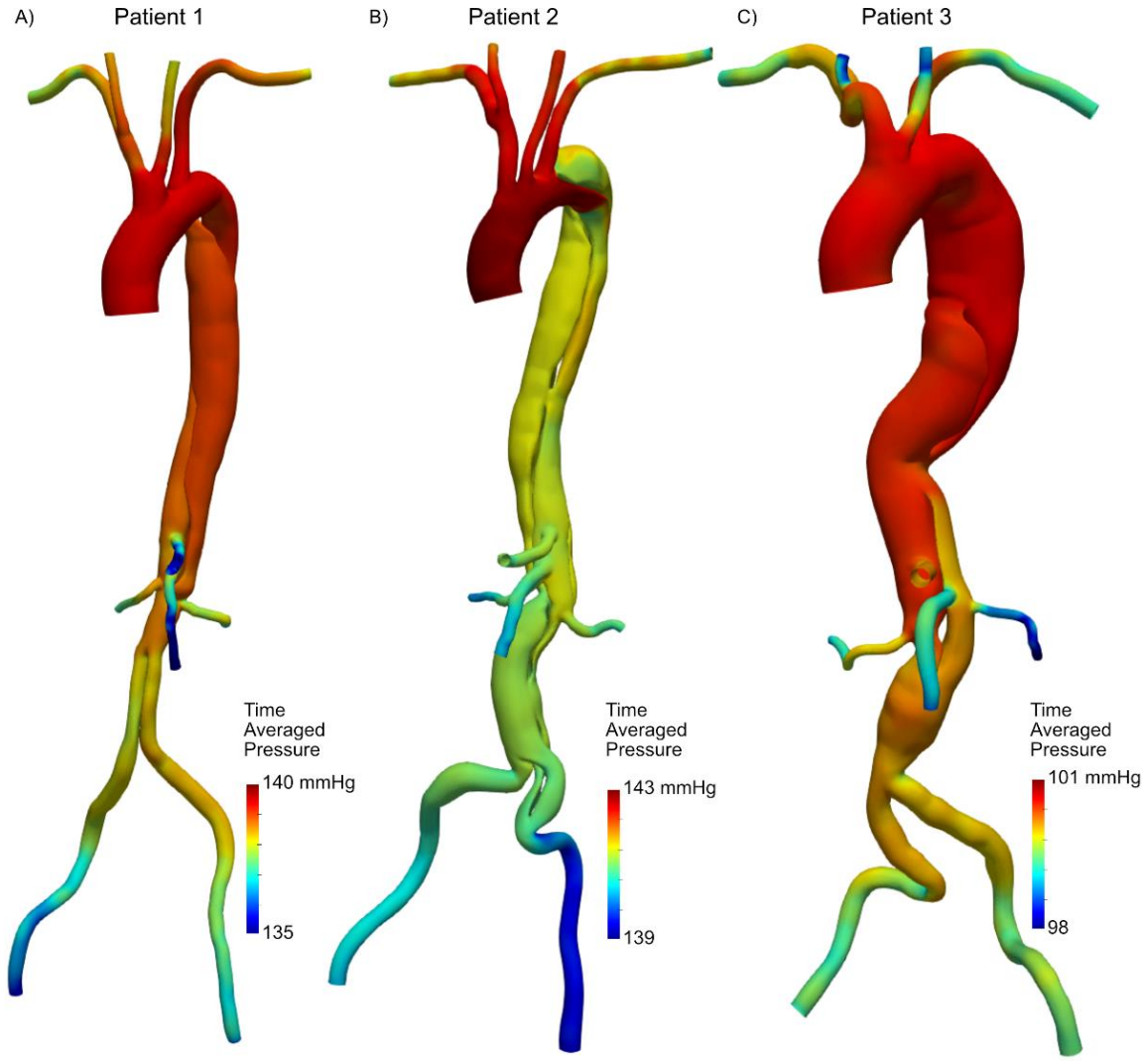

Figure 5.16: Time-averaged pressure distribution throughout the thoracic aorta of A) patient 1, B) patient 2, and C) patient 3 as a result of 0D-3D CFD simulations.

5.3.5 Pre vs Post-surgical Haemodynamics

In this section, we compareed the TAWSS and OSI of Patient 1 (Figure 5.17A-D), considering the pre- and post-operative geometries of the abdominal aorta. In the pre-surgical configuration, there was a marked decrease in TAWSS in the iliac aneurysm sacs compared to the proximal and distal segments of the iliac arteries. In the left iliac aneurysm, this was also accompanied by low OSI. Contrastingly, the right iliac aneurysm displayed a comparatively high OSI. This indicates that the flow regime differs between the aneurysm sacs due to differences in geometry. Crucially, this suggests the left aneurysm sac will have more of a tendency to induce thrombus accumulation and form atherosclerotic plaques, while the right aneurysm sac will have a tendency to expand more rapidly due to degeneration of the vessel wall [59] [257]. Notably, the proximal end of the left aneurysm sac also demonstrated a region

of fluid stagnation, confirmed by calculating the relative residence time (RRT) via Eq 5.1. This further reinforces the susceptibility to thrombus formation, where thrombi tend to form in areas of stagnant flow (high RRT) and low WSS regions [51] [73] [258]:

$$RRT = \frac{1}{1-(2\times OSI)\times WSS} \quad \textbf{(5.1)}$$

This analysis highlights the importance in determining the inter-aneurysmal differences in near-wall haemodynamics. For example, though the left iliac aneurysm is larger, the right aneurysm is perhaps less stable and prone to expand more quickly. To provide more detail on the aneurysmal flow regime, Figure 17E illustrates the velocity streamlines at different stages of the cardiac cycle. Due to the rapid change in cross sectional area at the proximal end of the aneurysms, there was a proportional decrease in velocity and fluid recirculation, creating a region of turbulent flow. Notably, this multi-directional flow regime was present throughout the entire cardiac cycle, even during systolic acceleration and peak systole.

Following surgical intervention with the anaconda graft, it is clear from Figure 5.17F that blood flow through the iliac arteries was unidirectional. Disturbed flow only appeared during diastole, which is characteristic of a normal flow regime. Further, there was a more consistent distribution of TAWSS throughout the proximal iliac arteries.

5.3.6 Sensitivity Analysis

Altering the 3EWM BCs (see Appendix A.6, Table 1-3) while retaining a constant arterial geometry (Patient 4) had a substantial effect on the overall perfusion distribution (Figure 5.18). For example, in the left iliac artery, altering the outlet BCs from BC2 to BC3 resulted in a 12.4% difference in net flow through the artery. In other branches however, such as the right renal artery, altering the change in BCs from BC1 to BC3 had a minimal effect on the flow split (1.98%). Initially, one may assume that changes in perfusion distribution would primarily be the result of modifying the net peripheral resistance, R. Considering the above information however, when resistance increases by a factor of 2.62, the net flow to the iliac artery decreases by 12.4%. In contrast, when resistance increases by a factor of 1.62, the net flow to the right renal artery decreases by only 1.98%. This indicates that changes in net flow are not linearly proportional to changes in peripheral resistance. It also confirms that the perfusion distribution throughout the arterial network was not only affected by isolated alterations in the BCs of a single branch, but by the synergistic relationship between all BCs.

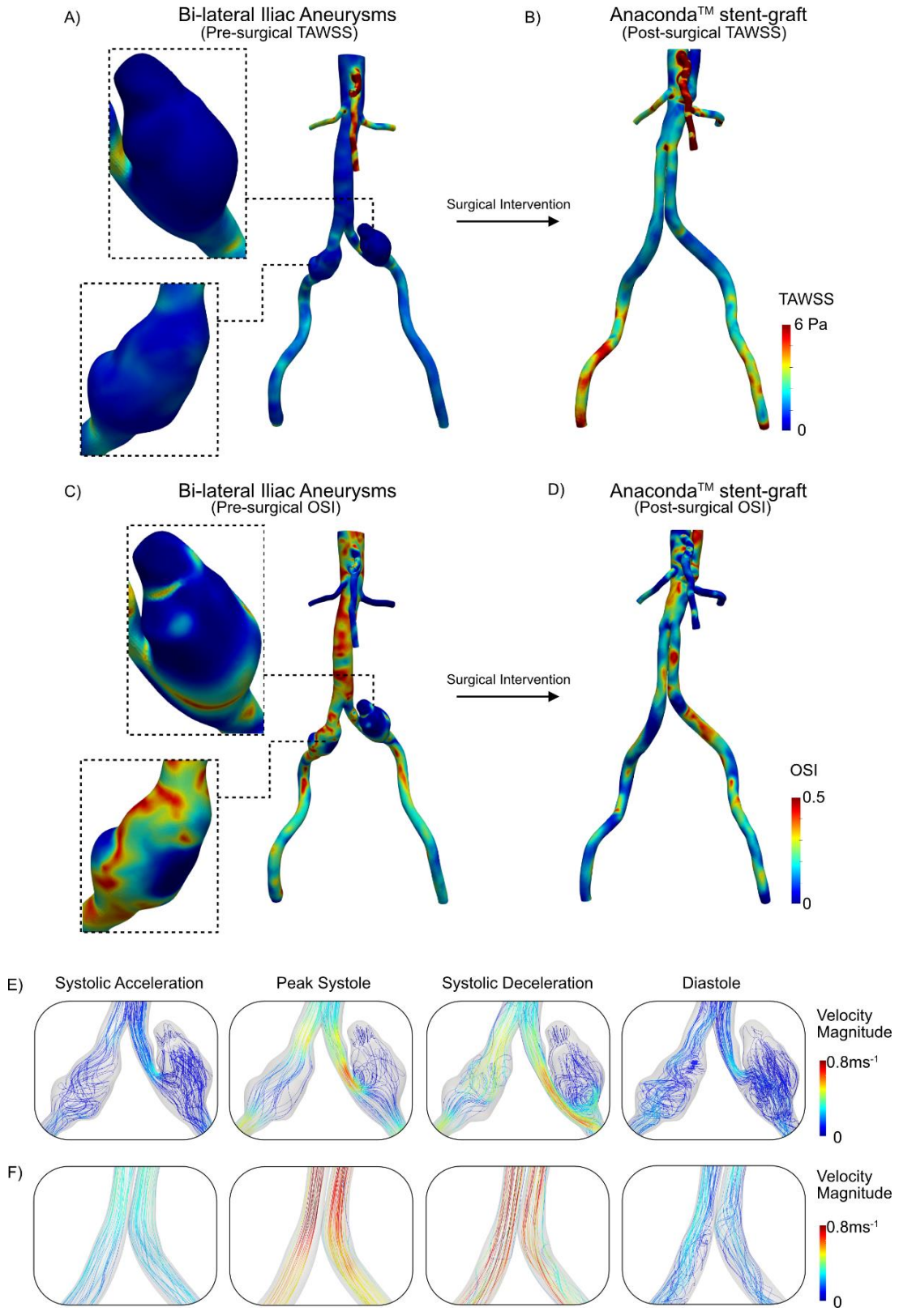

Figure 5.17: TAWSS distribution for the A) pre-surgical and B) post-surgical abdominal aorta of patient 1, highlighting the change in TAWSS distribution after deployment of an Anaconda™ stent-graft. Also illustrated are the corresponding OSI distributions for the C) pre-surgical and D) post-surgical geometries. The instantaneous velocity streamlines at systolic acceleration, peak systole, systolic deceleration, and diastole are also shown for the E) pre-surgical and F) post-surgical geometries.

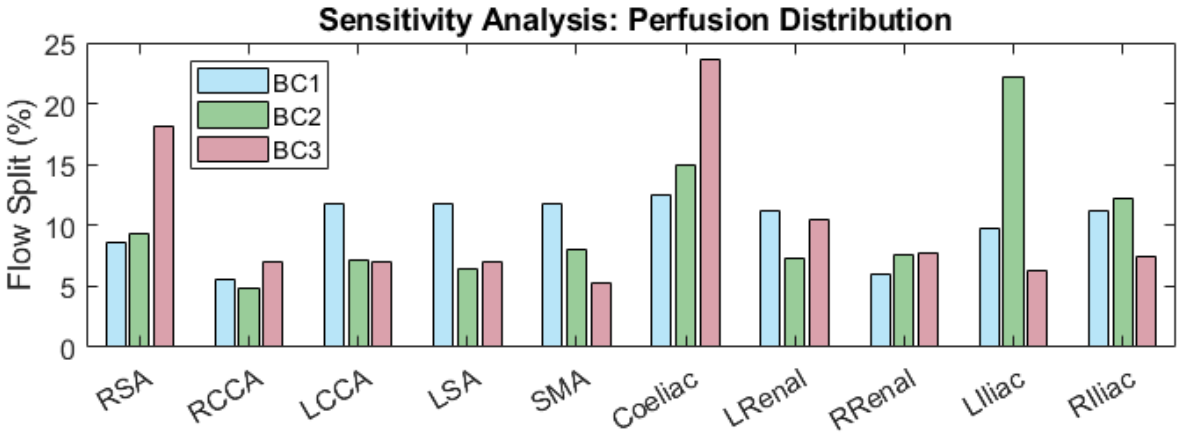

Figure 5.18: Blood flow perfusion distribution throughout the 0D–3D CFD model of Patient 4 with difference BC combinations, (BC combination 1 = blue, BC combination 2 = green, BC combination 3 = red, see Appendix A.6, Tables 1-3), conducted as a sensitivity analysis.

The prescription of different 3EWM BC combinations also had a substantial effect on the overall arterial pressure distribution, documented in Table 5.5. This table describes the global systolic, diastolic, and mean pressures associated with each BC combination. Our analysis showed that variations in BCs can result in systolic, diastolic, and mean arterial pressure shifts of up to 31.0mmHg, 25.2mmHg, and 26.0 mmHg, respectively.

Table 5.5: Global systolic, diastolic, and mean arterial pressure when prescribing a range of 3EWM BC combinations (see Appendix A.6, Table 1-3) to the thoracoabdominal aorta of patient 4.

	Patient 4		
Windkessel Paremeter Combination	**Global Systolic Pressure (mmHg)**	**Global Diastolic Pressure (mmHg)**	**Global Mean Pressure (mmHg)**
BC1	137 ± 10.3	72.9 ± 3.88	99.3 ± 1.78
BC2	149 ± 5.44	86.6 ± 0.738	115 ± 1.5
BC3	118 ± 1.46	61.4 ± 0.562	89.5 ± 0.758

Finally, the application of different 3EWM BC combinations also impacted the near-wall haemodynamics throughout the aorta. As a representative example, Figure 5.19 illustrates the differences in OSI and TAWSS between the boundary combination 1 (BC1), and boundary condition combination 2 (BC2). Regarding TAWSS, the spatial distribution remained relatively constant, though there was a notable change in magnitude (Figure 5.19A) of up to 14.3Pa. This was particularly apparent in the distal section of the iliac arteries, left subclavian artery, and coeliac artery. Throughout the rest of the aorta, the differences were minimal at roughly 0-1.5Pa. Similarly, there were substantial differences in OSI distribution between CFD

simulations due to the prescription of different BC combinations (Figure 5.19B). Noting that OSI is a non-dimensional quantity with a range of 0-0.5, the discrepancies of up to 0.39 observed in Figure 5.19B represent a substantial variation. Individual TAWSS & OSI distributions can be found in Appendix B.2.

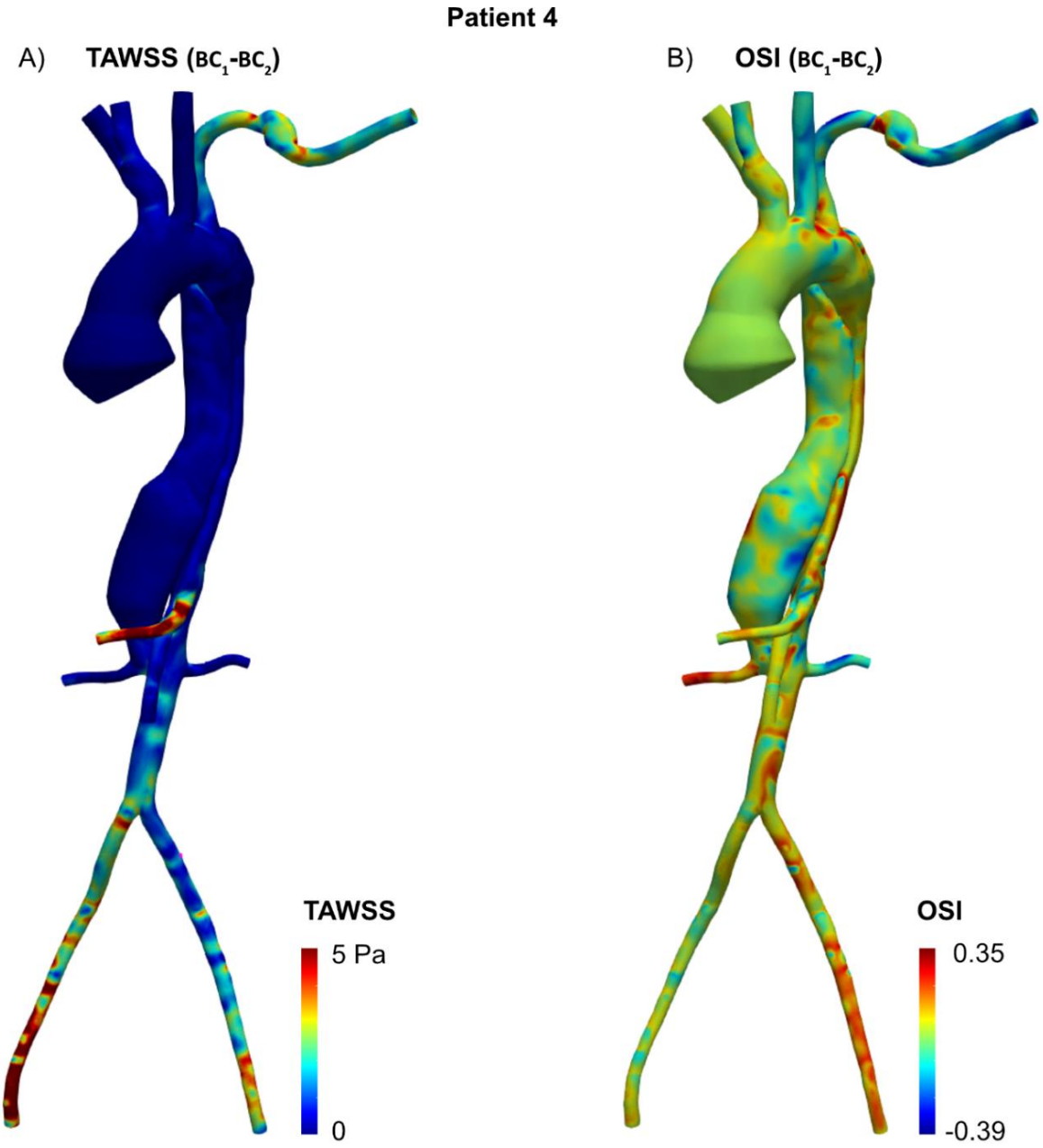

Figure 5.19: Differential distribution of A) TAWSS and B) OSI between 3EWM BC combination 1 (BC1) and 3EWM BC combination 2 (BC2). Contours represent the Boolean difference (BC_1-BC_2) between the 3D CFD results.

5.4 Discussion

5.4.1 1D Modelling

A 1D model was used to generate initial pressure waveforms for BC calibration for each individual. Literature suggests these comparatively simple and computationally efficient models still provide clinically relevant information [46] [47] [54] [86]. However, 1D models tend to yield more accurate results in healthy arteries when blood flow is predominantly unidirectional and there are no sudden changes in the vessel cross-sectional area [29] [49] [138]. This is because they require additional empirical laws to capture secondary flow in the radial and circumferential directions, and pressure losses in pathological regions, whereas 3D models intrinsically capture these geometric complexities [36] [49] [138]. Consequently, the 1D model may not have captured the intricacies of AD-related flow. However, this was not their primary purpose in this work; they were just used for an initial, computationally-efficient way to generate temporally resolved pressure estimates for each individual in the subsequent BC calibration process.

In the field of 1D arterial modelling, there is no consensus on the optimal number of arterial segments necessary to obtain the most physiologically accurate pressure and flow waveforms [48]. Some studies use as many as 4 million segments [48]. Of course, an increased number of segments results in an increased number of vessel wall parameters which must be assumed, meaning this becomes increasingly challenging and prone to errors. Thus, a 1D model with multiple segments is not necessarily better. However, there are some factors which must be considered with the more coarse models. For example, it is known that as vessel segments are lumped together, this can result in some smoothing of the pressure waveform [48].

In our study, we used between 23-33 segments for the 1D analogues of the clinical patients. In literature, such analogues often incorporate the aorta and large branches down to the fifth generation of bifurcations [48]. Regarding the 1D models presented in this study, these were limited to only the first generation of bifurcations for several reasons. Firstly, the imaging resolution of the 4D Flow-MRI model was insufficient to resolve flow past the first bifurcation, meaning there was no patient-specific flow information to assist with the parameter estimation and calibration process. Secondly, incorporating more segments into a 1D model requires a proportional increase in the number of assumptions which must be made for the vessel walls, and each generation of bifurcations results in an exponential increase in the number of outlet 3EWM BCs which must be estimated and prescribed.

For this study, it was of primary importance to maintain optimal patient-specificity in all computational models, rather than to resolve arterial vessels through several generations of bifurcations. Therefore, the 1D analogue was truncated after the first bifurcation of each branch vessel and coupled to a 0D 3EWM. Literature suggests this 0D-1D truncation is a valid approach which can be implemented with only a minimal increase in calculated pressure errors <5% [48]. Thus, we maintain patient-specificity and model simplicity, with minimal sacrifice to calculation errors.

5.4.2 Perfusion Distribution

The 4D Flow-MRI and CFD-derived perfusion distributions for the healthy volunteers closely match values found in literature, obtained through different techniques. For example, Konoura et al. [41] and Nakamura et al. [42] quantified the partitioning of flow (of healthy individuals) through phase-contrast magnetic resonance imaging (PC-MRI). They observed values of 13.0±1.5%, 15.7±3.2%, 15.7±3.2%, and 71.1±4.6% through the innominate, LCCA, LSA, and descending regions, respectively. This validates the 4D Flow-MRI sequence used in our study, also noting that the general technique of 4D Flow-MRI has been previously validated against 2D PC-MRI and echocardiography [88] [98].

The inter-patient discrepancy in perfusion distribution is low at each branch, indicating that, in the absence of aortic pathology, the perfusion distribution remains fairly constant. For example, differences in branch perfusion rates only range from 0.67% to up to 3.87% of inlet flow. This result may suggest that patient-specific 3EWM BCs are less important for healthy CFD cases since each combination yields similar results. It must be noted that this study represents a small sample size, meaning this observation cannot be suggested for the wider healthy population.

Regarding the dissection cases, the inter-patient differences in the branch perfusion distribution are more substantial. Here, the net perfusion discrepancies in individual branches can range from 2.20% to up to 16.2% of inlet flow, particularly in the subclavian arteries, superior mesenteric artery, and left iliac artery. This inter-patient variability suggests that the presence of an aortic dissection leads to a unique distribution of flow due to the highly individualised structural changes inflicted on the aorta. It is apparent, for instance, that the FL diverts blood away from the TL, thereby reducing flow to branches perfused by the TL. This is important clinically, as the direction and flow rate of blood between the TL and FL contribute significantly to the pathophysiology [51]. Further, the success of stent-graft implementation is contingent on an accurate knowledge of this inter-luminal flow exchange [252]. In TBAD

cases, it is also known that this flow exchange between the TL and FL is highly correlated to the enlargement of the FL [252]. Subsequent enlargement of the FL can lead to further compression of the TL, thus increasing the hydraulic resistance of the TL and reducing blood flow [59].

As such, there were several factors which impacted perfusion distribution. These were disease severity, pathological wall stiffening, the size of the FL, the primary tear initiation region, the location of intraluminal tears, the number and size of the intraluminal tears, and the degree of TL compression, the division of flow between the TL and FL, and whether the aortic branches originate from the TL as opposed to the FL. Consequently, capturing this perfusion distribution via 0D-3D CFD in AD patients requires carefully calibrated 3EWM parameters.

5.4.3 Instantaneous Flow Waveforms (CFD vs 4D Flow-MRI)

Though the 0D-3D models outlined in this Chapter successfully replicate the net perfusion distribution, they did not accurately capture the time-resolved branch flow rates observed via 4D Flow-MRI. This poses the question as to why the time-resolved branch flow rates were not prescribed directly at the CFD outlets. This was avoided for several reasons in favour of calibrated 3EWM BCs. Firstly, it is known from literature that the prescription of flow waveforms fails to yield correct pressure measurements since the downstream resistance and compliance is not accounted for, unlike in 3EWM BCs [86]. Secondly, for treatment planning and outcome prediction, prescription of time-resolved flow waveforms as BCs is not relevant since these waveforms themselves form part of the desired solution [33].

Initially, one may assume that the rigid wall simulation contributed to discrepancy in CFD and *in vivo* branch waveforms, and that modelling compliance may solve the issue. However, while compliant walls would result in increased cross-sectional area at systole, and thus a decrease in velocity, this would not impact flow rate. This suggests that the discrepancies between the *in vivo* and CFD-derived branch flow waveforms are a result of the 3EWM BC parameters. Prior to further investigation to identify a resolution to this issue, it is important to acknowledge a fundamental limitation of the 3EWM BCs. Literature indicates that while these BCs are used ubiquitously, they may struggle to deliver accurate, time-resolved pressure and flow waveforms at the branch outlets of 0D-3D CFD models [36]. Primarily, the aim of our study was to accurately model net perfusion distributions and near-wall haemodynamics within a 0D-3D numerical framework. This was achieved successfully. Consequently, the discrepancies in

the temporally resolved branch flow rates may represent an intrinsic, albeit secondary limitation of our proposed methodology.

Though this was of secondary importance, it is still important to determine a possible solution to the issue. Most notably, the 3EWM BCs were calibrated within a 0D framework, in the absence of a 3D component. In this domain, there was a very close match between the time-resolved CFD and *in* vivo flow rates. Thus, it is possible that the 3EWM parameter combination which performed optimally in the 0D domain did not translate well to the 0D-3D numerical framework. To rectify this, one possibility is to perform the entire parameter calibration process in a 0D-3D framework. However, this would be computationally prohibitive and time consuming since the results suggest the 3EWM parameter calibration requires roughly 100 iterations. For context, a single iteration within the 0D-3D domain would take 26 ± 9.6 hours.

There exists a potential compromise between these approaches. The CFD-derived waveforms demonstrate a tendency to overestimate flow rate during the systolic phase. During 3EWM calibration, it was noted that altering Z had a profound effect on the systolic peak, where a decrease in this parameter yielded an increase in peak systolic flow rate. Therefore, it may be possible to perform the initial calibration process in the computationally efficient 0D domain, followed by coupling the 3EWM with the 3D CFD model to run a few final iterations, tweaking Z as required. This remains a somewhat time-consuming process and requires a subjective, user-defined parameter change, but may represent a compromise to improve the temporal flow rates. Alternatively, future work should tune all branch BCs simultaneously in a more complex, multicompartmental 3EWM model [79].

5.4.4 Near-Wall Haemodynamics

It is crucial to capture both the TAWSS and OSI. This is because TAWSS captures the magnitude of shear stress, but contains no spatial information, while OSI characterises the directionality and variability of the flow. The spatial distribution of OSI and TAWSS remained fairly constant between the healthy models. This is because, while there are inter-patient variations in geometry, all healthy individuals share the same general aortic anatomy [9] [43]. Interestingly, for these healthy volunteers, the localised regions of high WSS distal to the LSA branch ostia coincide with the tear initiation regions of patient 1 and 2. This reinforces the principle that AD primary tears are spatially correlated with areas of high shear stress and disturbed flow [9] [69] [79].

Regarding the dissection patients, the magnitudes of TAWSS throughout the aorta and main branches were substantially larger (up to 34Pa) than those of the healthy volunteers (up to 9.85Pa). This was primarily due to a combination of jet flow through intraluminal tears, narrow sections of the false lumen which increases fluid velocity, and a more turbulent flow regime. The inter-patient variability of TAWSS was also increased in dissection patients in comparison to healthy volunteers, highlighting that the severity and configuration of the dissection have a significant impact on this parameter.

OSI was also heavily influenced by the presence and configuration of an aortic dissection. Notably, both OSI and TAWSS demonstrate a tendency to increase around regions of anatomical discontinuities which result in abnormal flow. This is consistent with previous studies [252]. As expected, the TL in all patients exhibited a low OSI since the direction of blood flow is unidirectional, while the FL experienced a higher OSI due to a more turbulent flow regime. Notably, the turbulent flow induced during the systolic deceleration and diastolic phases seemed to primarily influence regions of high OSI.

This disparity in OSI between the TL and FL is consistent with previous studies [4] [178] [59]. Importantly, TAWSS and OSI cannot be investigated in isolation. By considering the distribution and magnitude of both parameters, it was possible to see that the FL in all patients exhibits low TAWSS, yet high OSI. This detrimental combination of high OSI and low TAWSS indicated that the FL is unstable, with a proclivity to expand [15] [28] [60] [73] [79] [257] [258]. Through CFD analysis as presented in this study, derived from 4D Flow-MRI data, it may be possible to identify patients most at risk of FL rupture to permit patient triage for surgical intervention. This is especially true since risk assessments in TBAD patients are performed via analysis of WSS as a primary parameter [51]. Of course, such a statement requires a larger sample size and long-term analysis in order to be validated.

5.4.5 Wall Treatment

The 0D-1D models used to generate initial pressure waveforms were prescribed with wall elasticity. However, the 0D-3D CFD models were assumed to have rigid walls. The general consensus in literature is that wall compliance influences the haemodynamics of CFD models [34] [36] [76] [261] [262]. Generally, accounting for wall compliance yields reduced fluid velocities, reduced instantaneous WSS, and alters the magnitude of OSI [37] [76] [261]. However, it does not tend to significantly alter the ratio at which flow splits throughout the branch vessels, the magnitude and spatial distribution of TAWSS, or the spatial distribution of

OSI [37] [76] [261]. The degree to which wall motion and compliance should be modelled is therefore unclear. Some literature maintains that wall motion can be neglected in large arteries like the aorta [36] [261] [262]. Other studies suggest it is essential, especially in regions of aortic pathology [76] [60] [263]. This may be particularly important in AD cases, where wall motion may have a clinically relevant impact, especially since intraluminal pressure is impacted [60] [59] [78] [79]. Further, without modelling compliance, it was not possible to model the motion of the intimal flap which is known to influence the results of TBAD CFD models [76].

This is not a simple task, however. Besides being computationally expensive, models which include wall compliance rely on assumptions of vessel wall mechanical properties and thickness. However, there is no consensus on how best to define these [60] [59] [79]. In the case of ADs, assumptions relating to wall compliance are particularly challenging since the vessel wall tends to display more abnormal and anisotropic properties [60] [59] [79].

A final benefit of 4D Flow-MRI as a precursor to CFD modelling is that wall motion can be measured directly from the imaging dataset. In our study, both translational movement and changes in cross-sectional area were observed. Therefore, these can be prescribed directly to the CFD model to include wall motion without having to rely on assumptions. Previous studies suggest this is a viable, and perhaps more attractive alternative to FSI modelling [62] [78]. As planes of analysis can be placed retrospectively on imaging software to measure this wall motion from 4D Flow-MRI, it is possible to elucidate this information from any location throughout the aorta. Therefore, to balance model complexity with clinical relevance, one may prescribe average wall motion over large aortic segments, with highly refined motion in isolated areas of interest such as tear locations. This should be performed as part of future work.

Additionally, future work should also seek to address whether rigid wall CFD simulations, in comparison with compliant simulations, have a significant effect on near-wall haemodynamics in regions of aortic stent-grafts. Since it is known that stent-grafts are less compliant than the native artery wall, it is possible that the assumption of a rigid boundary is more valid in these cases.

5.5 Limitations

The study had several limitations. Though 4D Flow-MRI is an extremely versatile imaging modality, it also presented intrinsic weaknesses. These included a limited spatiotemporal resolution, velocity aliasing, and phase offset errors [51] [99] [59] [263]. Additionally, metal

artefacts were present due to the presence of the Anaconda™ stent graft, likely inducing a degree of error in the *in vivo* data of patient 1 [99].

In the 0D-1D models, gravity was neglected, though literature suggests it may be an important factor in the calculation of flow within large vessels such as the aorta [21]. Further, wall compliance was modelled as an isotropic, elastic material in the 1D segments. However, in native blood vessels, it is known that the wall demonstrates viscoelasticity with an anisotropic distribution of mechanical properties [29] [32] [34] [76]. The assumption of isotropy is generally accepted to permit simpler descriptions of the mechanical behaviour of the arterial wall, while the assumption of compliance was utilised to minimise the number of excess variables requiring calibration [32] [34] [76].

Like the previous chapter, a non-Newtonian assumption was utilised for blood viscosity. In future work, a shear-thinning Newtonian model for blood viscosity should be utilised.

At the inlet of the 0D-3D CFD models, the effect of the aortic valve was neglected. Literature suggests this valve can cause highly disturbed flow in regions of the supra-aortic branch vessels, altering shear stress and pressure within the arch, and thus in the region of the primary tears [264]. Also, the 4D Flow-MRI velocity information was not mapped exactly onto the CFD inlet. Instead, we use a spatially uniform profile since this information was not readily obtainable from cvi42®.

Finally, the proposed 0D-3D CFD models cannot model the homeostasis mechanisms which auto-regulate blood flow throughout the body of all individuals. For example, these models cannot account for sympathetic and parasympathetic neuro-regulation, biochemical regulation, pressure-dependent vessel compliance, cardiopulmonary interaction, and the effect of venous valves [36]. However, these mechanisms of homeostasis are outwith the scope of this research.

5.6 Conclusion

In conclusion, through patient-specific 0D-3D CFD modelling, it was determined that the healthy volunteers had minimal inter-patient variability in near-wall haemodynamics and perfusion distribution. The TBAD patients, however, exhibited substantially higher inter-patient variability in these metrics. Further, TBAD patients exhibited higher TAWSS values, higher pressures, and more extensive regions which experience higher OSI than healthy cases. This Chapter also showed that, for complex TBAD cases, the 3EWM BC calibration methodology yielded perfusion distributions which were very similar to the *in vivo* data. However, it must be noted that the CFD-derived time-resolved flow waveforms tended to

overestimate systolic flow, underestimate diastolic flow, and exhibit a more oscillatory magnitude during diastole when compared to the *in vivo* data. Finally, it was clear that different 3EWM BC combinations had a substantial impact on the perfusion distribution and near-wall haemodynamics. Consequently, TBADs are highly individualised pathologies which require careful calibration of BCs. Finally, to generate sufficient contrast within the lumen of TBAD patients for the creation of CPC-MRA images for subsequent reconstruction, this would require multi-VENC MRI. This is to capture the low velocity of blood within the FL, along with the high velocity of blood within the TL.

5.7 Research Contribution

In Chapter 5, we generated patient-specific, full thoracoabdominal CFD models of three TBAD patients. Similarly, we generated patient-specific CFD models of the thoracic aorta of three healthy volunteers. This Chapter primarily expands on the work outlined in Chapter 3 and 4. Here, we used these methodologies to investigate the arterial heamodynamics in a larger patient population and extended region of interest, thus facilitating a more comprehensive analysis. Specifically, this analysis involved a comparison between the flow regime and hemodynamics within the TBAD patients compared to healthy volunteers. Further, the inter-patient variations in perfusion distribution and near wall haemodynamics within the TBAD population were studied. Thereafter, we investigated the influence of the Windkessel BCs by assessing how different parameter combinations impact the haemodynamics of a single TABD arterial geometry. Finally, we evaluate the pre- and post-surgical (stent-graft deployment) heamodynamics of a single patient. The main contributions of this Chapter were:

1) With single-VENC 4D Flow MRI, the image processing methodology outlined in Chapter 3 did not generate sufficient contrast throughout the entire false lumen of TBAD patients to facilitate segmentation and reconstruction. Therefore, CT images were required. With multi-VENC 4D Flow-MRI, we expect this limitation would be resolved.
2) TAWSS and time-averaged pressure is elevated in TBAD patients when compared to healthy individuals, with regions of max TAWSS located in the region of intraluminal tears. Further, the inter-patient differences in TAWSS and OSI is greater in TBAD patients than the differences observed in healthy individuals.
3) Even in the presence of multiple large secondary tears, the distribution of flow between the true and false lumen remains consistent along the length of the dissection. Additionally, there was evidence of flow interaction between the true and false lumen,

with flow entering the true lumen, primarily during systolic acceleration and peak systole, and flow entering the false lumen primarily during systolic deceleration.

4) When a full thoracoabdominal model is considered, the difference in time-averaged pressure distribution between the true and false lumen was minimal. This was different to the thoracic model which, when truncated at the descending aorta, produced a different pressure relationship. This indicates that truncation of a TBAD before the re-entry tear will influence the CFD results.
5) Different combinations of Windkessel BCs resulted in considerable differences in the CFD-derived perfusion distribution and near wall haemodynamics. Regarding TAWSS, the spatial distribution remained relatively constant, with large differences in magnitude. For OSI, both the magnitude and spatial distribution differed substantially. This highlights the importance of using calibrated BCs of TBAD CFD models. Notably, the impact of BCs was less substantial in the aortae healthy volunteers.

6 Thesis Conclusion & Future Work

In this thesis, we showed for the first time that it was possible to enhance intraluminal contrast within the aorta by deriving velocity-based images from low-resolution 4D Flow-MRI data without sacrificing spatial information. With these novel CPC-MRA images, it was possible to distinguish the entire aorta of healthy volunteers, and the TL of dissected aortae. Notably, the processing techniques outlined are readily achieved on commercial software, which is essential for integration into future clinical pathways.

This proof-of-concept study demonstrated uniform signal intensity within the lumen, clearly contrasted with surrounding tissue, and preserved the 3D relationships of the vasculature, unlike conventional maximum intensity projection images which are the current gold-standard. Furthermore, our methodology required no intravenous contrast agents and could be performed on retrospective data sets. However, it was not possible to generate sufficient contrast within the FL of dissected aortae due to low blood velocity, resulting in a poor signal-to-noise ratio, or a complete inability to distinguish the FL. This meant CT imaging was required to reconstruct the aorta of TBAD cases. To rectify this, we propose that an accelerated multi-VENC 4D Flow-MRI scan sequence, utilising acceleration techniques such as SENSE or GRAPPA, should be investigated in future work as a prospective study. This would provide the dynamic range of velocities required to optimally capture flow information in both the TL and FL, while minimising scan time within clinically acceptable limits.

Additionally, these prospective studies should ensure an isotropic voxel resolution $<2mm^3$ in line with the recent consensus on 4D Flow-MRI for clinical and research use. By prescribing a high VENC to capture blood flow within the TL in combination with a low VENC to capture flow within the FL, we theorise that this will generate sufficient signal intensity to reconstruct both lumens from the CPC-MRA images. If successful, this would mean the full thoracoabdominal aorta of TBAD patients can be reconstructed from 4D Flow-MRI, thus negating the need for CT imaging. To promote clinical uptake, future work should seek to include machine-learning based segmentation and reconstruction techniques, for example the U-Net based architectures which employ convolutional neural networks. This would promote rapid, automated, and objective reconstructions which can be standardised across multiple centres.

Thereafter, we demonstrated a novel methodology to estimate and calibrate 3EWM BCs for 0D-3D CFD models from temporally resolved branch flow waveforms from retrospective 4D

Flow MRI data. To date, this has not been performed in previous studies. Based exclusively on non-invasive measurements, the arterial impedance, resistance, and compliance parameters were rapidly calibrated in a computationally efficient, reduced-order framework. Preliminary simulations then determined that the net perfusion distribution of these 0D-3D CFD models closely matched the *in vivo* data. However, the instantaneous branch flow waveforms in the CFD models displayed a tendency to overestimate flow during systole, and subsequently underestimate flow during diastole. To improve clinical applicability and enhance confidence in the simulation results, future work should employ FSI or MBM techniques to model wall compliance in the 3D domain, with a particular focus on resulting the intraluminal dissection flaps. Additionally, prospective scans should be accompanied by 2D PC-MRI to further validate the 4D Flow-MRI derived waveforms on a case-by-case basis.

Finally, these two novel methodologies were employed to generate patient-specific CFD models for multiple different TBAD case studies. This involved the numerical investigation of blood flow throughout the thoracic aorta of three healthy volunteers, and the thoracoabdominal aorta of four TBAD patients. This investigation highlighted that the net perfusion distribution in these more complex cases again closely matched *in vivo* data. To date, no other study has investigated the effect of AD geometry and boundary conditions on the resultant branch perfusion distribution as we have, particularly in relation to healthy individuals.

In the TBAD models, the FL was characterised by high OSI and low TAWSS as expected, while high TAWSS and high OSI were observed near intraluminal tears. Additionally, turbulent flow was present in bulbous aortic segments, and there was a clear interaction of blood flow between the TL and FL. TBAD patients also exhibited higher pressures and shear stresses when compared to healthy volunteers. Finally, it was determined that TBAD cases exhibited substantial inter-patient variability in the perfusion distribution, intraluminal pressure, and near-wall haemodynamics, especially when compared to the relatively low inter-patient variability of healthy cases. Consequently, this suggested that while generalised BCs may be applicable for healthy models, TBAD models require careful BC calibration to capture the unique characteristics of each case. It was evident that TBAD is a highly individualised pathology, each with unique haemodynamics, thus requiring patient-specific predictive models. This expands on much of the current literature, which often uses non-patient-specific BCs in TBAD simulations.

Leveraging CFD in combination with 4D Flow-MRI, effectively mitigates the intrinsic limitations of each approach. With 4D Flow-MRI, one may extract *in vivo* flow rates, wall motion, and elucidate qualitative and quantitative information on the evolution of the 3D flow regime throughout the cardiac cycle. However, the spatiotemporal resolution is limited, and it is difficult to extract pressure or near-wall haemodynamics. CFD, in contrast, offers a significantly enhanced level of detail, including extremely high spatiotemporal resolution and can readily calculate clinically relevant parameters such as pressure, TAWSS, and OSI. Of course, the disadvantage of CFD modelling is that the output is only as good as the inputs. With 4D-Flow MRI to inform these inputs, this source of uncertainty is minimised. It should be noted, however, that 4D Flow-MRI is not yet a routinely used imaging modality in clinical practice. Instead, it is predominantly a research tool. However, it should be noted that 4D Flow-MRI is becoming increasingly available and supported by major MRI vendors, with commercially available post-processing tools receiving FDA approval and CE marking for clinical use in certain countries.

The ultimate hypothesis this thesis sought to address was that fully patient-specific CFD models of TBADs can be created based exclusively on a single 4D Flow-MRI scan, and that these models can be used for treatment planning in TBAD cases. Though some elements require additional work for validation, the preliminary answer is yes, using the methodologies described. All of the information for patient-specific CFD modelling can be extracted from a single 4D flow-MRI scan, therefore reducing patient burden. Further, this is performed in the absence of intravenous contrast, ionising radiation, or invasive pressure and flow measurements. Hence, this approach would rely on readily obtainable *in vivo* data, thereby minimising assumptions. Due to the retrospective nature of the datasets utilised in this thesis, multi-VENC 4D Flow-MRI was not available. However, if multi-VENC imaging could be utilised, this would permit the reconstruction of the entire geometry, and allow for the extraction of wall motion at all regions.

To understand how this work presented in this thesis may impact future clinical care, it is important to identify where it may sit within the clinical pathway. Likely, 4D Flow-MRI would be employed as a complementary imaging modality to more conventional approaches including CT angiography and 2D PC-MRI. This would primarily be for complex cases such as AD's where the medical professional requires additional haemodynamic information and an understanding of the temporal evolution of flow throughout the cardiac cycle.

In cases where near wall haemodynamics and flow parameters which cannot readily be obtained *in vivo* are required, CFD modelling may be required. Therefore, patients who obtain this 4D Flow-MRI scan may undergo aortic reconstruction from CPC-MRA images to retrospectively improve intraluminal contrast, particularly if the scan is deemed low-resolution. Thereafter, automatic segmentation and reconstruction methodologies would likely be employed through a U-NET architecture, while automatic mesh generation and quality assessment could be performed through MVE-Net or MeshingNet3D. To be done in clinically acceptable timeframes, hospitals would require access to high-end graphical processing units or cloud computing to cope with the computational demand. Subsequently, CFD boundary conditions may be calibrated as described in Chapter 4, along with directly prescribed wall compliance through the MBM method, resulting in a high-fidelity simulation from readily obtainable *in vivo* information, with minimal assumptions.

Results, similar to those obtained in Chapter 5, could then provide information relating to the intraluminal flow regime, including blood velocity, turbulence, helicity, vorticity, and near-wall haemodynamics, along with pressure distribution and other parameters which are difficult to measure *in vivo*. This complementary *in silico* investigation could then be used for several clinical purposes. For example, it may be used for screening patients who are at risk of developing an AD, such as those with Marfan Syndrome or other connective tissue disorders. Additionally, these investigations can elucidate information regarding disease progression and false lumen thrombosis to identify unstable pathologies which require prompt intervention. In patients who require intervention, the same combination of 4D Flow-MRI and CFD could be used to simulate different open or endovascular or stent-graft repair scenarios to identify the most optimal graft and surgical approach on a case-by-case basis. Similarlythese models could be used to predict the risk of peripheral organ malperfusion, in-stent thrombosis, post-surgical aneurysm formation, endoleaks, or widening of the entry tear section following stent-graft deployment. Conversely, it would also be possible to obtain information on how the pulsatile environment within the aorta impacts the stent-graft, to identify potential regions of high mechanical stress which may damage the metal stent.

Therefore, the work presented in this thesis contributes towards the field of clinically relevant CFD modelling for data-driven clinical decision making, including patient screening, risk stratification, triage, diagnosis, surgical planning, and disease progression.

References

[1] M. Salameh and E. Ratchford, "Aortic Dissection," *Vascular Medicine,* vol. 21, no. 3, pp. 276-2800, 2016.

[2] D. Levy, A. Goyal, Y. Grigorova, F. Farci and J. K. Le., "Aortic Dissection," StatPearls, 2018.

[3] F. Criado, "Aortic Dissection: A 250-Year Perspective," *Texas Heart Institute Journal,* vol. 38, no. 6, pp. 694-700, 2011.

[4] D. Liu, Z. Fan, N. Zhang, Z. Sun, J. An, A. Stalder, A. Greiser and J. Liu, "Quantitative Study of Abdominal Blood Flow Patterns in Patients with Aortic Dissection by 4-Dimensional Flow MRI," *Scientific Reports,* vol. 8, no. 9111, 2018.

[5] T. Crawford, R. Beaulieu, B. Ehlert, E. Ratchford and J. Black, "Malperfusion Syndromes in Aortic Dissection," *Vascular Medicine,* vol. 21, no. 3, pp. 264 - 273, 2016.

[6] K.-S. Liu, C.-H. Lee, F.-C. Tsai, G.-H. Jhong, K.-C. Hung and S.-J. Liu, "Computational Analysis of the Mechanical Behaviors of Hemiarch and Total Arch Replacements," *Annals of Biomedical Engineering,* vol. 43, no. 12, pp. 2881-2891, 2015.

[7] B. Fitzgibbon, F. Jordan, N. Hynes, J. P. McGarry, E. P. Kavanagh, P. McHugh, D. Veerasingam and S. Sultan, "Endovascular versus open surgical repair for complicated chronic type B aortic dissection," *The Cochrane Database of Systematic Reviews,* vol. 12, no. 12, 2018.

[8] C. Nienaber, R. Clough, N. Sakalihasan, T. Suzuki, R. GIbbs, F. Mussa, M. Jenkins, M. Thompson, A. Evangelista, J. Yeh, N. Cheshire, U. Rosendahl and J. Pepper, "Aortic Dissection," *Nature Reviews Disease Primers,* vol. 2, no. 16053, 2016.

[9] F. M. Callaghan and S. M. Grieve, "Normal patterns of thoracic aortic wall shear stress measured using fourdimensional flow MRI in a large population," *American Journal of Physiology, Heart and Circulatory Physiology,* vol. 315, no. 5, pp. 1174-1181, 2018.

[10] S. W. English and J. P. Klaas, "Neurologic complications of diseases of the aorta," in *Handbook of Clinical Neurology*, 2021, pp. 221-239.

[11] R. Janosi, T. Buck and R. Erbel, "Mechanism of Coronary Malperfusion Due to Type-A Aortic Dissection," *Herz Kardiovaskuläre Erkrankungen,* vol. 34, no. 478, 2009.

[12] R. W. Hsieh, T.-C. Hsu, M. Lee, W.-T. Hsu, S.-T. Chen, A. H. Huang, A. L. Hsieh and C.-C. Lee, "Comparison of type B dissection by open, endovascular, and medical treatments," *Journal of Vascular Surgery,* vol. 70, no. 6, pp. 1792-1800, 2019.

[13] G. Kuzmik, A. Sang and J. Elefteriades, "Natural history of thoracic aortic aneurysms," *Journal of Vascular Surgery,* vol. 56, no. 2, pp. 565-571, 2012.

[14] S. Xydas, C. Mihos, R. Williams, A. LaPietra, M. Mawad, H. Wittels and O. Santana, "Hybrid repair of aortic arch aneurysms: a comprehensive review," *Journal of Thoracic Disease,* vol. 9, no. 7, pp. 629-634, 2017.

[15] A. Nardi and I. Avrahami, "Approaches for treatment of aortic arch aneurysm, a numerical study," *Journal of Biomechanics,* vol. 50, pp. 158-165, 2017.

[16] N. Aristokleous, N. Kontopodis, K. Tzirakis, C. Ioannou and Y. Papaharilaou, "Hemodynamic impact of abdoinal aortic aneurysm stent-graft implantation induced stenosis," *Medical and Biological Engineering and Computing,* vol. 54, pp. 1523-1532, 2016.

[17] G. Fung, S. Lam, S. Cheng and K. Chow, "On stent-graft models in thoracic aortic endovascular repair: A computational investigation of the hemodynamic factors," *Computers in Biology and Medicine,* vol. 38, pp. 484-489, 2008.

[18] I. WU, P. Liang, S. Huang, N. Chi, F. Lin and S. Wang, "The Significance of Endograft Geometry on the Incidence of Intraprosthetic Thrombus Deposits after Abdominal Endovascular Grafting," *European Journal of Vascular and Endovascular Surgery,* vol. 38, no. 6, pp. 741-747, 2009.

[19] X. Yang, X.-C. Dai, J.-C. Zhu, Y.-D. Luo, H.-L. Fan, Z. Feng, Y.-W. Zhang and F.-G. Hu, "Threatment for thoracoabdominal aortic aneurysm by fenestrated endovascular aortic repair with physician modified stent graft," *Journal of International edical Research,* vol. 46, no. 5, pp. 2014-2022, 2018.

[20] E. Cullen, E. Lantz, C. Johnson and P. Young, "Traumatic Aortic Injury: CT findings, mimics, and therapeutic options," *Cardiovasular Diagnosis and Therapy,* vol. 4, no. 3, pp. 238-244, 2014.

[21] I. Avrahami, M. Brand, T. Meirson, Z. Ovadia-Blechman and M. Halak, "Hemodynamic and mechanical aspects of fenestrated endografts for treatment of abdominal aortic aneurysm," *European Journal of Mechanics and Biofluids,* vol. 35, pp. 85-91, 2012.

[22] G. Kumpati, A. Patel and D. Bull, "Thrombosis of a descending thoracic aortic endovascular stent graft in a patient with factor V Leiden: case report," *Journal of Cardiothoracic Surgery,* vol. 9, no. 47, 2014.

[23] A. White, S. J. Bozso, M. Ouzounian, M. W. Chu and M. C. Moon, "Acute type A aortic dissection and the consequences of a patent false lumen," *JTCVS Techniques,* vol. 9, pp. 1-8, 2021.

[24] A. Coelho, C. Nogueira, M. Lobo, R. Gouveia, J. Campos, R. Augusto, N. Coelho, A. C. Semião, J. P. Ribeiro and A. Canedo, "Impact of Post-EVAR Graft Limb Kinking in EVAR Limb Occlusion: Aetiology, Early Diagnosis, and Management," *European Journal of Vascular and Endovascular Surgery,* vol. 58, no. 5, pp. 681-689, 2019.

[25] V. Govindarajan, V. Rakesh, J. Reifman and A. Y. Mitrophanov, "Computational Study of Thrombus Formation and Clotting Factor Effects under Venous Flow Conditions," *Biophysical Journal,* vol. 110, no. 8, pp. 1869-1885, 2016.

[26] K. A. Mosevoll, 1. S. Johansen, Ø. Wendelbo, I. Nepstad, Ø. Bruserud and H. Reikvam, "Cytokines, Adhesion Molecules, and Matrix Metalloproteases as Predisposing, Diagnostic, and Prognostic Factors in Venous Thrombosis," *Frontiers in Medicine,* vol. 22, no. 5, 2018.

[27] N. Mackman, "New insights into the mechanisms of venous thrombosis," *Journal of Clinical Investigation,* vol. 122, no. 7, pp. 2331-2336, 2012.

[28] D. N. Ku, "Blood Flow in Arteries," *Annual Review of Fluid Mechanics,* vol. 29, pp. 399 - 434, 1997.

[29] J. Alastruey, K. Parker and S. Sherwin, "Arterial pulse wave haemodynamics," in *11th International Conference on Pressure Surges*, Lisbon, 2012.

[30] Y. Qian, J. Liu, K. Itatani, K. Miyaji and M. Umezu, "Computational Hemodynamic Analysis in Congenital Heart Disease: Simulation of the Norwood Procedure," *Annals of Biomedical Engineering,* vol. 38, no. 7, pp. 2302-2313, 2010.

[31] T. Pedley, "Mathematical modelling of arterial fluid dynamics," *Journal of Engineering Mathematics,* vol. 47, pp. 419-444, 2003.

[32] J. K.-J. Li, "Sex-Specific Analysis of Cardiovascular Function," in *Arterial Wall Properties in Men and Women: Hemodynamic Analysis and Clinical Implications*, Springer International Publishing, 2018, pp. 291-323.

[33] L. Grinberg and G. E. Karniadakis, "Outflow Boundary Conditions for Arterial Networks with Multiple Outlets," *Annals of Biomedical Engineering,* vol. 36, no. 9, pp. 1496-1514, 2008.

[34] T. C. Gasser, "Chapter 8: Aorta," in *Biomechanical of Living Organs: Hyperelastic Constitutive Laws for Finite Element Modelling*, Elselvier Inc, 2017, pp. 169-191.

[35] K. Jarvis, M. B. Scott, G. Soulat, M. S. M. Elbaz, A. J. Barker, J. C. Carr and M. Markl, "Aortic pulse wave velocity evaluated by 4D flow MRI across the adult lifespan," *Journal of Magnetic Resonance Imaging,* vol. 56, no. 2, pp. 464-473, 2022.

[36] Y. Shi and P. Lawford, "Review of Zero-D and 1-D Models of Blood Flow in the Cardiovascular System," *Biomedical Engineering Online,* vol. 10, no. 1, 2011.

[37] S. Miyazaki, K. Itatani, T. Furusawa, T. Nishino, M. Sugiyama, Y. Takehara and S. Yasukochi, "Validation of numerical simulation methods in aortic arch using 4D Flow MRI," *Heart and Vessels,* vol. 32, no. 8, pp. 1032-1044, 2017.

[38] W. Seed and N. Wood, "Velocity patterns in the aorta," *Cardiovascular Research,* vol. 5, pp. 319-330, 1971.

[39] A. Stalder, A. Frydrychowicz, M. Russe, J. Korvink, J. Henning, K. Li and M. Markl, “Assessment of Flow Instabilities in the Healthy Aorta Using Flow-Sensitive MRI,” *Journal of Magnetic Resonance Imaging,* vol. 33, pp. 839-846, 2011.

[40] A. Deussen, V. Ohanyan, A. Jannasch, L. Yin and W. Chilian, “Mechanisms of metabolic coronary flow regulation,” *Journal of Mollecular and Cellular Biology,* vol. 52, no. 4, pp. 794-801, 2012.

[41] C. Konoura, T. Yagi, M. Nakamura, K. Iwasaki, Y. Qian, S. Okuda, A. Yoshitake, H. Shimizu, R. Yozu and M. Umezu, “Numerical analysis of blood flow distribution in 4- and 3-branch vascular grafts,” *Journal of Artificial Organs,* vol. 16, pp. 157-163, 2013.

[42] M. Nakamura, S. Wada, S. Yokosawa, H. Isoda, H. Takeda and T. Yamaguchi, “Measurement of Blood Flow in the Left Ventricle and Aorta Using 2D Cine Phase-Contrast Magnetic Resonance Imaging,” *Journal of Biomechanical Science and Engineering,* vol. 2, no. 2, pp. 46-57, 2007.

[43] M. Zamir, P. Sinclair and T. Wonnacott, “Relation Between Diameter and Flow in Major Branches of the Arch of the Aorta,” *Journal of Biomechanics,* vol. 25, no. 11, pp. 1303-1310, 1992.

[44] V. H. Huxley and S. S. Kemp, “Sex-Specific Analysis of Cardiovascular Function,” in *Sex-Specific Characteristics of the Microcirculation,* Springer , 2018, pp. 307-328.

[45] H. Kim, E. Vignon-Clementel, C. Figueroa, J. LaDisa, K. Jansen, J. Feinstein and C. Taylor, “On Coupling a Lumped Parameter Heart Model and a Three-Dimensional Finite Element Aorta Model,” *Annals of Biomedical Engineering,* vol. 37, no. 11, pp. 2153-2169, 2009.

[46] S. Zhou, L. Xu, L. Hao, H. Xiao, Y. Yao, L. Qi and Y. Yao, “A review on low-dimensional physics-based models of systemic arteries: application to estimation of central aortic pressure,” *Biomedical Engineering Online,* vol. 18, no. 41, 2019.

[47] J. Alastruey, “"Numerical modelling of pulse wave propagation in the cardiovascular system : development, validation and clinical applications' PhD Thesis,” Imperial College, London, 2006.

[48] S. Epstein, M. Willemet, P. J. Chowienczyk and J. Alastruey, “Reducing the number of parameters in 1D arterial blood flow modeling: less is more for patient-specific simulations,” *The American Journal of Physiology-Heart and Circulatory Physiology,* vol. 309, no. 1, pp. 222-234, 2015.

[49] N. Xiao, “"Simulation of 3D Blood Flow in the Full Systemic Arterial Tree and Computational Frameworks for Efficient Parameter Estimation' PhD Thesis,” Stanford University, Stanford, 2014.

[50] M. Markl, G. Wagner and A. Barker, “Blood flow analysis of the aortic arch using computational fluid dynamics,” *European Journal of Cardio-Thoracic Surgery,* vol. 49, pp. 1586-1587, 2016.

[51] H. Kamada, M. Nakamura, H. Ota, S. H. MD and K. Takase, “Blood flow analysis with computational fluid dynamics and 4D-flow MRI for vascular diseases,” *Journal of Cardiology,* vol. 80, no. 5, pp. 386-396, 2022.

[52] R. Romarowski, A. Lefieux, S. Morganti, A. Veneziani and F. Auricchio, “Patient-specific CFD modelling in the thoracic aorta withPC-MRI–based boundary conditions: A least-squarethree-element Windkessel approach,” *Numerical Methods in Biomedical Engineering,* vol. 34, no. 11, 2018.

[53] J. Alastruey, “Thesis,” 2006.

[54] H. Gharahi, B. Zambrano, D. Zhu, J. DeMarco and S. Baek, “Computational fluid dynamic simulation of human carotid artery bifurcation based on anatomy and volumetric blood flow rate measured with magnetic resonance imaging,” *International Journal of Advances in Engineering Sciences and Applied Mathematics,* vol. 8, no. 1, pp. 40-60, 2016.

[55] A. Brown, “Patient Specific Local and Systemic Haemodynamics in the Presence of a Left Ventricular Assist Device,” The University of Sheffield: School of Medicine and Biomedical Sciences, Sheffield, 2012.

[56] R. L. Spilker and C. A. Taylor, “Tuning Multidomain Hemodynamic Simulations to Match,” *Annals of Biomedical Engineering,* vol. 38, no. 8, pp. 2635-2648, 2010.

[57] P. A. Rudenick, B. H. Bijnens, D. García-Dorado and A. Evangelista, “An in vitro phantom study on the influence of tear size and configuration on the hemodynamics of the lumina in chronic type B aortic dissections,” *Journal of Vascular Surgery,* vol. 57, no. 2, pp. 464-474, 2013.

[58] D. Chen, M. Müller-Eschner, D. Kotelis, D. Böckler, Y. Ventikos and H. v. Tengg-Kobligk, “A longitudinal study of Type-B aortic dissection and endovascular repair scenarios: Computational analyses,” *Medical Engineering & Physics,* vol. 35, no. 9, pp. 1321-1330, 2013.

[59] M. Alimohammadi, O. Agu, S. Balabani and V. Diaz-Zuccarini, “Development of a patient-specific simulation tool to analyse aortic dissections: Assessment of mixed patient-specific flow and pressure boundary conditions,” *Medical Engineering & Physics,* vol. 36, pp. 275-284, 2014.

[60] A. Alimohammadi, J. Sherwood, M. Karimpour, O. Agu, S. Balabani and V. Diaz-Zuccarini, “Aortic dissection simulation models for clinical support: fluid-structure interaction vs. rigid wall models,” *Biomedical Engineering Online,* vol. 34, 2015.

[61] M. A. Abazari, D. Rafiei, M. Soltani and M. Alimohammadi, “The effect of beta-blockers on hemodynamic parameters in patient-specific blood flow simulations of type-B aortic dissection: a virtual study,” *Scientific Reports,* vol. 11, no. 1, 2021.

[62] C. Stokes, M. Bonfanti, Z. Li, J. Xiong, D. Chen, S. Balabani and V. Díaz-Zuccarini, "A novel MRI-based data fusion methodology for efficient, personalised, compliant simulations of aortic haemodynamics," *Journal of Biomechanics*, vol. 129, 2021.

[63] Y. Hohri, S. Numata, K. Itatani, K. Kanda, S. Yamazaki, T. Inoue and H. Yaku, "Prediction for future occurrence of type A aortic dissection using computational fluid dynamics," *European Journal of Cardio-Thoracic Surgery,* vol. 60, no. 2, pp. 384-391, 2021.

[64] Y. Zhu, X. Y. Xu, U. Rosendahl, J. Pepper and S. Mirsadraee, "Prediction of aortic dilatation in surgically repaired type A dissection: A longitudinal study using computational fluid dynamics," *The Journal of Thoracic and Cardiovascular Surgery*, vol. 9, pp. 11-27, 2022.

[65] D. Dillon-Murphy, A. Noorani, D. Nordsletten and C. A. Figueroa, "Multi-modality image-based computational analysis of haemodynamics in aortic dissection," *Biomechanics and Modelling in Mechanobiology,* vol. 15, no. 4, pp. 857-876, 2016.

[66] Y. Zhu, G. A. Saeed Mirsadraee, A. Gambaro, U. Rosendahl, J. Pepper and X. Y. Xu, "Association of hemodynamic factors and progressive aortic dilatation following type A aortic dissection surgical repair," *Scientific Reports,* vol. 11, no. 1, 2021.

[67] S. Moretti, F. Tauro, M. Orrico, N. Mangialardi and A. L. Facci, "Comparative Analysis of Patient-Specific Aortic Dissections through Computational Fluid Dynamics Suggests Increased Likelihood of Degeneration in Partially Thrombosed False Lumen," *Bioengineering (Basel),* vol. 10, no. 3, 2023.

[68] Y. Ikeno, Y. Takayama, T. Matsueda, M. Miyoshi, T. Motoki, A. Kurushima, T. Otani and Y. Fukumura, "Computational fluid dynamics-based prediction of aortic aneurysm rupture in a patient with chronic aortic dissection," *General Thoracic and Cardiovascular Surgery Cases,* vol. 2, no. 1, 2023.

[69] K. M. Tse, P. Chiu, H. P. Lee and P. Ho, "Investigation of hemodynamics in the development of dissecting aneurysm within patient-specific dissecting aneurismal aortas using computational fluid dynamics (CFD) simulations," *Journal of Biomechanics,* vol. 44, no. 5, pp. 827-836, 2011.

[70] J. Song, S. Gao, E. Xie, W. Wang, L. Dai, R. Zhao, C. Zhou, J. Qiu and C. Yu, "Systematic Review of the Application of Computational Fluid Dynamics for Adult Aortic Diseases," *Reviews in Cardiovascular Medicine,* vol. 24, no. 12, 2023.

[71] K. Fatma, G.-C. Carine, G. Marine, P. Philippe and D. Valérie, "Numerical modeling of residual type B aortic dissection: longitudinal analysis of favorable and unfavorable evolution," *Medical & Biological Engineering & Computing* , vol. 60, pp. 769-783, 2022.

[72] X. Li, H. Qiao, Y. Shi, J. Xue, T. Bai, Y. Liu and L. Sun, "Role of proximal and distal tear size ratio in hemodynamic change of acute type A aortic dissection," *Journal of Thoracic Disease,* vol. 12, no. 6, 2020.

[73] H. Xu, M. Piccinelli, B. G. Leshnower, A. Lefieux, W. R. Taylor and A. Veneziani, "Coupled Morphological–Hemodynamic Computational Analysis of Type B Aortic Dissection: A Longitudinal Study," *Annals of Biomedical Engineering,* vol. 46, no. 7, pp. 927-939, 2018.

[74] C. Menichini, Z. Cheng, R. G. J. Gibbs and X. Y. Xu, "Predicting false lumen thrombosis in patient-specific models of aortic dissection," *Journal of the Royal Society Interface,* vol. 13, no. 124, 2016.

[75] W. N. W. A. Naim, P. B. Ganesan, Z. Sun, J. Lei, S. Jansen, S. A. Hashim, T. K. Ho and E. Lim, "Flow pattern analysis in type B aortic dissection patients after stent-grafting repair: Comparison between complete and incomplete false lumen thrombosis," *International Journal for Numerical Methods in Biomedical Engineering,* vol. 34, no. 5, 2018.

[76] Y. Zhu, S. M. U. Rosendahl, J. Pepper and X. Y. Xu, "Fluid-Structure Interaction Simulations of Repaired Type A Aortic Dissection: a Comprehensive Comparison With Rigid Wall Models," *Frontiers in Physiology,* vol. 13, 2022.

[77] J. Zimmermann, K. Bäumler, M. Loecher, T. E. Cork, A. L. Marsden, D. B. Ennis and D. Fleischmann, "Hemodynamic effects of entry and exit tear size in aortic dissection evaluated with in vitro magnetic resonance imaging and fluid–structure interaction simulation," *Scientific Reports,* vol. 13, 2023.

[78] M. Bonfanti, G. Franzetti, G. Maritati, S. Homer-Vanniasinkam, S. Balabani and V. Diaz-Zuccarini, "Patient-specific haemodynamic simulations of complex aortic dissections informed by commonly available clinical datasets," *Medical Engineering & Physics,* vol. 71, pp. 45-55, 2019.

[79] M. Bonfanti, S. Balabani, J. Greenwood, S. Puppala, S. Homer-Vanniasinkam and V. Diaz-Zuccarini, "Computational tools for clinical support: a multi-scale compliant model for haemodynamic simulations in an aortic dissection based on multi-modal imaging data," *Journal of the Royal Society Interface,* vol. 14, no. 136, 2017.

[80] M. Bonfanti, G. Franzetti, S. Homer-Vanniasinkam, V. Díaz-Zuccarini and S. Balabani, "A Combined In Vivo, In Vitro, In Silico Approach for Patient-Specific Haemodynamic Studies of Aortic Dissection," *Annals of Biomedical Engineering,* vol. 48, no. 12, pp. 2950-2964, 2020.

[81] G. Franzetti, M. Bonfanti, S. Homer-Vanniasinkam, V. Diaz-Zuccarini and S. Balabani, "Experimental evaluation of the patient-specific haemodynamics of an aortic dissection model using particle image velocimetry," *Journal of Biomechanics,* vol. 134, 2022.

[82] b. c. C. Karmonika, J. Bismuth, D. Shah, M. Davies, D. Purdyc and A. Lumsden, "Computational Study of Haemodynamic Effects of Entry- and Exit-Tear Coverage in

a DeBakey Type III Aortic Dissection: Technical Report," *European Journal of Vascular & Endovascular Surgery,* vol. 42, no. 2, pp. 172-177, 2011.

[83] X. Kan, T. Ma, J. Lin, L. Wang, Z. Dong and X. Y. Xu, "Patient-specific simulation of stent-graft deployment in type B aortic dissection: model development and validation," *Biomechanics and Modeling in Mechanobiology,* vol. 20, pp. 2247-2258, 2021.

[84] X. Kan, T. Ma, Z. Dong and X. Y. Xu, "Patient-Specific Virtual Stent-Graft Deployment for Type B Aortic Dissection: A Pilot Study of the Impact of Stent-Graft Length," *Frontiers in Physiology: Computational Physiology and Medicine,* vol. 12, 2021.

[85] D. Chen, J. Wei, Y. Deng, H. Xu, Z. Li, H. Meng, X. Han, Y. Wang, J. Wan, T. Yan, J. Xiong and X. Tang, "Virtual stenting with simplex mesh and mechanical contact analysis for real-time planning of thoracic endovascular aortic repair," *Theranostics,* vol. 8, no. 20, pp. 5758-5771, 2018.

[86] I. Vignon-Clementel, C. Figueroa, K. Jansen and C. Taylor, "Outflow boundary conditions for 3D simulations of non-periodic blood flow and pressure fields in deformable arteries," *Computer Methods in Biomechanics and Biomedical Engineering,* vol. 13, no. 5, pp. 625-640, 2010.

[87] R. L. F. v. d. Palen, A. A. W. Roest, P. J. v. d. Boogaard, A. d. Roos, N. A. Blom and J. J. M. Westenberg, "Scan–rescan reproducibility of segmental aortic wall shear stress as assessed by phase-specifc segmentation with 4D fow MRI in healthy volunteers," *Magnetic Resonance Materials in Physics,* vol. 31, no. 5, pp. 653-663, 2018.

[88] Z. Stankovic, B. D. Allen, J. Garcia, K. B. Jarvis and M. Markl, "4D flow imaging with MRI," *Cardiovascular Diagnosis and Therapy,* vol. 4, no. 2, pp. 173-192, 2014.

[89] M. Cherry, Z. Khatir, A. Khan and M. Bissell, "The impact of 4D-Flow MRI spatial resolution on patient-specific CFD simulations of the thoracic aorta," *Scientific Reports,* vol. 12, no. 1, 2022.

[90] C. J. Garvey and R. Hanlon, "Computed tomography in clinical practice," *The BMJ,* vol. 324, no. 7345, pp. 1077-1080, 2002.

[91] J. G. Fletcher, J. M. Kofler, J. A. Coburn and D. H. Bruining, "Perspective on radiation risk in CT imaging," *Abdominal Imaging,* vol. 38, pp. 22-31, 2013.

[92] S. Bagherzadeh, N. Jabbari and H. R. Khalkhali, "Radiation dose and cancer risks from radiation exposure during abdominopelvic computed tomography (CT) scans: comparison of diagnostic and radiotherapy treatment planning CT scans," *Radiation and Environmental Biophysics,* vol. 60, no. 4, pp. 579-589, 2021.

[93] N. Sharma and L. M. Aggarwal, "Automated medical image segmentation techniques," *Journal of Medical Physics,* vol. 35, no. 1, pp. 3-14, 2010.

[94] D. Litmanovich, A. A. Bankier, L. Cantin, V. Raptopoulos and P. M. Boiselle, "CT and MRI in Diseases of the Aorta," *Vascular and Interventional Radiology,* vol. 193, no. 4, pp. 928-940, 2009.

[95] V. P. Grover, J. M. Tognarelli, M. M. Crossey, I. J. Cox, S. D. Taylor-Robinson and M. J. McPhail, "Magnetic Resonance Imaging: Principles and Techniques: Lessons for Clinicians," *Journal of Clinical and Experimental Hepatology,* vol. 5, no. 3, pp. 246-255, 2015.

[96] D. T. Wymer, K. P. Patel, W. F. B. III and V. K. Bhatia, "Phase-Contrast MRI: Physics, Techniques, and Clinical Applications," *RadioGraphics,* vol. 40, no. 1, 2020.

[97] E. Bollache, P. v. Ooij, A. Powell, J. Carr, M. Markl and A. J. Barker, "Comparison of 4D flow and 2D velocity-encoded phase contrast MRI sequences for the evaluation of aortic hemodynamics," *The International Journal of Cardiovascular Imaging,* vol. 32, no. 10, pp. 1529-1541, 2016.

[98] A. Alvarez, V. Martinez, G. Pizarro, M. Recio and J. Á. Cabrera, "Clinical use of 4D flow MRI for quantification of aortic regurgitation," *Open Heart,* vol. 7, no. 1, 2020.

[99] L. Shahid, J. Rice, H. Berhane, C. Rigsby, J. Robinson, L. Griffin, M. Markl and A. Roldán-Alzate, "Enhanced 4D Flow MRI-Based CFD with Adaptive Mesh Refinement for Flow Dynamics Assessment in Coarctation of the Aorta," *Annals of Biomedical Engineering,* vol. 50, no. 8, pp. 1001-1016, 2022.

[100] M. Markl, W. Wallis, C. Strecker, B. P. Gladstone, W. Vach and A. Harloff, "Analysis of Pulse Wave Velocity in the Thoracic Aorta by Flow-Sensitive Four-Dimensional MRI: Reproducibility and Correlation With Characteristics in Patients With Aortic Atherosclerosis," *Journal of Magnetic Resonance Imaging,* vol. 35, pp. 1162-1168, 2012.

[101] J. U. Ulloa, V. M. d. Vega, A. Á. Vázquez, J. R. Oyarzabal, A. F. Gil and J. Á. Cabrera, "4D-Flow Cardiac Magnetic Resonance Imaging in Chronic Aortic Dissection Assessment," *JACC: Case Reports,* vol. 4, no. 21, pp. 1399-1403, 2022.

[102] D. Marlevi, J. A. Sotelo, R. Grogan-Kaylor, Y. Ahmed, S. Uribe, H. J. Patel, E. R. Edelman, D. A. Nordsletten and N. S. Burris, "False lumen pressure estimation in type B aortic dissection using 4D flow cardiovascular magnetic resonance: comparisons with aortic growth," *Journal of Cardiovascular Magnetic Resonance,* vol. 23, no. 51, 2021.

[103] J. R. Kroeger, F. C. Pavesio, R. Mörsdorf, K. Weiss, A. C. Bunck, B. Baeßler, D. Maintz and D. Giese, "Velocity quantification in 44 healthy volunteers using accelerated multi-VENC 4D flow CMR," *European Journal of Radiology,* vol. 137, 2021.

[104] S. Chu, O. Kilinc, M. Pradella, E. Weiss, J. Baraboo, A. Maroun, K. Jarvis, C. K. Mehta, C. Malaisrie, A. W. Hoel, J. C. Carr, M. Markl and B. D. Allen, "Baseline 4D Flow-Derived in vivo Hemodynamic Parameters Stratify Descending Aortic Dissection

Patients With Enlarging Aortas," *Frontiers in Cardiovascular Medicine: Cardiovascular Imaging,* vol. 9, 2022.

[105] K. Takahashi, T. Sekine, Y. Miyagi, S. Shirai, T. Otsuka, S. Kumita and Y. Ishii, "Four-dimensional flow analysis reveals mechanism and impact of turbulent flow in the dissected aorta," *European Journal of Cardio-Thoracic Surgery,* vol. 60, no. 5, pp. 1064-1072, 2021.

[106] M. M. Bissell, F. Raimondi, L. A. Ali, B. D. Allen, A. J. Barker, A. Bolger, N. Burris, C.-J. Carhäll, J. D. Collins, T. Ebbers, C. J. Francois, A. Frydrychowicz, P. Garg, J. Geiger, H. Ha, M. D. Hope , A. Hsiao, K. Johnson, S. Kozerke, L. E. Ma, M. Markl, D. Martins, M. Messina and P. Dyverfeldt, "4D Flow cardiovascular magnetic resonance consensus statement: 2023 update," *Journal of Cardiovascular Magnetic Resonance,* vol. 25, no. 1, 2023.

[107] O. Kilinc, J. Baraboo, J. Engel, D. Giese, N. Jin, E. K. Weiss, A. Maroun, K. Chow, X. Bi, R. Davids, C. Mehta, S. C. Malaisrie, A. Hoel, J. Carr, M. Markl and B. D. Allen, "Aortic Hemodynamics with Accelerated Dual-Venc 4D Flow MRI in Type B Aortic Dissection," *Applied Sciences,* vol. 13, no. 10, 2023.

[108] S. Yoon, S. H. Park and D. Han, "Uncover This Tech Term: Compressed Sensing Magnetic Resonance Imaging," *Korean Journal of Radiology,* vol. 24, no. 12, pp. 1293-1302, 2023.

[109] M. J. F. G. Ramaekers, J. J. M. Westenberg, B. P. Adriaans, E. C. Nijssen, J. E. Wildberger, H. J. Lamb and S. Schalla, "A clinician's guide to understanding aortic 4D flow MRI," *Insights into Imaging,* vol. 14, 2023.

[110] S. Schnell, M. Markl, P. Entezari, R. J. Mahadewia, E. Semaan, Z. Stankovic, J. Collins, J. Carr and B. Jung, "k-t GRAPPA Accelerated Four-Dimensional Flow MRI in the Aorta: Effect on Scan Time, Image Quality, and Quantification of Flow and Wall Shear Stress," *Magnetic Resonance in Medicine,* vol. 72, no. 2, pp. 522-533, 2014.

[111] P. Righini, F. Secchi, D. Mazzaccaro, D. Giese, M. Galligani, D. Avishay, D. Capra, C. B. Monti and G. Nano, "Four-Dimensional Flow MRI for the Evaluation of Aortic Endovascular Graft: A Pilot Study," *Diagnostics,* vol. 13, no. 12, 2023.

[112] X. Chen, J. Liu, C. Gong, S. Li, Y. Pang and B. Chen, "MVE-Net: An Automatic 3-D Structured Mesh Validity Evaluation Framework Using Deep Neural Networks," *Computer-Aided Design,* vol. 4, 2021.

[113] Z. Zhang, P. K. Jimack and H. Wang, "MeshingNet3D: Efficient generation of adapted tetrahedral meshes for computational mechanics," *Advances in Engineering Software,* vol. 157, 2021.

[114] A. A. Duquette, P.-M. Jodoin, O. Bouchot and A. Lalande, "3D segmentation of abdominal aorta from CT-scan and MR images," *Computerized Medical Imaging and Graphics,* vol. 36, no. 4, pp. 294-303, 2012.

[115] D. Luo, Y. Zhang and J. Li, “Research on Several Key Problems of Medical Image Segmentation and Virtual Surgery,” *Contrast Media & Molecular Imaging,* 2022.

[116] S. Moccia, E. D. Momi, S. E. Hadji and L. S. Mattos, “Blood vessel segmentation algorithms — Review of methods, datasets and evaluation metrics,” *Computer Methods and Programs in Biomedicine,* vol. 158, pp. 71-91, 2018.

[117] A. Pepe, J. Li, M. Rolf-Pissarczyk, C. Gsaxner, X. Chen, G. A. Holzapfel and J. Egger, “Detection, segmentation, simulation and visualization of aortic dissections: A review,” *Medical Image Analysis,* vol. 65, 2020.

[118] A. Fluent, “ANSYS FLUENT 12.0 User's Guide”.

[119] Y. Zhu, R. Chen, Y.-H. Juan, H. Li, J. Wang, Z. Yu and H. Liu, “Clinical validation and assessment of aortic hemodynamics using computational fluid dynamics simulations from computed tomography angiography,” *Biomedical Engineering Online,* vol. 17, no. 53, 2018.

[120] Q. Du and D. Wang, “Recent progress in robust and quality Delaunay mesh generation,” *Journal of Computational and Applied Mathematics,* vol. 195, no. 1, pp. 8-23, 2006.

[121] ANSYS, “Customer Training Material: Lecture 6 - Turbulence Modelling,” ANSYS, 2010.

[122] H. Schlichting, Boundary-layer Theory, New York : London: McGraw-Hill, 1979.

[123] N. Lewandowska and J. Mosiezny, “Meshing strategy for bifurcation arteries in the context of blood flow simulation accuracy,” *E3s Web of Conferences,* vol. 128, 2019.

[124] Y. Ohhara, M. Oshima, T. Iwai, H. Kitajima, Y. Yajima, K. Mitsudo, A. Krdy and I. Tohnai, “Investigation of blood flow in the external carotid artery and its branches with a new 0D peripheral model,” *Biomedical Engineering Online,* vol. 15, no. 16, 2016.

[125] J. Xing, in *Fluid-Solid Interaction Dynamics: Theory, Variational Principles, Numerical Methods, and Applications,* Southampton, United Kingdom, Academic Press, 2019, pp. 487-575.

[126] S. Prakash and C. Ethier, “Requirements for Mesh Resolution in 3D Computational Haemodynamics,” *Transactions of the ASME,* vol. 123, pp. 134-144, 2001.

[127] N. Baker, G. Kelly and P. D. O'Sullivan, “A grid convergence index study of mesh style effect on the accuracy of the numerical results for an indoor airflow profile,” *International Journal of Ventilation,* vol. 19, no. 4, pp. 300-314, 2019.

[128] M. Olufsen, C. Peskin, W.-Y. Kim, E. Pedersen, A. Nadi and J. Larson, “Numerical Simulation and Experimental Validation of Blood Flow in Arteries with Structured-Tree Outflow Conditions,” *Annals of Biomedical Engineering,* vol. 28, no. 11, pp. 1281-1299, 2000.

[129] A. Anastasiou, A. Spyrogianni, K. Koskinas, G. Giannoglou and S. Paras, "Experimental investigation of the flow of a blood analogue fluid in a replica of a bifurcated artery," *Medical Engineering & Physics,* vol. 34, no. 2, pp. 211-218, 2012.

[130] N. Shahcheraghi, H. A. Dwyer, A. Y. Cheer, A. I. Barakat and T. Rutaganira, "Unsteady and Three-Dimensional Simulation of Blood Flow in the Human Aortic Arch," *Transactions of the ASME,* vol. 124, no. 4, pp. 378-387, 2002.

[131] M. Lui, S. Martino, M. Salerno and M. Quadrio, "On the Turbulence Modeling of Blood Flow in a Stenotic Vessel," *Journal of Biomechanical Engineering,* vol. 142, 2020.

[132] G. Alfonsi, "Reynolds-Averaged Navier-Stokes Equations for Turbulence Modeling," *Applied Mechanics Reviews,* vol. 62, no. 4, 2009.

[133] D. Lopes, R. Agujetas, H. Puga, J. Teixeira, R. Lima, J. Alejo and C. Ferrera, "Analysis of finite element and finite volume methods for fluid-structure interaction simulation of blood flow in a real stenosed artery," *International Journal of Mechanical Sciences,* vol. 207, 2021.

[134] K. Jain, S. Roller and K.-A. Mardal, "Transitional flow in intracranial aneurysms – A space and time refinement study below the Kolmogorov scales using Lattice Boltzmann Method," *Computers & Fluids,* vol. 127, pp. 36-46, 2016.

[135] Z. Pouransari, L. Vervisch and A. V. Johansson, "Reynolds Number Effects on Statistics and Structure of an Isothermal Reacting Turbulent Wall-Jet," *Flow Turbulence and Combustion,* vol. 92, no. 4, pp. 931-945, 2014.

[136] S. W. Day and D. B. Olsen, "Studies of Turbulence Models in a Computational Fluid Dynamics Model of a Blood Pump," *Artificial Organs,* 2003.

[137] A. Kabir, K. Sultana and A. Uddin, "Performance of k-ω and k-ε Model for Blood Flow Simulation in Stenosed Artery," *GANIT: Journal of Bangladesh Mathematical Society,* vol. 40, no. 2, pp. 111-125, 2020.

[138] N. Xiao, J. Alastruey and A. Figueroa, "A Systematic Comparison between 1-D and 3-D Hemodynamics in Compliant Arterial Models," *International Journal for Numerical Methods in Biomedical Engineering,* vol. 30, no. 2, pp. 204-231, 2014.

[139] J. Alastruye, K. Parker and S. Sherwin, "Arterial pulse wave haemodynamics," in *11th International Conference on Pressure Surges,* Lisbon, 2012.

[140] S. Sherwin, V. Franke, J. Peiró and K. Parker, "One-dimensional modelling of a vascular network in space-time variables," *Journal of Engineering Mathematics,* vol. 47, pp. 217-250, 2003.

[141] R. Whittaker, M. Heil, O. Jensen and S. Waters, "A Rational Derivation of a Tube Law from Shell Theory," *The Quarterly Journal of Mechanics and Applied Mathematics,* pp. 1 - 35.

[142] X. Deng, Y. Zheng, Y. Xu, X. Xi, N. Li and Y. Yin, "Graph cut based automatic aorta segmentation with an adaptive smoothness constraint in 3D abdominal CT images," *Neurocomputing,* vol. 310, pp. 46-58, 2018.

[143] S. Black, K. Ritos, C. Maclean, R. Brodie and A. Kazakidi, "P14 Blood flow analysis of the aortic arch using computational fluid dynamics in a coupled 3D-0D framework," *Heart,* vol. 106, no. Abstract retrieved from http://dx.doi.org/10.1136/heartjnl-2020-SCF.24, pp. 10-11, 2020.

[144] H. Berhane, M. Scott, M. Elbaz, K. Jarvis, P. McCarthy, J. Carr, C. Malaisrie, R. Avery, A. J. Barker, J. D. Robinson, C. K. Rigsby and M. Markl, "Fully automated 3D aortic segmentation of 4D flow MRI for hemodynamic analysis using deep learning," *International Society for Magnetic Resonance in Medicine,* vol. 84, no. 4, pp. 2204-2218, 2020.

[145] M. Tillich, K. A. Hausegger, K. Tiesenhausen, J. Tauss, R. Groell and D. H. Szolar, "Helical CT Angiography of Stent-Grafts in Abdominal Aortic Aneurysms: Morphologic Changes and Complications," *RadioGraphics,* vol. 19, no. 6, pp. 1573-1583, 1999.

[146] H. Lusic and M. W. Grinstaff, "X-ray-Computed Tomography Contrast Agents," *Chemical Reviews,* vol. 133, no. 3, pp. 1641-1666, 2013.

[147] M. A. A. D. Ragusi, R. W. v. d. Meer, R. M. S. Joemai, J. v. Schaik and C. S. P. v. Rijswijk, "Evaluation of CT Angiography Image Quality Acquired with Single-Energy Metal Artifact Reduction (SEMAR) Algorithm in Patients After Complex Endovascular Aortic Repair," *Cardiovascular and Interventional Radiology,* vol. 41, no. 2, pp. 323-329, 2018.

[148] S. Alawad and A. Abujamea, "Awareness of radiation hazards in patients attending radiology departments," *Radiation and Environmental Biophysics,* vol. 60, pp. 453-458, 2021.

[149] D. J. Brenner and E. J. Hall, "Computed Tomography — An Increasing Source of Radiation Exposure," *The New England Journal of Medicine,* vol. 357, no. 22, pp. 2277-2284, 2007.

[150] R. Fazel, H. M. Krumholz, Y. Wang, J. S. Ross, J. Chen, H. H. Ting, N. D. Shah, K. Nasir, A. J. Einstein and B. K. Nallamothu, "Exposure to Low-Dose Ionizing Radiation from Medical Imaging Procedures in the United States," *The New England Journal of Medicine,* vol. 361, no. 9, pp. 849-857, 2009.

[151] D. Tack and P. A. Gevenois, "Risks from Ionising Radiation," in *Radiation Dose from Adult and Pediatric Multidetector Computed Tomography*, Berlin, Springer, 2007, pp. 11-31.

[152] A. Sanderud, A. England, P. Hogg, K. Fosså, S. Svensson and S. Johansen, "Radiation dose differences between thoracic radiotherapy planning CT and thoracic diagnostic CT scans," *Radiography*, vol. 22, no. 2, pp. 107-111, 2016.

[153] M. S. Pearce, J. A. Salotti, M. P. Little, K. McHugh, C. Lee, K. P. Kim, N. L. Howe, C. M. Ronckers and P. Rajaraman, "Radiation exposure from CT scans in childhood and subsequent risk of leukaemia and brain tumours: a retrospective cohort study," *Lancet*, vol. 380, no. 9840, pp. 499-505, 2012.

[154] S. J. Westra, "The communication of the radiation risk from CT in relation to its clinical benefit in the era of personalized medicine," *Pediatric Radiology,* vol. 44, no. 3, pp. 515-518, 2014.

[155] D. Han, J. H. Lee, B. ó. Hartaigh and J. K. Min, "Role of computed tomography screening for detection of coronary artery disease," *Clinical Imaging,* vol. 40, no. 2, pp. 307-310, 2016.

[156] P. M. Graffy, R. M. Summers, A. A. Perez, V. Sandfort, R. Zea and P. J. Pickhardt, "Automated assessment of longitudinal biomarker changes at abdominal CT: correlation with subsequent cardiovascular events in an asymptomatic adult screening cohort," *Abdominal Radiology*, vol. 46, pp. 2976-2984, 2021.

[157] V. Tewari, D. Tewari and F. G. Gress, "Computed Tomography Colonography for Colorectal Cancer Screening," *Gastroenterology & Hepatology,* vol. 9, no. 3, pp. 158-163, 2013.

[158] Z. Sun, "Endovascular stent graft repair of abdominal aortic aneurysms: Current status and future directions," *World Journal of Radiology,* vol. 1, no. 1, pp. 63-71, 2009.

[159] A. H. Kuo, P. Nagpal, B. B. Ghoshhajra and S. S. Hedgire, "Vascular magnetic resonance angiography techniques," *Cardiovascular Diagnosis & Therapy,* vol. 9, no. 1, pp. 28-36, 2019.

[160] N. Schieda, J. I. Blaichman, A. F. Costa, R. Glikstein, C. Hurrell, M. James, P. J. Maralani, W. Shabana, A. Tang, A. Tsampalieros, C. B. v. d. Pol and S. Hiremath, "Gadolinium-Based Contrast Agents in Kidney Disease: A Comprehensive Review and Clinical Practice Guideline Issued by the Canadian Association of Radiologists," *Canadian Journal of Kidney Health and Disease,* vol. 69, no. 2, pp. 136-150, 2018.

[161] S. Hagiwara, S. Saima, K. Negishi, R. Takeda, N. Miyauchi, Y. Akiyama, S. Horikoshi and Y. Tomino, "High incidence of renal failure in patients with aortic aneurysms," *Nephrology Dialysis Transplantation*, vol. 22, no. 5, pp. 1361-1368, 2007.

[162] X. An, X. Guo, N. Ye, W. Bian, X. Han, G. Wang and H. Cheng, "Risk factors of acute kidney injury in patients with Stanford type B aortic dissection involving the renal artery who underwent thoracic endovascular aortic repair," *Renal Failure,* vol. 43, no. 1, pp. 1130-1136, 2021.

[163] A. Kato, E. Ito, N. Kamegai, M. Mizutani, H. Shimogushi, A. Tanaka, H. Shinjo, Y. Otsuka, D. Inaguma and A. Takeda, "Risk factors for acute kidney injury after initial acute aortic dissection and their effect on long-term mortality," *Renal Replacement Therapy volume,* vol. 2, no. 53, 2016.

[164] H.-B. Wu, W.-G. Ma, H.-L. Zhao, J. Zheng, J.-R. Li, O. Liu and L.-Z. Sun, "Risk factors for continuous renal replacement therapy after surgical repair of type A aortic dissection," *Journal of Thoracic Disease,* vol. 9, no. 4, pp. 1126-1132, 2017.

[165] Z. Wang, M. Ge, T. Chen, C. Chen, Q. Zong, L. Lu and D. Wang, "Independent risk factors and the long-term outcomes for postoperative continuous renal replacement treatment in patients who underwent emergency surgery for type a acute aortic dissection," *Journal of Cardiothoracic Surgery,* vol. 15, no. 100, 2020.

[166] J. Szajer and K. Ho-Shon, "A comparison of 4D flow MRI-derived wall shear stress with computational fluid dynamics methods for intracranial aneurysms and carotid bifurcations - A review," *Magnetic Resonance Imaging,* vol. 48, pp. 62-69, 2018.

[167] L. Johnston, M. Boumpouli and A. Kazakidi, "Hemodynamics in the Aorta and Pulmonary Arteries of Congenital Heart Disease Patients: A Mini Review," *Journal of Cardiology and Cardiovascular Sciences,* vol. 5, no. 2, pp. 1-5, 2021.

[168] T. Fujiwara, H. Berhane, M. B. Scott, E. K. Englund, M. Schäfer, B. Fonseca, A. Berthusen, J. D. Robinson, C. K. Rigsby, L. P. Browne, M. Markl and A. J. Barker, "Segmentation of the Aorta and Pulmonary Arteries Based on 4D Flow MRI in the Pediatric Setting Using Fully Automated Multi-Site, Multi-Vendor, and Multi-Label Dense U-Net," *Journal of Magnetic Resonance Imaging,* 2021.

[169] J. Aviles, G. D. M. Talou, O. Camara, M. M. Córdova, X. M. Ferez, D. Romero, E. Ferdian, K. Gilbert, A. Elsayed, A. A. Young, L. Dux-Santoy, A. Ruiz-Munoz, G. Teixido-Tura, J. Rodriguez-Palomares and A. Guala, "Domain Adaptation for Automatic Aorta Segmentation of 4D Flow Magnetic Resonance Imaging Data from Multiple Vendor Scanners," *Functional Imaging and Modeling of the Heart. FIMH 2021. Lecture Notes in Computer Science,* vol. 12738, pp. 112-121, 2021.

[170] M. Bustamante, V. Gupta, D. Forsberg, C.-J. Carlhäll, J. Engvall and T. Ebbers, "Automated multi-atlas segmentation of cardiac 4D flow MRI," *Medical Image Analysis,* vol. 49, pp. 128-140, 2018.

[171] F. Odille, J. A. Steeden, V. Muthurangu and D. Atkinson, "Automatic segmentation propagation of the aorta in real-time phase contrast MRI using nonrigid registration," *Journal of Magnetic Resonance Imaging,* vol. 33, no. 1, pp. 232-238, 2011.

[172] L. F. Valencia, J. Montagnat and M.Orkisz, "3D models for vascular lumen segmentation in MRA images and for artery-stenting simulation," *IRBM,* vol. 28, no. 2, pp. 65-71, 2007.

[173] M. Bustamante, V. Gupta, C.-J. Carlhäll and T. Ebbers, "Improving visualization of 4D flow cardiovascular magnetic resonance with four-dimensional angiographic data:

generation of a 4D phase-contrast magnetic resonance CardioAngiography (4D PC-MRCA)," *Journal of Cardiovascular Magnetic Resonance,* vol. 19, no. 47, 2017.

[174] M. Markl, A. Frydrychowicz, S. Kozerke, M. Hope and O. Wieben, "4D flow MRI," *Journal of Magnetic Resonance Imaging,* vol. 36, no. 5, pp. 1015-1036, 2012.

[175] L. A. E. Brown, S. C. Onciul, D. A. Broadbent, K. Johnson, G. J. Fent, J. R. J. Foley, P. Garg, P. G. Chew, K. Knott, E. Dall'Armellina, P. P. Swoboda, H. Xue, J. P. Greenwood, J. C. Moon and P. Kellman, "Fully automated, inline quantification of myocardial blood flow with cardiovascular magnetic resonance: repeatability of measurements in healthy subjects," *Journal of Cardiovascular Magnetic Resonance,* vol. 20, no. 1, 2018.

[176] Mathworks, "Image Processing Toolbox (TM) User's Guide (R2022a)," Mathworks, Natick, MA, 2022.

[177] H. Lan, A. Updegrove, N. M. Wilson, G. D. Maher, S. C. Shadden and A. L. Marsden, "A Re-Engineered Software Interface and Workflow for the Open-Source SimVascular Cardiovascular Modeling Package," *Journal of Biomechanical Engineering,* vol. 140, no. 2, 2018.

[178] M. Piccinelli, A. Veneziana, D. A. Steinman, A. Remuzzi and L. Antiga, "A Framework for Geometric Analysis of Vascular Structures: Application to Cerebral Aneurysms," *IEEE Transactions on Medical Imaging,* vol. 28, no. 8, pp. 1141-1155, 2009.

[179] R. Solanki, RebeccaGosling, V. Rammohan, G. Pederzani, PankajGarg, J. Heppenstall, D. R. Hose, P. Lawford, A. J. Narracott, J. Fenner, J. P.Gunn and P. D. Morris, "The importance of three dimensional coronary artery reconstruction accuracy when computing virtual fractional fow reserve from invasive angiography," *Scientific Reports,* vol. 11, no. 19694, 2021.

[180] K. H. Zou, S. K. Warfield, A. Bharatha, C. M. Tempany, M. R. Kaus, S. J. Haker, W. M. W. III, F. A. Jolesz and R. Kikinis, "Statistical Validation of Image Segmentation Quality Based on a Spatial Overlap Index," *Academic Radiology,* vol. 11, no. 2, pp. 178-189, 2004.

[181] É. O. Rodrigues, "An efficient and locality-oriented Hausdorff distance algorithm: Proposal and analysis of paradigms and implementations," *Pattern Recognition ,* vol. 117, 2021.

[182] O. U. Aydin, A. A. Taha, A. Hilbert, A. A. Khalil, I. Galinovic, J. B. Fiebach, D. Frey and V. I. Madai, "An evaluation of performance measures for arterial brain vessel segmentation," *BMC Medical Imaging,* vol. 11, no. 113, 2021.

[183] A. Klepaczko, P. Szczypiński, A. Deistung, J. R. Reichenbach and A. Materka, "Simulation of MR angiography imaging for validation of cerebral arteries segmentation algorithms," *Computer Methods and Programs in Biomedicine,* vol. 137, pp. 293-309, 2016.

[184] J. B. Thomas, L. Antiga, S. L. Che, J. S. Milner, D. A. H. Steinman, J. D. Spence, B. K. Rutt and D. A. Steinman, "Variation in the Carotid Bifurcation Geometry of Young vs Older Adults: Implications for Geometric Risk of Atherosclerosis," *Stroke,* vol. 36, no. 11, pp. 2450-2456, 2005.

[185] L. Johnston, R. Allen, P. Hall-Barrientos, A. Mason and A. Kazakidi, "Hemodynamic Abnormalities in the Aorta of Turner Syndrome Girls," *Frontiers of Cardiovascular Medicine,* vol. 8, no. 670841, 2021.

[186] M. Boumpouli, E. L. Sauvage, C. Capelli, S. Schievano and A. Kazakidi, "Characterization of flow dynamics in the pulmonary bifurcation of patients with repaired Tetralogy of Fallot: a computational approach," *Frontiers in Cardiovascular Medicine,* vol. 8, no. 703717, 2021.

[187] A. Kazakidi, S. J. Sherwin and P. D. Weinberg, "Effect of Reynolds number and flow division on patterns of haemodynamic wall shear stress near branch points in the descending thoracic aorta," *Journal of the Royal Society Interface,* vol. 6, no. 35, pp. 539-548, 2008.

[188] A. López, W. Nicholls, M. T. Stickland and W. M. Dempster, "CFD study of Jet Impingement Test erosion using Ansys Fluent® and OpenFOAM," *Computer physics communications,* vol. 12, no. 197, pp. 88-95, 2015.

[189] S. M. Black, C. Maclean, P. H. Barrientos, K. Ritos and A. Kazakidi, "Calibration of patient-specific boundary conditions for coupled CFD models of the aorta derived from 4D Flow-MRI," *Frontiers in Bioengineering and Biotechnology,* vol. 11, 2023.

[190] M. Boumpouli, M. H. D. Danton, T. Gourlay and A. Kazakidi, "Blood flow simulations in the pulmonary bifurcation in relation to adult patients with repaired tetralogy of Fallot," *Medical Engineering & Physics,* vol. 85, pp. 123-138, 2020.

[191] I. C. Campbell, J. Ries, S. S. Dhawan, A. A. Quyyumi, W. R. Taylor and J. N. Oshinski, "Effect of Inlet Velocity Profiles on Patient-Specific Computational Fluid Dynamics Simulations of the Carotid Bifurcation," *Journal of Biomechanical Engineering,* vol. 134, no. 5, 2012.

[192] A. Kazakidi, A. M. Plata, S. J. Sherwin and P. D. Weinberg, "Effect of reverse flow on the pattern of wall shear stress near arterial branches," *Journal of the Royal Society Interface,* vol. 8, no. 64, pp. 1594-1603, 2011.

[193] G. Hyde-Linaker, P. H. Barrientos, S. Stoumpos and A. Kazakidi, "Patient-specific computational haemodynamics associated with surgical creation of an arteriovenous fistula," *Medical Engineering & Physics,* vol. 105, 2022.

[194] V. Peiffer, S. Sherwin and P. Weinberg, "Does low and oscillatory wall shear stress correlate spatially with early atherosclerosis? A systematic review," *Cardiovascular Research,* vol. 99, no. 2, pp. 242-250, 2013.

[195] R. Amaya, L. Cancel and J. Tarbell, “Interaction between the Stress Phase Angle (SPA) and the Oscillatory Shear Index (OSI) Affects Endothelial Cell Gene Expression,” *PloS One,* vol. 11, no. 11, 2015.

[196] M. A. V. Doormaal, A. Kazakidi, M. Wylezinska, A. Hunt, J. L. Tremoleda, A. Protti, Y. Bohraus, W. Gsell, P. D. Weinberg and C. R. Ethier, “Haemodynamics in the mouse aortic arch computed from MRI-derived velocities at the aortic root,” *Journal of the Royal Society Interface,* vol. 9, no. 76, pp. 2834-2844, 2012.

[197] M. J. v. d. Laan, L. W. Bartels, C. J. Bakker, M. A. Viergever and J. D. Blankensteijn, “Suitability of 7 Aortic Stent-Graft Models for MRI Based Surveillance,” *Journal of Endovascular Therapy,* vol. 11, no. 4, pp. 366-371, 2004.

[198] J. Bertels, T. Eelbode, M. Berman, D. Vandermeulen, F. Maes, R. Bisschops and M. Blaschko, “Optimizing the Dice Score and Jaccard Index for Medical Image Segmentation: Theory & Practice,” Cornell University, Ithica, New York, 2019.

[199] T. Eelbode, J. Bertels, M. Berman, D. Vandermeulen, F. Maes, R. Bisschops and M. B. Blaschko, “Optimization for Medical Image Segmentation: Theory and Practice when evaluating with Dice Score or Jaccard Index,” *IEEE Transactions on Medical Imaging,* vol. 39, no. 11, pp. 3679 - 3690, 2020.

[200] J. C. Carr and T. J. Carroll, Magnetic Resonance Angiography, New York: Springer, 2012.

[201] D. Taniguchi, D. Tokunaga, R. Oda, H. Fujiwara, T. Ikeda, K. Ikoma, A. Kishida, T. Yamasaki, Y. Kawahito, T. Seno, H. Ito and T. Kubo, “Maximum intensity projection with magnetic resonance imaging for evaluating synovitis of the hand in rheumatoid arthritis: comparison with clinical and ultrasound findings,” *Clinical Rheumatology,* vol. 33, no. 7, pp. 911-917, 2014.

[202] A. Barrera-Naranjo, D. M. Marin-Castrillon, T. Decourselle, S. Lin, S. Leclerc, M.-C. Morgant, C. Bernard, S. D. Oliveira, A. Boucher, B. Presles, O. Bouchot, J.-J. Christophe and A. Lalande, “Segmentation of 4D Flow MRI: Comparison between 3D Deep Learning and Velocity-Based Level Sets,” *Journal of Imaging,* vol. 9, no. 6, 2023.

[203] H. Berhane, M. Scott, M. Elbaz, K. Jarvis, P. McCarthy, J. Carr, C. Malaisrie, R. Avery, A. J. Barker, J. D. Robinson, C. K. Rigsby and M. Markl, “Fully automated 3D aortic segmentation of 4D flow MRI for hemodynamic analysis using deep learning,” *Magnetic Resonance in Medicine,* vol. 84, no. 4, pp. 2204-2218, 2020.

[204] H. N. Roy van Pelt, B. t. H. Romeny and A. Vilanova, “Automated segmentation of blood-flow regions in large thoracic arteries using 3dcine pc-mri measurements,” *International Journal of Computer Assisted Radiology and Surgery,* vol. 7, pp. 217-224, 2011.

[205] S. M. Rothenberger, N. M. Patel, J. Zhang, S. Schnell, B. A. Craig, S. A. Ansari, M. Markl, P. P. Vlachos and V. L. Rayz, “Automatic 4D flow MRI Segmentation Using

the Standardized Difference of Means Velocity," *IEEE Transactions on Medical Imaging,* vol. 42, no. 8, pp. 2360-2373, 2023.

[206] Y.-L. Lee, Y.-K. Huang, L.-S. Hsu, P.-Y. Chen and C.-W. Chen, "The use of non-contrast-enhanced MRI to evaluate serial changes in endoleaks after aortic stenting: a case report," *BMC Medical Imaging,* vol. 19, no. 82, pp. doi:10.1186/s12880-019-0379-4, 2019.

[207] R. A. Lookstein, J. Goldman, L. Pukin and M. L. Marin, "Time-resolved magnetic resonance angiography as a noninvasive method to characterize endoleaks: initial results compared with conventional angiography," *Journal of Vascular Surgery,* vol. 39, no. 1, pp. 27-33, 2004.

[208] E. Tremblay, E. Thérasse, I. Thomassin-Naggara and I. Trop, "Quality Initiatives: Guidelines for Use of Medical Imaging during Pregnancy and Lactation," *RadioGraphics,* vol. 32, no. 3, 2012.

[209] F. Garcia-Bournissen, A. Shrim and G. Koren, "Safety of gadolinium during pregnancy," *Canadian Family Physician,* vol. 52, no. 3, pp. 309-310, 2006.

[210] A.-E. Millischer, L. J. Salomon, R. Porcher, M. Brasseur-Daudruy, A.-L. Gourdier, P. Hornoy, S. Silvera, D. Loisel, V. Tsatsaris, B. Delorme, N. Boddaert, Y. Ville and L. Sentilhes, "Magnetic resonance imaging for abnormally invasive placenta: the added value of intravenous gadolinium injection," *BJOG: an International Journal of Obstetrics & Gynaecology,* vol. 124, no. 1, pp. 88-95, 2016.

[211] A. Guala, L. Dux-Santoy, G. Teixido-Tura, A. Ruiz-Muñoz, L. Galian-Gay, M. L. Servato, F. Valente, L. Gutiérrez, T. González-Alujas, K. M. Johnson, O. Wieben, G. Casas-Masnou, A. S. Avilés, R. Fernandez-Galera, I. Ferreira-Gonzalez, A. Evangelista and J. F. Rodríguez-Palomares, "Wall Shear Stress Predicts Aortic Dilation in Patients With Bicuspid Aortic Valve," *JACC: Cardiovascular Imaging,* 2021.

[212] B. Zhuang, A. Sirajuddin, S. Zhao and M. Lu, "The role of 4D flow MRI for clinical applications in cardiovascular disease: current status and future perspectives," *Quantitative Imaging in Medicine and Surgery,* vol. 11, no. 9, pp. 4193-4210, 2021.

[213] K. Misaki, K. Futami, T. Uno, I. Nambu, A. Yoshikawa, T. Kamide and M. Nakada, "Inflow Hemodynamics of Intracranial Aneurysms: A Comparison of Computational Fluid Dynamics and 4D Flow Magnetic Resonance Imaging," *Journal of Stroke & Cerebrovascular Diseases,* vol. 30, no. 5, 2021.

[214] M. D'Elia, L. Mirabella, T. Passerini, M. Perego, M. Piccinelli, C. Vergara and A. Veneziani, "Applications of variational data assimilation in computational hemodynamics," in *Modeling of Physiological Flows,* Springer, 2012, pp. 363-394.

[215] K. Nayak, J. Nielsen, M. Bernstein, M. Markl, P. Gatehouse, R. Botnar, D. Saloner, C. Lorenz, H. Wen, B. Hu, F. Epstein, J. Oshinski and S. Raman, "Cardiovascular magnetic

resonance phase contrast imaging," *Journal of Cardiovascular Magnetic Resonance,* vol. 17, no. 71, 2015.

[216] S. Madhavan and E. Kemmerling, "The effect of inlet and outlet boundary conditions in image-based CFD modeling of aortic flow," *Biomedical Engineering Online,* vol. 17, no. 66, 2018.

[217] M. E. Moghadam, I. E. Vignon-Clementel, R. Figliola and A. L. Marsden, "A modular numerical method for implicit 0D/3D coupling in cardiovascular finite element simulations," *Journal of Computational Physics,* vol. 244, pp. 63-79, 2013.

[218] S. Pirola, Z. Cheng, O. A. Jarral, D. P. O'Regan, J. R. Pepper, T. Athanasiou and X. Y. Xu, "On the choice of outlet boundary conditions for patient-specific analysis of aortic flow using computational fluid dynamics," *Journal of Biomechanics,* pp. 15-21, 2017.

[219] E. Fevola, F. Ballarin, L. Jiménez-Juan, S. Fremes, S. Grivet-Talocia, G. Rozza and P. Triverio, "An optimal control approach to determine resistance-type boundary conditions from in-vivo data for cardiovascular simulations," *International Journal for Numerical Methods in Biomedical Engineering,* vol. 37, no. 10, 2021.

[220] S. Black, C. Maclean, P. Hall-Barrientos, K. Ritos and A. Kazakidi, "Reconstruction and Validation of Arterial Geometries from 4D Flow-MRI Images: A Novel Approach," *Cardiovascular Engineering and Technology: Under Review,* 2022.

[221] R. Shad, S. Kong, R. Fong, C. Bowles, A. Lee and W. Hiesinger, "Computational Fluid Dynamics Simulations to Predict False Lumen Enlargement After Surgical Repair of Type-A Aortic Dissection," *Seminars in Thoracic and Cardiovascular Surgery,* vol. 34, no. 2, pp. 443-448, 2022.

[222] M. A. Van-Doormaal, A. Kazakidi, M. Wylezinska, A. Hunt, J. L. Tremoleda, A. Prottis, Y. Bohraus, W. Gsell, P. D. Weinberg and C. R. Ethier, "Haemodynamics in the mouse aortic arch computed from MRI-derived velocities at the aortic root," *Journal of the Royal Society Interface,* vol. 9, pp. 2834-2844, 2012.

[223] J. Alastruey, J. Peiro and S. Sherwin, "Lumped parameter outflow models for 1-D blood flow simulations: Effect on pulse waves and parameter estimation," *Communicationsin Computational Physics,* vol. 4, no. 2, pp. 317-336, 2008.

[224] J. Alastruey, T. Passerini, L. Formaggia and J. Peiro, "Physical determining factors of the arterial pulse waveform: theoretical analysis and calculation using the 1-D formulation," *Journal of Engineering Mathematics,* vol. 77, pp. 19-37, 2012.

[225] P. Reymond, F. Merenda, F. Perren, D. Rufenacht and N. Stergiopulo, "Validation of a One-Dimensional Model of the Systemic Arterial Tree," *American Journal of Physiology-Heart and Circulatory Physiology,* pp. 208-222, 2009.

[226] E. S. Kröner, R. J. v. d. Geest, A. J. Scholte, P. J. v. d. Boogaard, D. Hendriksen, L. J. Kroft, M. Groenink, T. Radonic, J. J. Bax, A. d. Roos, J. H. Reiber and J. J. Westenberg, "Accuracy of aortic pulse wave velocity assessment with velocity-encoded MRI:

validation in patients with Marfan syndrome," *Journal of Cardiovascular Magnetic Resonance,* vol. 13, no. 1, 2011.

[227] M. Markl, W. Wallis, S. Brendecke, J. Simon, A. Frydrychowicz and A. Harloff, "Estimation of Global Aortic Pulse Wave Velocity by Flow-Sensitive 4D MRI," *Magnetic Resonance in Medicine,* vol. 63, no. 6, pp. 1575-1582, 2010.

[228] Y. Ohyama, B. Ambale-Venkatesh, C. Noda, J. Kim, Y. Tanami, G. Teixdo-Tura, A. Chigh, A. Redheuil, C. Liu, C. Wu, W. Hundley, D. Bluemke, E. Guallar and J. Lima, "Aortic Arch Pulse Wave Velocity Assessed by Magnetic Resonance Imaging as a Predictor of Incident Cardiovascular Events," *Hypertension,* vol. 70, no. 3, pp. 524-530, 2017.

[229] N. Westerhof, J. Lankhaar and B. Westerhof, "The Arterial Windkessel," *Medical and Biological Engineering & Computing,* vol. 47, pp. 131-141, 2009.

[230] I. Vignon-Clementel, C. Figueroa, K. Jansen and C. Taylor, "Outflow boundary conditions for three-dimensional finite element modeling of blood flow and pressure in arteries," *Computer Methods in Applied Mechanics and Engineering,* vol. 195, pp. 3776 - 3769, 2006.

[231] M. Alimohammadi, J. M. Sherwood, M. Karimpour, O. Agu, S. Balabani and V. Díaz-Zuccarini, "Aortic dissection simulation models for clinical support: fluid-structure interaction vs. rigid wall models," *BioMedical Engineering OnLine,* vol. 14, no. 34, 2015.

[232] N. Westerhof, F. Bosman, C. J. D. Vries and A. Noordergraaf, "Analog studies of the human systemic arterial tree," *Journal of Biomechanics,* vol. 2, no. 2, pp. 121-143, 1969.

[233] M. Hansen, "Boundary Conditions for 3D Fluid-Structure Interaction Simulations of Compliant Vessels," Norwegian University of Science and Technology, Department of Structural Engineering, Trondheim, 2013.

[234] M. Ismail, W. A. Wall and M. W. Gee, "Adjoint-based inverse analysis of windkessel parameters for patient-specific vascular models," *Journal of Computational Physics,* vol. 244, pp. 113-130, 2013.

[235] J. DaLisa, C. Figueroa, I. Vignon-Clementel, H. Ki, N. Xiao, L. Ellwein, F. Chan, J. Feinstein and C. Taylor, "Computational Simulations for Aortic Coarctation: Representative Results from a Sampling of Patients," *American Society of Mechanical Engineering,* vol. 133, 2011.

[236] S. Hope and A. Hughes, "Drug Effects on the Mechanical Properties of Large Arteries in Humans," *Clinical and Experimental Pharmacology and Physiology,* vol. 34, pp. 388-693, 2007.

[237] G. Papageorgiou and N. Jones, "Arterial system configuration and wave reflection," *Journal of Biomedical Engineering,* vol. 9, pp. 299-301, 1987.

[238] N. Xiao, J. Alastruey and C. A. Figueroa, “A systematic comparison between 1-D and 3-D hemodynamics in compliant arterial models,” *International Journal for Numerical Methods in Biomedical Engineering,* vol. 30, no. 2, pp. 204-231, 2014.

[239] J. Alastruey, J. Aramburu, P. Charlton, W. Jin and M. Willemet, “Nektar1D Reference Manual,” King’s College, London, UK, 2021.

[240] V. K. Mehta and B. Dasgupta, “A constrained optimization algorithm based on the simplex search method,” *Engineering Optimization,* vol. 44, no. 5, pp. 537-550, 2012.

[241] J. C. Lagarias, J. A. Reeds, M. H. Wright and P. E. Wright, “Convergence Properties of the Nelder-Mead Simplex Method in Low Dimensions,” *SIAM Journal on Optimization,* vol. 9, no. 1, pp. 112-147, 1998.

[242] R. M. Lewis, V. Torczona and M. W. Trosset, “Direct search methods: then and now,” *Journal of Computational and Applied Mathematics,* vol. 124, pp. 191-207, 2000.

[243] F. Gijsen, Y. Katagiri, P. Barlis, C. Bourantas, C. Collet, U. Coskun, J. Daemen, J. Dijkstra, E. Edelman, P. Evans, K. Heiden, R. Hose, B. Koo, R. Krams, A. Marsden, A. Migliavacca, Y. Onuma, A. Ooi, E. Poon, H. Samady, P. Stone, K. Takahashi, D. Tang, V. Thondapu and P. Serruys, “Expert recommendations on the assessment of wall shear stress in human coronary arteries: existing methodologies, technical considerations, and clinical applications,” *European Society of Cardiology*, vol. 40, pp. 3421-3433, 2019.

[244] S. Celi, E. Vignali, K. Capellini and E. Gasparotti, “On the Role and Effects of Uncertainties in Cardiovascular in silico Analyses,” *Frontiers in Medical Technology,* vol. 3, 2021.

[245] C. M. McEniery, J. R. Cockcroft, M. J. Roman, S. S. Franklin and I. B. Wilkinson, “Central blood pressure: current evidence and clinical importance,” *European Heart Journal,* vol. 35, no. 26, pp. 1719-1725, 2014.

[246] A. Wykretowicz, A. Rutkowska, T. Krauze, D. Przymuszala, P. Guzik, R. Marciniak and H. Wysocki, “Pulse pressure amplification in relation to body fatness,” *British Journal of Clinical Pharmacology,* vol. 73, no. 4, pp. 546-552, 2012.

[247] M. Gabbour, C. Rigsby and M. Markl, “Comparison of 4D flow and 2D PC MRI blood flow quantification in children and young adults with congenital heart disease,” *Journal of Cardiovascular Magnetic Resonance,* vol. 15, no. 1, 2013.

[248] A. Ghosh, A. Dharmarajan, P. K. Swain, D. Das, P. Verma and P. R. Tripathy, “Impact of Cardiovascular Factors on Pulse Wave Velocity and Total Vascular Resistance in Different Age Group Patients with Cardiovascular Disorders,” *Current Aging Science,* vol. 11, no. 4, pp. 261-268, 2018.

[249] M. J. v. Hout, I. A. Dekkers, L. Lin, J. J. Westenberg, M. J. Schalij, J. W. Jukema, R. L. Widya, S. C. Boone, R. d. Mutsert, F. R. Rosendaal, A. J. Scholte and H. J. Lamb, “Estimated pulse wave velocity (ePWV) as a potential gatekeeper for MRI-assessed PWV: a linear and deep neural network based approach in 2254 participants of the

Netherlands Epidemiology of Obesity study," *The International Journal of Cardiovascular Imaging,* vol. 38, no. 1, pp. 183-193, 2022.

[250] R. Shahzad, A. Shankar, R. Amier, R. Nijveldt, J. J. M. Westenberg, A. d. Roos, B. P. F. Lelieveldt and R. J. v. d. Geest, "Quantification of aortic pulse wave velocity from a population based cohort: a fully automatic method," *Journal of Cardiovascular Magnetic Resonance,* vol. 21, no. 1, 2019.

[251] D. M. A. Zaman, J. Hacker, D. Mendelow and D. Birchall, "Analysis of haemodynamic factors involved in carotid atherosclerosis using computational fluid dynamics," *The British Journal of Radiology,* vol. 82, pp. 33 - 38, 2009.

[252] D. Chen, M. Müller-Eschner, H. V. Tengg-Kobligk, D. Barber, D. Böckler, R. Hose and Y. Ventikos, "A patient-specific study of type-B aortic dissection: Evaluation of true-false lumen blood exchange," *BioMedical Engineering OnLine* , vol. 12, no. 1, 2013.

[253] A. Evangelista, V. Galuppo, D. Gruosso, H. Cuéllar, G. Teixidó and J. Rodríguez-Palomares, "Role of entry tear size in type B aortic dissection," *Annals of Cardiothoracic Surgery,* vol. 3, no. 4, pp. 403-405, 2014.

[254] M. E. Safar, R. Asmar, A. Benetos, J. Blacher, P. Boutouyrie, P. Lacolley, S. Laurent, G. London, B. Pannier, A. Protogerou and V. Regnault, "Interaction Between Hypertension and Arterial Stiffness," *Hypertension,* vol. 72, no. 4, pp. 796-805, 2018.

[255] F. Lotz, C. Meier, A. Leppert and M. Galanski, "Cardiovascular Flow Measurement with Phase-Contrast MR Imaging: Basic Facts and Impleentation," *Radiographics,* vol. 22, no. 3, pp. 651-671, 2002.

[256] J. Weddell, J. Kwack, P. Imoukhuede and A. Masud, "Haemodynamic Analysis in an Idealised Artery Tree: Differences in Wall Shear Stress between Newtonian and Non-Newtonian Blood Models," *PLoS One,* vol. 10, no. 4, 2015.

[257] H. Wang, D. Balzani, V. Vedula, K. Uhlmann and F. Varnik, "On the Potential Self-Amplification of Aneurysms Due to Tissue Degradation and Blood Flow Revealed From FSI Simulation," *Frontiers in Physiology,* vol. 12, 2021.

[258] Y. Jiang, G. Lu, L. Ge, L. Huang, H. Wan, J. Wan and X. Zhang, "Rupture point hemodynamics of intracranial aneurysms: Case report and literature review," *Annals of Vascular Surgery - Brief Reports and Innovations,* vol. 1, no. 2, 2021.

[259] H. Roos, M. Ghaffari, M. Falkenberg, V. Chernoray, A. Jeppsson and H. Nilsson, "Displacement Forces in Iliac Landing Zones and Stent Graft Interconnections in Endovascular Aortic Repair: An Experimental Study," *European Journal of Vascular & Endovascular Surgery,* vol. 47, no. 3, pp. 262-267, 2014.

[260] L. Morris, P. Delassus, M. Walsh and T. McGloughlin, "A mathematical model to predict the in vivo pulsatile drag forces acting on bifurcated stent grafts used in endovascular treatment of abdominal aortic aneurysms (AAA)," *Journal of Biomechanics,* vol. 37, no. 7, pp. 1087-1095, 2004.

[261] J. Lantz, P. Dyverfeldt and T. Ebbers, “Improving Blood Flow Simulations by Incorporating Measured Subject-Specific Wall Motion,” *Cardiovascular Engineering and Technology*, vol. 5, no. 3, pp. 261-269, 2015.

[262] M. Albadawi, Y. Abuouf, S. Elsagheer, H. Sekiguchi, S. Ookawara and M. Ahmed, “Influence of Rigid–Elastic Artery Wall of Carotid and Coronary Stenosis on Hemodynamics,” *Bioengineering*, vol. 9, no. 11, 2022.

[263] S. Numata, K. Itatani, K. Kanda, K. Doi, S. Yamazaki and K. Morimoto, “Blood flow analysis of the aortic arch using computational fluid dynamics,” *European Journal of Cardio-Thoracic Surgery*, vol. 49, pp. 1578-1585, 2016.

[264] F. Sotiropoulos, T. B. Le and A. Gilmanov, “Fluid Mechanics of Heart Valves and Their Replacements,” *Annual Review of Fluid Mechanics* , vol. 48, pp. 259-283, 2016.

7 Appendix

7.1 Appendix A.1: Flow Waveforms for Pulse Wave Velocity

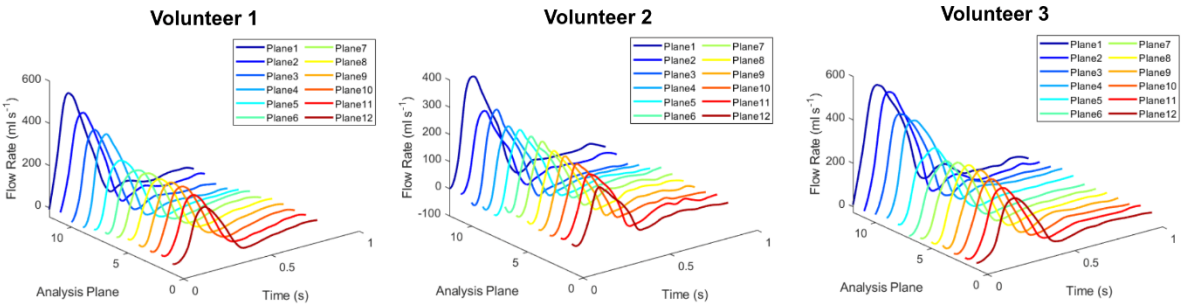

Figure A.1*: Branch flow waveforms derived from the methodology outlined in Chapter 4, which were used to calculate arterial PWV in the thoracic aorta of each healthy volunteer.*

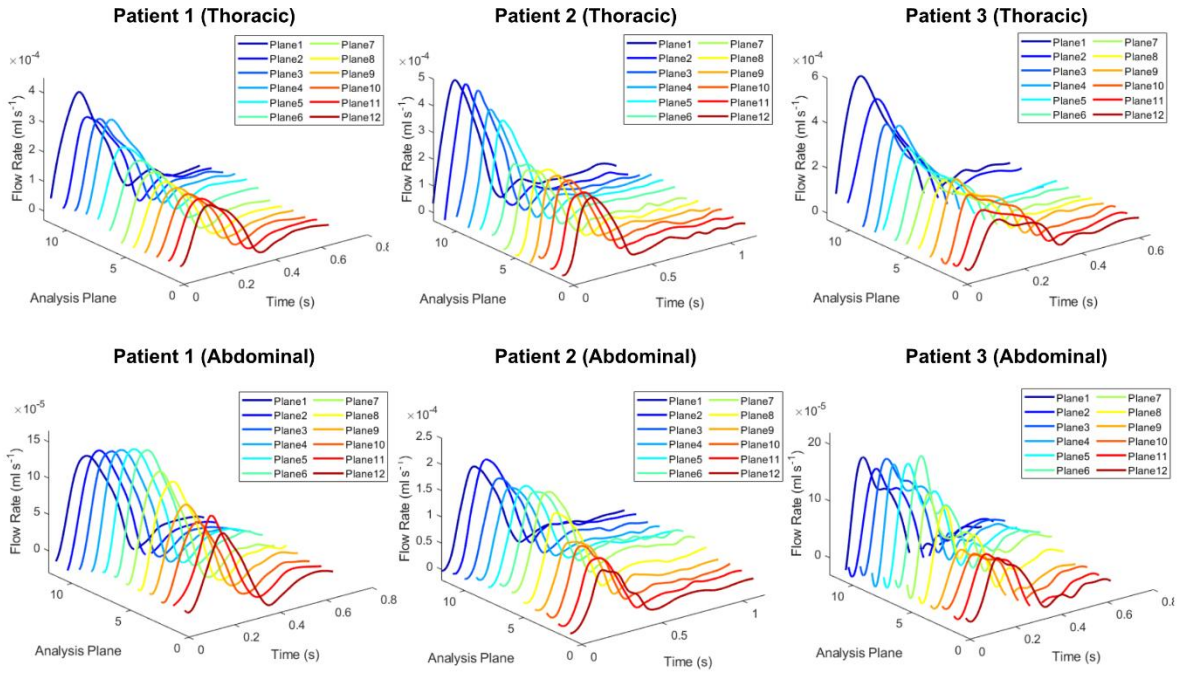

***Figure A.2**: Branch flow waveforms derived from the methodology outlined in Chapter 4, which were used to calculate arterial PWV in the thoracic and abdominal aorta of each TBAD patient.*

7.2 Appendix A.2 Aortic Dissection TL & FL Area

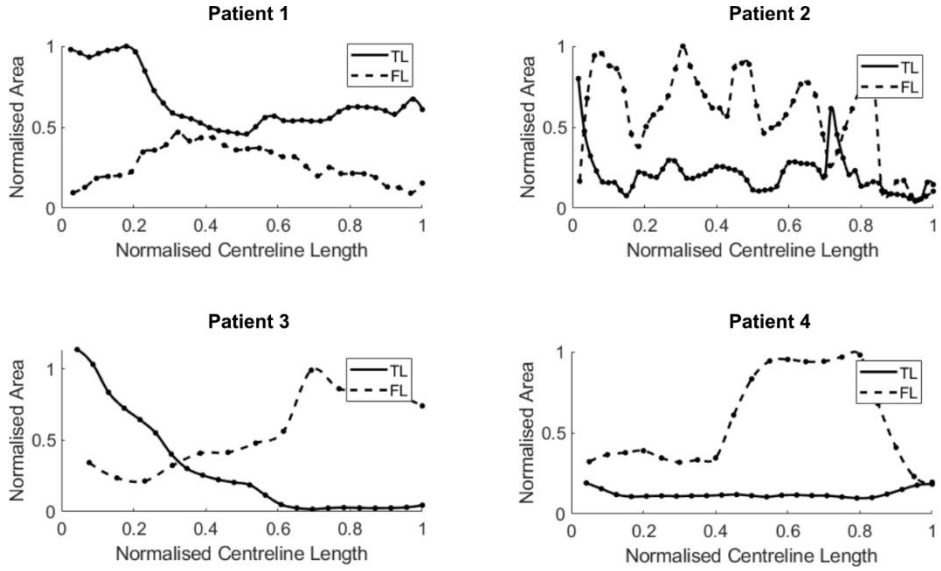

Figure A.3*: Area of the TL vs the FL in dissection patients, highlighting the degree of TL collapse due to an expanding FL.*

7.3 Appendix A.3: 1D Pulse Waveforms

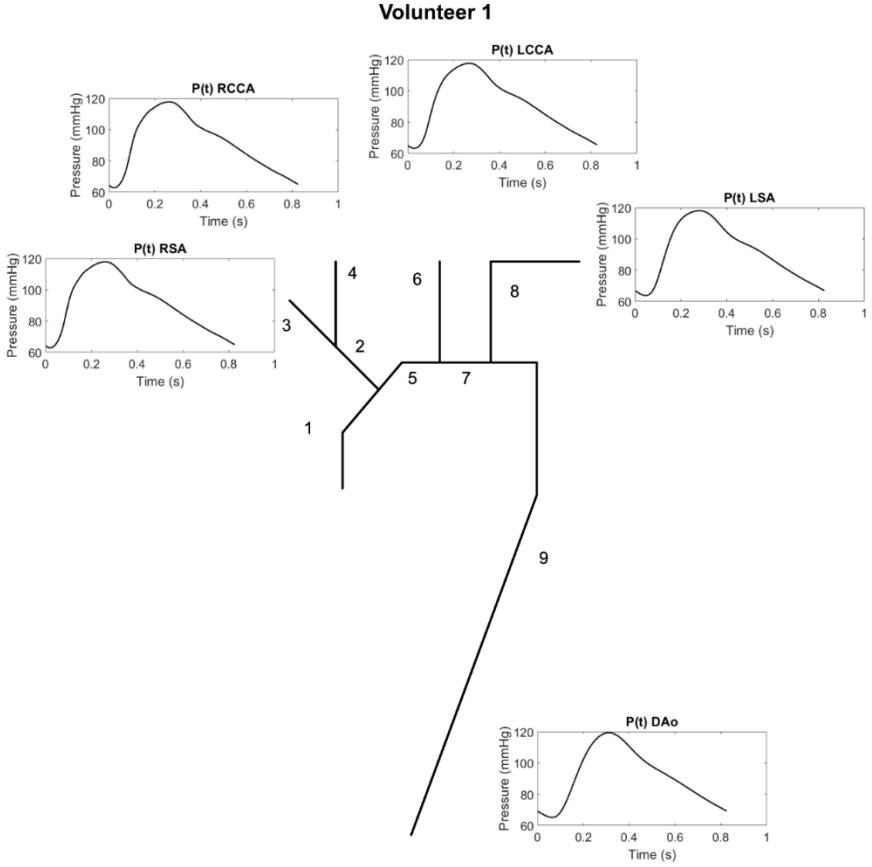

Figure A.4*: Schematic of the 0D-1D model of healthy volunteer 1, showing 9 discrete arterial segments. At each terminal branch, the resultant pressure waveform after 20 cardiac cycles is presented.*

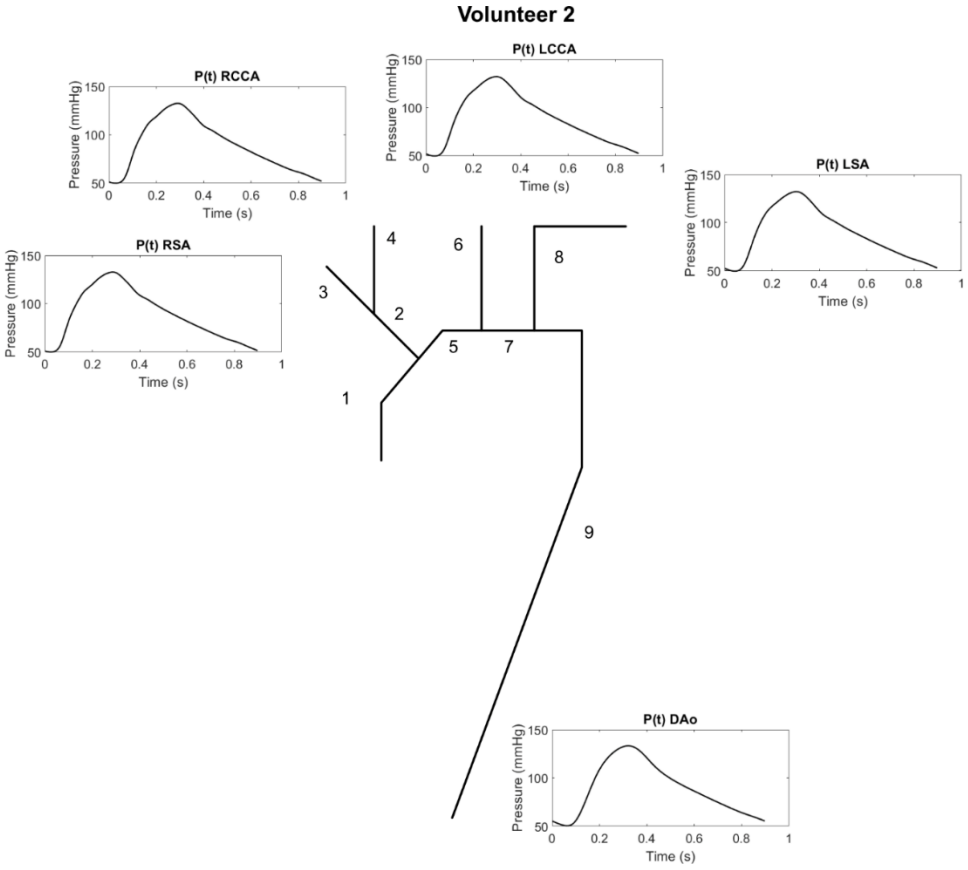

Figure A.5*: Schematic of the 0D-1D model of healthy volunteer 2, showing 9 discrete arterial segments. At each terminal branch, the resultant pressure waveform after 20 cardiac cycles is presented.*

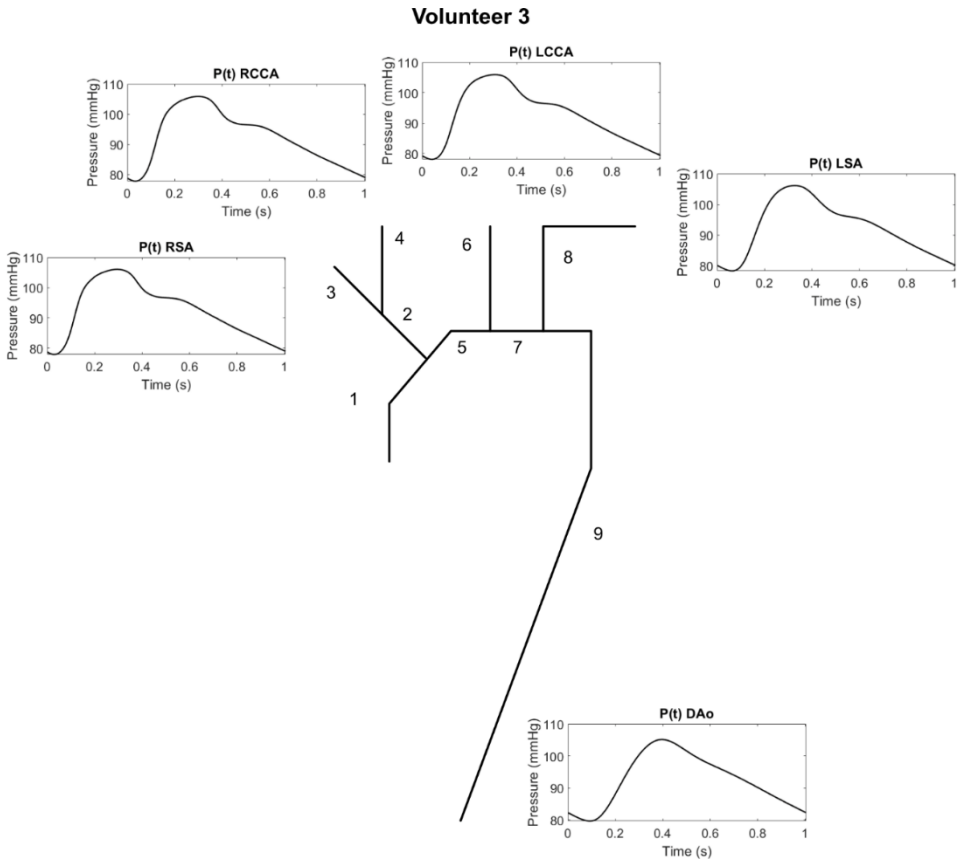

Figure A.6*: Schematic of the 0D-1D model of healthy volunteer 3, showing 9 discrete arterial segments. At each terminal branch, the resultant pressure waveform after 20 cardiac cycles is presented.*

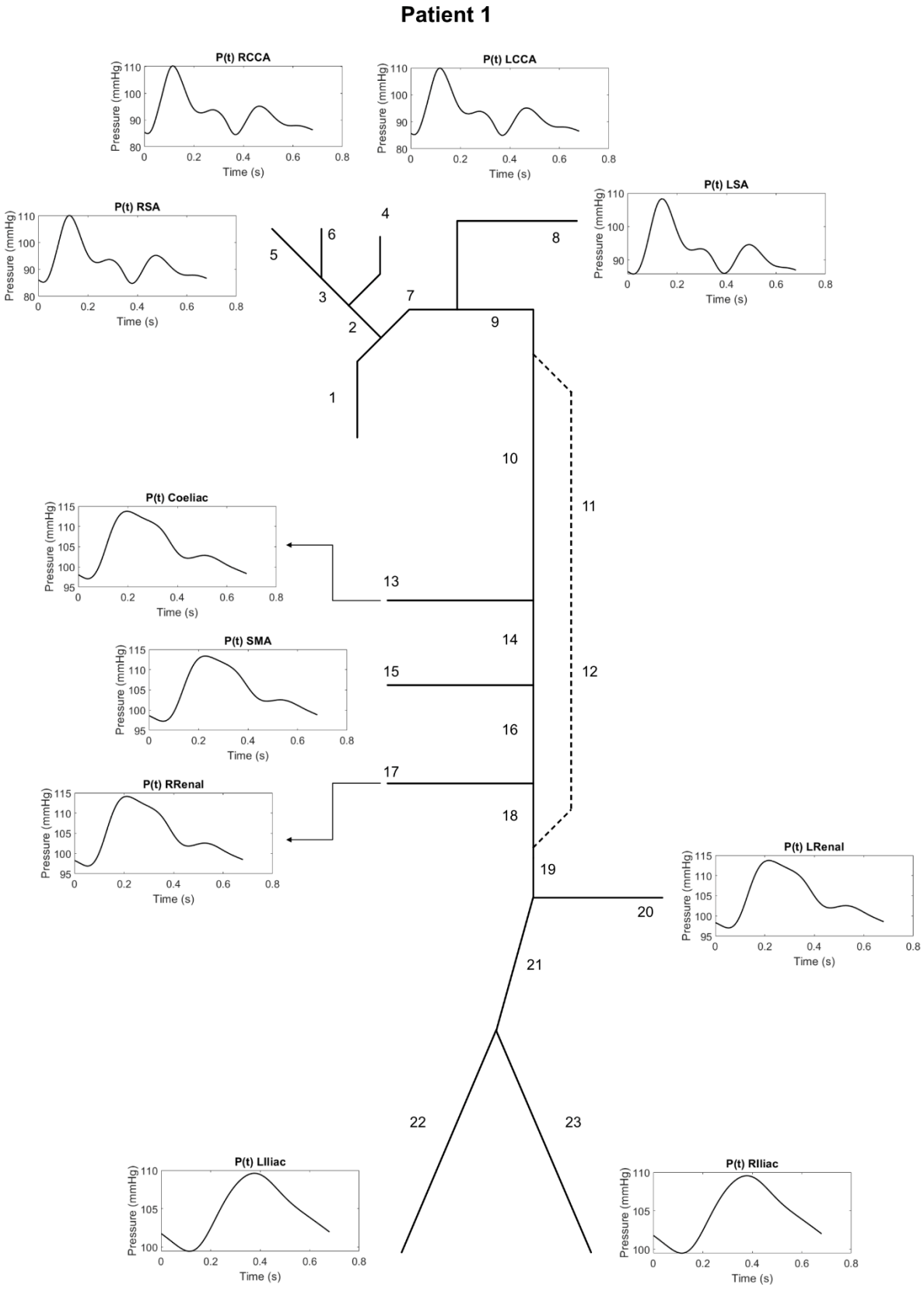

Figure A.7*: Schematic of the 0D-1D model of patient 1, showing 23 discrete arterial segments and including the true lumen (solid line) and false lumen (dashed line). At each terminal branch, the resultant pressure waveform after 20 cardiac cycles is presented.*

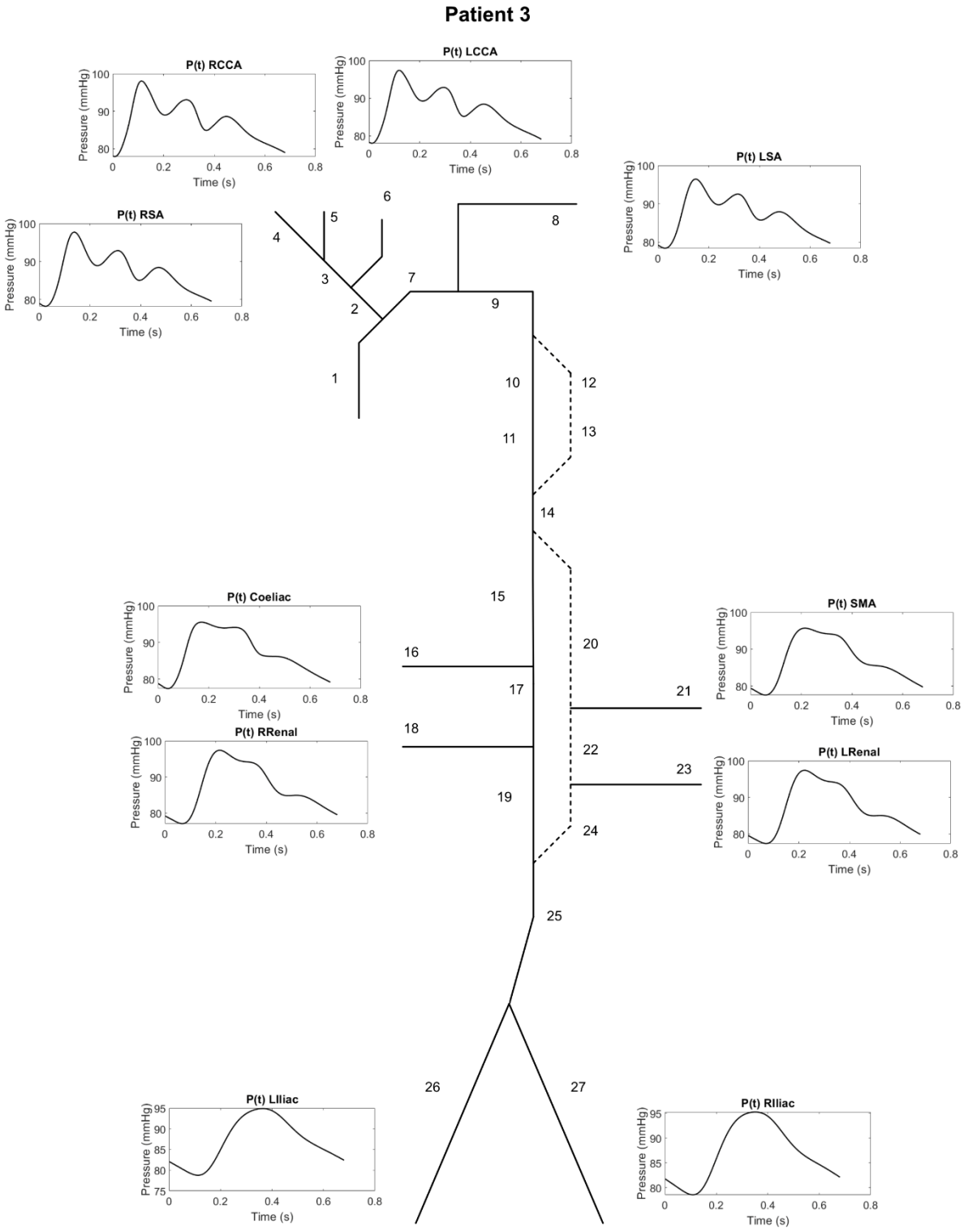

Figure A.8*: Schematic of the 0D-1D model of patient 3, showing 27 discrete arterial segments and including the true lumen (solid line) and false lumen (dashed line). At each terminal branch, the resultant pressure waveform after 20 cardiac cycles is presented.*

7.4 Appendix A.4: Information on 1D Model Segments

Table A.1*: Length, radius, area, and beta (stiffness) for each segments of healthy volunteer 1, utilised to create the 1D model for Nektar1D.*

Volunteer 1				
Segment	Length (m)	Mean Radius (m)	Area (m2)	Beta
1	6.20E-02	1.48E-02	6.90E-04	4.97E+06
2	5.06E-02	5.39E-03	9.14E-05	1.37E+07
3	2.48E-02	4.73E-03	7.03E-05	1.56E+07
4	3.40E-02	3.53E-03	3.91E-05	2.09E+07
5	6.91E-03	1.33E-02	5.56E-04	5.54E+06
6	6.55E-02	3.32E-03	3.46E-05	2.22E+07
7	1.42E-02	1.25E-02	4.87E-04	5.92E+06
8	1.35E-01	4.64E-03	6.75E-05	1.59E+07
9	2.61E-01	1.18E-02	4.35E-04	6.26E+06

Table A.2*: Length, radius, area, and beta (stiffness) for each segments of healthy volunteer 2, utilised to create the 1D model for Nektar1D.*

Volunteer 2				
Segment	Length (m)	Mean Radius (m)	Area (m2)	Beta
1	5.63E-02	1.32E-02	5.51E-04	1.57E+07
2	2.88E-02	5.21E-03	8.54E-05	4.00E+07
3	1.28E-02	3.83E-03	4.62E-05	5.44E+07
4	3.66E-02	3.17E-03	3.16E-05	6.57E+07
5	1.48E-02	1.31E-02	5.39E-04	1.59E+07
6	7.30E-02	2.70E-03	2.29E-05	7.72E+07
7	2.05E-02	1.19E-02	4.43E-04	1.76E+07
8	1.00E-01	2.89E-03	2.62E-05	7.21E+07
9	2.41E-01	1.10E-02	3.77E-04	1.90E+07

Table A.3*: Length, radius, area, and beta (stiffness) for each segments of healthy volunteer 3, utilised to create the 1D model for Nektar1D.*

Volunteer 3				
Segment	Length (m)	Mean Radius (m)	Area (m2)	Beta
1	7.97E-02	1.48E-02	6.91E-04	1.54E+06
2	2.79E-02	6.31E-03	1.25E-04	3.62E+06

3	2.76E-02	4.69E-03	6.90E-05	4.87E+06
4	3.67E-02	3.56E-03	3.98E-05	6.42E+06
5	8.57E-03	1.43E-02	6.46E-04	1.59E+06
6	5.83E-02	3.97E-03	4.95E-05	5.75E+06
7	1.48E-02	1.28E-02	5.15E-04	1.78E+06
8	1.16E-01	4.58E-03	6.58E-05	4.99E+06
9	2.51E-01	1.04E-02	3.38E-04	2.20E+06

Table A.4*: Length, radius, area, and beta (stiffness) for each segments of clinical patient 1, utilised to create the 1D model for Nektar1D.*

Patient 1				
Segment	Length (m)	Mean Radius (m)	Area (m2)	Beta
1	5.47E-02	1.70E-02	9.04E-04	6.68E+06
2	3.13E-02	1.05E-02	3.46E-04	1.08E+07
3	2.44E-02	5.09E-03	8.13E-05	2.23E+07
4	6.92E-02	3.44E-03	3.72E-05	3.29E+07
5	1.01E-01	4.08E-03	5.23E-05	2.77E+07
6	5.21E-02	2.97E-03	2.77E-05	3.81E+07
7	1.39E-02	1.46E-02	6.66E-04	7.78E+06
8	1.62E-01	4.85E-03	7.38E-05	2.34E+07
9	1.52E-02	1.19E-02	4.45E-04	9.52E+06
10	2.53E-04	8.97E-03	2.53E-04	1.26E+07
11	1.21E-04	6.20E-03	1.21E-04	1.83E+07
12	8.59E-05	5.23E-03	8.59E-05	2.17E+07
13	3.05E-02	3.31E-03	3.45E-05	3.95E+06
14	1.79E-02	8.01E-03	2.01E-04	1.64E+06
15	7.18E-02	3.25E-03	3.31E-05	4.04E+06
16	8.94E-03	8.11E-03	2.07E-04	1.62E+06
17	5.44E-02	2.80E-03	2.46E-05	4.69E+06
18	9.43E-03	8.25E-03	2.14E-04	1.59E+06
19	8.71E-03	8.57E-03	2.31E-04	1.53E+06
20	4.25E-02	3.37E-03	3.58E-05	3.88E+06
21	2.68E-02	8.53E-03	2.28E-04	1.54E+06
22	3.08E-01	5.14E-03	8.30E-05	2.55E+06
23	3.11E-01	5.15E-03	8.33E-05	2.55E+06

Table A.5*: Length, radius, area, and beta (stiffness) for each segments of clinical patient 2, utilised to create the 1D model for Nektar1D.*

Patient 2				
Segment	Length (m)	Mean Radius (m)	Area (m2)	Beta
1	5.76E-02	1.47E-02	6.78E-04	1.56E+06
2	4.59E-02	5.51E-03	9.55E-05	4.16E+06
3	1.05E-01	4.57E-03	6.57E-05	5.02E+06
4	4.58E-02	3.34E-03	3.50E-05	6.87E+06
5	9.06E-03	1.29E-02	5.27E-04	1.77E+06
6	7.97E-02	3.68E-03	4.26E-05	6.23E+06
7	8.62E-03	1.21E-02	4.60E-04	1.90E+06
8	1.49E-01	4.04E-03	5.12E-05	5.68E+06
9	6.24E-03	1.13E-02	4.02E-04	2.03E+06
10 & 11	1.70E-01	5.77E-03	1.04E-04	3.98E+06
12	7.19E-03	3.90E-03	4.79E-05	5.88E+06
13 & 14	1.80E-01	1.01E-02	3.19E-04	2.28E+06
15	1.22E-02	1.62E-02	8.28E-04	1.41E+06
16	7.56E-02	5.36E-03	9.03E-05	5.36E+06
17	5.25E-02	3.99E-03	4.99E-05	7.20E+06
18	2.11E-02	5.06E-03	8.06E-05	5.67E+06
19	6.63E-02	4.35E-03	5.95E-05	6.60E+06
20	8.09E-03	4.80E-03	7.24E-05	5.98E+06
21	6.91E-02	2.95E-03	2.73E-05	9.75E+06
22	2.15E-02	4.87E-03	7.45E-05	5.90E+06
23	4.26E-02	3.39E-03	3.61E-05	8.47E+06
24	4.56E-02	3.54E-03	3.94E-05	8.11E+06
25 & 26	1.81E-01	9.58E-03	2.88E-04	3.00E+06
27	2.46E-02	1.61E-02	8.18E-04	1.42E+06
28	2.12E-02	7.84E-03	1.93E-04	3.66E+06
29 & 30	7.41E-02	3.95E-03	4.91E-05	7.26E+06
31	2.24E-01	6.40E-03	1.29E-04	4.49E+06
32	6.50E-02	5.72E-03	1.03E-04	5.02E+06
33	1.80E-01	5.72E-03	1.03E-04	5.02E+06

***Table A.6**: Length, radius, area, and beta (stiffness) for each segments of clinical patient 3, utilised to create the 1D model for Nektar1D.*

Patient 3				
Segment	Length	Radius	Area	Beta
1	5.49E-02	1.87E-02	1.09E-03	4.63E+06
2	9.50E-03	1.07E-02	3.57E-04	8.11E+06
3	3.95E-02	6.73E-03	1.42E-04	1.28E+07
4	1.06E-01	5.15E-03	8.33E-05	1.68E+07
5	1.83E-02	3.44E-03	3.72E-05	2.51E+07
6	5.07E-02	3.88E-03	4.72E-05	2.23E+07
7	1.52E-02	1.72E-02	9.34E-04	5.01E+06
8	1.37E-01	4.79E-03	7.20E-05	1.81E+07
9	1.15E-01	2.16E-02	1.47E-03	3.99E+06
10 & 11	8.04E-02	1.09E-02	3.73E-04	7.93E+06
12 & 13	6.85E-02	1.06E-02	3.55E-04	8.13E+06
14	2.66E-02	1.67E-02	8.71E-04	5.19E+06
15	4.27E-02	1.58E-02	7.86E-04	5.46E+06
16	2.98E-02	5.23E-03	8.58E-05	4.04E+06
17	3.79E-02	1.16E-02	4.21E-04	1.82E+06
18	7.32E-02	2.86E-03	2.57E-05	7.38E+06
19	1.68E-02	5.66E-03	1.01E-04	3.73E+06
20	5.20E-02	2.92E-03	2.68E-05	7.22E+06
21	7.48E-02	4.68E-03	6.89E-05	4.50E+06
22	1.27E-02	5.73E-03	1.03E-04	3.68E+06
23	6.07E-02	2.80E-03	2.47E-05	7.53E+06
24	3.24E-02	8.38E-03	2.21E-04	2.52E+06
25	5.92E-02	1.33E-02	5.54E-04	1.59E+06
26	2.41E-01	6.44E-03	1.30E-04	3.27E+06
27	2.20E-01	6.22E-03	1.22E-04	3.39E+06

7.5 Appendix A.5: Estimated Windkessel Parameters

***Table A.7**: Estimated 3EWM parameters based on arterial PWV and vessel geometry for the thoracic aorta of healthy volunteer 1, where Z = impedance, R = net peripheral resistance, and C = compliance.*

Volunteer 1				
Branch	**Z**	**R**	**C**	**Beta**
RSA	6.53E+07	1.50E+09	4.77E-11	7.17E+01
RCCA	1.17E+08	2.70E+09	3.64E-11	9.84E+01
LCCA	1.33E+08	3.05E+09	6.21E-11	1.89E+02
LSA	6.80E+07	1.57E+09	2.50E-10	3.91E+02
Dao	1.06E+07	2.43E+08	3.11E-09	7.54E+02

***Table A.8**: Estimated 3EWM parameters based on arterial PWV and vessel geometry for the thoracic aorta of healthy volunteer 2, where Z = impedance, R = net peripheral resistance, and C = compliance.*

Volunteer 2				
Branch	**Z**	**R**	**C**	**Beta**
RSA	1.02E+08	2.34E+09	1.01E-11	2.37E+01
RCCA	1.49E+08	3.43E+09	1.98E-11	6.78E+01
LCCA	2.05E+08	4.72E+09	2.86E-11	1.35E+02
LSA	1.79E+08	4.13E+09	4.50E-11	1.86E+02
Dao	1.25E+07	2.87E+08	1.55E-09	4.46E+02

***Table A.9**: Estimated 3EWM parameters based on arterial PWV and vessel geometry for the thoracic aorta of healthy volunteer 3, where Z = impedance, R = net peripheral resistance, and C = compliance.*

Volunteer 3				
Branch	**Z**	**R**	**C**	**Beta**
RSA	4.65E+07	1.07E+09	1.68E-10	1.80E+02
RCCA	8.07E+07	1.86E+09	1.29E-10	2.39E+02
LCCA	6.48E+07	1.49E+09	2.55E-10	3.80E+02
LSA	4.88E+07	1.12E+09	6.73E-10	7.55E+02
Dao	9.51E+06	2.19E+08	7.48E-09	1.64E+03

***Table A.10**: Estimated 3EWM parameters based on arterial PWV and vessel geometry for the thoracoabdominal aorta of patient 1, where Z = impedance, R = net peripheral resistance, and C = compliance.*

Patient 1				
Branch	**Z**	**R**	**C**	**Beta**
RSA	5.21E+07	1.20E+09	9.43E-11	1.13E+02
RCCA	9.82E+07	2.26E+09	2.58E-11	5.82E+01
LCCA	7.32E+07	1.68E+09	4.59E-11	7.73E+01
LSA	3.69E+07	8.49E+08	2.13E-10	1.81E+02
Coeliac	7.90E+07	1.82E+09	1.62E-10	2.95E+02
SMA	8.22E+07	1.89E+09	3.66E-10	6.93E+02
Left Renal	7.62E+07	1.75E+09	2.34E-10	4.10E+02
Right Renal	1.11E+08	2.55E+09	2.06E-10	5.24E+02
Left Iliac	3.28E+07	7.55E+08	3.93E-09	2.97E+03
Right Iliac	3.27E+07	7.52E+08	3.99E-09	3.00E+03

***Table A.11**: Estimated 3EWM parameters based on arterial PWV and vessel geometry for the thoracoabdominal aorta of patient 2, where Z = impedance, R = net peripheral resistance, and C = compliance.*

Patient 2				
Branch	**Z**	**R**	**C**	**Beta**
RSA	8.44E+07	1.94E+09	6.09E-10	1.18E+03
RCCA	1.58E+08	3.64E+09	1.41E-10	5.14E+02
LCCA	1.30E+08	2.99E+09	2.99E-10	8.95E+02
LSA	1.08E+08	2.49E+09	6.73E-10	1.67E+03
Coeliac	1.11E+08	2.55E+09	1.84E-10	4.70E+02
SMA	9.32E+07	2.14E+09	2.77E-10	5.94E+02
Left Renal	1.54E+08	3.53E+09	1.08E-10	3.82E+02
Right Renal	2.04E+08	4.68E+09	1.32E-10	6.20E+02
Left Iliac	4.31E+07	9.91E+08	2.02E-09	2.00E+03
Right Iliac	5.40E+07	1.24E+09	1.30E-09	1.62E+03

***Table A.12**: Estimated 3EWM parameters based on arterial PWV and vessel geometry for the thoracoabdominal aorta of patient 3, where Z = impedance, R = net peripheral resistance, and C = compliance.*

Patient 3				
Branch	**Z**	**R**	**C**	**Beta**
RSA	9.58E+07	2.20E+09	2.07E-10	4.55E+02
RCCA	2.14E+08	4.93E+09	1.59E-11	7.82E+01
LCCA	1.69E+08	3.88E+09	5.60E-11	2.17E+02
LSA	1.11E+08	2.55E+09	2.30E-10	5.86E+02
Coeliac	4.59E+07	1.06E+09	2.45E-10	2.59E+02
SMA	5.72E+07	1.31E+09	4.93E-10	6.48E+02
Left Renal	1.60E+08	3.67E+09	1.43E-10	5.26E+02
Right Renal	1.53E+08	3.53E+09	1.80E-10	6.34E+02
Left Iliac	3.02E+07	6.95E+08	3.01E-09	2.09E+03
Right Iliac	3.24E+07	7.45E+08	2.57E-09	1.91E+03

7.6 Appendix A.6: Calibrated Windkessel Parameters

***Table A.13**: Calibrated 3EWM parameters applied to the 0D-3D CFD model of healthy volunteer 1, where Z = impedance, R = net peripheral resistance, and C = compliance.*

Volunteer 1 (Calibrated 3EWM Parameters)				
	Z	R	C	Beta
RSA	1.30E+06	1.76E+09	3.80E-10	6.71E+02
RCCA	1.26E+07	3.12E+09	1.41E-10	4.40E+02
LCCA	3.19E+06	3.73E+09	1.53E-10	5.73E+02
LSA	1.44E+07	1.92E+09	4.24E-10	8.15E+02
Dao	4.34E+06	1.78E+08	4.73E-09	8.40E+02

***Table A.14**: Calibrated 3EWM parameters applied to the 0D-3D CFD model of healthy volunteer 2, where Z = impedance, R = net peripheral resistance, and C = compliance.*

Volunteer 2 (Calibrated 3EWM Parameters)				
	Z	R	C	Beta
RSA	2.05E+08	1.50E+09	2.77E-12	4.16E+00
RCCA	1.05E+09	2.09E+09	7.04E-13	1.47E+00
LCCA	1.71E+08	4.87E+09	6.69E-11	3.26E+02
LSA	6.07E+06	4.11E+09	8.23E-11	3.38E+02
Dao	8.72E+06	2.13E+08	2.89E-09	6.15E+02

***Table A.15**: Calibrated 3EWM parameters applied to the 0D-3D CFD model of healthy volunteer 3, where Z = impedance, R = net peripheral resistance, and C = compliance.*

Volunteer 3 (Calibrated 3EWM Parameters)				
	Z	R	C	Beta
RSA	1.14E+07	9.89E+08	8.91E-10	8.82E+02
RCCA	4.82E+07	2.69E+09	4.48E-10	1.20E+03
LCCA	1.65E+07	3.63E+09	5.16E-10	1.87E+03
LSA	2.78E+07	3.16E+09	8.74E-10	2.76E+03
Dao	3.63E+06	1.49E+08	1.46E-08	2.18E+03

***Table A.16**: Calibrated 3EWM parameters applied to the 0D-3D CFD model of patient 1, where Z = impedance, R = net peripheral resistance, and C = compliance.*

Patient 1 (Calibrated 3EWM Parameters)				
	Z	R	C	Beta
RSA	1.10E+08	2.29E+09	3.16E-09	7.24E+03
RCCA	4.82E+08	3.22E+09	1.06E-09	3.41E+03
LCCA	3.13E+08	1.45E+09	8.67E-10	1.26E+03
LSA	2.62E+08	1.49E+09	3.01E-10	4.48E+02
Coeliac	4.31E+06	1.68E+09	7.24E-10	1.22E+03
SMA	6.02E+07	1.57E+09	1.15E-09	1.81E+03
Left Renal	3.76E+08	1.46E+09	6.66E-10	9.72E+02
Right Renal	-4.69E+06	3.47E+09	1.06E-10	3.68E+02
Left Iliac	2.63E+07	1.98E+09	3.89E-09	7.70E+03
Right Iliac	1.91E+07	1.72E+09	5.23E-09	9.00E+03

***Table A.17**: Calibrated 3EWM parameters applied to the 0D-3D CFD model of patient 2, where Z = impedance, R = net peripheral resistance, and C = compliance.*

Patient 2 (Calibrated 3EWM Parameters)				
	Z	R	C	Beta
RSA	7.06E+07	2.65E+09	1.87E-09	4.96E+03
RCCA	1.38E+08	5.05E+09	8.93E-10	4.51E+03
LCCA	1.46E+08	3.30E+09	7.94E-10	2.62E+03
LSA	7.42E+07	3.84E+09	1.71E-09	6.57E+03
Coeliac	1.06E+07	2.97E+09	2.71E-10	8.05E+02
SMA	5.42E+07	1.56E+09	1.05E-09	1.64E+03
Left Renal	1.28E+07	3.27E+09	2.32E-10	7.59E+02
Right Renal	4.02E+08	2.79E+09	6.68E-10	1.86E+03
Left Iliac	4.91E+07	1.03E+09	3.43E-09	3.53E+03

Right Iliac	6.70E+07	1.97E+09	3.08E-09	6.07E+03

Table A.18*: Calibrated 3EWM parameters applied to the 0D-3D CFD model of patient 3, where Z = impedance, R = net peripheral resistance, and C = compliance.*

Patient 3 (Calibrated 3EWM Parameters)				
	Z	R	C	Beta
RSA	1.87E+08	8.32E+08	7.45E-10	6.20E+02
RCCA	5.49E+07	2.45E+09	1.91E-09	4.67E+03
LCCA	5.63E+07	2.44E+09	1.76E-09	4.30E+03
LSA	4.70E+07	2.45E+09	1.56E-09	3.82E+03
Coeliac	3.75E+07	3.34E+09	9.33E-10	3.12E+03
SMA	4.36E+07	7.32E+08	3.95E-10	2.89E+02
Left Renal	3.87E+06	1.76E+09	1.29E-10	2.26E+02
Right Renal	2.72E+08	2.12E+09	1.80E-10	3.81E+02
Left Iliac	3.75E+07	2.69E+09	2.15E-09	5.77E+03
Right Iliac	3.63E+07	2.29E+09	1.72E-09	3.93E+03

7.7 Appendix B.1 Instantaneous Flow Waveforms

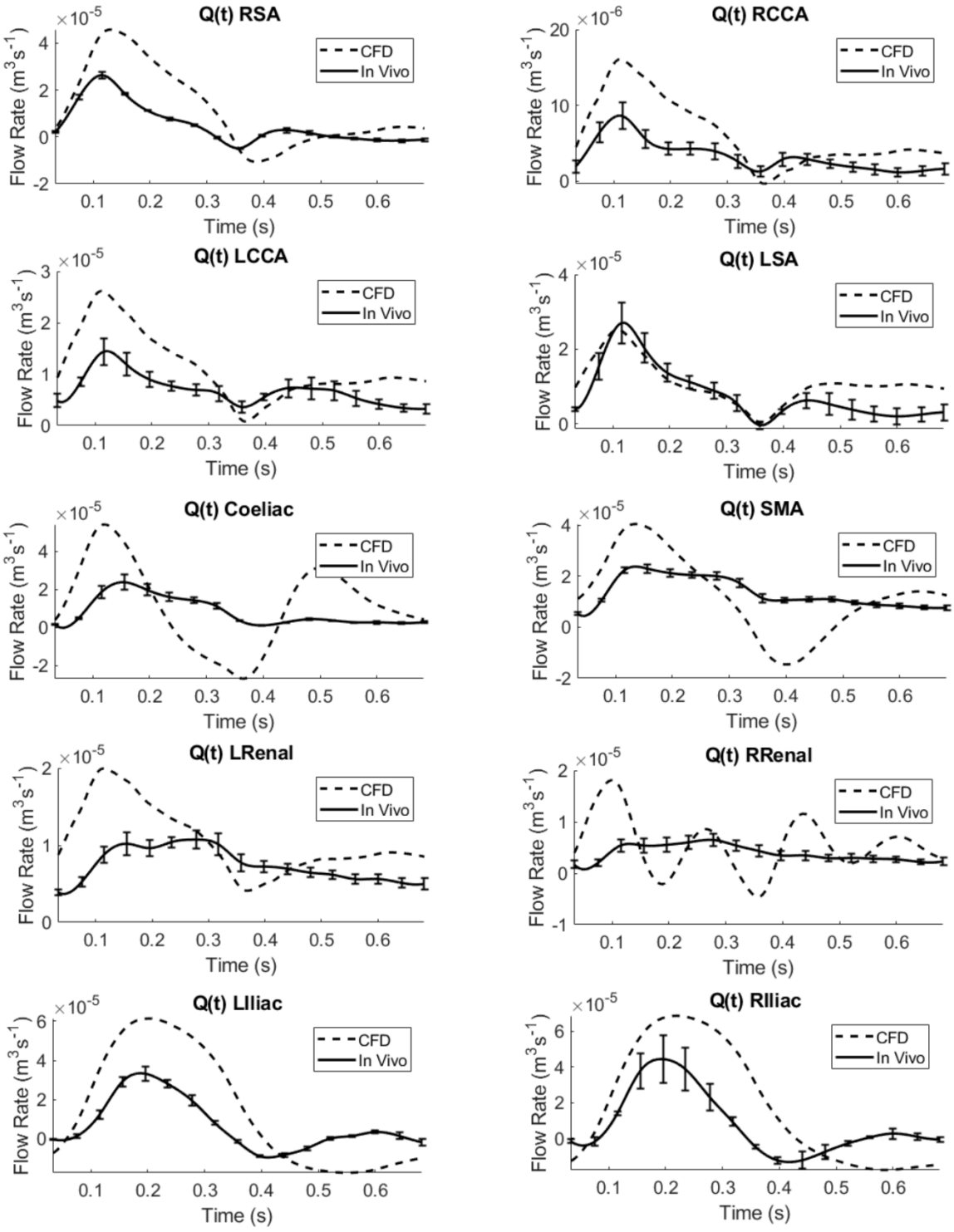

Figure A.19*: Instantaneous flow waveforms as derived from CFD models (dashed line) and in vivo 4D Flow-MRI data (dashed line) at each terminal branch of the thoracic aorta of patient 1. Error bars represent mean ± standard deviation.*

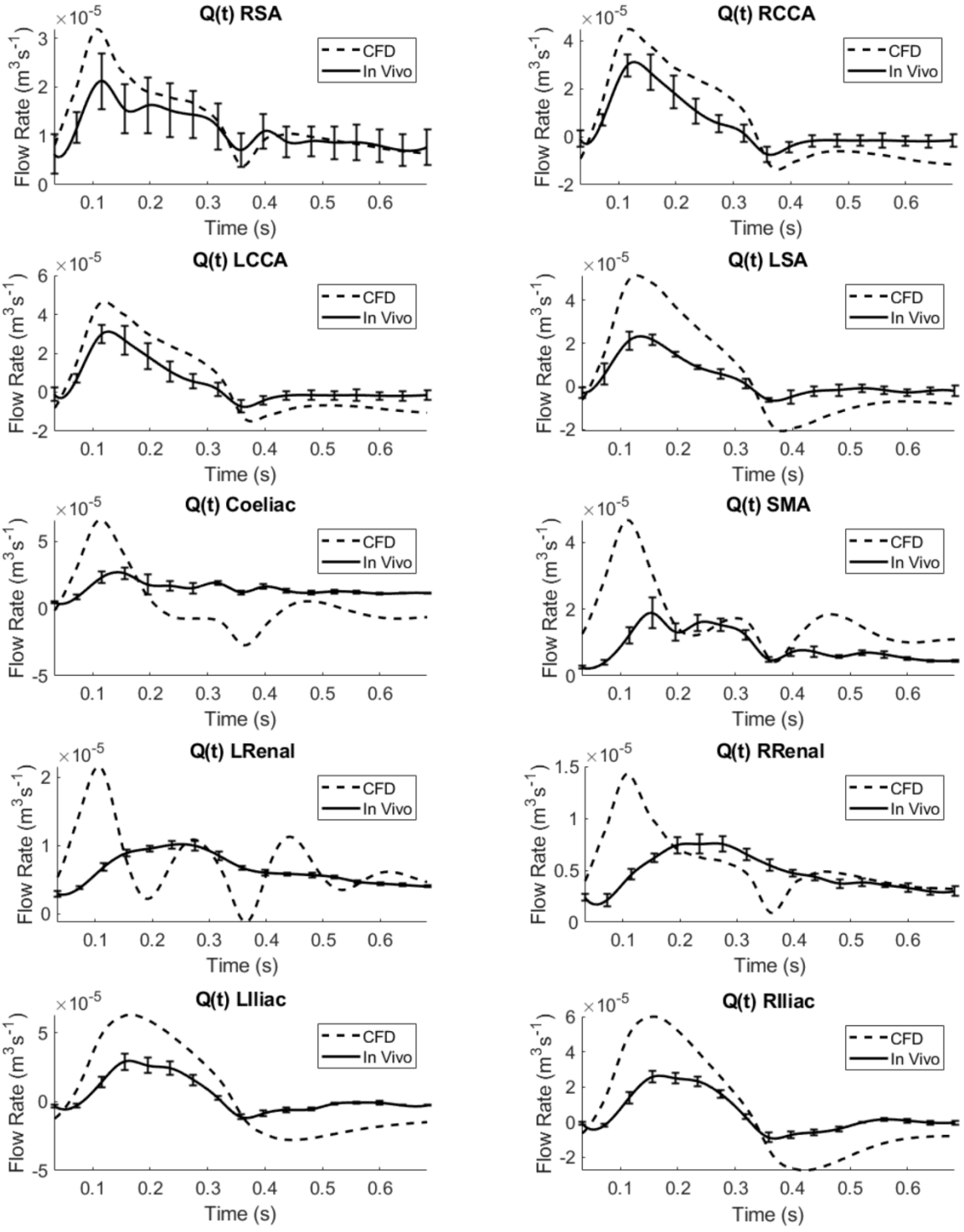

***Figure A.20**: Instantaneous flow waveforms as derived from CFD models (dashed line) and in vivo 4D Flow-MRI data (dashed line) at each terminal branch of the thoracic aorta of patient 3. Error bars represent mean ± standard deviation.*

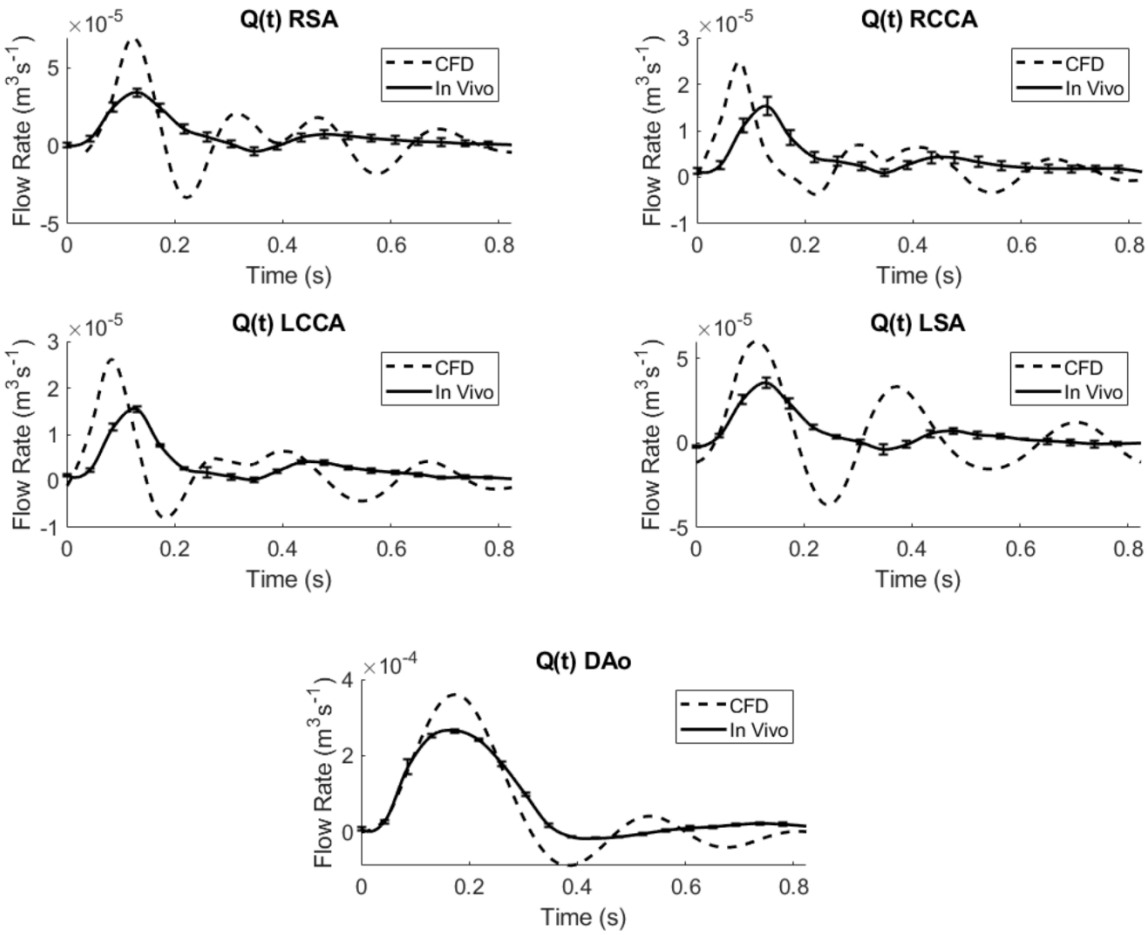

Figure A.21*: Instantaneous flow waveforms as derived from CFD models (dashed line) and in vivo 4D Flow-MRI data (dashed line) at each terminal branch of the thoracic aorta of healthy volunteer 1. Error bars represent mean ± standard deviation.*

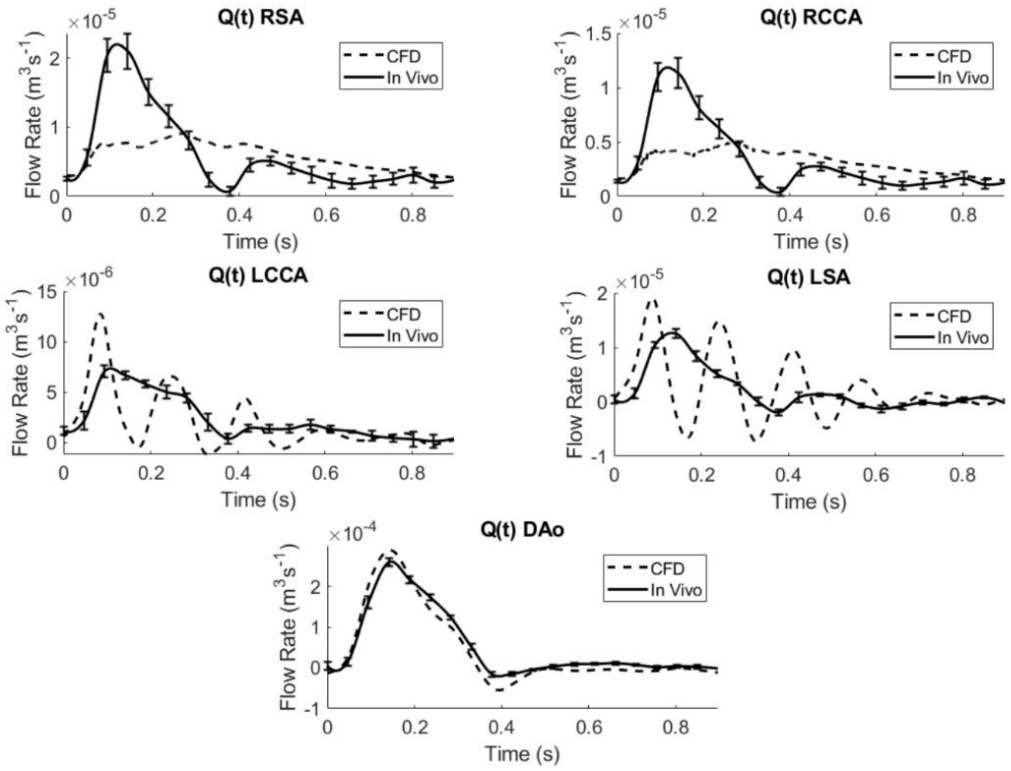

Figure A.22*: Instantaneous flow waveforms as derived from CFD models (dashed line) and in vivo 4D Flow-MRI data (dashed line) at each terminal branch of the thoracic aorta of healthy volunteer 2. Error bars represent mean ± standard deviation.*

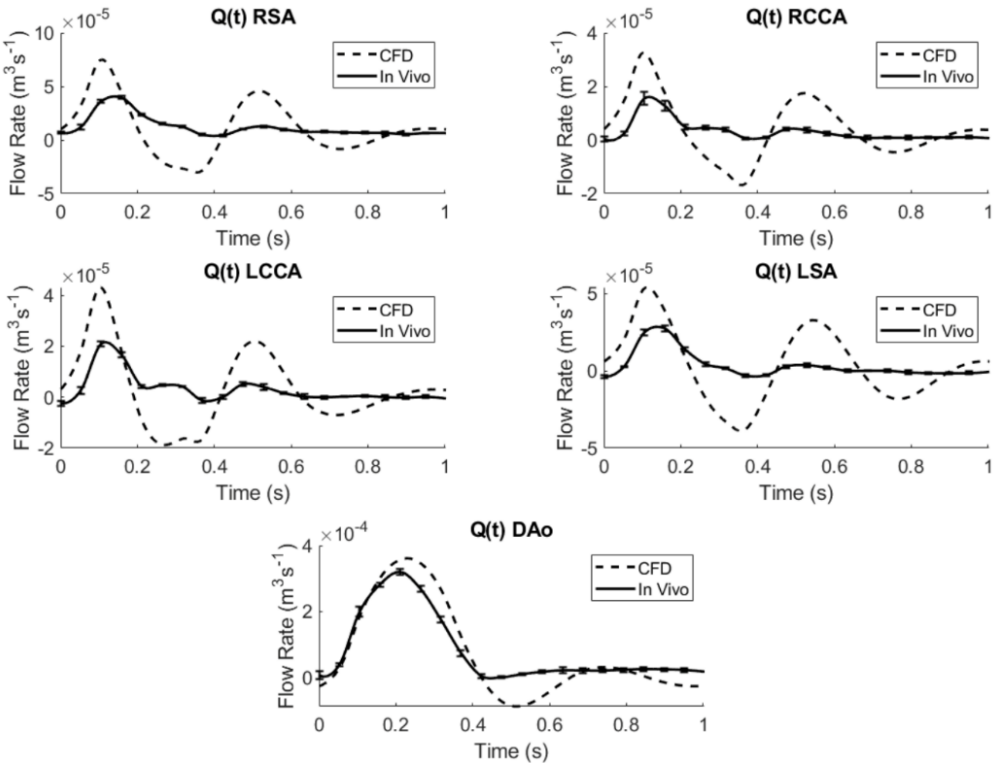

Figure A.23*: Instantaneous flow waveforms as derived from CFD models (dashed line) and in vivo 4D Flow-MRI data (dashed line) at each terminal branch of the thoracic aorta of healthy volunteer 3. Error bars represent mean ± standard deviation.*

7.8 Appendix B.2 Sensitivity Analysis

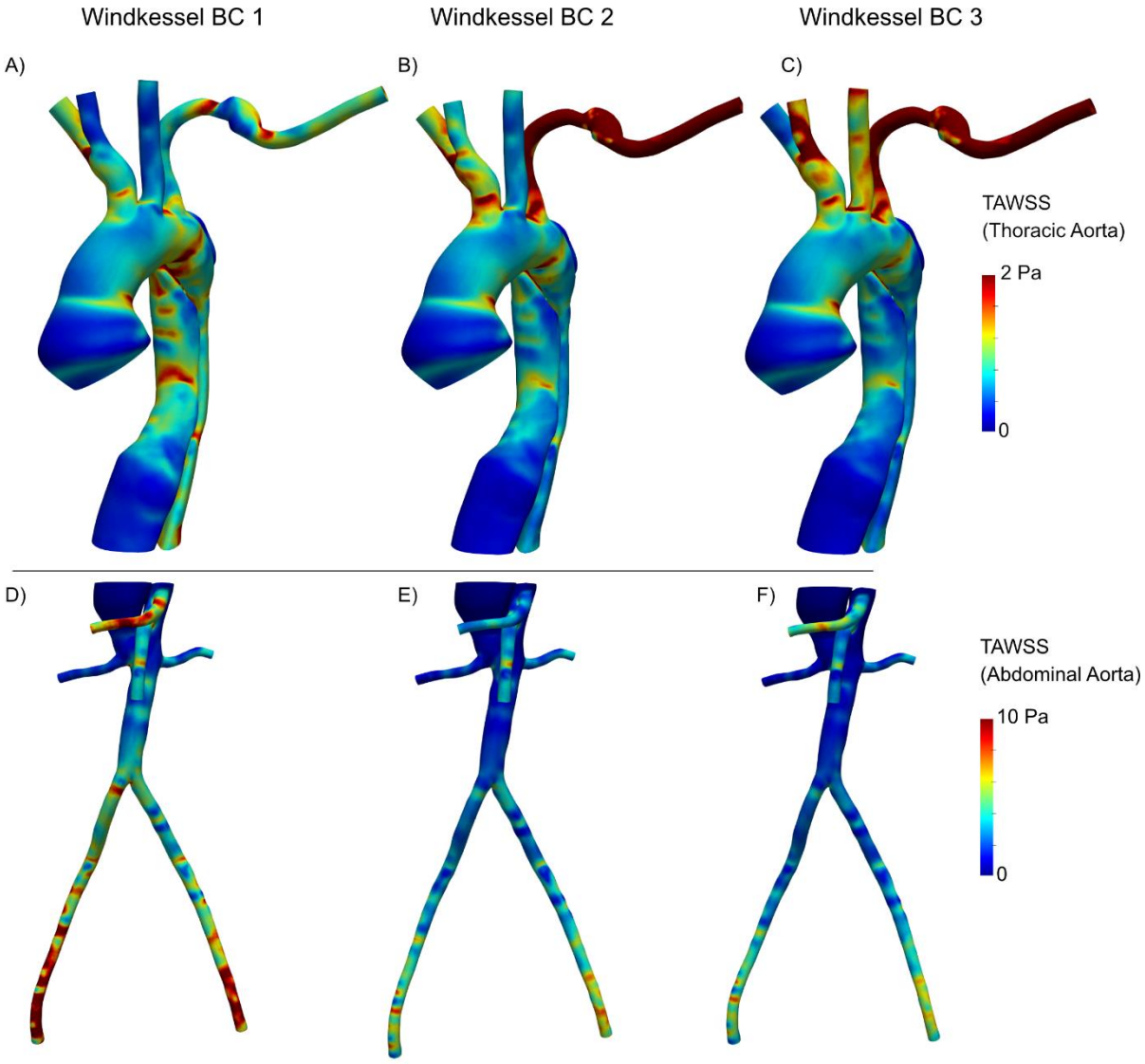

Figure A.24: *Time averaged wall shear stress throughout the geometry of patient 4 as a result of 0D-3D CFD modelling with the prescription of boundary condition combination A,D) 1, B,E) 2, and C,F) 3.*

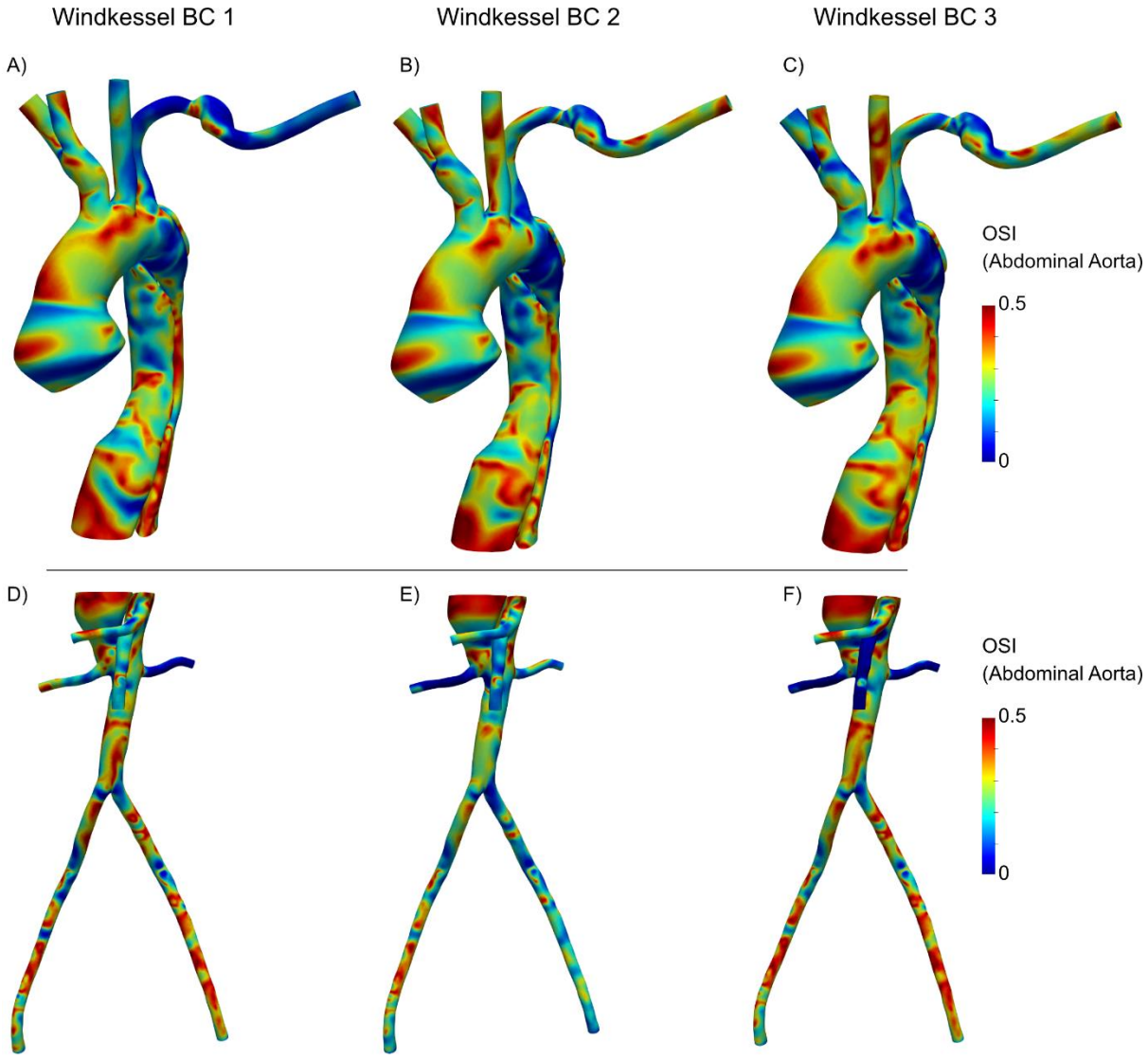

Figure A.25: *Oscillatory shear index throughout the geometry of patient 4 as a result of 0D-3D CFD modelling with the prescription of boundary condition combination A,D) 1, B,E) 2, and C,F) 3.*

7.9 Appendix B.3 Turbulence Intensity

Table A.19: *Turbulence intensity prescribed at the inlet and outlet of each CFD simulation.*

	Turbulence Intensity (%)		
Branch	**Patient 1**	**Patient 2**	**Patient 3**
Inlet	6.70	6.82	7.09
RSA	7.86	7.90	7.51
RCCA	8.21	8.40	8.08
LCCA	7.53	8.16	8.13
LSA	7.54	8.16	8.72
SMA	7.11	7.50	7.74
Coeliac	7.30	7.86	7.47
Lrenal	7.58	7.93	7.64
Rrenal	8.03	7.75	7.85
Liliac	7.87	7.55	8.81
Riliac	7.74	8.01	8.61